Imperial College London

Examining the Effect of the Environment on the Creep and Creep-Fatigue Properties of Type 316H Stainless Steel

by

Mustafa Nasser

A thesis submitted for the degree of Doctor of Engineering of
Imperial College London
and
Diploma of Imperial College

September 2017

Declaration of Originality

I hereby declare that the work presented in this thesis is original and has not been submitted for a degree or diploma at any other university or institution. Information derived from the published and unpublished work of others has been acknowledged in the text and references are given in the list of sources.

Mustafa Nasser
September 2017

Copyright Declaration

The copyright of this thesis rests with the author and is made available under a Creative Commons Attribution Non-Commercial No Derivatives licence. Researchers are free to copy, distribute or transmit the thesis on the condition that they attribute it, that they do not use it for commercial purposes and that they do not alter, transform or build upon it. For any reuse or redistribution, researchers must make clear to others the licence terms of this work.

Abstract

The United Kingdom's advanced gas-cooled nuclear reactors (AGR) contain many 316H stainless steel components that operate within high temperature carbon dioxide gaseous environments. Recently, cracking has been discovered within some of these components which could not be predicted by current assessment methodologies. Further examination has shown that this premature cracking is due to the interaction between stainless steel and AGR gas environment, resulting in significant carburisation which, has not previously been considered as a potential degradation mechanism. Gaining an understanding of how carburisation affects mechanical properties (under high temperature creep and fatigue conditions in particular) is essential, as it underpins the ability to accurately conduct component lifetime assessment. This is vital to substantiate a nuclear safety case and therefore this plays a crucial role in ensuring continued plant operation.

In this thesis, the influence of AGR gas carburisation on the tensile, creep and fatigue properties of 316H has been investigated experimentally. Under laboratory test conditions, it has been found that carburisation generally results in a degradation of material performance (creep and fatigue life) at high temperatures, the extent of which has shown to be dependent on the applied loading scenario. This is driven by a substantial loss of surface ductility within the outer hardened layer and the subsequent premature initiation of widespread surface cracking. The reduced ductility is a consequence of the carburisation process that leads to significant intergranular carbide precipitation, weakening grain boundary strengths at the surface.

The ability to detect carburisation on components in-situ would be of significant advantage to component lifetime assessment and this was explored through application of a magnetic non-destructive evaluation tool. Through experimental measurement and finite element analysis, it was found that the presence and severity of carburisation could be evaluated non-destructively under controlled laboratory conditions. Application of this technique to plant components was however concluded to invite significant challenges due to the inherent variability of carburised material across plant.

The work of this thesis has significantly contributed to further the understanding of how carburisation may affect component lifetime with the findings directly influencing

preliminary R5 structural integrity recommendations on how to treat carburisation in plant. Further testing is required to fully substantiate the effect of carburisation across a greater range of stresses and strains and recommendations for future research have been made.

Acknowledgements

I would like express my sincere gratitude to my academic supervisors Dr. Catrin Davies and Prof. Kamran Nikbin for their continuous support and encouragement throughout the course of this research. Your knowledge and advice has been invaluable and is greatly appreciated.

I would like to thank EDF Energy Nuclear Generation for providing me with the opportunity to undertake this EngD. In particular, I am thankful for the sustained guidance and technical input from my industrial supervisors Prof. David Dean and Dr. Marc Chevalier.

I would also like to thank Prof. George Webster and Dr. Peter Skelton for sharing their vast knowledge of high temperature fracture mechanics and fatigue testing during this project.

Above all, I am forever grateful for the extraordinary dedication and support that my parents have given me throughout life. The sacrifices you have made have allowed me to realise my achievements and for this, I am forever indebted.

Contents

1. Introduction **1**

1.1. Background and Motivation for Research 1
1.2. Research Aim and Objectives 2
1.3. Thesis Structure 3

2. Theoretical Background **5**

2.1. Introduction 5
2.2. Deformation Mechanisms 5
2.3. Elastic-Plastic Deformation 5
2.4. Ramberg-Osgood Material Model 7
2.5. Fundamental Fracture Mechanics 8
2.5.1. Linear Elastic Fracture Mechanics 8
2.5.2. Energy Balance Criterion 9
2.5.3. Stress Intensity Factor 10
2.5.4. Limited Crack Tip Plasticity 10
2.5.5. Elastic-Plastic Fracture Mechanics 11
2.5.6. The J Contour Integral 11
2.6. Creep Deformation 12
2.6.1. Power-Law Creep 16
2.6.2. Creep Fracture and Damage 17
2.7. Fatigue Degradation 18
2.7.1. Stress-Based Approach 18
2.7.2. Strain-Based Approach 21
2.7.3. Fatigue Fracture and Damage 26

3. Carburisation of Stainless Steels **30**

3.1. Introduction 30
3.2. Industrial Gas Carburisation 30
3.3. AGR Gas Carburisation 33
3.3.1. Introduction & Historical Background 33
3.3.2. Mechanism 35
3.4. Effect of Carburisation on Mechanical Properties 38

3.5. Discussion 44

4. Material and Preconditioning **45**
4.1. Introduction 45
4.2. Ex-Service As-Received Material 45
4.3. Preconditioning 49

5. Effect of Carburisation on Creep **53**
5.1. Introduction 53
5.2. Influence of Carburisation on Tensile Response 54
5.2.1. Introduction 54
5.2.2. Tensile Properties 54
5.2.3. Derivation of Ramberg-Osgood Constants 55
5.2.4. Fracture Behaviour 58
5.3. Modelling Cracking within Carburised 316H 60
5.3.1. Introduction 60
5.3.2. Model Configuration 60
5.3.3. Model Validation 61
5.3.4. Elastic Crack Analysis 62
5.3.5. Elastic-Plastic Constraint Analysis 64
5.4. Effect of Carburisation on Creep Behaviour 66
5.4.1. Creep Test Setup 66
5.4.2. Load-up Behaviour 68
5.4.3. Creep Rupture Testing 70
5.4.4. Interrupted Creep Testing 77
5.4.5. Creep Strain - Crack Length Relationship 80
5.4.6. Review of Creep Data 81
5.4.7. Effect of Thermal Ageing 81
5.5. Discussion 83
5.5.1. Tensile Response 83
5.5.2. Creep Behaviour 84
5.6. Conclusions 86

6. Effect of Carburisation on Fatigue **88**
6.1. Introduction 88
6.2. High Temperature Fatigue Test Setup 89
6.2.1. Introduction 89
6.2.2. Instron Thermo-Mechanical Fatigue (TMF) Machine 89
6.2.3. Load Frame Alignment 94
6.2.4. Test Procedure 97

6.3. Fatigue and Creep Fatigue Testing 100
6.3.1. Fatigue 102
6.3.2. Creep-Fatigue 107
6.3.3. Comparison of Inelastic Strain Energy Density 113
6.3.4. Metallography 115
6.4. Discussion 127
6.4.1. Fatigue 127
6.4.2. Creep-Fatigue 128
6.5. Conclusions 130

7. Detecting Carburisation via Magnetic NDE Measurement 131
7.1. Introduction 131
7.2. Carburisation and Induced Magnetism 131
7.3. Magnetic Measurement 132
7.3.1. Feritscope 133
7.3.2. Surface Measurement 134
7.3.3. Through Depth Measurement 138
7.4. Multi-Frequency Finite Element Modeling 139
7.4.1. Introduction 139
7.4.2. Modeling the Feritscope 140
7.4.3. Mesh Configuration and Sensitivity Analysis 142
7.4.4. Model Validation 143
7.4.5. Multi-Frequency Feritscope 144
7.5. Discussion 148
7.5.1. Magnetic Measurement 148
7.5.2. Multi-Frequency Feritscope 149
7.5.3. Application to Plant Components 150
7.6. Conclusions 151

8. Thesis Review and Future Work 152
8.1. Thesis Review 152
8.2. Recommendations for Future Work 155

Bibliography 157

Appendix A. LCF Alignment Reports 170

Appendix B. Four-Point Bend Digital Image Correlation 172

List of Figures

2.1. Elastic loading of a uniaxial bar in tension. 6
2.2. The response of a elastic-plastic strain hardening material under monotonic tensile loading conditions. 7
2.3. Primary modes of loading to enable crack propagation within fracture mechanics. 9
2.4. Creep deformation mechanism map for 316 stainless steel containing a 50 µm grain size [9]. 13
2.5. The mechanism of dislocation creep showing the diffusion assisted climb of an edge dislocation around an inclusion. 14
2.6. The mechanism of diffusion creep (Nabarro-Herring) in a single grain showing the movement of vacancies and atoms that result in grain elongation and macroscopic creep deformation, adapted from [10]. 15
2.7. Illustration of a typical creep curve generated from a uniaxial specimen held under a constant tensile load. 16
2.8. Section taken through a sample of 316H crept for 4000 hours, showing extensive voiding and intergranular microcracking (current work). 17
2.9. Stress histories from stress-controlled constant amplitude cycling in (a) completely reversed (b) non-zero mean (c) positive mean stress states. . 20
2.10. Illustrated example S-N curve for a material under various stress ratios. 20
2.11. Illustration of typical hysteresis loop resulting from strain controlled cyclic testing. 22
2.12. (a) Hardening and (b) softening response of a material subjected to continuous strain cyclic loading. 23
2.13. Comparison of monotonic and cyclic stress-strain curves. 24
2.14. Coffin-Manson equation describing the relationship between plastic strain range and cycles to failure for the LCF regime. 25
2.15. Graphical representation of the total strain life equation. 26
2.16. Stage I & II fatigue crack propagation. 27
2.17. PSB formation mechanism during cyclic loading leading to the creation of initiation sites at the surface. 27

2.18. Striations present on the fracture surface of a 316H fatigue specimen tested under high temperature LCF conditions (current work). 28

3.1. Metallographic section of carburised 316 taken from [23]. 31
3.2. Illustration of typical carbon concentration and hardness profiles. 32
3.3. Hardness trace taken through an ex-service 316H component [39] in close proximity to a surface crack. 33
3.4. Carbon measurement through ex-service carburised sections under different exposure times and temperatures (a) 18kH @ 560°C (b) 49kH @ 560°C and (c) 39kH @ 600°C [43]. 34
3.5. Overview of the AGR gas carburisation mechanism, adapted from [46]. . 36
3.6. Section taken through an ex-service carburised component, demonstrating the effect of a healing layer (darker grey) on carburisation behaviour [44]. 36
3.7. SEM images taken of an ex-service carburised component showing (a) the carburisation of grain boundaries & (b) the distribution of chromium content via EDX mappping [43]. 37
3.8. SEM image of an ex-service component comapring grain boundary decoration in (a) the carburised region and in (b) the bulk material [43]. . . 38
3.9. Optical microscopy of a 9Cr1Mo carburised specimen surface after tensile testing showing widespread intergranular surface cracking taken (a) towards and (b) away from the fracture surface [59]. 39
3.10. Micrographs of 9Cr1Mo creep specimens tested at in a vacuum environment (a) 200MPa Uncarburised (b) 200MPa Carburised (c) 165MPa Carburised (d) 155MPa Carburised (e) 120MPa Carburised [61]. 40
3.11. Widespread surface cracking from low cycle fatigue testing on oxidised 9Cr1Mo steel. [62] 41
3.12. Creep damage across carburised grain boundaries in HK40 steel [70]. . . 42
3.13. Fractography of (a) untreated and (b) low temperature carburised 316 fatigue specimens showing the initiation of sub-surface cracking below the carburised case [77]. 43

4.1. 316H header HRA 1C2/3, cast 55915 prior to sectioning and sample extraction, red lines denoting cutting planes [83]. 47
4.2. Uniaxial (a) creep (b) LCF and (c) Instron LCF specimen design. 48
4.3. Focused Ion Beam cross sections of 316 specimens oxidised at 550°C for 500h with (a) OPS polish and (b) 600-grit SiC ground suface finishes [84]. 49
4.4. Hardness and carbon profiles of preconditioned carburised specimens taken at various exposure times at 600°C [43]. 51

4.5. Metallographic section taken through a preconditioned carburised specimen at a 3kH exposure (current work). 51
4.6. A comparison of hardness traces taken through both as-received and preconditioned 316H (current work). 52

5.1. A comparison of the tensile response of as-received and preconditioned carburised 316H based on (a) engineering and (b) true stress-strain at 550°C. 55
5.2. Power-law fits to plastic strain data derived from tensile testing on (a) as-received and (b) preconditioned material shown alongside Ramberg-Osgood fits (c)(d) to tensile data. 56
5.3. Ramberg-Osgood fits (a) (b) to tensile data for as-received, preconditioned and pure carburised 316H (shown at two different strain ranges). 57
5.4. (a) Preconditioned and (b) as-received samples surfaces after high temperature tensile testing at 550°C. 58
5.5. Micrograph taken from a preconditioned tensile specimen showing (a) (b) widespread intergranular surface cracking along the entire gauge length. 59
5.6. SEM images taken of the fracture surface from a preconditioned tensile specimen showing the difference in failure mode of carburised and bulk 316H. 59
5.7. An overview of the finite element tensile model showing the boundary conditions and crack tip mesh configuration. 61
5.8. A comparison of the tensile curves of (a) as-received and (b) preconditioned materials from tensile testing and FE modelling. 62
5.9. A comparison of K values over increasing crack lengths for (a) single cracked and (b) multi-cracked LEFM finite element models. 63
5.10. Crack tip stress fields in preconditioned material within a single crack elastic FE model. 63
5.11. Crack tip stress fields in preconditioned material within a multi-crack elastic FE model. 64
5.12. A comparison of principal stresses extracted from FE modelling of an in-tact carburised layer within a tensile preconditioned sample. 65
5.13. A comparison of principal stresses extracted from FE modelling of a partially cracked carburised layer within a tensile preconditioned sample. 65
5.14. A comparison of principal stresses extracted from FE modelling of a fully cracked carburised layer within a tensile preconditioned sample. 66
5.15. Experimental setup for high temperature uniaxial creep testing. 67
5.16. (a) Creep load-up data (b) compared with derived Ramberg-Osgood material models from Section 5.2.3. 69

5.17. Creep rupture curves of as-received and preconditioned specimens tested at 300 MPa displayed in (a) absolute and (b) normalised form. 72
5.18. Creep rupture curves of as-received and preconditioned specimens tested at 320 MPa displayed in (a) absolute and (b) normalised form. 73
5.19. Comparison of normalised creep behaviour at 300 and 320 MPa. 73
5.20. Comparison of failed creep sample surfaces from as-received ASR1 (a) and preconditioned C1 (b). 74
5.21. Half gauge length section view taken from preconditioned creep rupture specimen C1. 75
5.22. Surface metallography taken from creep samples (a) C1 (preconditioned) and (b) ASR1 (as-received). 75
5.23. Oxidation of surface crack mouths from specimen C1 (a) near to and (b) far from the fracture surface. 75
5.24. Fracture surfaces of (a)(b) ASR1 and (c)(d) C1 showing the difference in creep failure mode between as-received and preconditioned material. . . 76
5.25. Interrupted creep test specimen curves at (a) 260 and (b) 220 MPa. . . 78
5.26. Micrographs of interrupted creep specimens (a) C4 and (b) C3 showing the contrast in surface crack density at different creep strains. 79
5.27. Maximum measured crack depth within interrupted creep specimens (a) C3 and (b) C4 showing the contrast in crack face oxide thickness. 79
5.28. Maximum measured crack depth within interrupted creep specimens (a) C5 and (b) C6 showing limited surface damage. 79
5.29. Maximum observed crack length plotted against (a) creep and (b) total strain in interrupted preconditioned creep specimens; the dotted line denotes the interface between the carburised layer and bulk material. . . 80
5.30. True stress plotted against (a) rupture time and (b) minimum creep rate for all specimen test data. 82

6.1. Instron TMF system overview, image adapted from [94]. 90
6.2. Hydraulic TMF grips. 91
6.3. LCF sample adapters. 91
6.4. High temperature LCF extensometer setup. 92
6.5. Optimized induction coil design resulting in a maximum temperature variation of 1°C. 93
6.6. Possible sources of misalignment in fatigue testing (a) concentricity, (b) angularity and (c) a combination of both. 94
6.7. Instron AlignPro fixture, adapted from [94]. 95
6.8. Bespoke alignment cell fabricated for use with LCF adapters. 96

6.9. Dial gauge used to check horizontal movement of the servo-hydraulic actuator. 97
6.10. Illustration of thermocouple attachment to as-received LCF specimens. . 98
6.11. An illustration of the effect of PID tuning on requested waveform values. 99
6.12. Cyclic stress response of as-received and preconditioned materials under $\Delta\varepsilon = \pm 1.2\%$ at 550°C. 103
6.13. Cyclic stress response of as-received and preconditioned materials under $\Delta\varepsilon = \pm 0.9\%$ at 550°C. 103
6.14. Cyclic stress response of preconditioned 316H under $\Delta\varepsilon = \pm 0.6\%$ and $\Delta\varepsilon = \pm 0.4\%$ at 550°C. 104
6.15. Stress strain response of as-received and preconditioned materials under $\Delta\varepsilon = \pm 1.2\%$ at (a) first and (b) stabilised cycles. 104
6.16. Stress strain response of as-received and preconditioned materials under $\Delta\varepsilon = \pm 0.9\%$ at (a) first and (b) stabilised cycles. 105
6.17. Stress strain response of 7 mm preconditioned samples under $\Delta\varepsilon = \pm 0.6\%$ and $\Delta\varepsilon = \pm 0.4\%$ at (a) first and (b) stabilised cycles. 105
6.18. Strain-Life fatigue data for as-received, preconditioned and thermally aged materials. 106
6.19. Cyclic stress response of as-received and preconditioned materials under creep-fatigue conditions at $\Delta\varepsilon = \pm 1.2\%$ with a 60 minute hold time. . . 108
6.20. Cyclic stress response of preconditioned samples under fatigue conditions at $\Delta\varepsilon = \pm 1.2\%$ with and without a 60 minute hold time. 108
6.21. Cyclic stress response of preconditioned samples under fatigue conditions at $\Delta\varepsilon = \pm 0.9\%$ with and without a 60 minute hold time. 109
6.22. Stress strain response of as-received and preconditioned materials under $\Delta\varepsilon = \pm 1.2\%$ at (a) first and (b) stabilised cycles. 109
6.23. Stress strain response of preconditioned samples under $\Delta\varepsilon = \pm 1.2\%$ at (a) first and (b) stabilised cycles with and without a 60 minute hold time. 110
6.24. Stress strain response of preconditioned samples under $\Delta\varepsilon = \pm 0.9\%$ at (a) first and (b) stabilised cycles with and without a 60 minute hold time. 110
6.25. Stress relaxation during four stabilised cycles for as-received and preconditioned creep-fatigue samples. 111
6.26. Strain-Life fatigue data for as-received, preconditioned and thermally aged materials both with and without hold times. 112
6.27. Illustration of inelastic strain energy density taken from a uniaxial cyclic hysteresis loop. 113
6.28. A comparison of the inelastic strain energy density against the number of cycles to failure for as-received and preconditioned specimens with and without hold times. 114

6.29. A comparison of stabilised inelastic strain energy density against the number of cycles to failure for as-received, preconditioned and carburised 316H. 115
6.30. Comparison of fatigue sample surfaces (a) ASRF2, as-received and (b) CF2, preconditioned carburised. 116
6.31. X-Ray tomogram of specimen CF2 showing multiple major surface cracks that had initiated within the carburised layer. 117
6.32. Axial tomogram showing multiple crack initiation sites and radial propagation in sample CF2. 117
6.33. Section metallography of preconditioned fatigue sample CF2 displaying transgranular fatigue fracture. 118
6.34. Fractograph of carburised fatigue specimen CF1 ($\Delta\varepsilon = 1.2\%$) showing the presence of (a)(b) multiple fatigue ratchet marks originating at the surface, (c) difference in failure modes and (d) striation-like features. . 119
6.35. Fractograph of carburised fatigue specimen CF3 ($\Delta\varepsilon = 0.6\%$) showing the presence of (a) multiple ratchet marks (b) river markings at the surface, (c) difference in failure modes and (d) striation like features. 120
6.36. Section of the fracture surface of CF1 ($\Delta\varepsilon = 1.2\%$) showing transgranular fatigue failure across the primary crack front. 121
6.37. Section of the fracture surface of CF3 ($\Delta\varepsilon = 0.6\%$) showing transgranular fatigue failure across the primary crack front. 121
6.38. Section taken of the outer edge from sample CF4 $\Delta\varepsilon = 0.4\%$ showing no widespread surface cracking and an intact inner spinel oxide layer. . . . 121
6.39. Gauge length of samples (a) CCF1 & (b) CCF2 showing widespread surface cracking that had propagated into the bulk material. 122
6.40. Fractograph of as-received creep-fatigue specimen ASRCF1 ($\Delta\varepsilon = 1.2\%$) with a 60 minute hold time, showing the presence of (a) multiple ratchet marks (b) fatigue striations at the surface and the difference in crack morphology in areas of (c) overload and (d) fatigue fracture. 123
6.41. Fractograph of carburised creep-fatigue specimen CCF1 ($\Delta\varepsilon = 1.2\%$) with a 1 hour hold time showing the presence of (a) (b) multiple ratchet marks at the surface, difference in fatigue failure modes within the (c) carburised layer (brittle) and in the (d) bulk material (striations). . . . 124
6.42. Fractograph of carburised fatigue specimen CCF2 ($\Delta\varepsilon = 0.9\%$) with a 1 hour time, showing the presence of multiple ratchet marks and cracks at the surface and the difference in failure mode within the (a) carburised, (c) bulk fatigue and (d) overload fracture surfaces. 125
6.43. Major fatigue crack section within ASRCF1 $\Delta\varepsilon = 1.2\%$ showing mixed trans- and intergranular fracture. 126

6.44. Section taken of the fracture surface of sample CCF1 $\Delta\varepsilon = 1.2\%$ showing mixed trans- and intergranular fracture across the crack front with crack initiation and growth from both sides. 126
6.45. Section taken of the fracture surface of sample CCF2 $\Delta\varepsilon = 0.9\%$ showing mixed trans- and intergranular fracture. 126

7.1. Illustration of Feritscope magnetic measurement principle. 133
7.2. Magnetic inspection grid. 135
7.3. Magnetic surface measurements across as-received, ex-service carburised and preconditioned carburised 316H. 136
7.4. Sections taken from samples (a) AS1 (b) EX1 (c) EX2 (d) P1. 137
7.5. Average measured oxide thickness plotted against the averaged magnetic response from samples AS1, EX1, EX2 and P1. 137
7.6. Preconditioned plate (a) prior to measurement (b) after 50 µm of oxide removal (c) after carburised layer removal. 138
7.7. Through depth magnetic profile of preconditioned carburised material. . 139
7.8. Feritscope finite element model configuration. 140
7.9. Material model of the magnetic permeability of carburised 316H based on trends observed from hardness testing. 141
7.10. Feritscope model mesh configuration. 142
7.11. Feritscope model mesh sensitivity study. 143
7.12. A comparison of experimentally measured and modelled through depth magnetic profiles for preconditioned carburised 316H. 144
7.13. Comparison of the effect of increasing carburisation depth on different Feritscope measurement frequencies. 146
7.14. Comparison of the effect of increasing oxide depth on different Feritscope measurement frequencies. 146
7.15. Effect of increasing excitation frequency on the Feritscope response to samples with different depths of carburisation. 147
7.16. Set versus predicted carburised layer depths from multi-frequency magnetic measurement. 147
7.17. The effect of frequency on skin depth for modelled carburised and oxide layers. 148

B.1. Difference in distributed moment and maximum tensile stress between (a) three and (b) four point bend testing. 173
B.2. Illustration of the DIC measurement technique. 174
B.3. Illustration of the DIC measurement technique. 175
B.4. Speckle pattern on a carburised four point bend specimen showing the typical facet size computed using DIC. 176

B.5. The strain field of a carburised bend specimen captured using digital image correlation, showing the onset of widespread cracking at approximately 0.65% bending strain. 177
B.6. The evolution and growth of surface cracks during four-point bend testing of carburised 316H and resulting localized crack tip strain fields. 178

List of Tables

4.1. Chemical Composition of 316H as-received Header 1C2/3 (% WT) [83]. 47
4.2. Stages of specimen polishing prior to preconditioning [83]. 50

5.1. High temperature tensile properties of as-received and preconditioned carburised materials. 54
5.2. Ramberg-Osgood Constants fitted to tensile data for as-received and preconditioned materials with inferred pure carburised values. 55
5.3. Creep Test Matrix. 68
5.4. Creep Load-up Data. 69
5.5. Creep rupture and failure strain data. 72
5.6. Interrupted creep test matrix. 77
5.7. Uniaxial creep properties of as-received and preconditioned material. . . 81

6.1. TMF machine PID control variables for as-received and preconditioned fatigue specimens. 100
6.2. Fatigue and Creep-Fatigue Test Matrix. 101
6.3. Average stress relaxation during creep-fatigue testing. 111

7.1. Magnetic surface measurement test matrix. 135
7.2. Feritscope model material properties. 141

Nomenclature

α	Power Law Material Hardening Constant
β	Plastic Zone Constant
ΔW	Inelastic Strain Energy Density
$\Delta\sigma$	Stress Range
Δ_c	Axial Creep Displacement
$\dot{\varepsilon}^c$	Creep Strain Rate
$\dot{\varepsilon}^c_s$	Steady-State Creep Strain Rate
$\dot{\varepsilon}^c_{min}$	Minimum Creep Strain Rate
Γ	J Integration Contour
l_o	Original Sample Gauge Length
σ	Stress
σ^p_0	Normalising Plastic Stress
$\sigma^p_{0.2}$	0.2% Proof Stress
σ'_f	Fatigue Strength Coefficient
σ_a	Applied Stress
σ_a	Stress Amplitude
σ_e	Fatigue Endurance Limit
σ_m	Mean Stress
σ_y	Yield Stress
σ_{max}	Maximum Applied Stress
σ_{min}	Minimum Applied Stress

σ_{nom}	Nominal Stress
σ_{true}	True Stress
σ_{yy}	Stress Normal to a Crack
θ	Angle Relative to the Crack Plane
ε	Strain
ε^e	Elastic Strain
ε^p	Plastic Strain
ε_0^p	Normalising Plastic Strain
ε_f'	Fatigue Ductility Coefficient
$\varepsilon_{c,f}^{eng}$	Engineering Creep Failure Strain
$\varepsilon_{c,int}^{eng}$	Engineering Creep Interruption Strain
ε_{load}^{eng}	Engineering Loading Strain
ε_{load}^{eng}	True Loading Strain
$\varepsilon_{p,load}^{eng}$	True Plastic Loading Strain
ε_y	Yield Strain
$\varepsilon_{0.2}$	0.2% Proof Strain
A	Power Law Creep Temperature Dependent Strain Constant
a	Crack Length
A_c	Crack Area
A_f	Final Gauge Length Area
A_o	Original Gauge Length Area
A_p	Ramberg-Osgood Material Constant
B	Specimen Thickness
b	Fatigue Strength Exponent
B_r	Power Law Creep Temperature Dependent Rupture Constant
c	Fatigue Ductility Exponent

C_1	Basquin Equation Constant
D	Total Fatigue Damage Resulting from Miner's Rule
E	Elastic/Young's Modulus
G	Energy Release Rate
G_c	Critical Crack Resistance Force
H'	Cyclic Strength Coefficient
J	Elastic-Plastic Fracture Mechanics Parameter
J	Non-Linear Energy Release Rate per Unit Thickness
J_c	Critical Value of J
K	Stress Intensity Factor
K_C	Fracture Toughness of a Material
N	Power Law Plasticity Stress Exponent
n	Ramberg-Osgood Hardening Exponent
n'	Cyclic Hardening Exponent
N_f	Number of Fatigue Cycles to Failure
P	Applied Force
p	Basquin Equation Constant
Q	Stress Modified Activation Energy
R	Fatigue Stress/Strain Ratio
R	Universal Gas Constant
r	Radial Distance from the Crack Tip
r_p	Crack Tip Plastic Zone Radius
s	J Integral Traction Vector Length
T	Absolute Temperature
T_i	J Integral Traction Vector
T_m	Material Melting Temperature

t_r	Creep Rupture Time
t_{int}	Creep Interruption Time
U_a	Surface Energy
U_e	External Applied Energy
U_i	Internal Elastic Stored Energy
u_i	J Integral Displacement Vector
U_p	Potential Energy
v_r	Stress Rupture Exponent
W_s	Strain Energy Density
Y	Geometric Shape Function

1. Introduction

1.1. Background and Motivation for Research

Many engineering components are often required to operate under high temperature, high pressure conditions within aggressive environments for sustained periods of time. As a result, these components must be designed to resist any significant changes in material properties for the duration of their designated service life. Such changes are induced by modification of the inherent material microstructure and can often result in the premature damage and failure of components. It is therefore essential that these changes (and resulting effects on material properties) are well understood, to ensure that components can fulfil their design life safely. This is especially true within the nuclear power generation industry whereby the onus is on operators to comply with strict safety regulations.

The United Kingdom's commitment to reduce emissions targets combined with predictions of increased energy demand has led to the decision to extend the lifetime of its ageing fleet of advanced gas cooled (AGR) nuclear reactors. A proportion of these AGR's have been in operation for over 35 years, in excess of their original design lives of 25 or 30 years. For their continual operation, a safety case must be made and approved by the office of nuclear regulation (ONR) that substantiates the structural integrity of the plant and demonstrates that all risks have been reduced as low as reasonably practicable. Cracking within components has been discovered within some AGR reactors which could not be predicted by current assessment methodologies. To mitigate further damage, reactor operating temperatures have been lowered, reducing operating efficiency. Historically, these defects have been found in the super-heater regions of the steam boilers. Here, components are fabricated from type 316H austenitic stainless steel and are directly exposed to high pressure gas coolant at temperatures of around 550°C. At this temperature, type 316H becomes susceptible to both creep and creep fatigue degradation. This is especially true for nuclear power plant components owing to the varying loading conditions associated with plant operation, maintenance and shutdown. The coolant gas is a combination of carbon dioxide, carbon monoxide, methane,

hydrogen and water with carbon dioxide forming the major constituent. Constant exposure to the coolant gas has led to the AGR carburisation of some 316H components throughout life. This has resulted in the formation of a hardened outer surface layer which is thought to impact on component lifetime through the initiation of surface cracking, resulting from an increase in hardness and subsequent loss of material surface ductility.

Little is currently known about the effect of AGR gas exposure on the creep and fatigue properties of 316H and as a result, carburisation remains unaccounted for within structural integrity assessment procedures. It is essential that the influence of carburisation is well understood as it underpins the ability to accurately predict the lifetime of affected components and thus create a fully substantiated, robust plant safety case. To solve this, EDF Energy have embarked on a 4 year collaboration project aimed at investigating the effect of carburisation on the high temperature tensile, creep and fatigue properties of 316H: Environmental Impact on the Structural Integrity of Nuclear Components (ENVISINC), funded through Innovate UK [1]. The programme of work was split amongst five project partners: Imperial College London, EDF Energy, The University of Manchester, The University of Bristol and AMEC Foster-Wheeler. Imperial College's contribution largely fell on the work of this EngD thesis and was primarily concerned with experimental testing and the development of non-destructive evaluation (NDE) techniques. It is anticipated that the findings of this research will have a direct impact on the understanding of carburisation on components in plant, leading to modification of current high temperature structural integrity assessment procedures.

1.2. Research Aim and Objectives

The general aim of this research was to investigate the effects of carburisation on the high temperature mechanical properties of 316H stainless steel. Ideally, this would contribute to an increased understanding of the interaction between carburisation and damage initiation, under both creep and fatigue conditions. The specific objectives of the work were to:

1. Review the mechanisms of carburisation within stainless steels and identify how these could affect material properties under the influence of creep and fatigue.
2. Design, precondition and manufacture test specimens that accurately represented the effects of AGR gas carburisation, validating this against testing of ex-service carburised material.

3. Develop appropriate experimental methods to perform uniaxial creep, fatigue, creep-fatigue and four-point bend testing within high temperature environments (550°C) on both carburised and as-received materials.

4. Conduct a series of high temperature tensile, creep and fatigue tests to examine the effects of AGR carburisation on sample lifetime and damage initiation.

5. Explore the potential of non-destructive evaluation (NDE) in detecting and characterising the presence of carburisation on components in plant.

6. Provide key experimental data and additional understanding of carburisation to the ENVISINC project in order to help develop improved assessment methodologies within R5 procedures for predicting component lifetime under the influence of carburisation.

1.3. Thesis Structure

Chapter 2 introduces key theoretical concepts relevant to this research. Fundamental material behaviour and fracture mechanics theory is described alongside the mechanisms of creep and fatigue degradation.

A review of the carburisation of stainless steels and the resulting impact on mechanical properties is provided in Chapter 3 with a particular focus placed on AGR gas carburisation and it's interaction with creep and fatigue.

Chapter 4 describes the preconditioning process undertaken to replicate the effects of AGR gas carburisation on laboratory samples. A comparison to ex-service carburised material is made through metallographic examination, hardness testing and carbon profile measurement.

Chapters 5 and 6 investigate the impact of carburisation on the mechanical properties of 316H through a series of high temperature tensile, creep and fatigue tests. A comparison is made to as-received material which is then used alongside metallographic examination to evaluate the interaction between carburisation and damage initiation.

Chapter 7 explores the potential of a magnetic NDE technique in detecting and characterising the presence of carburisation on components in plant. The results from a series of preliminary surface and through depth laboratory measurements are presented which are then used to derive the magnetic properties of the carburised layer. These have then been implemented into a validated finite element (FE) model which is then used to assess the capability of magnetic NDE in predicting the depth of carburisation. The

potential limitations of this technique when attempting to conduct in situ component assessment are discussed.

A complete discussion is contained within each results chapter alongside the primary conclusions drawn. The entire thesis is summarised in Chapter 8 where the potential impact of this work on component lifetime assessment is discussed, followed by recommendations for future work.

Appendix A details a novel high temperature four-point bend test setup and presents the results of a preliminary crack detection exercise, aimed at determining the suitability of digital image correlation (DIC) in evaluating the tensile and creep ductility of carburised material. Results are compared to findings in Chapters 5 and 6.

2. Theoretical Background

2.1. Introduction

This chapter introduces the fundamental concepts applicable to material behaviour under high temperature plant conditions. Deformation theory of polycrystalline metals is described alongside the mechanisms of creep and fatigue degradation relevant to this research.

2.2. Deformation Mechanisms

When designing engineering components against failure, it is essential to possess a thorough understanding of how materials respond to load and deform both instantaneously and over time. The response of most metals can be accurately predicted by using material properties alongside constitutive laws derived from experimental testing and observation. It is also important to consider a components operating conditions as this can highly influence material behaviour. Over time, the exposure to varying load histories, temperatures and environmental chemistries can give rise to additional forms of deformation and damage. This includes both creep and fatigue degradation and environmentally assisted cracking [2].

The following sections briefly introduce mechanics of materials deformation theory followed by a description of both creep and fatigue degradation alongside constitutive material models relevant to this research.

2.3. Elastic-Plastic Deformation

All metals deform when subjected to an external force. Consider the case of a cylindrical bar loaded in uniaxial tension, Figure 2.1. When a small load is applied to the bar that is lower than a certain limit intrinsic to the material itself (the elastic limit), the bar will deform elastically and will able to recover it's original dimensions upon

removal of all external force. This is because the applied load hence stress is not high enough to overcome the inter-atomic forces contained within the material's crystal lattice structure. This is known as elastic material behaviour and can be described in terms of the applied stress (σ) and resulting elastic strain (ε^e) using the relationship shown in Equation 2.1, where E is the material's elastic or Young's modulus. Essentially, this is a measure of material stiffness.

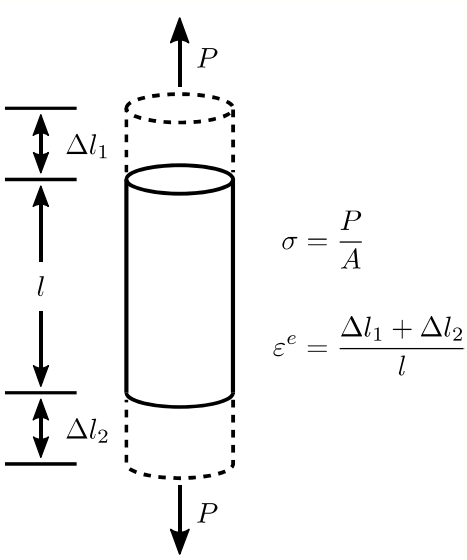


Figure 2.1: Elastic loading of a uniaxial bar in tension.

$$\varepsilon^e = \frac{\sigma}{E} \tag{2.1}$$

If the applied stress is increased above the elastic limit, permanent deformation of the cylinder will occur. This is known as plastic deformation and results from an irreversible disruption to the atomic lattice structure often in the form of dislocation movement above the yield stress (σ_y). When plastically deforming, the stress-strain response ceases to be linear and can often be described by a power law relationship such as that shown in Equation 2.2. Here, ε^p is the plastic strain, α is a material constant, N is the power law plasticity stress exponent and ε_0^p and σ_0^p are the normalising strains and stresses respectively. From Figure 2.2, it can be seen that the bar will exhibit an increasing resistance to deformation above the yield stress, commonly known as strain hardening. This strengthening via plastic deformation results from a progressive increase in the number and density of dislocations within the crystal lattice which impede further dislocation motion.

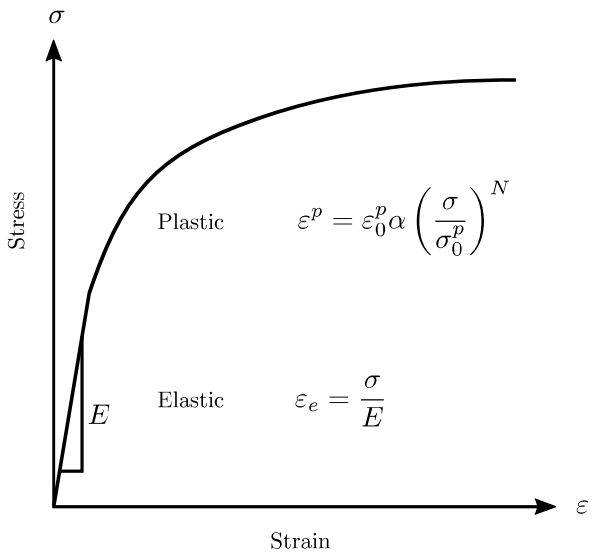


Figure 2.2: The response of a elastic-plastic strain hardening material under monotonic tensile loading conditions.

$$\varepsilon^p = \varepsilon_0^p \alpha \left(\frac{\sigma}{\sigma_0^p}\right)^N \tag{2.2}$$

Generally, for stresses below the yield stress, material behaviour can be described as linear whilst a power law relation characterises the response beyond yield.

$$\frac{\varepsilon}{\varepsilon_y} = \frac{\sigma}{\sigma_y} \; ; \quad \text{for} \;\; \sigma < \sigma_y \tag{2.3}$$

$$\frac{\varepsilon}{\varepsilon_y} = \left(\frac{\sigma}{\sigma_y}\right)^N \; ; \quad \text{for} \;\; \sigma > \sigma_y \tag{2.4}$$

2.4. Ramberg-Osgood Material Model

The entire monotonic response of a strain hardening material can be described by separately considering then summing the total elastic and plastic strains. This is commonly referred to as the Ramberg-Osgood material model which is shown in the equations below in non-dimensional (2.5) and uniaxial (2.6) form [3]. The constants A_p and n are obtained by fitting Equation 2.6 to experimental tensile data.

The Ramberg-Osgood model cannot be explicitly solved for stress, instead, it provides a single smooth stress-strain relationship across a range of stress values and does not define

an absolute, discontinuous yield point. Therefore, the normalising plastic stress in Equation 2.5 is often taken as the 0.2% proof stress ($\sigma^p_{0.2}$). This is the stress that corresponds to a plastic strain of 0.2% ($\varepsilon^p_{0.2}$) and is used to approximate the yield stress of a material. The power hardening relationship described in Equation 2.2 and Ramberg-Osgood model are essentially equivalent if the plastic strain dominates the total strain within the material, deeming the elastic contribution to be negligible.

$$\frac{\varepsilon}{\varepsilon^p_0} = \frac{\sigma}{\sigma^p_0} + \alpha \left(\frac{\sigma}{\sigma^p_0}\right)^n \tag{2.5}$$

$$\varepsilon = \frac{\sigma}{E} + A_p \sigma^n \tag{2.6}$$

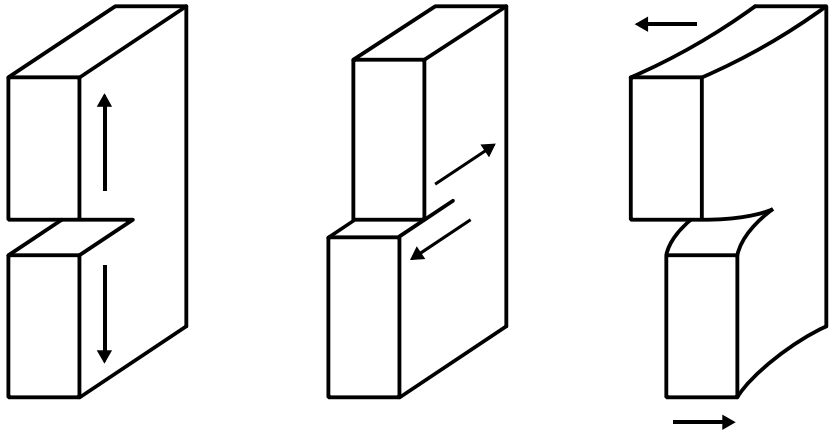
2.5. Fundamental Fracture Mechanics

In the power generation industry, the initiation and subsequent propagation of cracking is responsible for the failure of many components. It is therefore essential for engineers to understand how a crack can influence the surrounding body of material to ensure reliable design against failure. This involves resolving stresses and strains local to a crack tip to determine whether or not it will propagate and to what extent over a components lifetime. Crack tip stresses are often simplified into a single scaling parameter with a failure criterion derived from material properties. For linear-elastic materials this is known as the stress intensity factor K and for elastic-plastic materials (the majority of engineering metals), the J-integral. K and J concepts are described within the following sub-sections.

In fracture mechanics, there are three primary methods of applying a force to enable a crack to propagate: opening, sliding and tearing which are labelled Mode I, II & III respectively. These are illustrated in Figure 2.3 and identified by the subscript I, II or III on fracture mechanics parameters. Mode I corresponds to a force that is applied normal to the crack plane and is the typical crack loading scenario found within components in plant. As such, the remainder of this section is focused on Mode I loading.

2.5.1. Linear Elastic Fracture Mechanics

A crack contained within a body of material acts as a stress raiser meaning that the stresses local to the crack tip will be considerably higher than those far away (remote



Mode I Mode II Mode III

Figure 2.3: Primary modes of loading to enable crack propagation within fracture mechanics.

stresses). There are two common approaches used to described this behaviour within a linear-elastic material: the Griffith energy balance criterion and stress intensity factor approach, both of which are described below.

2.5.2. Energy Balance Criterion

It was proposed by Griffith [4] that fracture was based on the concept of a material reaching a minimum potential energy required to break atomic bonds in order to form new fracture surfaces. He postulated that the reduction in strain energy due to the formation of a crack must be equal to or greater than the increase in surface energy required by new crack faces. This reduction in strain energy is commonly referred to as the strain energy release rate (G) which, is the strain energy that is released per unit area of crack growth. This can be expressed by Equation 2.7 where a is the crack length, B is the plate thickness and U_e and U_i are the external applied energy and internal elastic stored energy respectively. A crack will grow when the energy release rate equals the critical crack resistance force (G_c) which is expressed in Equation 2.8 as a function of the surface energy (U_a) per unit area.

$$G = \frac{1}{B}\left(\frac{dU_e}{da} - \frac{dU_i}{da}\right) \tag{2.7}$$

$$G_c = \frac{1}{B}\left(\frac{dU_a}{da}\right) = 2\gamma \tag{2.8}$$

2.5.3. Stress Intensity Factor

Irwin formulated an equation to mathematically describe the stress field in the vicinity of an infinitely sharp crack tip [5] contained within a linear elastic material, shown in Equation 2.9. The first term on the right hand side describes the magnitude of crack tip stresses whilst the second their distribution in terms of a polar coordinate system relative to the radial distance from the crack tip (r) and angle from the crack plane (θ).

The stress intensity factor (K) is defined in Equation 2.10 where σ_a is the applied stress and Y is a dimensionless shape function dependent on the finite geometry of the body which, is used to account for the additional release in strain potential energy caused by the presence of a free surface boundary. Analytical solutions to calculate the value Y for a number of traditional crack geometries are readily availible within the literature and fracture mechanics design handbooks [6].

$$\sigma_{ij} = \frac{K}{\sqrt{2\pi r}} \cos\frac{\theta}{2}\left(1 - \sin\frac{\theta}{2}\sin\frac{3\theta}{2}\right) \tag{2.9}$$

$$K = \sigma_a Y \sqrt{a} \tag{2.10}$$

For a given cracked geometry, Y is constant so the value of K is entirely dependent on the externally applied stress and square root of the crack length. This means that K is effectively a scale factor that characterises the magnitude of stress at some coordinates near the creak tip and that the shape of stress distribution remains constant for all crack lengths. When K exceeds a critical value known as the fracture toughness of a material K_C, fracture will occur.

2.5.4. Limited Crack Tip Plasticity

The stress intensity factor approach is based on the assumption of elastic material behaviour and implies that as you progress towards the crack tip ($r \to 0$) the magnitude of stress approaches infinity ($\sigma_{yy} \to \infty$). However in reality, this stress is limited to at least the yield stress of the material thereby making the elastic assumption invalid for regions in close proximity to the crack tip, known as the plastic zone. If the plastic zone is relatively small, the elastic stress solution (hence K) remains valid and this is called small scale yielding.

Assuming an elastic-perfectly platic material, the area (r_y) ahead of a crack tip in which a material exceeds it's yield stress may be obtained from Equation 2.11. Under plane stress conditions $\beta = 2$ and for plane stress conditions $\beta = 6$. Irwin [7] showed through the equilibrium of internal and external forces, that the size of the plastic zone (r_p) is equal to twice that of r_y.

$$r_y = \frac{K^2}{\beta \pi \sigma_y^2} \tag{2.11}$$

The accuracy of the elastic stress field in small scale yielding conditions can be improved by using an effective crack length that accounts for the plastic zone. This is calculated by adding the plastic zone radius (r_p) to the crack length (a) and iteratively solving for K.

2.5.5. Elastic-Plastic Fracture Mechanics

LEFM and small scale yield conditions are only applicable to materials with very limited plasticity, confining the plastic zone to a relatively small region surrounding the crack tip. However, many engineering materials exhibit elastic-plastic behaviour resulting in significant plasticity and a plastic zone that dominates the K region. Here, LEFM is no longer valid so an alternative non-linear approach is required to characterise fracture behaviour: elastic-plastic fracture mechanics (EPFM). The realm of EPFM contains multiple methods that can be used to resolve the stresses and strains in close proximity to the crack tip (the J integral and crack mouth opening displacement). A commonly used method is the J contour integral which is described in the following section.

2.5.6. The J Contour Integral

The J contour integral was first introduced by Rice [8] and describes the behaviour of a crack within a non-linear material by idealising elastic-plastic deformation as non-linear elastic under monotonic load conditions. Providing no unloading occurs, the energy release rate per unit thickness in a non-linear material (J) has been shown to be equivalent to the energy release rate within an elastic material (G) and is defined in Equation 2.12. U_p is the potential energy whilst A_c is the crack area. It can be assumed that a crack will grow if the value of J reaches a critical value inherent to the material itself known as J_c. This is a measure of fracture toughness and is defined near the initiation of stable crack growth, often evaluated from experimental testing.

$$J = -\frac{\partial U_p}{\partial A_c} \tag{2.12}$$

The value of J can be calculated by taking a path independent anticlockwise line integral around the crack tip. This is known as the J-integral and is defined in Equation 2.13 where Γ is the anticlockwise integration contour, T_i is the traction vector, s is it's length, u_i is the displacement vector and W_s is the strain energy density.

$$J = \int_{\Gamma} (W_s dy - T_i \frac{\partial u_i}{\partial x} ds) \tag{2.13}$$

The strain energy density (W_s) is defined in Equation 2.14 where σ_{ij} and εij are the stress and strain tensors respectively.

$$W_s = \int_0^{\varepsilon_{ij}} \sigma_{ij} d\varepsilon_{ij} \tag{2.14}$$

2.6. Creep Deformation

Many AGR components operate under high temperature conditions leaving them susceptible to the time dependent deformation mechanism known as creep. This can result in the permanent deformation and damage of components so must be accounted for within structural integrity assessment procedures. The ability to accurately predict the long-term creep behaviour of materials continues to present a significant challenge to the power plant industry. This is because components can undergo significant microstructural changes during their service life which alter material properties and result in unexpected creep behaviour.

Creep deformation takes place when a material is subjected to a constant load (or displacement) above approximately one third of it's absolute melting temperature ($0.35T_m$). This arises from thermally activated microstructural changes that occur over time. Within polycrystalline metals there are thought to be two primary mechanisms that are responsible for this: diffusion and dislocation (or power-law) creep. The dominant mechanism is dependent on material properties and is a function of the applied stress and temperature. The relationship between stress, temperature and creep mechanism is often presented as a creep deformation mechanism map. An example for 316 stainless steel is shown in Figure 2.4. At relatively high temperatures ($> 0.5T_m$) and intermediate to high stresses, it can be seen that power-law creep is the dominant mechanism.

These conditions are representative of plant operation where the majority creep deformation falls under this regime and therefore dislocation creep is the primary mechanism of interest in this research.

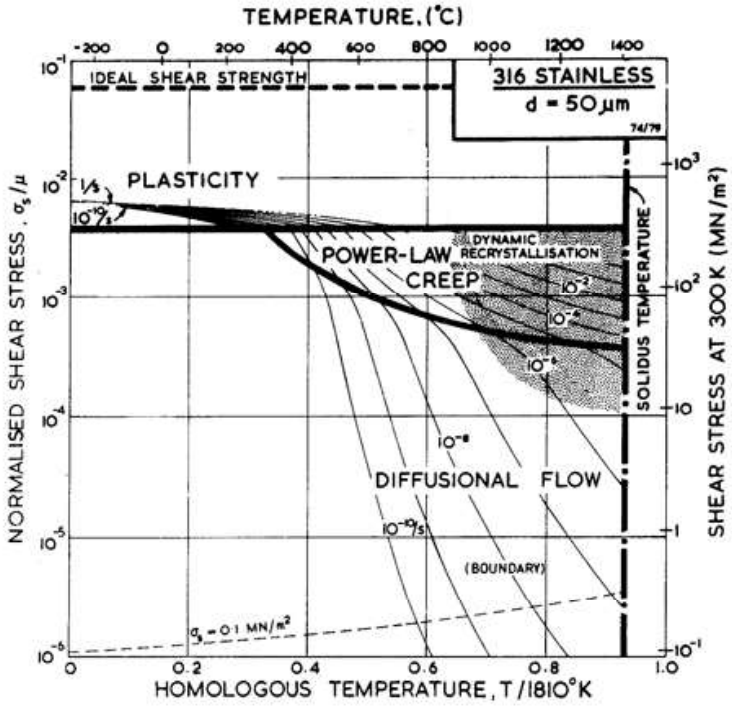


Figure 2.4: Creep deformation mechanism map for 316 stainless steel containing a 50 μm grain size [9].

The exact underlying processes responsible for dislocation creep are not fully understood. However, it is known that the mechanism relies upon the climb and glide of dislocations. This is explained as follows. For a crystalline material to flow plastically, the instantaneous applied load must be high enough to generate stresses greater than yield, enabling dislocations to move/glide through the lattice structure. The reason for this is that dislocations must be in a high enough energy state to overcome the inherent resistance to their movement in the form of inter-atomic forces and the obstructing effect of obstacles (solute atoms, precipitates and entangled dislocations or knots).

In contrast, inelastic deformation under creep conditions can occur at stresses much lower than yield. Over time, dislocation movement is assisted by diffusion processes that allow dislocations to climb over obstacles at lower energy states, enabling further glide and thus permanent deformation. This process is known as dislocation creep and is illustrated in Figure 2.5. The underlying diffusion processes are ther-

mally activated and are most significant at temperatures greater than approximately $0.35T_m$. Because dislocation creep is governed by diffusion, the rate of dislocation climb and thus macroscopic creep strain is highly sensitive to both temperature and applied stress.

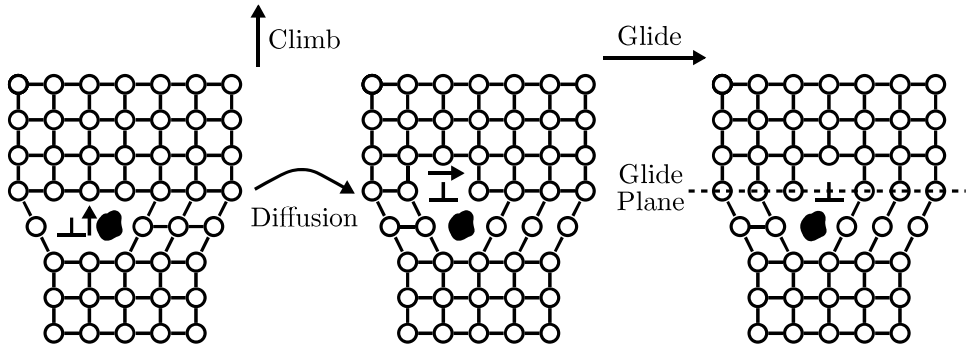


Figure 2.5: The mechanism of dislocation creep showing the diffusion assisted climb of an edge dislocation around an inclusion.

The mechanism of diffusion creep (or diffusional flow) involves the diffusion of vacancies within the crystal lattice. This results from a mismatch of stresses along grain boundaries that arises from their varying orientation relative to the applied stress.

Consider the case of a single grain within a polycrystalline metal under the influence of both tensile and compressive stresses, Figure 2.6. The grain boundaries that are contained within zones which are primarily under tension see a stress induced decrease in activation energy to create vacancies and a corresponding increase in activation energy for vacancy formation in grain boundaries under compression. Because this results in the vacancy concentration being higher in tensile regions than in compressive, a net flow of vacancies occurs from regions of high concentration (tensile) to low (compressive) which is equivalent to net atomic diffusion in the opposite direction. This progressive diffusion eventually leads to the elongation of the grain and on a macroscopic scale, creep deformation of the entire material. Depending on the diffusion pathway, transgranular or intergranular, this behaviour is respectively known as either Nabarro-Herring or Cobalt creep.

The macroscopic behaviour of a material under creep conditions can be described by examining the strain-time relationship generated from a uniaxial creep test. A round-bar specimen is held under a constant load at high temperature and the creep strain is recorded as a function of time. This is known as a material creep curve and a typical example is shown in Figure 2.7. The creep curve can be delineated into three distinct stages according to the change strain rate over time ($\dot{\varepsilon}^c$): primary, secondary and

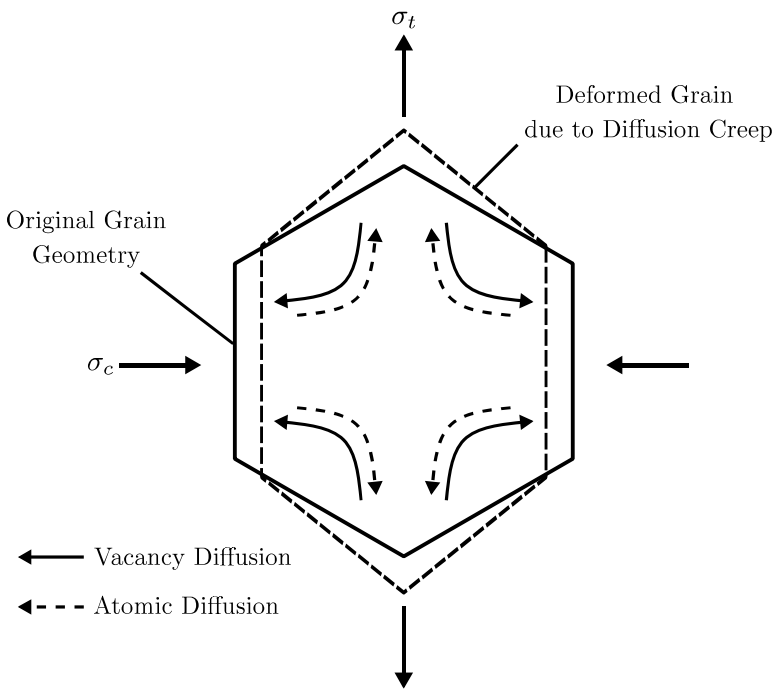


Figure 2.6: The mechanism of diffusion creep (Nabarro-Herring) in a single grain showing the movement of vacancies and atoms that result in grain elongation and macroscopic creep deformation, adapted from [10].

tertiary. The changes in strain rate arise from competition between two microstructural processes: work (strain) hardening and thermal softening (recovery). Softening occurs as a result of a reduction in the energy state and number of dislocations which is associated with increased diffusion rates at higher temperatures.

In reference to Figure 2.7, during primary creep, work hardening dominates, increasing the resistance to deformation and reducing the strain rate. Over time, this continues until eventually, a balance is achieved between work hardening and thermal recovery leading to a constant strain rate throughout the secondary creep region [11]. The steady-state creep rate ($\dot{\varepsilon}_s^c$) is also referred to as the minimum creep rate ($\dot{\varepsilon}_{min}^c$). In the final tertiary stage, the strain rate accelerates until fracture. This is caused by a number of factors including: an increase in effective stress, the formation of a neck (localised deformation) and sub-surface damage in the form of voiding and micro-cracking (discussed further on).

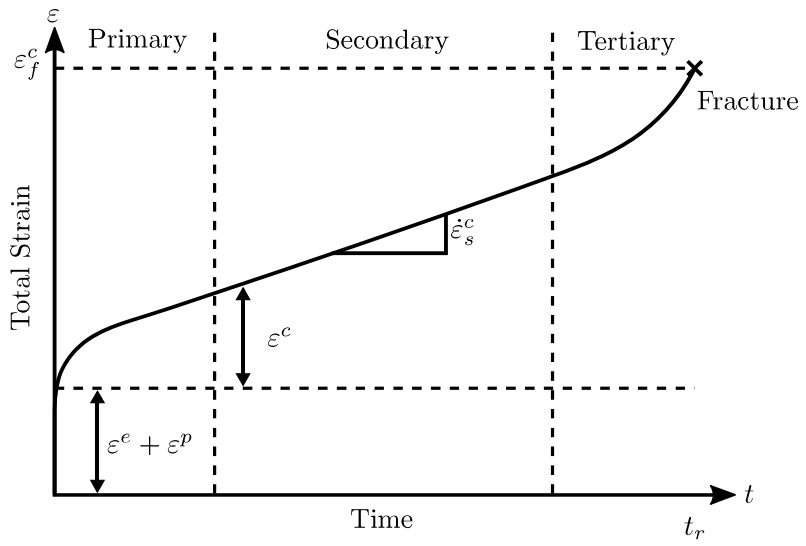


Figure 2.7: Illustration of a typical creep curve generated from a uniaxial specimen held under a constant tensile load.

2.6.1. Power-Law Creep

AGR plant components typically spend the majority of their lives creeping under steady-state power law conditions. Therefore, the secondary region is considered to be of most significance when designing against creep. This is usually conducted by assigning a maximum permissible amount of creep strain over life, such as 1% in 100,000 hours, for a given operating temperature and stress. As previously mentioned, creep is a thermally activated process. The dependency of steady state creep strain rate ($\dot{\varepsilon}_s^c$) on stress and temperature is therefore based on an Arrhenius rate formula and can be expressed by Equation 2.15.

$$\dot{\varepsilon}_s^c = C\sigma^n e^{-Q/RT} \tag{2.15}$$

It can be seen that the strain rate is proportional to the stress raised to the power n which is commonly referred to as the Norton stress exponent. C is a material constant, Q is the stress modified activation energy, R is the gas constant and T is the absolute temperature. For a uniaxial specimen under isothermal power law creep conditions, Equation 2.15 can be simplified to Equation 2.16 where A is a temperature dependent material constant. At any given temperature, material constants are usually derived from a large number of uniaxial rupture tests over a range of stresses. By plotting minimum creep rate versus nominal stress, an exponential line of best fit to the data can be created, providing the values of A and n.

$$\dot{\varepsilon}_s^c = A\sigma^n \tag{2.16}$$

A similar approach can be taken to evaluate rupture time (t_r) which is also related to the applied stress through a power law relationship as shown Equation 2.17. B_r is a temperature dependent material constant and v_r is the stress rupture exponent.

$$t_r = \frac{B_r}{\sigma^{v_r}} \tag{2.17}$$

2.6.2. Creep Fracture and Damage

Creep degradation can lead to the significant internal damage of components, resulting in excessive deformation and the initiation and growth of multiple cracks. The microstructural nature of creep damage is highly dependent on the material and exhibited temperatures and stresses. Within polycrystalline metals, both intergranular and/or transgranular fracture mechanisms may be observed. Intergranular cracking usually coincides with long-term exposure to high temperatures and low stresses and the opposite is true for transgranular fracture [12]. This is because at high temperatures, grain boundaries act as vacancy sinks and also provide a path for the rapid diffusion of atoms, making them inherently weaker than actual grains and more susceptible to the initiation of creep damage, shown in Figure 2.8.

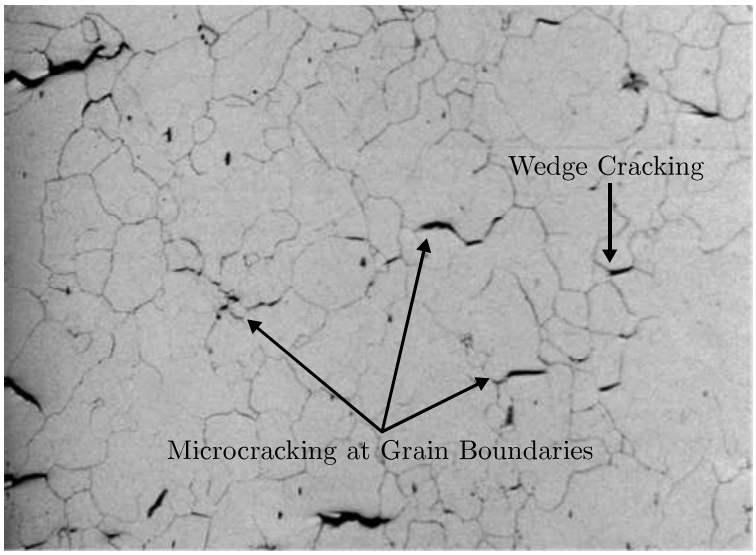


Figure 2.8: Section taken through a sample of 316H crept for 4000 hours, showing extensive voiding and intergranular microcracking (current work).

Such grain boundary damage often means that creep ductilities are much less than those observed under pure tensile conditions. Integranular fracture results from the nucleation of voids along grain boundaries that are aligned perpendicular to the maximum principle tensile stress. These grow over time and link up to form wedge cracks at triple points that propagate to final fracture. This is often found to be the dominant damage mechanism that results in the failure of austenitic steels under uniaxial creep conditions [13]. The grain boundary strength of a material can therefore dominate it's overall macroscopic creep resistance.

2.7. Fatigue Degradation

In addition to being subjected to creep, many plant components frequently endure repeated thermal and mechanical cyclic loading, resulting from variations in temperature and pressure (stress) during reactor maintenance and a fluctuating demand for power output. The resulting cyclic stresses can lead to an accumulation of microstructural damage that over time, induces cracking and the subsequent failure of components. This process is known as fatigue and can result in fracture even when the applied stresses are much lower than a materials ultimate tensile strength. Because fatigue has the potential to reduce component lifetime, it presents a major concern within plant structural integrity assessment.

There are three conventional approaches that are used to design against fatigue failure: stress-, strain- and fracture mechanics based. The stress based approach calculates the average stresses in a component area susceptible to fatigue and compares this against known fatigue behaviour at that particular stress. Consideration is first given to the component mean stress which is then scaled to account for geometric effects and stress concentration factors. The strain based approach involves a more detailed analysis of localized yielding at stress concentrations that may occur during cyclic loading. A fracture mechanics based approach aims to characterise and evaluate crack growth due to fatigue. The correct approach to use is based upon a combination of component material properties, loading characteristics and operating environment. The stress and strain based approaches are described in the following sections.

2.7.1. Stress-Based Approach

Generally, when a component is subjected to cyclic stresses that do not exceed it's material's yield strength, it can sustain a high number of load cycles until failure. This is commonly referred to as high cycle fatigue (HCF) and for stainless steels is applicable

when the total number of cycles exceeds 10,000. When designing in the HCF regime, the stress based approach is often used due to its historic reliability (large amounts of validation test data) and simplicity in performing analytical calculations (linear elastic material response).

To calculate the total HCF damage that a component will accumulate over it's life, engineers make use of linear damage accumulation models (such as Miner's Rule) alongside graphs describing the relationship between the applied stress amplitude (σ_a) or mean stress (σ_m) and number of cycles to failure (N_f). These are referred to as Wohler or S-N curves and are created based upon data generated from uniaxial stress-controlled fatigue tests in both fully reversed and zero compression loading. S-N curves rely on fatigue parameters that are characterised by the maximum (σ_{max}) and minimum (σ_{min}) peak stresses exhibited by the material each cycle. These are detailed in Equations 2.18 to 2.21 and illustrated in Figure 2.9 where $\Delta\sigma$ is the stress range, σ_m mean stress and σ_a stress amplitude. The stress ratio R describes the relative level of tension and compression within each cycle with $R = 1$ being a constant applied stress, $0 < R < 1$ tension-tension cycling, $R = 0$ zero-tension cycling and $R = -1$ fully reversed cycling.

$$\Delta\sigma = \sigma_{max} - \sigma_{min} \tag{2.18}$$

$$\sigma_m = \frac{\sigma_{max} + \sigma_{min}}{2} \tag{2.19}$$

$$\sigma_a = \frac{\sigma_{max} - \sigma_{min}}{2} \tag{2.20}$$

$$R = \frac{\sigma_{min}}{\sigma_{max}} \tag{2.21}$$

A typical set of S-N curves for varying values of R is illustrated in Figure 2.10. The number of cycles to failure is displayed logarithmically and can be seen to be highly sensitive to changes in both stress amplitude and R ratio over several orders of magnitude. The flattening of the curves indicates a stress amplitude below which fatigue failure will not occur and this is called the fatigue endurance limit (σ_e). If a material is cycling at a constant stress amplitude, the number of cycles to failure can easily be determined by simply reading off the appropriate curve. S-N data can usually be described by Basquin's equation shown in Equation 2.22 where p and C_1 are empirical constants.

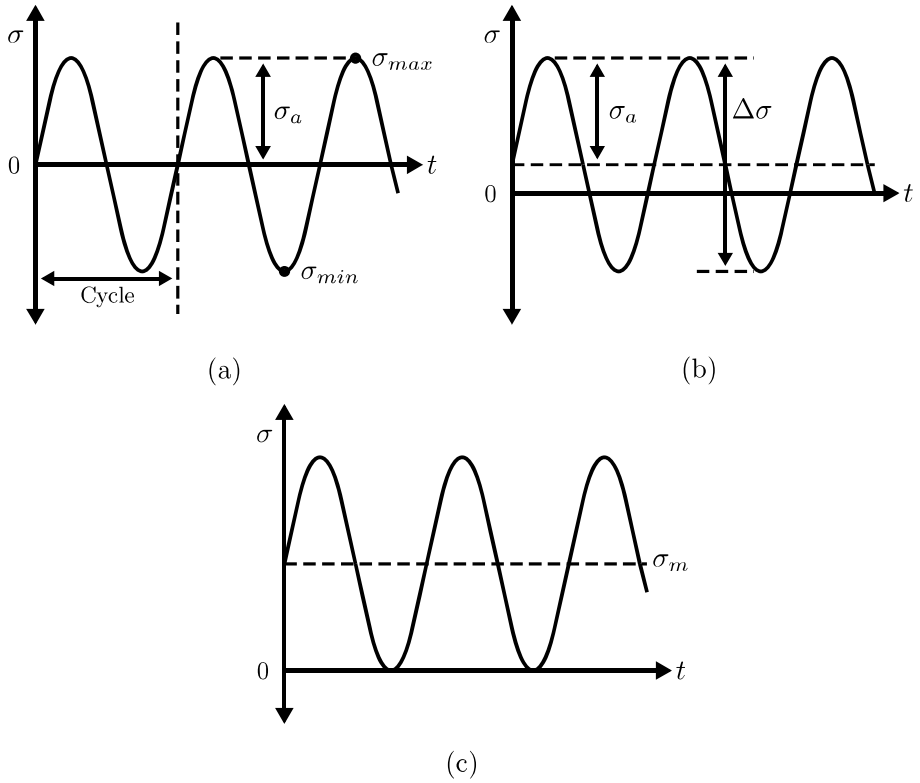


Figure 2.9: Stress histories from stress-controlled constant amplitude cycling in (a) completely reversed (b) non-zero mean (c) positive mean stress states.

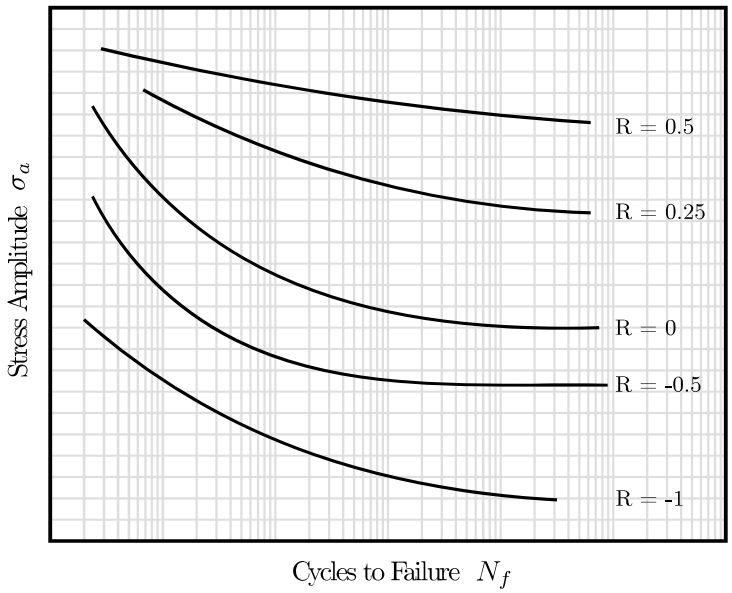


Figure 2.10: Illustrated example S-N curve for a material under various stress ratios.

$$N_f \sigma_a^p = C_1 \tag{2.22}$$

In reality, components seldom run under constant loading conditions and are exposed to a multitude of stress amplitudes throughout their life. In this case, a linear summation model, such as Miner's Rule, is often employed to calculate total component damage providing that the loading history of the component is known. For every stress amplitude that the material will cycle, the number of cycles is divided by the total number of cycles at that amplitude to cause failure (taken from the S-N curve) giving a value of "damage", below a threshold of 1. This is then repeated for each amplitude and the total damage accumulated is summed. For design purposes, a value greater than 1 indicates component failure. Miner's rule is shown in Equation 2.23 where k is the total number of different stress amplitudes, n_i is the number of contributing cycles, N_{fi} is the number of cycles to failure and D is the total damage.

$$\sum_{n=1}^{k} \frac{n_i}{N_{fi}} = D \tag{2.23}$$

2.7.2. Strain-Based Approach

For components operating at high temperatures, the applied cyclic stresses may be greater than yield, introducing significant cyclic plasticity within the material. This is especially true within plant applications where cyclic thermal stresses are induced upon reactor start-up and shut-down. Under these conditions, the number of cycles to failure are significantly lower than that of a material cycling elastically. This is characterised as low-cycle fatigue (LCF) and involves relatively short fatigue failure lives (<10,000 cycles). A strain based design approach enables consideration of these plastic strains and thus improved estimates of intermediate and short fatigue endurances. In a similar manner to the stress based approach, strain-life (ε-N) curves are generated from multiple strain controlled laboratory fatigue tests and are used to design against failure.

Cyclic hysteresis loops are a key feature generated from strain-controlled tests. An example loop is illustrated in Figure 2.11 showing the load up and stabilised cyclic behaviour of a material yielding in both tension and compression. Upon initial loading the material follows it's monotonic stress-strain curve O-A-B. As the upper strain limit is reached, loading is reversed and the material unloads elastically until it yields in compression at a lower stress C due to the Bauschinger effect. Reloading in tension

completes the hysteresis loop and under stabilised conditions, the material returns to B.

The Bauschinger effect is thought to result from the generation of back stresses [14] during forward plastic deformation. As dislocations move through the lattice structure they interact and are pinned by numerous obstacles including entangled piles, grain boundaries and precipitates. This generates numerous back stresses around the pinned contact points that resist further movement. As the material is unloaded in compression, these back stresses repel dislocations from the pinned objects, assisting their movement in the reverse strain direction. This decreases the total energy required to yield in compression by a value equal to the total back stress and results in a lower compressive yield stress.

Life predictions can be made from stabilised hysteresis loops by plotting stress against inelastic stain and calculating the total loop area. This provides the total inelastic strain energy absorbed by the material each cycle and can be used to calculate damage accumulation [15].

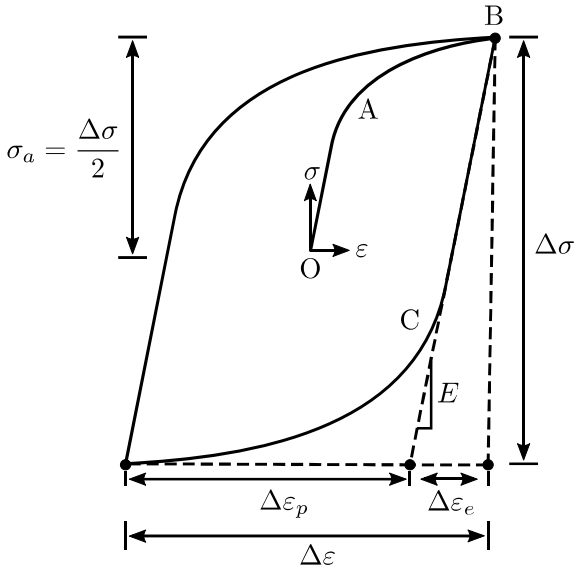


Figure 2.11: Illustration of typical hysteresis loop resulting from strain controlled cyclic testing.

Many materials experience irreversible changes within their microstructure as they are cycling that result from continuous plastic yielding. This alters their overall stress-strain response and depending on the initial conditions and material properties, a material may either cyclically harden and/or soften. These mechanisms are illustrated in Figure 2.12 for fully reversed strain-controlled conditions. For most metals, the effects of hardening or softening are usually rapid at first, decreasing with an increasing number of cycles

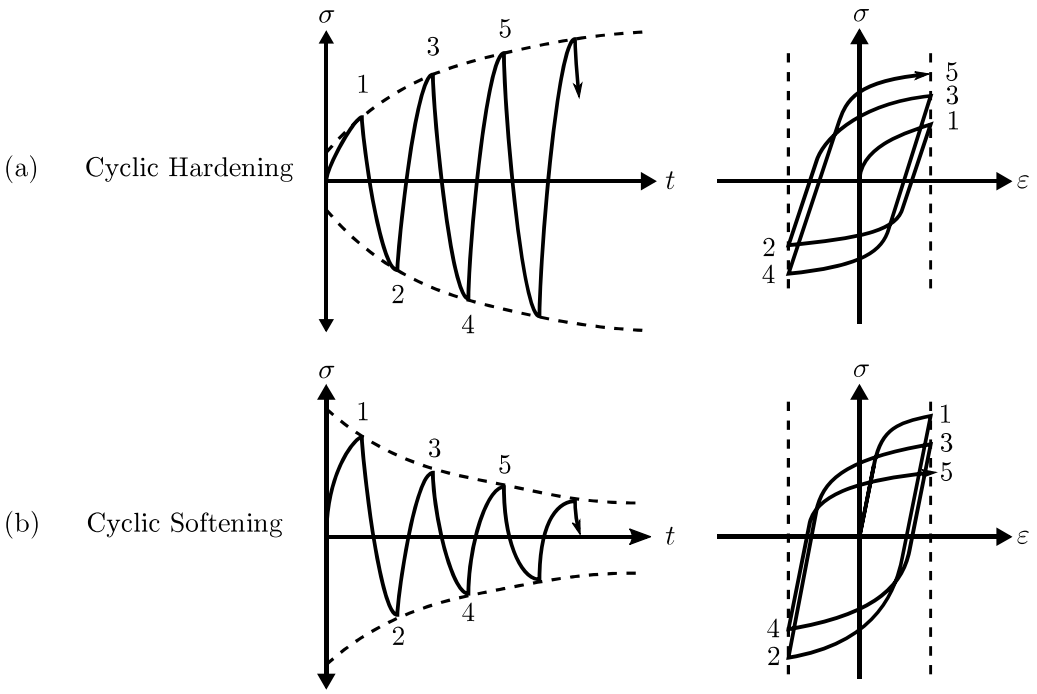


Figure 2.12: (a) Hardening and (b) softening response of a material subjected to continuous strain cyclic loading.

until a stabilised cyclic state is achieved. This initial stage of cyclic instability is known as the loop closure period and typically lasts up to 10% to 20% of a material's total fatigue life. Here, a material will continuously exhibit changes in it's dislocation substructure until a stable configuration is reached. Beyond this point, the hysteresis loop essentially remains the same until the material contains significant damage. It should be noted that a stabilised state will only be reached if the applied strain conditions remain constant.

The stabilised hysteresis loop is used to determine a material's cyclic stress-strain curve, illustrated in Figure 2.13. It is constructed by connecting the peak stresses from stable loops taken from strain-controlled tests across a range of strain amplitudes. If a material does not display stabilisation, either the maximum (hardening) or minimum (softening) stress amplitudes are used [16]. The total cyclic stress-strain response can be characterised by a relationship that is analogous to the Ramberg-Osgood material model, shown Equation 2.24. The variables $\Delta\sigma$ and $\Delta\varepsilon$ represent changes relative to coordinate axes at either loop tip. H' and n' are known as the cyclic strength coefficient and cyclic hardening exponent respectively.

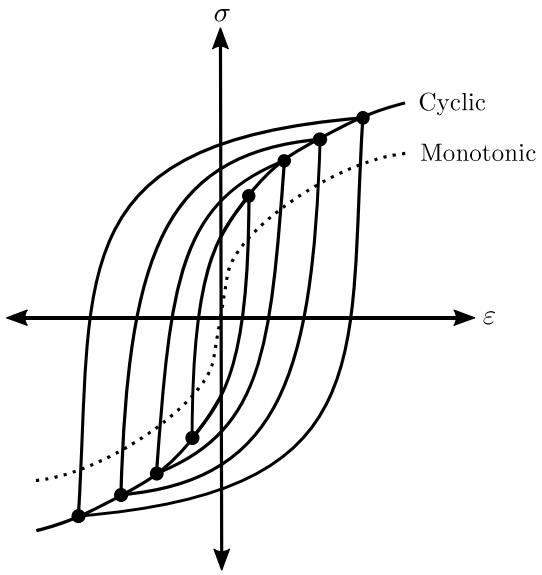


Figure 2.13: Comparison of monotonic and cyclic stress-strain curves.

$$\Delta\varepsilon = \frac{\Delta\sigma}{E} + 2\left(\frac{\Delta\sigma}{2H'}\right)^{1/n'} \tag{2.24}$$

Low cycle fatigue test data is typically presented by plotting the plastic strain range ($\Delta\varepsilon^p$) against number of cycles to failure, N, on a logarithmic axis, Figure 2.14. The definition of failure can vary and is defined as a certain decrease in load from the stabilised maximum peak value (30% within the context of this study). The relationship between plastic strain range and number of cycles to failure can be described by the Coffin-Manson equation [17], shown in Equation 2.25. The left hand side is the plastic strain amplitude, ε'_f the fatigue ductility coefficient which is approximately equal to the true fracture strain and c is the fatigue ductility exponent.

$$\frac{\Delta\varepsilon_p}{2} = \varepsilon'_f(2N_f)^c \tag{2.25}$$

It is often useful to construct an expression capable of describing the fatigue behaviour of a material over both LCF and HCF regimes. This can be done by reformulating the Basquin equation (Equation 2.26) and superimposing it onto the Coffin-Mansion relation. σ'_f is the fatigue strength coefficient (often taken as the monotonic true rupture stress) and b is the fatigue strength exponent.

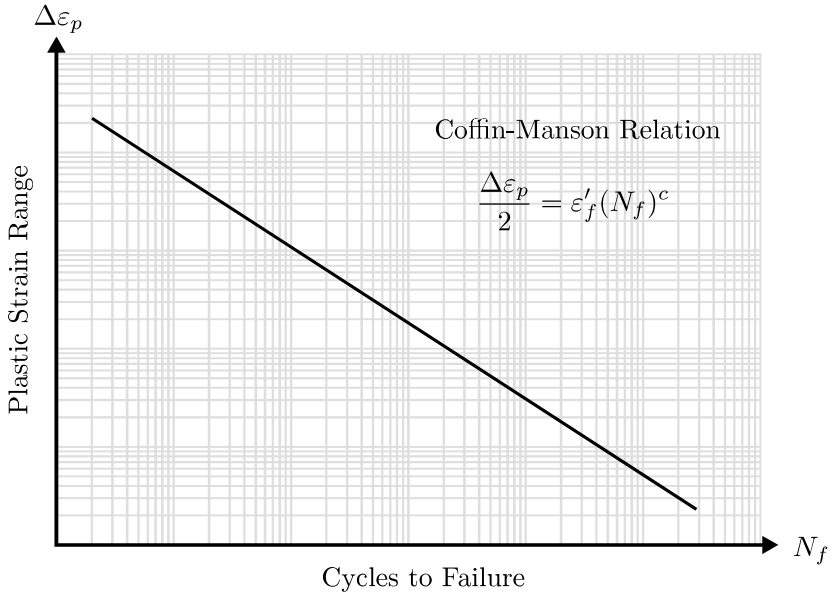


Figure 2.14: Coffin-Manson equation describing the relationship between plastic strain range and cycles to failure for the LCF regime.

Combining the elastic and plastic contributions (Equation 2.27) from Equations 2.25 and 2.26 yields an equation valid for both low and high cycle fatigue lives, this is known as the Strain-Life relation (Equation 2.28) and is shown in Figure 2.15. At large strain amplitudes the curve tends towards the plastic line and at smaller amplitudes, the elastic line.

$$\sigma_a = \frac{\Delta\varepsilon_e}{2}E = \sigma'_f(2N_f)^b \tag{2.26}$$

$$\frac{\Delta\varepsilon}{2} = \frac{\Delta\varepsilon_e}{2} + \frac{\Delta\varepsilon_p}{2} \tag{2.27}$$

$$\frac{\Delta\varepsilon}{2} = \frac{\sigma'_f}{E}(2N_f)^b + \varepsilon'_f(2N_f)^c \tag{2.28}$$

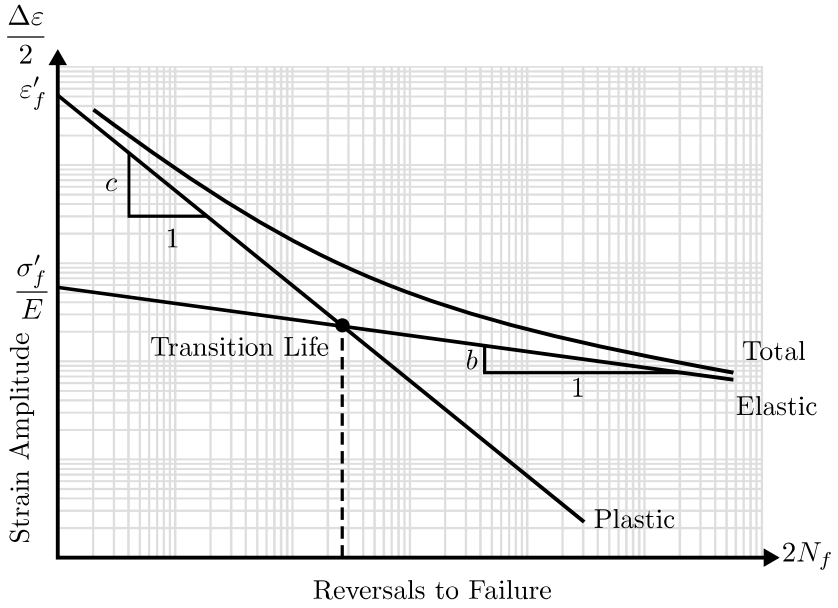


Figure 2.15: Graphical representation of the total strain life equation.

2.7.3. Fatigue Fracture and Damage

Fatigue degradation can often lead to significant damage and cracking within components. To understand how this occurs, it is useful to separate the entire damage mechanism into four progressive stages. With reference to Figure 2.16, these are:

1. Fatigue crack nucleation - the early development of fatigue damage and initiation.
2. Slip band crack growth - the subsequent propagation of a crack through surface grains of high shear stress. Also known as Stage I crack growth.
3. Crack propagation - often referred to as Stage II crack growth, this is where a well defined crack grows normal to the applied maximum stress.
4. Final failure - the acceleration of crack growth rates (Stage III) that sufficiently reduce the net section area to cause overload fracture.

When a polycrystalline metal deforms, the stress field across the entire microstructure is anisotropic and non-uniform due to varying grain orientations and crystal planes. When a grain has an adverse orientation in relation to the applied macroscopic stress it can develop slip bands. These are regions of intense deformation that arise from the shearing of crystal planes. Under cyclic loading conditions, persistent slip bands (PSB)

can form and lead to the initiation of cracking through the creation of stress raisers at the surface.

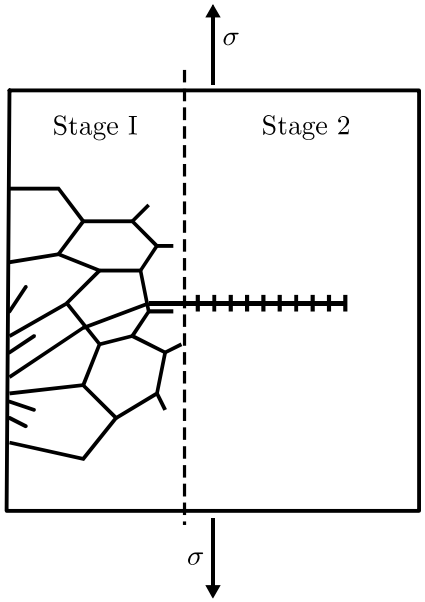


Figure 2.16: Stage I & II fatigue crack propagation.

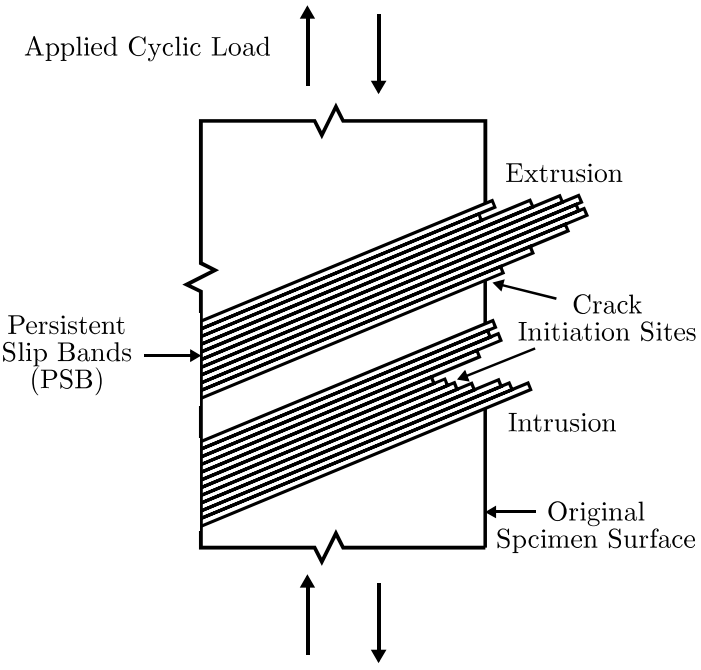


Figure 2.17: PSB formation mechanism during cyclic loading leading to the creation of initiation sites at the surface.

The mechanism of PSB formation is illustrated in Figure 2.17. Nucleation sites for initiating cracks tend to occur within intrusions and at the interface between PSBs and the original material surface. Once a Stage I crack has initiated it preferentially grows along a PSB across approximately a few grain diameters before transforming into a Stage II crack; becoming aligned and propagating in a direction perpendicular to the maximum applied stress. Stage II propagation occurs through a plastic crack blunting process which involves the repeated blunting and compression of the crack face surface through each cycle. Blunting occurs because of plastic shearing in tension along slip planes at a 45°angle to the crack plane.

This repeated blunting sometimes results in the formation of fatigue striations on the fracture surface. This is pictured in Figure 2.18, taken from the fracture surface of a failed fatigue specimen. Each striation represents an advancement of the crack front for a successive fatigue cycle. It should be noted that striations are not always readily observable on fatigue fracture surfaces. This can be due to limited plasticity (and ductility) within the parent material and/or damage to striations upon crack closure or at final failure.

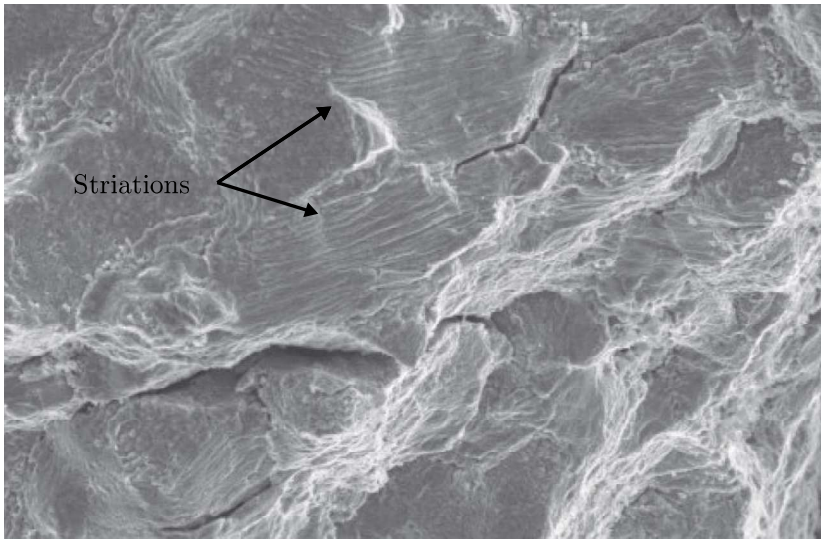


Figure 2.18: Striations present on the fracture surface of a 316H fatigue specimen tested under high temperature LCF conditions (current work).

The final stage of propagation (Stage III) involves the acceleration of crack growth rates through a reducing cross-sectional area, eventually leading to unstable crack growth and fracture. Depending on the material, final fracture may either be ductile (dimpled fracture surface) or brittle (cleavage or intergranular fracture) or a combination of both. The length of each stage relative to the total life is a function of test conditions and material properties. Usually, at higher applied strain ranges (LCF),

Stage II crack growth dominates with the opposite being true for Stage I crack growth (HCF).

Since cracks initiate at stress raisers on the surface of a material, the condition of a surface can have a large influence on the time to crack nucleation thus fatigue strength. A hardened surface layer generally increases fatigue limits and this is often the motivation for industrial preconditioning treatments such as carburising, nitriding and induction hardening. Surface finish is also important; a rougher surface tends to contain an increased proportion of stress raisers that can encourage premature crack initiation, resulting in a loss of fatigue endurance.

3. Carburisation of Stainless Steels

3.1. Introduction

This chapter provides a review of the literature concerning the carburisation of steels and its resulting impact on mechanical properties within the context of both industrial preconditioning and AGR plant corrosion.

Carburisation can be broadly defined as the ingress of carbon into a metal via diffusion mechanisms [18]. Usually occurring under high-temperature conditions, it can result in drastic changes to a materials microstructure at the surface, significantly altering mechanical properties. It is therefore frequently used as an industrial surface treatment process to enhance the performance of both low and high carbon steel components [19]. However, under certain circumstances, carburisation is also seen as a form of environmental corrosion. This is especially true for components exposed to high temperature hydrocarbon gaseous environments (i.e. CO & CH_4) where, mechanical properties can be degraded, reducing component lifetime. This is a significant concern within the petrochemical and nuclear industries [20]. Recently, it has been postulated that carburisation is responsible for initiating premature damage within AGR components exposed to CO_2 coolant gas [21].

The remainder of this literature review is dedicated to introducing both industrial gas (IG) and AGR carburisation and reviewing their resulting effect on the mechanical properties of stainless steels. IG preconditioning methods are described, followed by an overview on the historical background and current work undertaken to date in investigating carburisation within the context of AGR plant. In the final section, a review of the literature exploring the impact of carburisation on the creep and fatigue performance of stainless steels is provided.

3.2. Industrial Gas Carburisation

The carburisation of steels is a thoroughly understood process and has been extensively used within industrial applications to enhance the fatigue and wear resistance of compo-

nents [22]. Steels are usually treated within a high temperature carbonaceous medium (either gas or salts) which through diffusion, creates a carbon enriched outer hardened case layer (Figure 3.1).

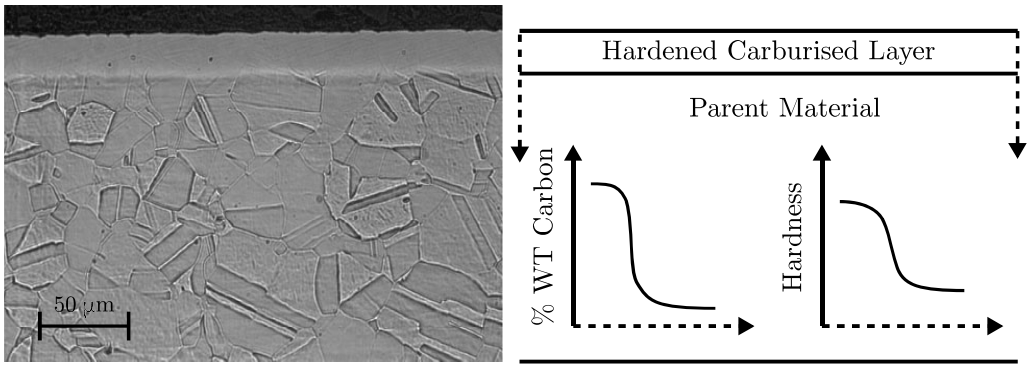


Figure 3.1: Metallographic section of carburised 316 taken from [23].

The basic principle of carburisation is based on the diffusion of carbon atoms into a metallic crystal lattice. Depending on the exposure environment, atoms can either remain in solid solution or combine with other solute atoms to form carbide precipitates [24] within near surface regions. Both outcomes result in a significant increase in lattice strain and therefore material surface hardness which, can be up to four times greater than the parent material; enhancing wear resistance [25]. The increase in lattice strain at the surface is often accompanied by the generation of high compressive residual stresses [26] that assist in suppressing fatigue crack nucleation, often resulting in an enhanced material fatigue strength [27, 28, 29].

Carburisation is diffusion driven. Therefore, carbon concentration and hardness profiles follow decreasing trends from peak values at the surface to parent material levels through depth [22]. This is illustrated in Figure 3.2. Carbon content and depth profile are determined by several preconditioning parameters including: exposure time, temperature and gas composition [30]. It is often desirable to induce a gradual change in material properties with depth to avoid any extreme mismatch in internal stresses between the hardened layer and parent material interface that can potentially cause spallation and cracking.

The majority of steels are carburised under very high temperature conditions, often exceeding 900°C. Here, they undergo a change in crystal lattice structure from ferritic body centered cubic (BCC) to austenitic face centered cubic (FCC). An FCC structure is often preferable owing to its higher diffusivity and solubility limits [31] which, can increase the speed of carburisation and promote higher levels of carbon content. However, such temperatures are not suitable when attempting to carburise austenitic stainless steels. This is because exposure above 900°C severely depletes chromium from

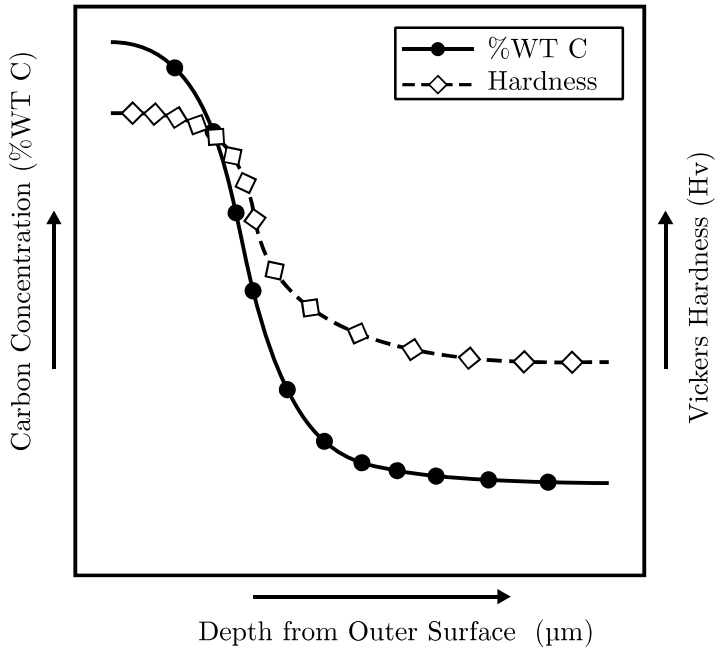


Figure 3.2: Illustration of typical carbon concentration and hardness profiles.

the austenite matrix resulting in the formation of undesriable chromum bearing carbides [32] and the deposition of a thick oxide scale [33]. The precipitation of these carbides, predominantly on surface grain boundaries, is detrimental to both ductility and corrosion resistance due to sensitisation of the matrix and significant grain boundary embrittlement [34].

Austenitic stainless steels are therefore carburised via alternative low-temperature techniques that aim to minimise carbide precipitation [23]. To enhance the inherently slower diffusion rates at these lower temperatures, carbon ingress is accelerated via surface 'activation' through removal of the Chromium (III) Oxide (Cr_2O_3) passive layer [35]. Here, the mobility of chromium and nickel atoms within the austenite matrix is restricted, limiting carbide precipitation to extremely long exposure times [36]. As a result, the diffused carbon forms a single-phase solid solution carbon rich outer case layer that remains austentitic [37]. Under these conditions, it is possible for the equilibrium solubility limit of carbon to be exceeded by orders of magnitude resulting in a carbon supersaturated layer that does not compromise on ductility or corrosion resistance [25]. The performance of low-temperature carburised austenitics has been extensively reported in the literature; a complete review is provided by Collins [25].

3.3. AGR Gas Carburisation

3.3.1. Introduction & Historical Background

Components operating within an AGR coolant gas environment are directly exposed to high temperature CO_2 at 550°C, making them susceptible to environmental attack [38]. Under certain conditions, it has been observed that some 316H components become carburised, leading to the formation of an outer hardened surface layer. This is thought to impact on component lifetime through the initiation of premature surface cracking, resulting from an increase in surface hardness and subsequent loss of ductility. Because AGR carburisation poses a potential risk to component operation, a significant amount of effort is being dedicated to understand it's possible effects on the high temperature mechanical properties of 316H.

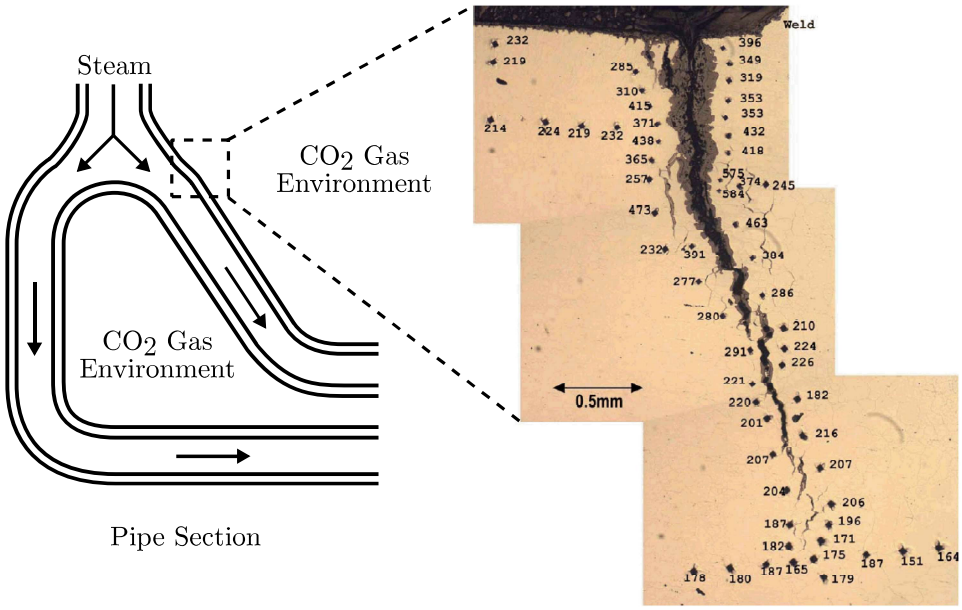


Figure 3.3: Hardness trace taken through an ex-service 316H component [39] in close proximity to a surface crack.

AGR carburisation was first postulated when unforeseen cracking was discovered in 316H boiler tubes and tailpipe weldments [40]. The initiation of these cracks could not be explained nor predicted by EDF Energy Component Life Assessment (CLA) procedures [41, 42]. As a result, it was thought that an additional crack initiation mechanism was in play, possibly involving an interaction with the environment. Metallographic examination of these cracks revealed severe oxidation of both surface boundaries and

crack faces along with an elevated hardness across the surface exposed to CO_2 [39]. Figure 3.3 shows a section view of one of these cracks. An increased hardness can be seen in measurements taken in close proximity to the outer surface, with hardness values often exceeding twice that of the parent material.

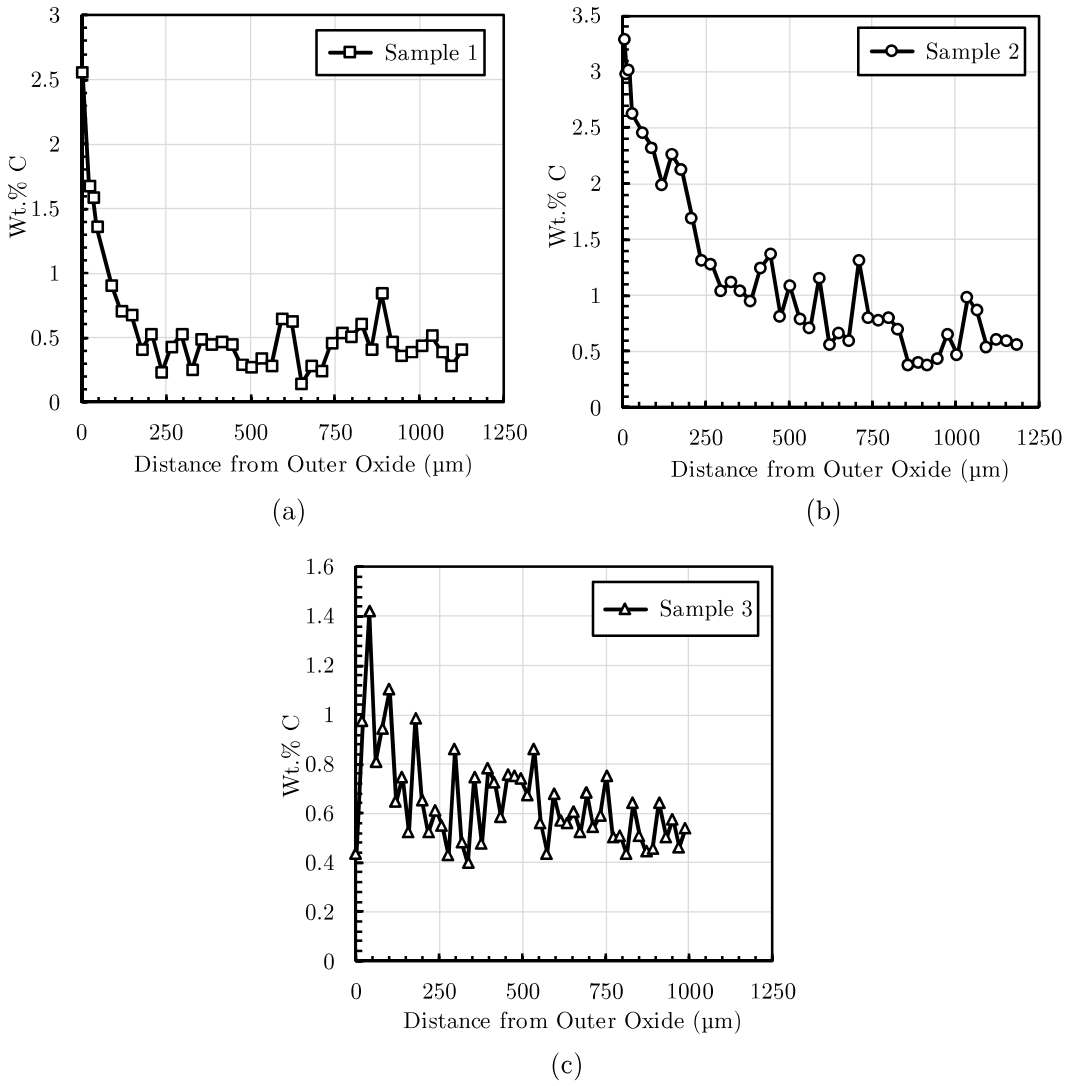


Figure 3.4: Carbon measurement through ex-service carburised sections under different exposure times and temperatures (a) 18kH @ 560°C (b) 49kH @ 560°C and (c) 39kH @ 600°C [43].

To verify that the increase in hardness was a serviced induced state and not as a result of initial component manufacture, Angell [44] conducted a series of preliminary examinations on oxide monitoring scheme samples (OMS). These are miniature cylindrical bar specimens used to study oxidation kinetics and are housed within a chamber exposed

to the AGR gas. Through hardness measurement, EDX (energy-dispersive X-ray spectroscopy) analysis and comparative metallography, it was concluded that the increase in hardness observed in larger components was as a direct result of exposure to the AGR gas environment [44]. This work was then extended by Younes et al. [45] to explore the root cause of environmental hardening. A significant change to the microstructure of parent material below the oxide layer was observed along with increased levels of measured carbon. This led to the conclusion that the hardening was due to a carburisation mechanism.

Within ex-service carburised material, Younes et al. observed the maximum carbon concentration to vary between 0.8 - 1.6 wt.% with a total penetration depth of 150-500 µm. The carbon profiles of three separate samples are presented in Figure 3.4. Each was exposed to a slightly different carburising temperature for separate durations. It should be noted that the values of wt.% carbon shown have not been corrected to remove any background carbon contribution. Based on these conclusions, a programme of work was initiated (ENVISINC) to develop an understanding of AGR carburisation and its potential impact on component lifetime.

3.3.2. Mechanism

The mechanism of AGR gas carburisation is thought to be well understoood [40] and is based on the observed oxidation behaviour of austenitics found in EDF Energy's CO_2 oxidation handbook, R67 [46].

The process is initiated in a similar manner to low-temperature IG carburisation techniques where the passive chromium surface film (Cr_2O_3) is broken down. Due to the AGR gas composition, this is accompanied by the simultaneous formation of a duplex oxide layer consisting of outer magnetite (Fe_3O_4) and inner spinel. Auger electron microscopy has shown that the inner spinel contains discrete chromium and nickel rich regions. Chromium is preferentially oxidised in the austenite matrix below the oxide layer and this leads to the formation of chromium rich oxides within a nickel rich matrix.

Carburisation is thought to occur as a result of the Boudouard reaction taking place at the alloy surface. Carbon ingress is facilitated by the breakdown of the chromia scale into carbides [47]. Within 316, these have been identified to include both $M_{23}C_6$ and M_7C_3 configurations. A summary of the chemical reactions occurring at the surface of carburised 316 is illustrated in Figure 3.5. The oxidation and carburisation of a component will continue until a chromium (and to a lesser extent silicon) rich healing layer forms between the inner spinel of the duplex oxide and metal substrate. This occurs when the

demand for chromium from the oxidation reaction is exceeded by the supply from the underlying parent material. The healing layer effectively acts as a barrier to diffusion and prevents further carburisation from occurring.

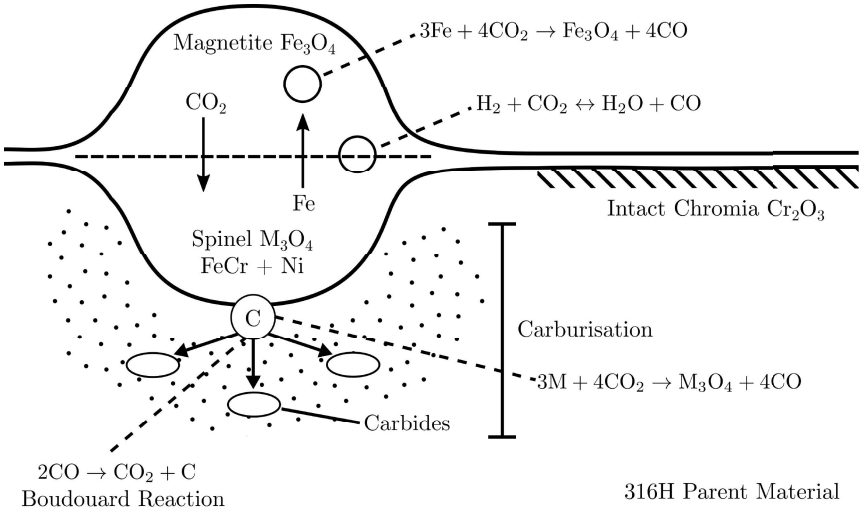


Figure 3.5: Overview of the AGR gas carburisation mechanism, adapted from [46].

An example of healing layer behaviour can be seen in a section taken from an ex-service carburised component, Figure 3.6. Where a healing layer has broken down or not formed, severe planar and intergranular carburisation has occurred. The development of a healing layer is highly dependent on the temperature of gas exposure and material chemical composition. Historical component data has suggested that between 480-600°C, a healing layer may never form, resulting in the continual oxidation and carburisation of a component throughout life [40]. Furthermore, it is thought that increased levels of chromium and silicon assist healing layer development.

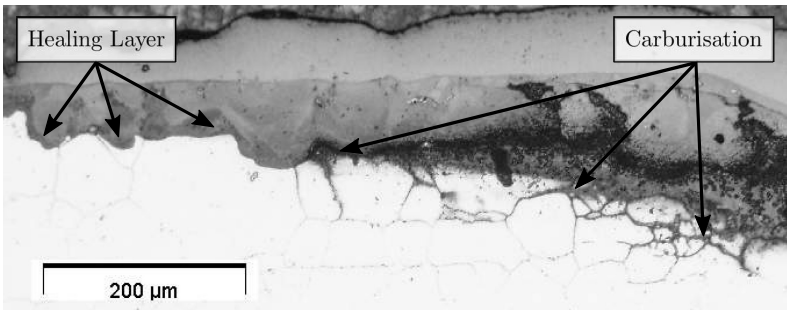


Figure 3.6: Section taken through an ex-service carburised component, demonstrating the effect of a healing layer (darker grey) on carburisation behaviour [44].

Due to enhanced diffusion rates down grain boundaries, intergranular carburisation develops much more rapidly than planar carburisation (contained inside grains) [43]. This can be seen in Figure 3.7. The diffusivity of carbon within grains is much lower as it is retarded by the development of the healing layer and growth of intragranular carbides [43] at the metal substrate interface.

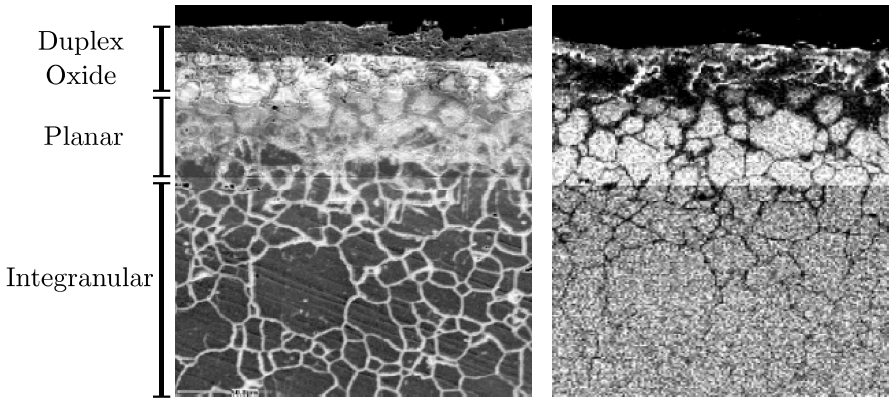
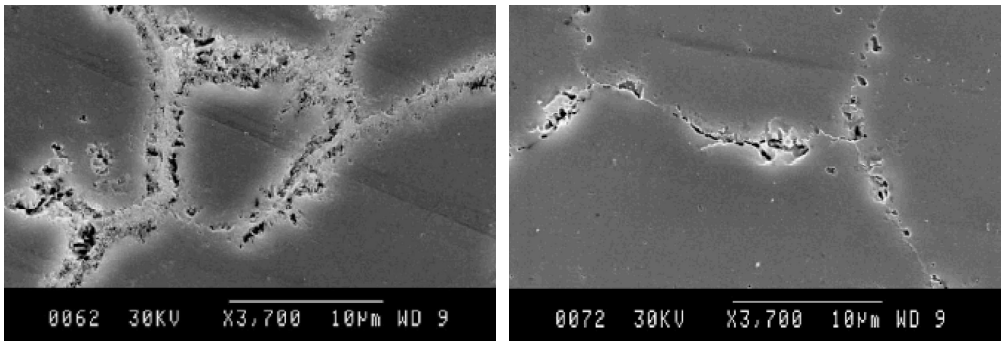


Figure 3.7: SEM images taken of an ex-service carburised component showing (a) the carburisation of grain boundaries & (b) the distribution of chromium content via EDX mappping [43].

Carbon ingress is aided by the precipitation of carbides amongst other secondary phase particles along grain boundaries. Over time, these carbides coarsen resulting in extensive grain boundary chromium depletion, seen in Figure 3.7 (b). A proportion of chromium also diffuses to the surface in order to form the spinel. The precipitation of these secondary phase particles, in the form of brittle carbides and oxides, results in a general increase of grain boundary thickness towards surface regions, Figure 3.8. This can lead to the formation of a zone between grains having a severely reduced or inherent poor ductility. As a result, it is highly likely that the morphology of these features in and around grain boundaries dominate macroscopic material properties.

There are a number of factors that influence the kinetic behaviour of 316 in a CO_2 environment [48]. These determine the rate and severity of carburisation and include: CO_2 gas chemistry, prior cold working, material grain size and surface finish. The variation of these features across different components in plant often leads to irregular carburisation behaviour which, is difficult to characterise [21].

The spinel oxide layer provides the necessary pathway for carbon difussion mechanisms [48]. Therefore, carburisation is highly dependent on the rate and intensity of oxide growth. This is diffusion driven and is influenced by the pressure difference between



(a) (b)

Figure 3.8: SEM image of an ex-service component comapring grain boundary decoration in (a) the carburised region and in (b) the bulk material [43].

the corrosive environment and oxide-metal interface. Generally, an increasing pressure shifts the equilibrium of the reaction towards the products which, results in a higher carbon activity at the metal-gas interface [49, 50]. It can therefore be expected that components exposed to the highest pressures of gas coolant contain the most acute levels of carburisation.

There are three material characteristics that also play an important role in determining oxidation rates. They are: grain size, prior cold work and surface finish. It has been found that grain size can affect the overall oxide resistance and healing layer growth within 300 series steels in AGR environments [51]. A smaller grain size decreases the average path length of a mid-grain diffusing chromium atom to the grain boundary which allows for an increased rate of transgranular chromium diffusion and encourages formation of a healing layer [52, 53, 54], also increasing oxidation resistance [55]. Prior cold work facilitates the oxidation of microstructural features such as grain boundaries and slip bands. This is because deformation induces a high density of dislocations at these points which, act as fast diffusion pathways for oxygen and iron [56]. The high variability in cold work and grain size across components therefore results in inconsistent carburisation behaviour even within the same component cast. This has been significantly reported within the literature [40, 45, 57, 58].

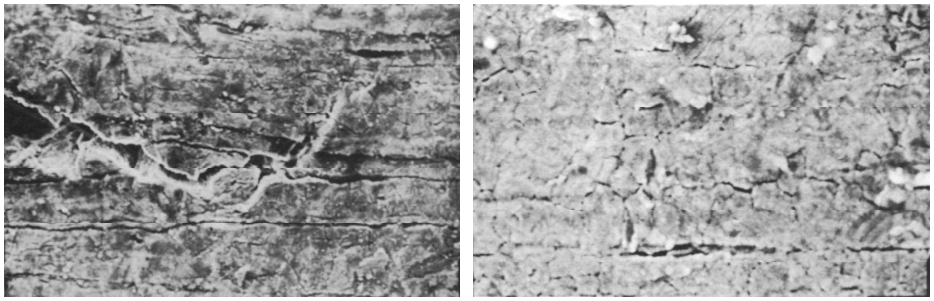
3.4. Effect of Carburisation on Mechanical Properties

There is a substantial difference between the mechanisms of AGR and IG carburisation, resulting in materials that possess very different surface microstructures. The former leads to a severely oxidised outer surface with heavily decorated grain boundaries and

significant carbide precipitation. The opposite is true for IG carburisation which, deliberately suppresses the precipitation of secondary phase particles so as to maintain the stainless steels innate ductility and corrosion resistance [30], leading to the formation of a single-phase austenitic carburised layer [25]. Due to these differences, it can be expected that each mechanism has a distinct effect on macroscopic material behaviour despite both resulting in the creation an outer hardened layer.

The remainder of this section explores the effects of carburisation on the tensile, creep and fatigue properties of steels. This has been scarcely reported upon within the context of AGR plant because carburisation was only recently realised as an important degradation mechanism [40]. Consequently, a large proportion of this review is reliant on investigative industry reports and historical component examination.

A number of early carburisation studies were undertaken by Jeffocat and Thorley [59]. They conducted a series of experiments investigating the effect of AGR carburisation on the high temperature (at 500°C) tensile properties of 9Cr1Mo ferritic steels. Parent material was preconditioned in a carbonaceous environment and carbon profile confirmed via nuclear microprobe. The resulting depth of carburisation was found to vary between 300 - 500 µm. Although this is similar to the depth of carburisation found in 316H [43], values of hardness and carbon content were not reported. Whilst preconditioning resulted in an increase in yield stress, failure ductility was degraded. Metallographic examination found that this resulted from intergranular cracking within the carburised layer, seen in Figure 3.9. This occurred at very low plastic strains ($< 0.5\%$), reducing the specimen cross sectional area and overloading the remaining bulk material. Despite being relatively ductile, no necking was observed towards the fracture surface. It was suggested that the increase in yield strength observed, may contribute to an enhanced creep life through the suppression of secondary creep rates.



(a) (b)

Figure 3.9: Optical microscopy of a 9Cr1Mo carburised specimen surface after tensile testing showing widespread intergranular surface cracking taken (a) towards and (b) away from the fracture surface [59].

Bolton and McLauchlin [60] extended this work to include creep testing. A number

of constant load creep tests were performed in both high temperature vacuum and CO_2 environments on preconditioned material. Despite decreasing the creep failure ductility, carburisation was found to reduce secondary creep rates and thus result in an overall increase in rupture life. This effect occurred only when tests were run at lower stresses. It was not reported why this was. However, because a significant reduction in surface ductility was previously observed by Jeffcoat [59], it is likely that the carburised layer was cracking in the early stages of tests run at the higher stresses. The overall reduction in creep ductility was found to be as a result of the initiation of widespread surface cracking, pictured in Figure 3.10.

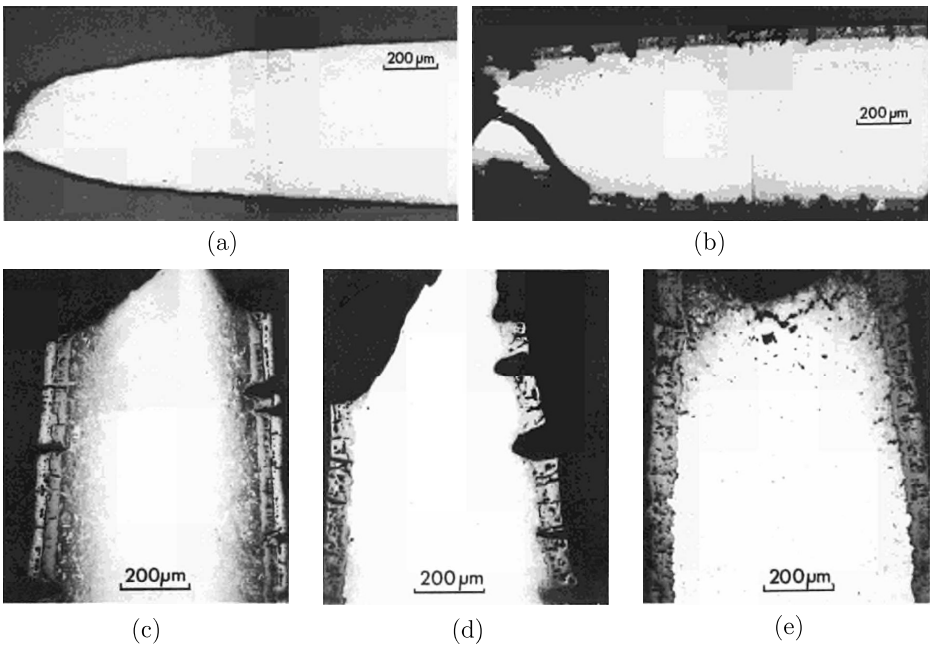
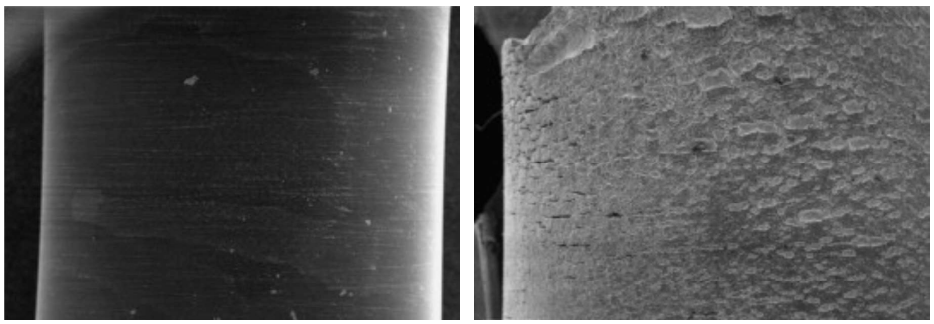


Figure 3.10: Micrographs of 9Cr1Mo creep specimens tested at in a vacuum environment (a) 200MPa Uncarburised (b) 200MPa Carburised (c) 165MPa Carburised (d) 155MPa Carburised (e) 120MPa Carburised [61].

A comprehensive review undertaken by Lister [56] includes these studies and considers the overall impact of carburisation on the structural integrity of 9Cr1Mo components situated in AGR conditions. Based on previous internal reports and historic component data, Lister concluded that carburisation generally led to an increase in tensile strength and decrease in ductility due to the presence of an outer hardened layer that exhibits widespread surface cracking. The overall impact on creep life was considered to be uncertain however, limited test data showed a general increase in creep resistance under laboratory conditions. Despite the lack of any fatigue data, it was postulated that the behaviour of the low ductility carburised surface would dominate overall fatigue strength and therefore be highly influenced by test conditions. At lower strains

that do not surpass the surface ductility, fatigue life could be enhanced due to the addition of compressive residual stresses and strengthening of the material. The opposite would be true for higher strain conditions where surface cracking would occur almost instantaneously, causing premature failure.

This phenomenon has been observed by Fournier et al. who conducted high temperature fatigue and creep-fatigue tests on oxidised 9Cr1Mo steel in air [62, 63, 64]. The impact of the brittle oxide layer was found to be highly dependent on the applied strain amplitude. At low strain ranges, final fracture was due to a single elliptical crack that had initiated at the specimen free surface and subsequently propagated via fatigue crack growth. The opposite was true for the higher strain ranges where multiple cracks had initiated on the outer edge and propagated till failure. This was accompanied by widespread cracking of the oxide layer along the entire specimen gauge length (Figure 3.11). It was concluded that the effect of the environment and influence of oxide layer on fatigue crack initiation and thus life, was highly dependent on the applied test conditions.



(a) (b)

Figure 3.11: Widespread surface cracking from low cycle fatigue testing on oxidised 9Cr1Mo steel. [62]

A limited number of studies have investigated the mechanical behaviour of 300 series stainless steels under high temperature carburising environments (> 500°C) [65, 66, 67, 68]. In a similar manner to 9Cr1Mo steel, carburisation generally resulted in a reduction of tensile and creep ductility [65]. The most relevant study was conducted by Quaglia [68] who performed slow strain rate tensile tests on samples of carburised 304. A reduction in ductility was observed that was reported to result from surface grain boundary embrittlement. This was found to be due to the severe precipitation of intergranular carbides that initiated widespread cracking on the outer surface. Here, the morphology of carbides dominated the macroscopic tensile properties.

Similar findings have been reported for carburised steels under creep conditions [69, 70, 71, 72]. Ramanarayanan conducted a series of very high temperature (>1000°C) tests

on carburised 30Cr30Ni austenitic steel [69]. Samples were preconditioned within a carbonaceous environment at two different temperatures giving rise to multiple surface microstructures with varying carbide morphologies. Carbide precipitation was limited at the lower temperature of 950°C whilst preconditioning at 1150°C resulted in the formation of heavy intergranular carbides. The former led to an enhancement of creep resistance due to an increased material strength whilst the latter resulted premature failure due to the weakening and embrittlement of grain boundaries. No details were provided on the nature of final fracture or the presence of widespread surface cracking.

Compareable findings have been reported by Guttman [70] who investigated the creep behaviour of high chromium HK40 and Alloy 800H within a CO_2 environment. Carburised HK40 contained extremely coarse intergranular precipitates which were less effective in restricting creep deformation than the smaller, more densely distributed carbides found in unaffected HK40. Embrittlement of grain boundaries ensued reducing rupture lives and increasing creep rates. An example of the damage and void development observed across the weakened grain boundaries can be seen in Figure 3.12. The opposite was seen for Alloy 800H where carburisation resulted in very fine, evenly distributed precipitates that increased creep resistance through the pinning of dislocation movement.

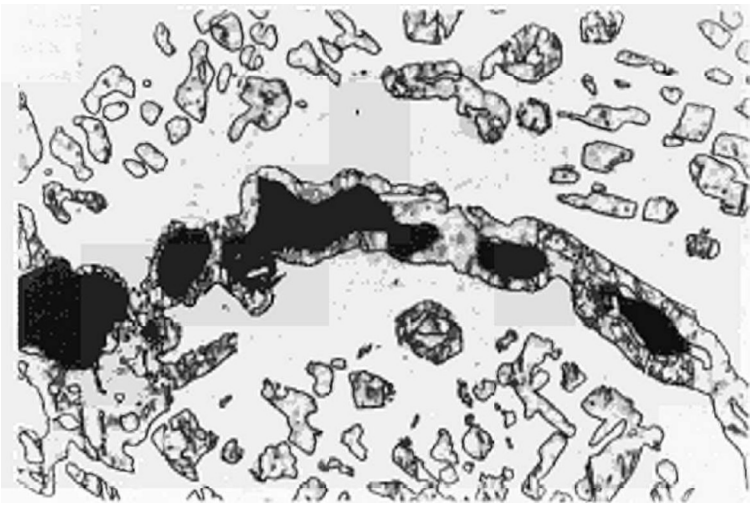
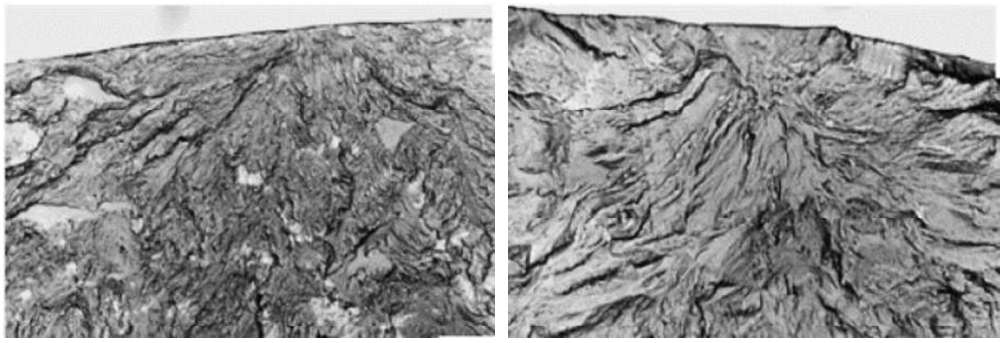


Figure 3.12: Creep damage across carburised grain boundaries in HK40 steel [70].

An internal CEGB technical note by Priddle [73] contains the only reported case of fatigue testing on AGR carburised steel. A series of preliminary high frequency LCF tests were undertaken on serviced aged and carburised 316H. It was found that carburisation reduced the fatigue endurance of specimens by up to a factor of 2 through the initiation of intergranular surface cracking across the hardened layer. This resulted from

carbide precipitation and the subsequent embrittlement of grain boundaries leading to a reduction in surface ductility. The depth of carburisation was very small (approximately 30 µm) compared to that considered within AGR components in this project (150 - 500 µm).

A considerable amount of research has focused on characterising the performance of IG carburised stainless steels. This is because they possess superior mechanical properties that are desirable within a wide range industrial applications [22, 32, 23, 26, 74, 28, 27, 30, 75, 76]. The treatment process results in the creation of an enhanced outer hardened layer that is a single austenite phase (deemed the "S-phase"), supersaturated with carbon with little to no carbide precipitation. The resulting material often displays enhanced fatigue and wear resistance with no discernible loss in surface ductility.



(a) (b)

Figure 3.13: Fractography of (a) untreated and (b) low temperature carburised 316 fatigue specimens showing the initiation of sub-surface cracking below the carburised case [77].

Several authors have studied the room temperature fatigue behaviour of IG carburised austenitic steels. Michal et al. [30] conducted both extensive tensile and high cycle fatigue testing to examine the influence of the S-phase on bulk mechanical properties. Whilst the hardened layer had no clear impact on the macroscopic yield stress, a significant increase in the fatigue endurance limit was observed under fully reversed cyclic conditions. This was due to residual compressive stresses within the hardened layer that inhibited the nucleation of surface fatigue cracks. The residual stresses were generated from lattice expansion due to carbon diffusion [74]. Fractography showed no evidence of widespread surface microcracking, instead, only a single initiating crack below the hardened layer. The outer compressive residual stresses served to shield typical surface nucleation sites leading to internal crack formation [30] with similar findings having been consistently observed throughout the literature [77, 78, 27]. An enhanced high cycle fatigue endurance limit coincided with delayed crack initiation just below the

hardened case. An example of this behaviour is shown in Figure 3.13. Many authors have commented that the depth of carburisation seemed to have no effect on fatigue life [36, 27] and this stands to reason as HCF endurance is dominated by the surface crack nucleation phase.

3.5. Discussion

This chapter has provided a review of gas carburisation and it's resulting impact on the mechanical properties of stainless steels.

A review of the literature found that the effects of carburisation are highly dependent on whether carbides precipitate within the hardened outer layer. An increase in the size and density of carbides generally resulted in a loss of surface ductility and corrosion resistance. This was observed to be due to chromium depletion and an embrittlement of grain boundaries within the austenitic matrix at the surface. This loss of ductility governed the resulting impact on tensile, creep and fatigue behaviour. When surpassed, widespread surface cracking was found to occur that generally reduced tensile strength and creep and fatigue life.

Metallurgical examination of ex-service 316H provides evidence that AGR carburisation results in severe carbide precipitation and grain boundary decoration. For this reason, it is anticipated that carburisation within this environment will generally lead to a reduction in the performance of 316H under both creep and fatigue loading conditions. This is likely to result from premature cracking of the hardened layer and has previously been observed within AGR carburised 9Cr1Mo steels.

The only work conducted to date on AGR carburised 316H was found to be contained in a single technical note that presented very limited fatigue test data. Therefore, there remains a need for a thorough understanding of how AGR gas carburisation affects the mechanical properties of 316H. This is crucial for EDF Energy's structural integrity assessment procedures and forms the majority of work in this thesis.

4. Material and Preconditioning

4.1. Introduction

Type 316H is a stainless steel belonging to the austenitic 300 series family. Compared to regular 316, this "H" variant contains a slightly higher carbon content that enhances its creep resistance at elevated temperatures. For this reason, it has been extensively used within AGR steam header and boiler tube components. Under certain conditions, these components have shown a high susceptibility to carburisation mechanisms. This research focuses on the testing and characterisation of both plain and carburised 316H. A description of the material used and an overview of the preconditioning process used to carburise specimens is provided in this chapter.

4.2. Ex-Service As-Received Material

The material tested within this study has been supplied by EDF Energy, taken from a service exposed (not radioactive) forged 316H steam header (HRA 1C2/3, Cast 55915), Figure 4.1. This had seen approximately 100,000 hours of service at 500°C and was chosen to allow for the production of a large number of specimens. It should be noted that the material was never directly exposed to the AGR gas environment and was therefore not carburised but had undergone significant thermal ageing over its life. In addition, because the applied service stresses were very low (< 50 MPa) it was anticipated that the material had not accumulated any significant creep deformation or internal damage. The chemical composition of the header can be seen in Table 4.1. Measurements were conducted by Podesta [79] and were taken at both the internal and external skins; all compositions fell with AISI specification for 316H.

The ENVISINC project encompassed a broad testing programme at numerous institutions hence required a large number of samples to be manufactured. To maintain consistency, machining was assigned to a single project partner: AMEC Foster Wheeler. The header was initially sectioned into two pieces; cutting planes denoted by the red

lines in Figure 4.1. Removing the nozzle and surrounding areas ensured that no samples were taken from heat affected weld zones. Uniaxial tensile, creep, fatigue and four-point bend specimens were then extracted from the remaining as-received material. In addition, a limited number of cylindrical bars were produced for preconditioning and oxidation trial purposes. Sample blanks were taken from the centre of the wall to avoid any possible microstructural inhomogeneity arising within near surface regions and were orientated parallel to the axial pipe direction. Material extracted from the header with no further treatment is referred to as as-received material from hereafter.

The dimensions of tensile, creep and fatigue samples were defined in accordance with ASTM standards E8M [80], E139 [81] and E606 [82]. The tensile and creep specimens contained chamfered ridges at either side of the gauge length to enable the attachment of capacitive extensometers. A number of modified LCF specimens were created with extended shoulder geometries to enable hydraulic clamping for testing within an Instron TMF machine at Imperial College London. An overview of all sample designs can be seen in Figure 4.2.



Figure 4.1: 316H header HRA 1C2/3, cast 55915 prior to sectioning and sample extraction, red lines denoting cutting planes [83].

Table 4.1: Chemical Composition of 316H as-received Header 1C2/3 (% WT) [83].

Element	**AISI 316H**	**External Skin**	**Core**	**Internal Skin**
C	0.04 - 0.10	0.051	0.051	0.050
N	-	0.082	x	0.080
O	-	0.011	x	0.016
Si	<1.0	0.49	x	0.49
P	<0.04	0.019	x	0.019
S	<0.03	0.013	0.013	0.013
Ti	-	0.01	x	0.01
Cr	16.0 - 18.0	16.8	x	16.8
Mn	<2.0	1.6	x	1.6
Fe	Bal.	Bal.	x	Bal.
Co	-	0.069	0.051	0.069
Ni	10.0 - 14.0	11.5	x	11.5
Mo	2.0 - 3.0	2.3	x	2.3

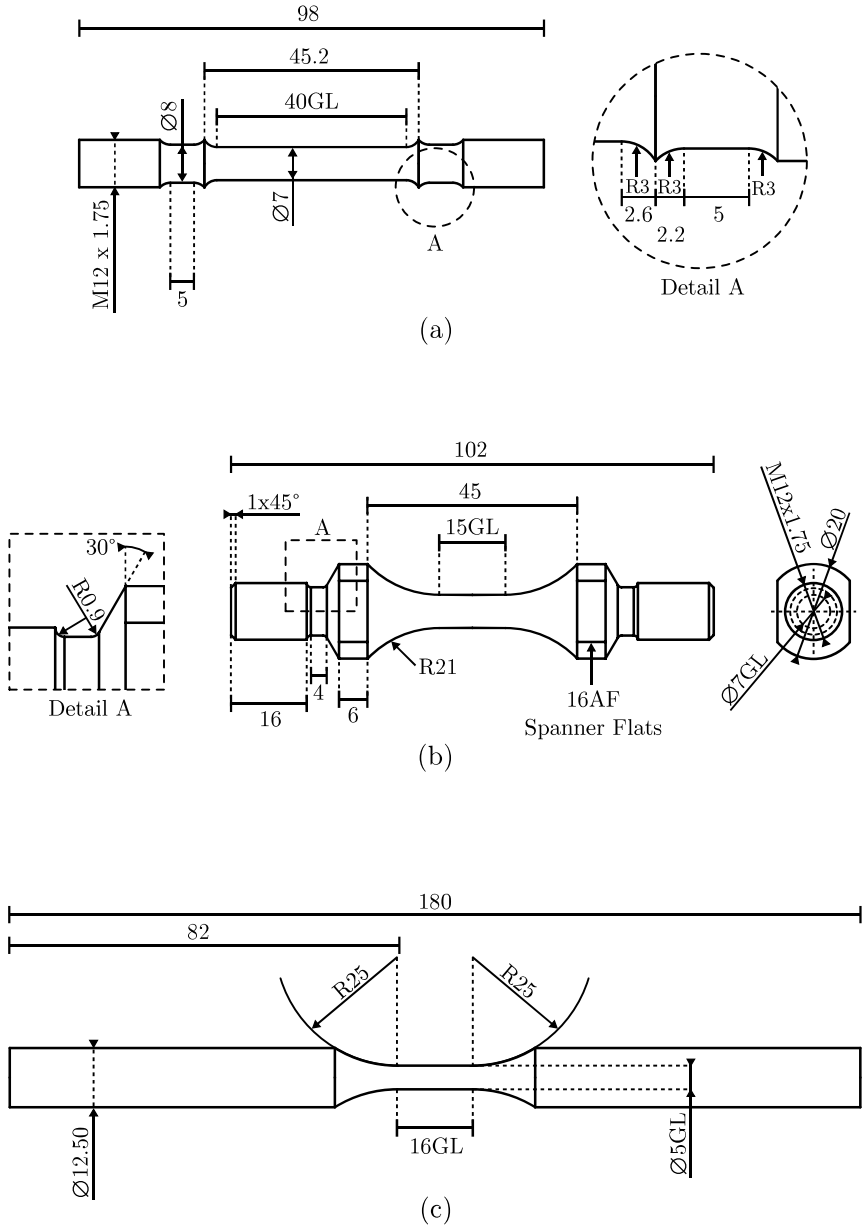
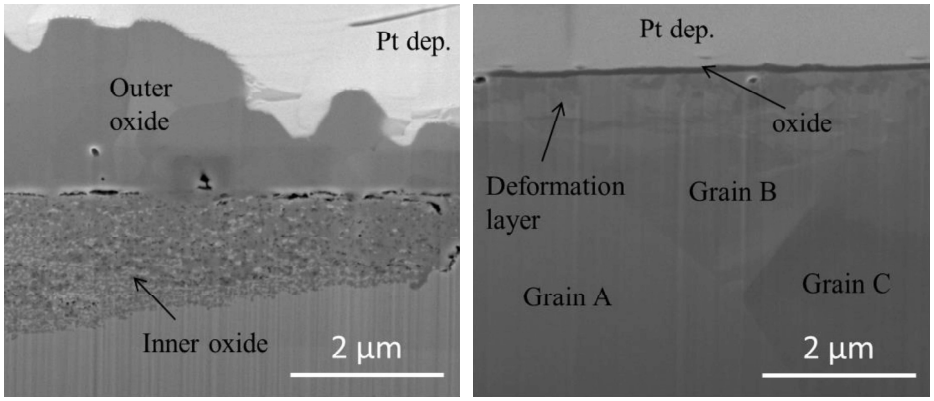


Figure 4.2: Uniaxial (a) creep (b) LCF and (c) Instron LCF specimen design.

4.3. Preconditioning

In situ AGR plant carburisation may take up to tens of thousands of hours to occur and also results in radioactive material that is not suitable for laboratory testing. Therefore, for the purpose of this research, as-received specimens were carburised within a simulated, accelerated AGR gas environment. To ensure meaningful results, it was essential that the preconditioning process resulted in a carburised layer that was representative of that found on components in plant. Achieving this within appropriate time-scales required significant optimisation of both the specimen preparation and preconditioning processes, undertaken by AMEC-Foster Wheeler [83].

A study conducted by Chen et al. [84] explored how AGR gas composition and surface finish affected the oxidation behaviour of 316 with the aim of accelerating carburisation mechanisms. It was found that by adding H_2O into the gas mixture and finely polishing the material surface, the rate of oxide formation could be significantly accelerated. This behaviour can be seen in Figure 4.3 where under the same conditions, a very fine oxide polishing suspension (OPS) finish promoted much thicker duplex oxide formation compared with 600-grit. This is because the rougher surface was able to better maintain it's chromium rich protective film.



(a) (b)

Figure 4.3: Focused Ion Beam cross sections of 316 specimens oxidised at 550°C for 500h with (a) OPS polish and (b) 600-grit SiC ground suface finishes [84].

The findings of this work influenced how as-received sample surfaces were prepared prior to preconditioning, ensuring rapid oxide growth. The preparation procedure is shown in Table 4.2 and is described as follows. Firstly, the work hardened layer resulting from final machining was removed through surface grinding using progressively finer grades of silicon carbide paper, up to 2400-grit. Samples were then polished to a final finish by using increasingly finer diamond suspension solutions followed by an final OPS polish.

This enabled almost instantaneous duplex oxide growth; saving a considerable amount of time on the overall preconditioning process.

Table 4.2: Stages of specimen polishing prior to preconditioning [83].

Stage	Material	Time
1	Silicon Carbide P300 - P2400	-
2	9 µm diamond suspension	5 minutes
3	6 µm diamond suspension	5 minutes
4	1 µm diamond suspension	5 minutes
5	OPS suspension	10 minutes

A number of carburisation trials were initially undertaken by AMEC Foster-Wheeler [83] at a slightly higher exposure temperature compared to that experienced by components in plant (600 °C). Despite this temperature being synonymous with the formation of a healing layer, it was thought that this would not occur over the relatively short preconditioning times and such temperature was necessary to accelerate carbon diffusion.

Trial samples were housed in pressurised autoclaves in a simulated AGR gas coolant containing 1%CO, 500 VPPM (+/- 50 VPPM) H_2 + H_2O and 230 VPPM CH_4. The gas was maintained at a temperature and pressure of 600°C and approximately 4 MPa respectively. Interruptions were conducted at 1 kh intervals up till a total time of 3 kh to examine the evolution of carbon diffusion. The resulting hardness and carbon profiles for each interruption are presented in Figure 4.4. It should be noted that data for the carbon profile at 1 kh was not recorded however it is anticipated that it's overall trend would lie below that of 2 kh with a lower peak value.

A comparison of data showed that a 3 kh exposure resulted in a similar peak surface hardness to that of ex-service carburised and OMS material and was therefore chosen as the optimum preconditioning time. The depth of carbon penetration was also comparable at approximately 250 µm. A 3 kh exposure was therefore seen to sufficiently induce a level of carburisation with a potential effect on mechanical properties comparable to that of ex-service material in a practical time-scale for this study.

A section taken from a 3 kh preconditioned plate can be seen Figure 4.5 with easily identifiable magnetite, spinel oxide and carburised layers. Hardness traces through both as-received and preconditioned 316H clearly show an elevated hardness across the outer carburised layer, Figure 4.6. It should be noted that measurements within the oxide spinel are not included as these were expected to be inherently higher than the bulk material.

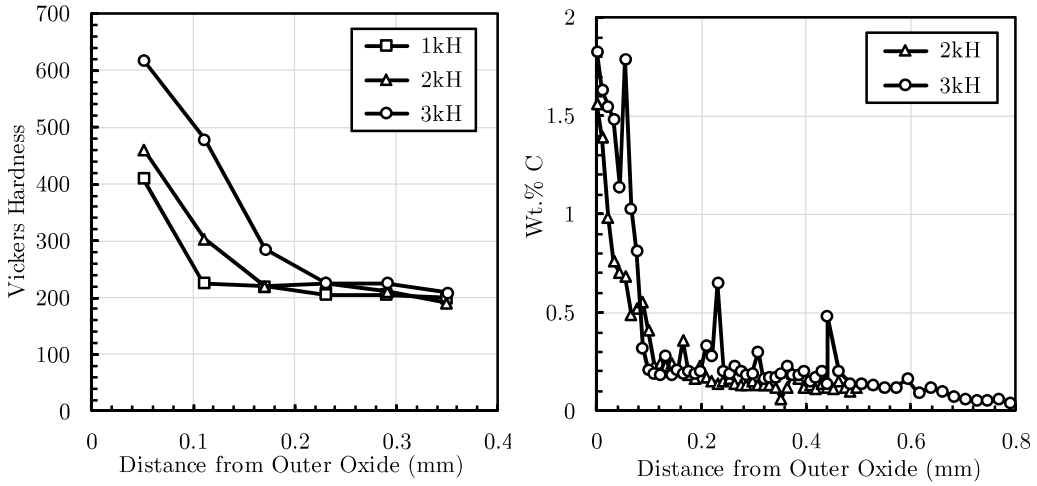


Figure 4.4: Hardness and carbon profiles of preconditioned carburised specimens taken at various exposure times at 600°C [43].

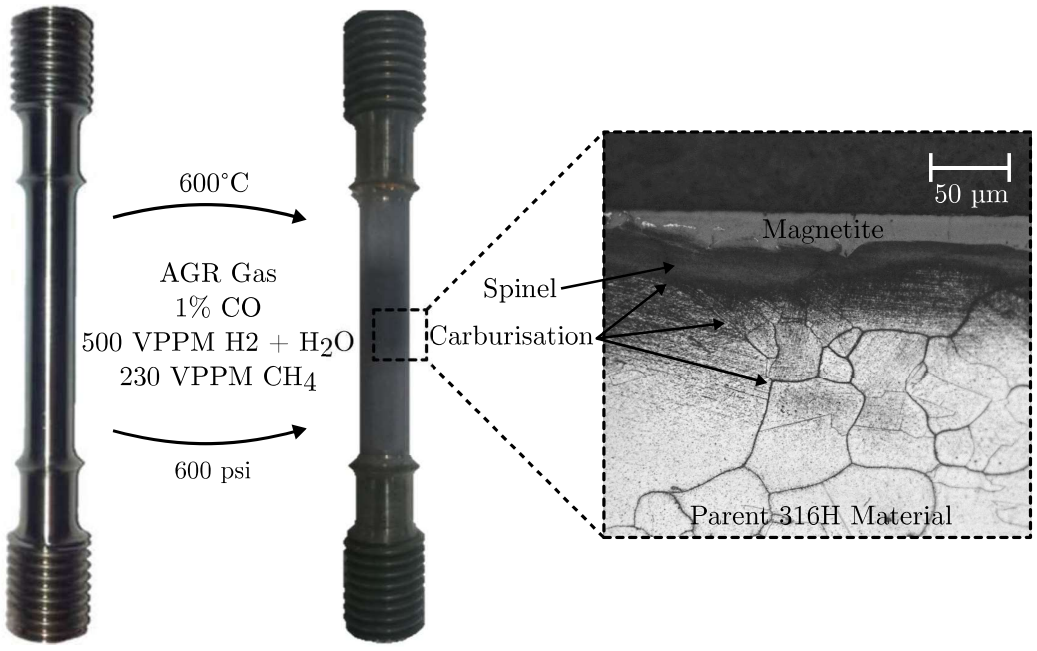


Figure 4.5: Metallographic section taken through a preconditioned carburised specimen at a 3kH exposure (current work).

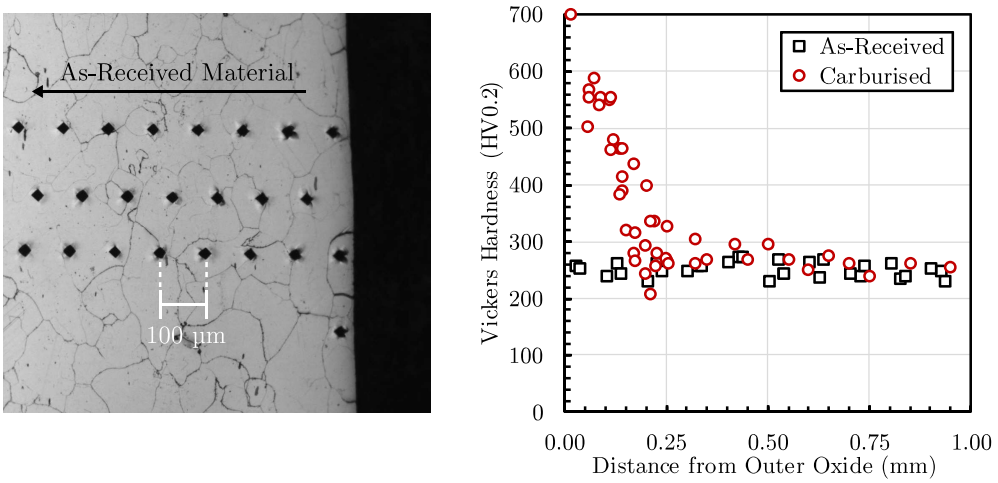


Figure 4.6: A comparison of hardness traces taken through both as-received and preconditioned 316H (current work).

Younes et al. [43] undertook a detailed analysis of preconditioned 316H to verify it's similarity with ex-service carburised material found in plant. Little evidence for the presence of a healing layer was found which was not anticipated to form within the relatively short exposure times. EDX mapping performed on regions adjacent to the oxide spinel showed intergranular carbide precipitation with little or no carbides formed within grains. These ranged in size between 270 - 780 nm and were primarily found to be in an $M_{23}C_6$ configuration. The carbides were often surrounded by a sizeable population of finer M_7C_3 precipitates, indicating a high activity of carbon in these areas upon exposure to the CO_2 gas mixture.

Although the nature of carburisation was similar to that observed in plant, the morphology of carbides greatly differed. This was due to a shorter gas exposure time which limited precipitation growth and resulted in much smaller, less densely populate carbides on grain boundaries. The evolution and growth of these could not be accelerated and required significantly longer thermal ageing. The maximum depth of carburisation and resulting elevated surface hardness was measured to be between 200 - 250 µm which was comparable to ex-service and OMS material.

The preconditioning process held samples at 600°C which, was likely to have introduced additional thermal ageing within the bulk material. This potentially affected the mechanical properties of 316H and therefore, had to be ruled out as a variable when considering the influence carburisation. A number of as-received tensile, creep and fatigue samples were accordingly aged under the same conditions in air and are known as 'thermally-aged' specimens from hereafter. The testing of thermally-aged material is included in Chapters 5 and 6.

5. Effect of Carburisation on Creep

5.1. Introduction

Within AGR plant, many components endure continuous loading under high temperature conditions for significant periods of time. Here, they can undergo creep degradation, leading to excessive deformation and damage. The mechanisms responsible for this have been explored in Section 2.6. Creep is often the life limiting factor of many components as it can result in cracking, therefore, an understanding of the interaction between carburisation and creep is essential to evaluate the effect of AGR carburisation on component lifetime.

A review of the literature found that the influence of carburisation on creep behaviour was highly dependent on the precipitation and morphology of carbides in and around grain boundaries at the surface (Section 3.4). Whilst finely dispersed carbides maintained inherent material ductility and reduced creep rates via dislocation pinning, coarse intergranular carbides resulted in embrittlement which gave rise to the initiation of surface cracking and a reduction in material creep strength.

This chapter investigates the effect of AGR carburisation on both the tensile and creep properties of 316H via a series of high temperature tests on as-received and preconditioned materials. Complete details of the carburisation process and sample geometry are found in Chapter 4. To rule out any effect of thermal ageing induced during preconditioning, a number of thermally aged specimens have been tested. A proportion of the creep data presented in this chapter includes testing from project partners AMEC Foster-Wheeler and The University of Manchester and is marked where applicable. The addition of this data helped mitigate the inherent scatter associated with creep deformation, enabling a more robust analysis to be undertaken of the behaviour of as-received and carburised material.

5.2. Influence of Carburisation on Tensile Response

5.2.1. Introduction

The effect of AGR carburisation on the tensile properties of 316H has been explored through a number of high temperature tensile tests performed on both as-received and preconditioned materials. Samples were housed within a windowed furnace at 550°C, contained within a Mayes servo-electric driven loading frame. This enabled the observation of sample surfaces throughout each test via a DSLR camera and macro lens. Tests were conducted under displacement controlled conditions at a constant crosshead displacement rate of $1\,\mathrm{mm\,min^{-1}}$. For a 40 mm gauge length, this translates to a strain rate of approximately $2.5\,\%\,\mathrm{min^{-1}}$ or $4.2 \times 10^{-2}\,\%\,\mathrm{s^{-1}}$ which enabled the continual inspection of sample surfaces during gradual deformation. Gauge length displacement thus strain was measured using high temperature capacitance extensometers clamped onto specimen shoulders. An illustration of this set-up can be seen in (Figure 5.15).

5.2.2. Tensile Properties

The tensile response of each material is shown in Figure 5.1 in terms of both engineering and true stress-strain values. Preconditioning was found to increase the yield stress of 316H and significantly change its hardening behaviour. A 20% reduction in failure strain was also observed with no obvious changes in Young's modulus or ultimate tensile strength. The properties of each material are contained in Table 5.1. Values of Young's modulus, ultimate tensile strength and failure strain were taken from Figure 5.1 (a) whilst 0.2% proof stresses were calculated based on true strain from Figure 5.1 (b). As-received material displayed a slightly elevated proof stress in comparison with that found in R66 for 316H at 550°C (131 MPa). This has historically been observed in other steam headers and is thought to be due to either in-service ageing or the header manufacture process [85].

Table 5.1: High temperature tensile properties of as-received and preconditioned carburised materials.

Material	$\boldsymbol{E}$ **(GPa)**	$\boldsymbol{\sigma^{\mathrm{p}}_{0.2}}$ **(MPa)**	**UTS (MPa)**	$\boldsymbol{\varepsilon^{\mathrm{eng}}_{\mathrm{f}}}$ **(%)**
As-Received	147	174	452	43.0
Preconditioned	145	223	449	34.5

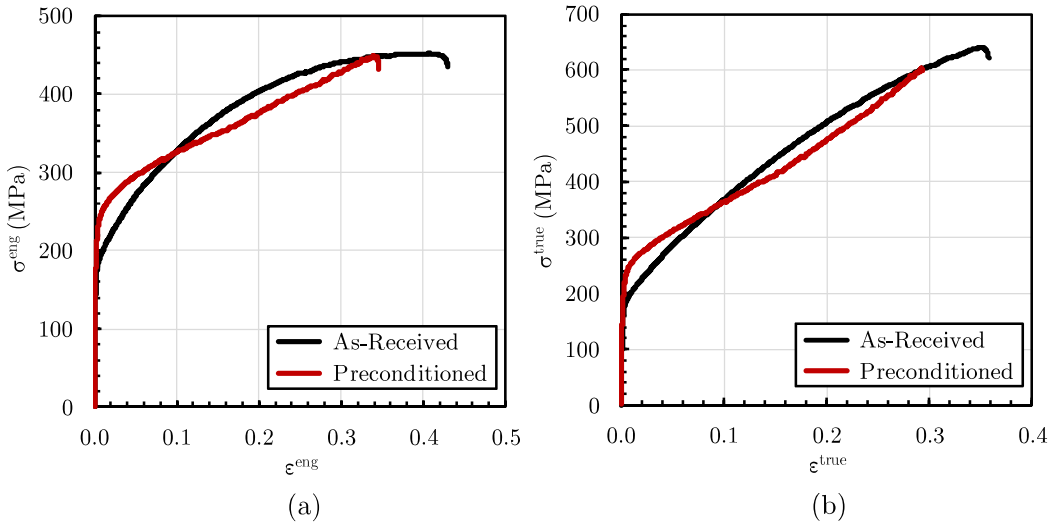


Figure 5.1: A comparison of the tensile response of as-received and preconditioned carburised 316H based on (a) engineering and (b) true stress-strain at 550°C.

5.2.3. Derivation of Ramberg-Osgood Constants

To describe the non-linear stress-strain behaviour of each material, a power-law relationship has be fitted to the true stress versus plastic strain data in the form of Equation 2.2. Distinct regions of strain: small, intermediate and large are each represented by different values of the stress exponent, N (Figures 5.2 (a) and (b)). The entire tensile response has then been characterised by a Ramberg-Osgood material model fit with constants shown Table 5.2. Constants for the carburised layer in isolation are also shown, the derivation of which are described in the following paragraphs. A comparison between the idealised models and experimental data is shown in Figures 5.2 (c) and (d). It should be noted that the coefficients were optimised to fit the tensile response below 10% strain as this was the plastic region of most significance to creep loading.

Table 5.2: Ramberg-Osgood Constants fitted to tensile data for as-received and preconditioned materials with inferred pure carburised values.

Material	As-Received	Preconditioned	Carburised Layer
N	4	6	12
A_p (MPa^{-N})	6×10^{-12}	4×10^{-17}	5×10^{-36}
ε_0^p	1.2×10^{-3}	1.5×10^{-3}	2.5×10^{-3}
$\sigma_{0.2}^p$ (MPa)	174	223	529

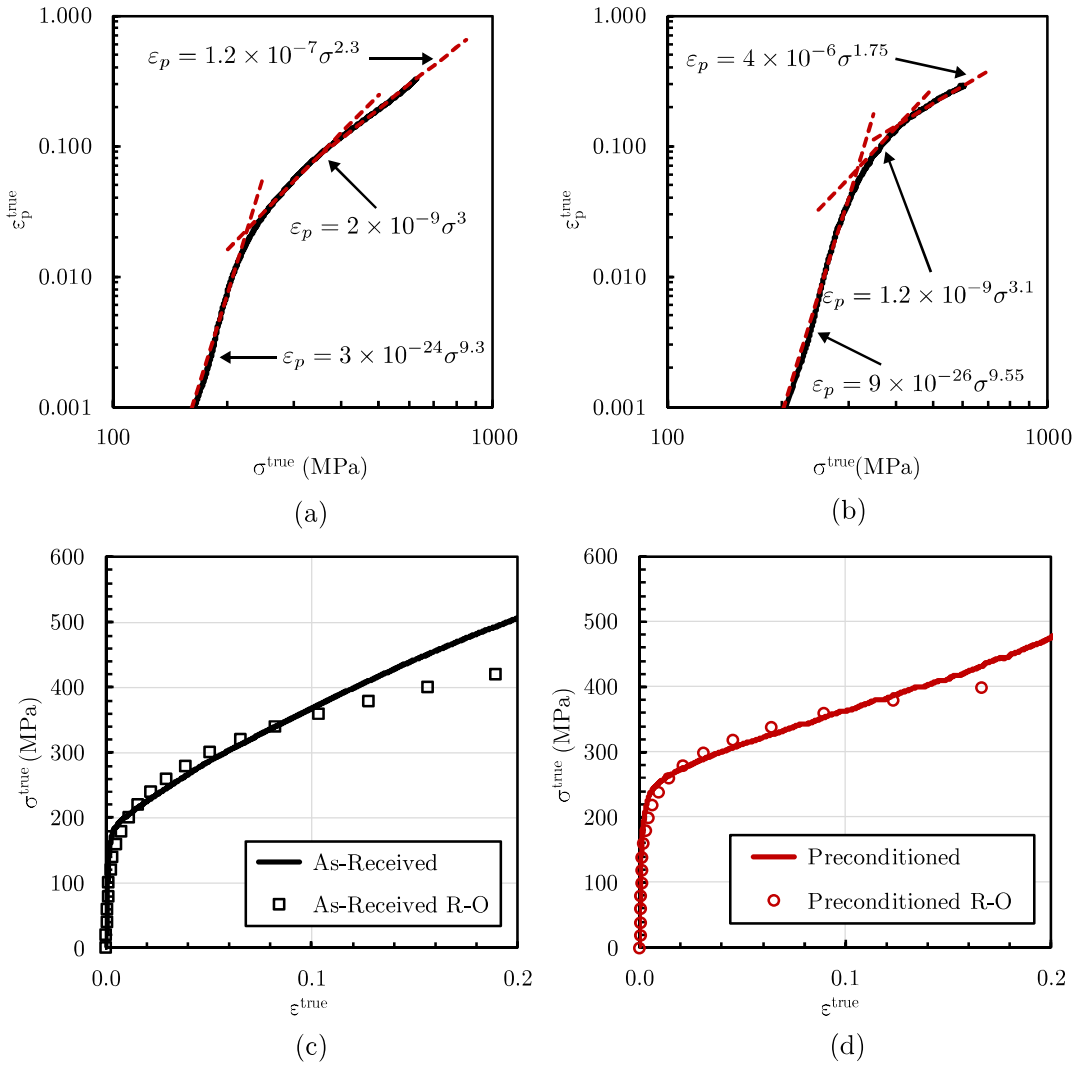


Figure 5.2: Power-law fits to plastic strain data derived from tensile testing on (a) as-received and (b) preconditioned material shown alongside Ramberg-Osgood fits (c)(d) to tensile data.

By assuming that the carburised layer is homogeneous with averaged material properties across it's depth, an idealised Ramberg-Osgood model for pure carburised 316H can be constructed. In reality, it is anticipated that the yield strength across the carburised layer follows a similar trend to hardness, peaking at the surface and reducing to parent material levels after approximately 250 µm. This characteristic depth is based on hardness data and has been defined as the region over which the hardness is at least 10% greater than the bulk [86].

An averaged area-fraction rule has been used alongside previous tensile data to create a Ramberg-Osgood model for carburised material. The stress across the layer at a particular strain has been calculated using Equation 5.1 which scales the contribution of as-received and preconditioned material based on an area ratio of $f = (A_c \setminus A_{AsR})$. Here, it is considered that preconditioned 316H effectively behaves as a bimetallic material containing a 250 µm outer layer. In Equation 5.1 σ_{pre}, σ_{AsR} and σ_c denote the stresses within the preconditioned, as-received and pure carburised materials, respectively [87]. The Young's modulus of the carburised layer has been taken to be 205 GPa. This value was calculated by Wiseby [87] from an extrapolation of tensile data generated from hollow-bar preconditioned specimens. The Ramberg-Osgood constants can be seen in Table 5.2 with a comparison of material models in Figure 5.3.

$$\sigma_{pre} = (1 - f)\sigma_{AsR} + f\sigma_c \tag{5.1}$$

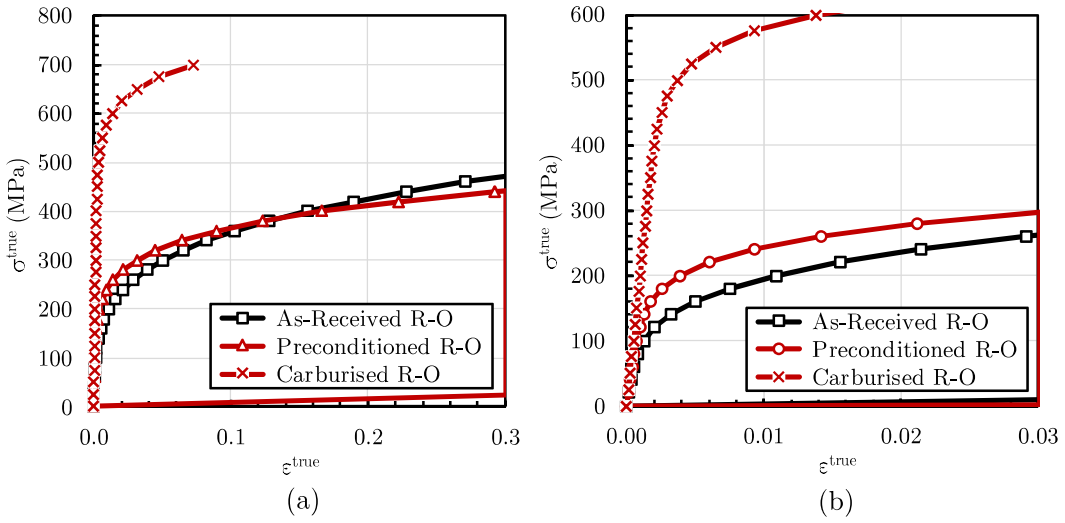


Figure 5.3: Ramberg-Osgood fits (a) (b) to tensile data for as-received, preconditioned and pure carburised 316H (shown at two different strain ranges).

5.2.4. Fracture Behaviour

To investigate the difference in tensile response between as-received and preconditioned materials, sample gauge lengths were examined under optical microscopy. This revealed a contrast in deformation and fracture behaviour, shown in Figure 5.4. The as-received specimen failed in a ductile manner typically known as 'Cup and Cone' fracture, associated with high levels of necking and plastic deformation. In contrast, there was little to no observable necking of the preconditioned sample which failed with a fracture surface orientated at a 45°angle to the direction of load. This behaviour is associated with brittle shear fracture as the plane of maximum shear stress acts at a 45°angle to the primary torsion axis. The lack of a neck was consistent with the engineering tensile response where no significant load drop was observed prior to fracture.

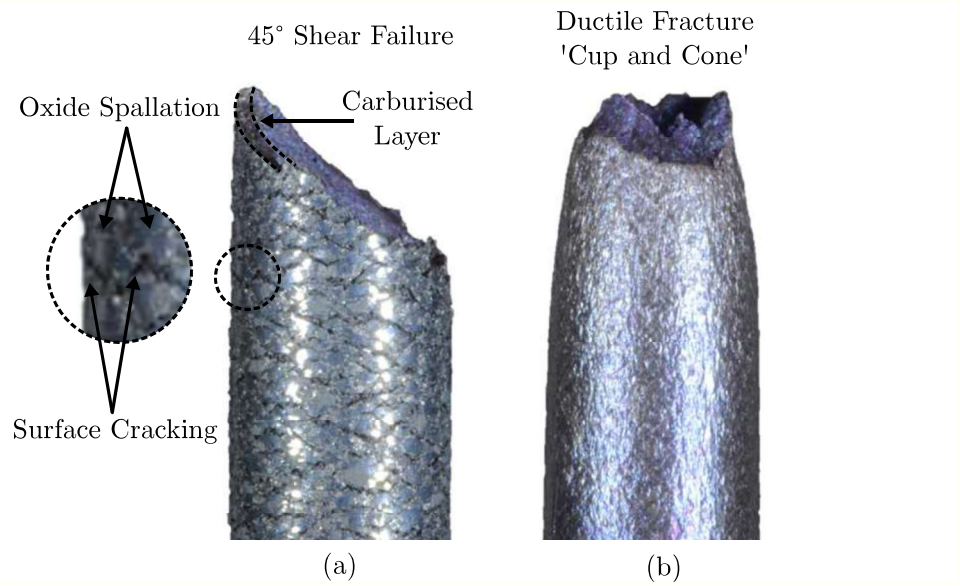


Figure 5.4: (a) Preconditioned and (b) as-received samples surfaces after high temperature tensile testing at 550°C.

The preconditioned material contained widespread surface cracking alongside severe spallation of the magnetite layer. Such surface damage occurred within the early stages of test, below approximately 2% total and resulted in magnetite being deposited on the furnace floor. To examine the nature of this cracking, the sample was sectioned, polished to a 1 µm finish and etched using Ferric Chloride solution, revealing the underlying carburisation and microstructure (Figure 5.5). Cracking appeared to have initiated on the outer surface and propagated along grain boundaries through the carburised layer. The majority of cracks were arrested at the carburised layer-bulk material interface with the depth of cracking increasing towards the fracture surface.

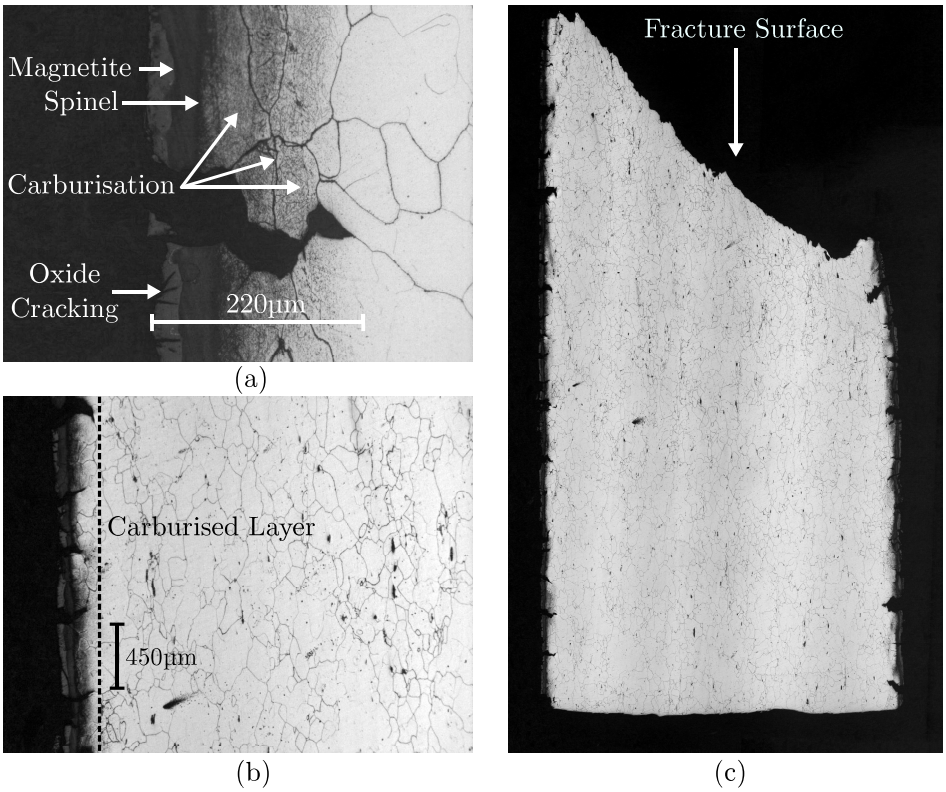


Figure 5.5: Micrograph taken from a preconditioned tensile specimen showing (a) (b) widespread intergranular surface cracking along the entire gauge length.

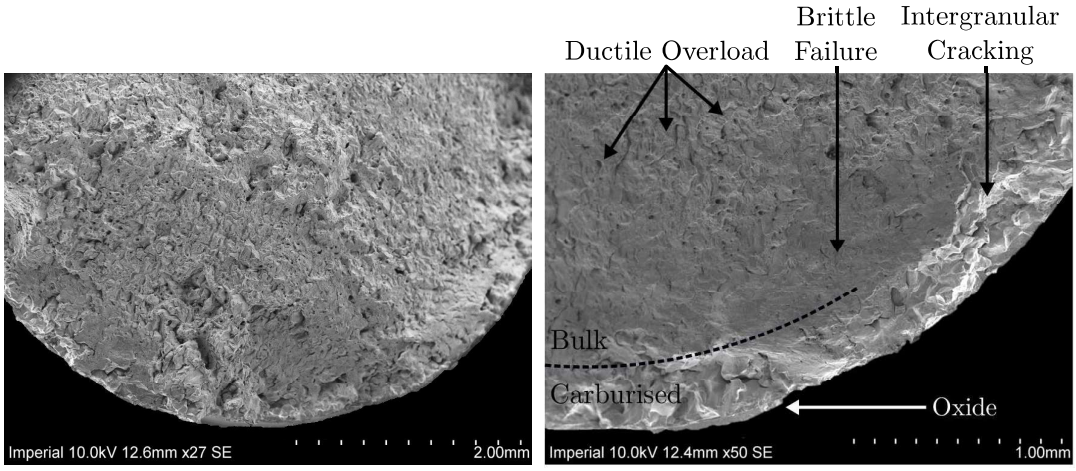


Figure 5.6: SEM images taken of the fracture surface from a preconditioned tensile specimen showing the difference in failure mode of carburised and bulk 316H.

The fracture surface of the preconditioned specimen was imaged under scanning electron microscopy, shown in Figure 5.6. A clear distinction between the mode of failure within carburised and bulk 316H can be observed with each failing through intergranular and mixed-mode overload brittle fracture, respectively.

5.3. Modelling Cracking within Carburised 316H

5.3.1. Introduction

Tensile testing confirmed that carburisation resulted in an increase in nominal yield stress, reduction in ductility and widespread surface cracking within the outer hardened layer. It was observed that the majority of surface cracks had been arrested at the interface between the carburised and underlying parent material. In addition, the sample failed with negligible necking of the gauge length and a fracture surface orientated at a 45°angle to the direction of load. To further understand this fracture behaviour, a series of finite element models were created that investigated the interaction between multiple surface crack stresses fields and the influence of a carburised layer on parent material deformation.

5.3.2. Model Configuration

A finite element analysis has been conducted on a two dimensional, axisymmetric uniaxial tensile sample using Abaqus [88] FEA software. An overview of the model configuration can be seen in Figure 5.7. The specimen geometry was identical to the physical tensile samples, containing a 7 mm diameter gauge length. To increase computational efficiency, the model employed both axisymmetric and in plane symmetry boundary conditions along the zero y- and x-axis, respectively. A mode I loading tensile force was applied through either a uniformly distributed load or set nodal displacement along the upper specimen edge.

Surface cracking of the carburised layer was represented by a number of analytical seams that acted as edges that were free to open during the analysis. For each seam, a virtual crack extension direction was specified using a q-vector that lay perpendicular to the direction of axial load, parallel to the crack plane. A singularity was defined at the inner tip of each crack which was also accompanied by a circular partitioned geometry (shown in yellow in Figure 5.7). This facilitated the generation of a focused, swept mesh that defined a singularity at the crack tip using a number of collapsed quadrilateral elements.

The entire mesh was constructed from 4-noded bilinear axisymmetric quadrilateral elements (CAX4R) with density biases set up to reduce element size on approach to a crack. This enabled accurate resolution of crack tip stress/strain fields with the average modelled element size being approximately 25 µm.

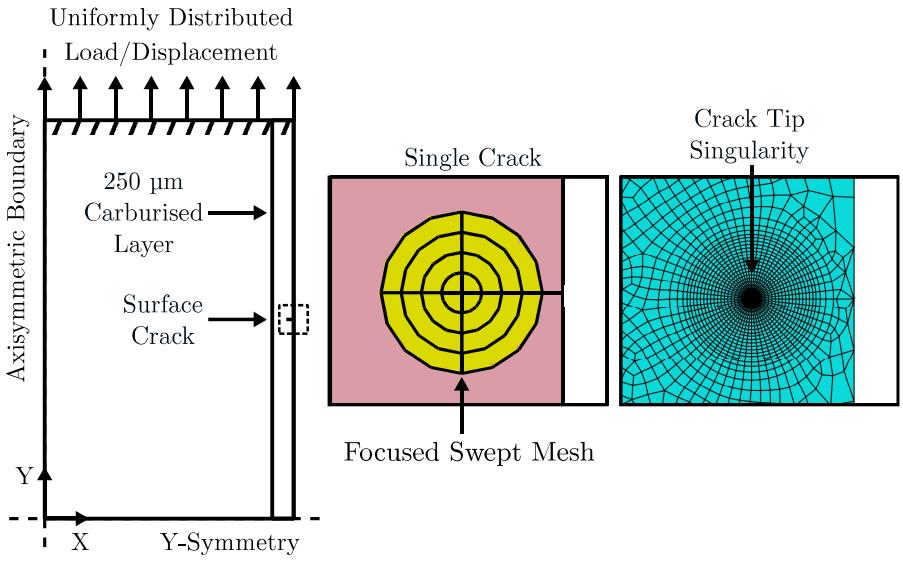


Figure 5.7: An overview of the finite element tensile model showing the boundary conditions and crack tip mesh configuration.

The preconditioned material was represented as a bimetallic metal consisting of a discrete carburised layer having a set depth of 250 µm. For simplicity, it was assumed that the layer contained isotropic material properties that did not vary as a function of depth (as was anticipated from hardness testing). The tensile response of each material was modelled as a Ramberg-Osgood fit to previous tensile data where carburised properties were derived from an area ratio rule. Material constants can be found in Table 5.2.

5.3.3. Model Validation

A validation exercise was undertaken to ensure that the axisymmetric model and corresponding material properties accurately represented the tensile behaviour of as-received and preconditioned material. This involved simulating the tensile tests conducted in Section 5.2 by adding a displacement boundary condition to the upper sample edge. A comparison with the experimental engineering stress-strain response has been made by extracting the total vertical reaction force and dividing this by the model area. Strain has been calculated through simply dividing the total displacement by the effective gauge length.

A comparison between experimental and FE tensile curves for both preconditioned and as-received materials is shown in Figure 5.8. Both models were found to be in good agreement with experimental data with the enhanced yield stress due to the addition of an outer hardened layer successfully represented. This provided confidence in the derived material properties and simplified Ramberg-Osgood model at these low strains. The hardening behaviour of the preconditioned sample was slightly over predicted by the model which is likely to be due to the isotropic material assumption overestimating the total carburised layer strength.

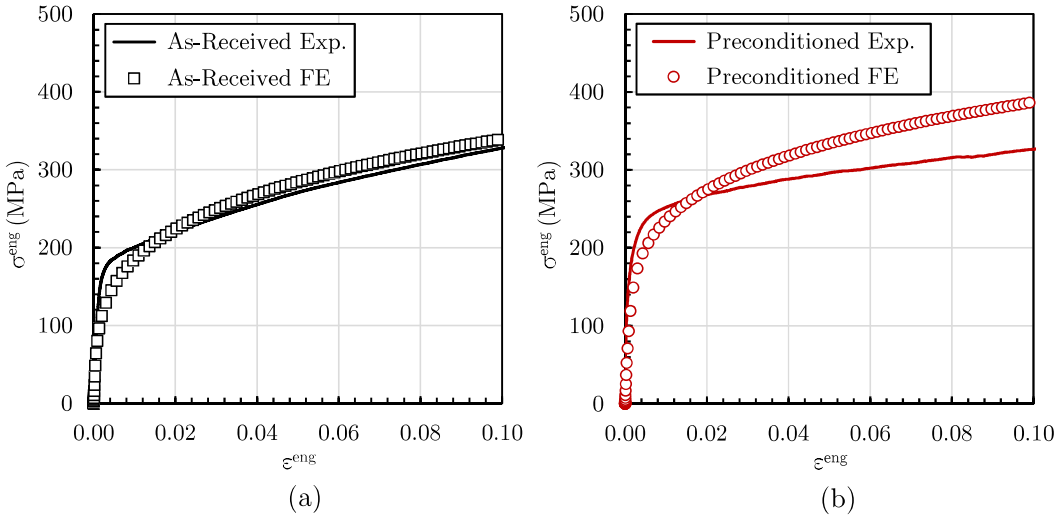


Figure 5.8: A comparison of the tensile curves of (a) as-received and (b) preconditioned materials from tensile testing and FE modelling.

5.3.4. Elastic Crack Analysis

The cracking behaviour of preconditioned samples was investigated through a series of models containing both a single and multiple surface cracks at various depths within the carburised layer and bulk material. A simple elastic analysis containing a single circumferential crack was first conducted and this was compared to an analytical LEFM solution. A nominal strain of 0.6% was applied to the sample through both displacement and load control at which values of stress intensity at the crack tip (K) were extracted. The model was then extended to include multiple surface cracks spaced at 250 µm intervals as observed within section metallography. The total crack length, a, ranged from 50 - 1000 µm, providing a/w values between 0.014 and 0.29.

The results of the elastic analysis can be seen in Figure 5.9. The derived values of K were found to be in excellent agreement with the analytical LEFM solution for a double edge

notch specimen [89] under both displacement and load controlled conditions. When multiple cracks were introduced into the model, the stress intensity at the crack tips was seen to reduce significantly, Figure 5.9 (b) with the difference in K values increasing at higher crack depths. Figures 5.10 and 5.11 shows a comparison of crack tip stress fields for a 150 µm depth in a single and multi-crack case. Here, stresses towards the crack tips approach infinity due to LEFM assumptions. An interaction between the stress fields from multiple crack stress concentrations was seen which in turn, created a shielding effect that lowered maximum tip stresses.

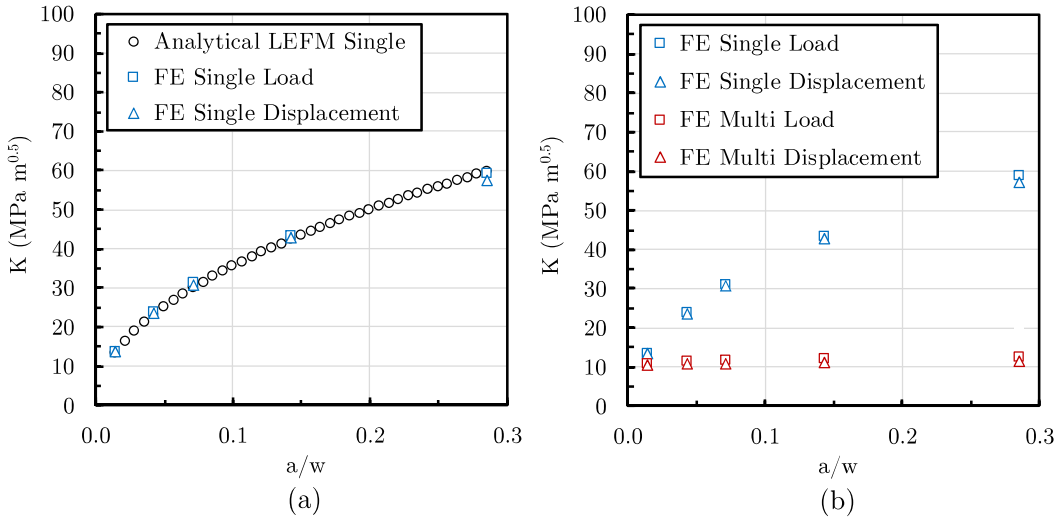


Figure 5.9: A comparison of K values over increasing crack lengths for (a) single cracked and (b) multi-cracked LEFM finite element models.

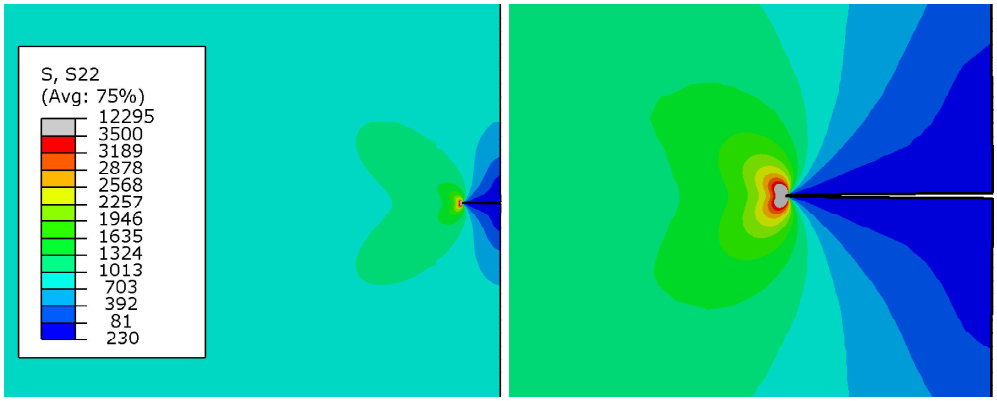


Figure 5.10: Crack tip stress fields in preconditioned material within a single crack elastic FE model.

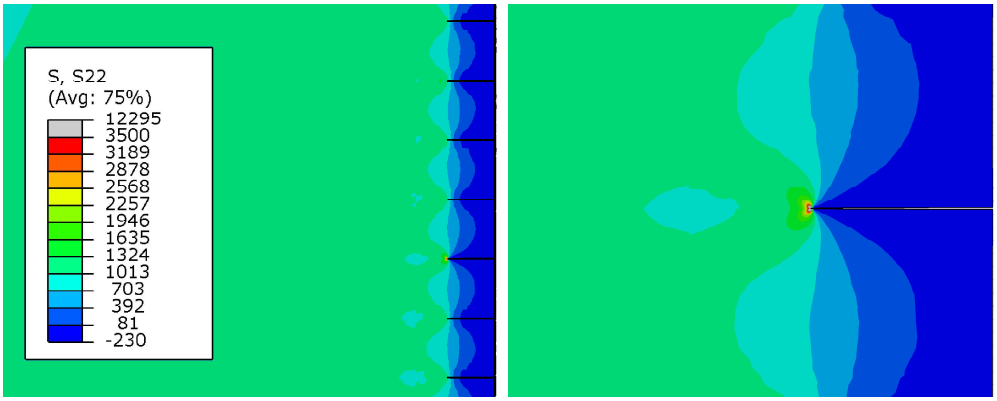
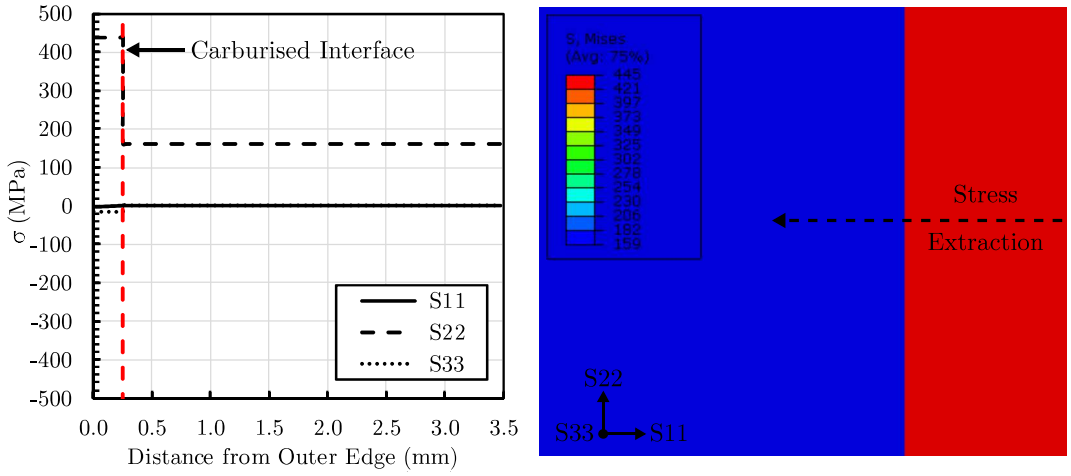


Figure 5.11: Crack tip stress fields in preconditioned material within a multi-crack elastic FE model.

5.3.5. Elastic-Plastic Constraint Analysis

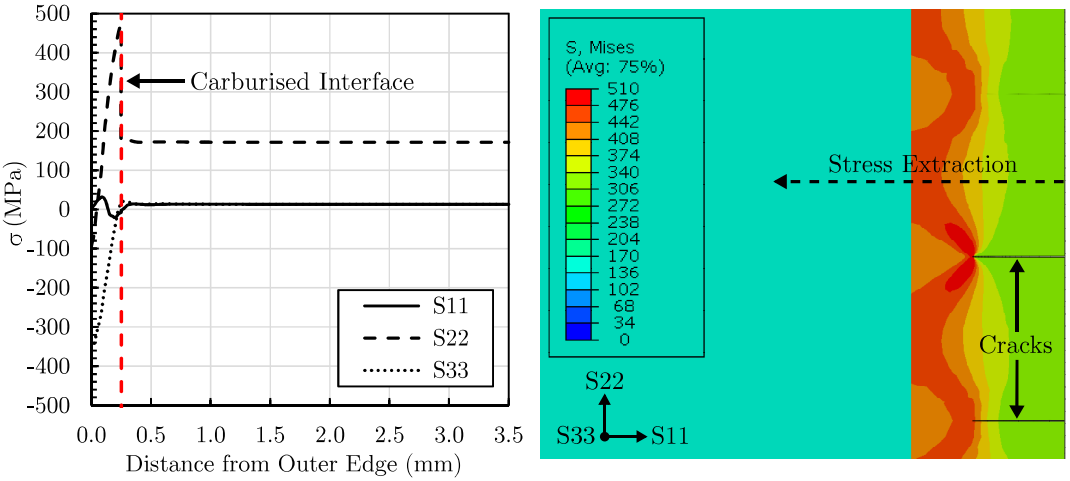
To investigate how the carburised layer affected the deformation of the underlying parent material, an elastic-plastic analysis was conducted for varying crack depths. Axial (S22), radial (S11) and hoop (S33) stress profiles were created for three separate scenarios: no fracture of the carburised layer, partial ($a = 150\,\mu m$) and full cracking ($a = 250\,\mu m$). For each, an axial strain of 0.6% was applied to the sample top surface using a displacement controlled boundary condition. The principal stresses were extracted across a section taken through the entire sample radius (normal to the direction of load) and where applicable, mid-way between two crack faces (Figure 5.13).

The resulting stress profiles across both carburised and bulk material are shown in Figures 5.12 to 5.14. As expected for all scenarios, axial stresses (S22) peaked higher within the carburised layer compared to bulk material with the difference in peak stress decreasing with increasing crack length. The radial (S11) stresses were negligible in the uncracked case with increased magnitudes in the partially and full cracked cases. For all models, compressive hoop stresses (S33) were generated within the carburised layer that translated to slightly positive tensile stresses in the bulk material. The magnitude of these increased at larger crack depths suggesting that the carburised layer was providing a level of constraint to the underlying material. The implications of these findings are discussed in Section 5.5.



(a) (b)

Figure 5.12: A comparison of principal stresses extracted from FE modelling of an intact carburised layer within a tensile preconditioned sample.



(a) (b)

Figure 5.13: A comparison of principal stresses extracted from FE modelling of a partially cracked carburised layer within a tensile preconditioned sample.

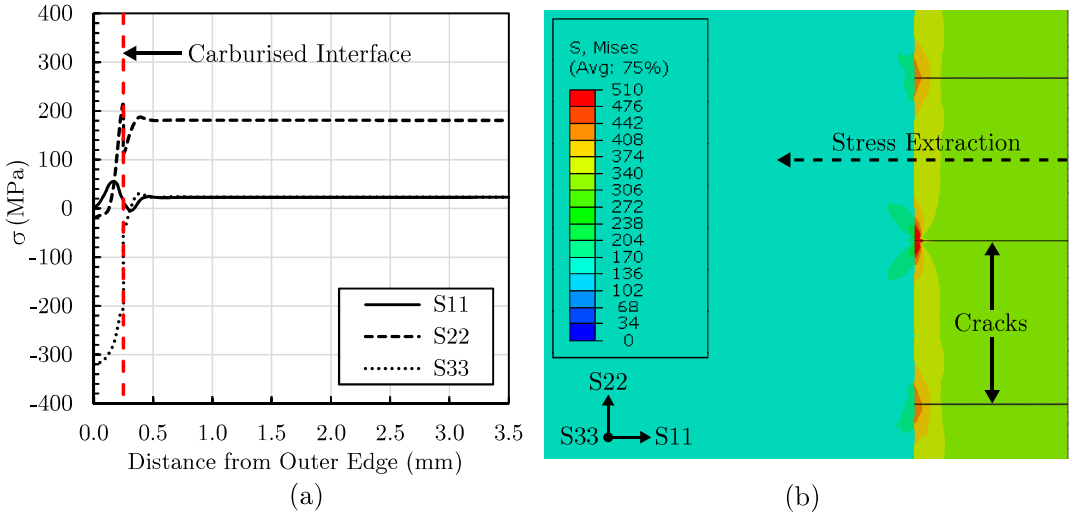


Figure 5.14: A comparison of principal stresses extracted from FE modelling of a fully cracked carburised layer within a tensile preconditioned sample.

5.4. Effect of Carburisation on Creep Behaviour

A series of high temperature creep tests were conducted to examine the effect of carburisation on the creep behaviour of 316H. Samples were taken to rupture and also interrupted at various stages during creep to allow for the evolution of cracking/damage to be monitored. The results of all tests are presented within this section.

5.4.1. Creep Test Setup

An overview of the creep test setup is shown in Figure 5.15. Testing was undertaken at a temperature of 550°C which was representative of that experienced by components in plant. Samples were heated within a 3-zone PID controlled furnace and allowed to heat soak for a minimum of 24 hours. Surface temperatures were measured using two K-Type thermocouples attached at the opposite ends of specimen gauge lengths. These were kept within ± 2.5°C of each other to ensure even gauge temperatures. Creep strain was measured using capacitive extensometers clamped onto specimen shoulders which were able to resolve very small changes in displacement, up to 5 µm. These functioned by detecting the change in capacitance of the air gap between the gauge and target at increasing distances as samples deformed. A gauge calibration was undertaken prior to each test using a micrometer calibration device at known displacement values. This enabled the calculation of a gauge factor which was used to convert the output voltage

into displacement hence strain. Temperature and strain data was remotely logged via a separate RIO server.

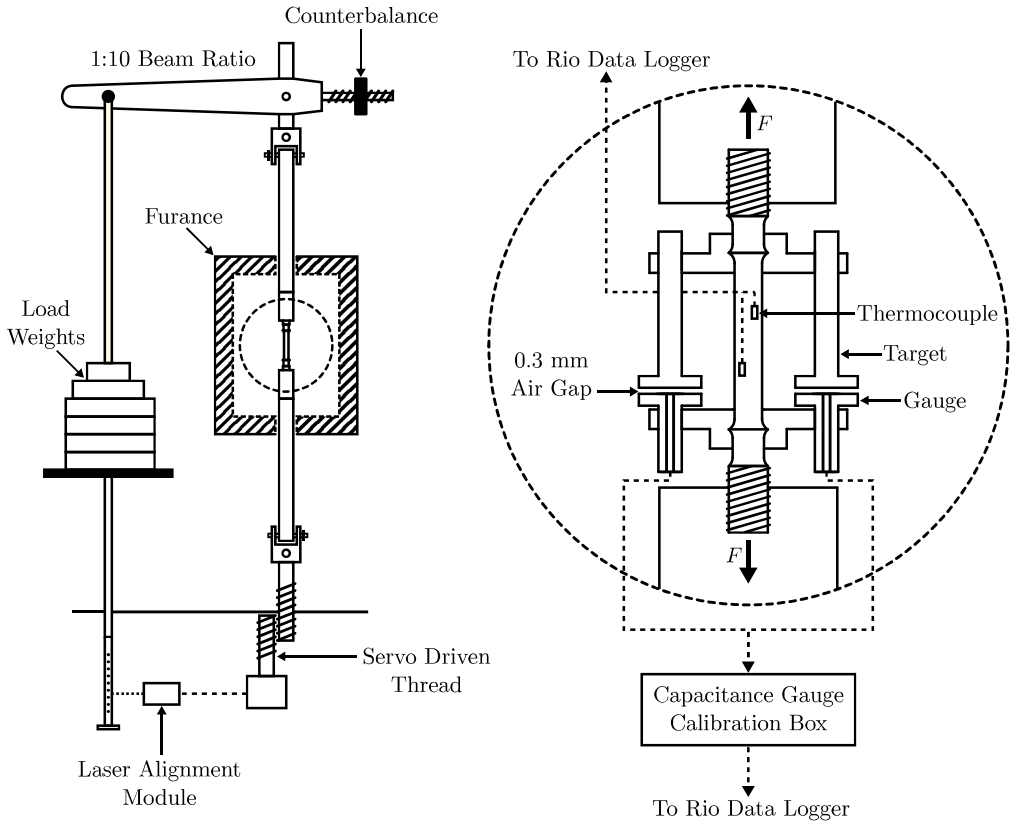


Figure 5.15: Experimental setup for high temperature uniaxial creep testing.

Samples were tested under constant load conditions. An initial engineering creep stress was calculated by dividing the total load (factoring a 1:10 beam ratio) over the measured cross sectional gauge area. The load up procedure consisted of progressively applying each weight then waiting for the machine to automatically balance the cross-head. This ensured a constant moment arm thus stress was being applied to the specimen and that the load frame was being kept within its operational limits. Automatic balancing was controlled through a laser alignment module that fed back to a servo driven adjustable base screw thread. The module's beam was calibrated against a known height marker that corresponded to a balanced load.

A total of nine creep tests were performed at Imperial College London with some being taken until rupture and others interrupted at various stages during creep. The applied stresses were typical of accelerated high temperature creep testing and ranged from 220 - 320 MPa. The entire test matrix can be seen in Table 5.3.

Table 5.3: Creep Test Matrix.

Specimen	Material	Temperature (°C)	Creep Stress (MPa)	Test Type
ASR1	As-Received	550	300	Rupture
ASR2	As-Received	550	320	Rupture
C1	Carburised	550	300	Rupture
C2	Carburised	550	320	Rupture
TA1	Thermally Aged	550	300	Rupture
C3	Carburised	550	260	Interrupted
C4	Carburised	550	260	Interrupted
C5	Carburised	550	220	Interrupted
C6	Carburised	550	220	Interrupted

Additional tests were conducted by AMEC Foster-Wheeler and The University of Manchester with the aim of creating a robust creep data set for the entire ENVISINC project. Since data was going to be sourced from three separate institutions, it was important to ensure consistency for meaningful comparison. Each laboratory was therefore required to strictly follow a pre-set work instruction that detailed test setup procedure and data collection. Key values such as strain on loading and change in specimen diameter were recorded in order to enable a creep analysis based on applied true stress. Baseline creep tests of as-received material were conducted at each institution to validate consisentency between laboratories. Tensile load-up and creep data from Imperial College London and AMEC Foster-Wheeler were shown to be in excellent agreement with rupture times and minimum creep rates matching within a 5% range suggesting that the data was acceptable for use within comparative studies [83].

5.4.2. Load-up Behaviour

Load-up data was recorded to confirm plastic strain upon loading and to examine the differences in tensile response between as-received and preconditioned materials. Because strain measurements were taken in stages, after each weight was added to the load frame, the tensile behaviour of each sample is described by only a limited set of data points.

Table 5.4 details the key load up characteristics for each specimen. Figure 5.16 (a) shows the overall load response for each material (as-received, preconditioned and thermally aged) while Figure 5.16 (b) compares this with previously derived Ramberg Osgood material models. This figure includes data from both AMEC-Foster Wheeler

and The University of Manchester to strengthen the trends observed for each material.

Table 5.4: Creep Load-up Data.

Specimen	Material	σ_{nom} (MPa)	σ_{true} (MPa)	ε^{eng}_{load} (%)	$\varepsilon^{true}_{load}$ (%)	$\varepsilon^{eng}_{p,load}$ (%)
ASR1	As-Received	300	319	6.3	6.1	5.9
ASR2	As-Received	320	352	10	9.5	9.3
C1	Carburised	300	315	5.3	5.1	4.9
C2	Carburised	320	338	5.9	5.8	5.5
TA1	Thermally Aged	300	317	5.7	5.5	5.3
C3	Carburised	260	263	1.4	1.3	1.2
C4	Carburised	260	261	0.7	0.7	0.47
C5	Carburised	220	221	0.4	0.4	0.22
C6	Carburised	220	221	0.4	0.4	0.22

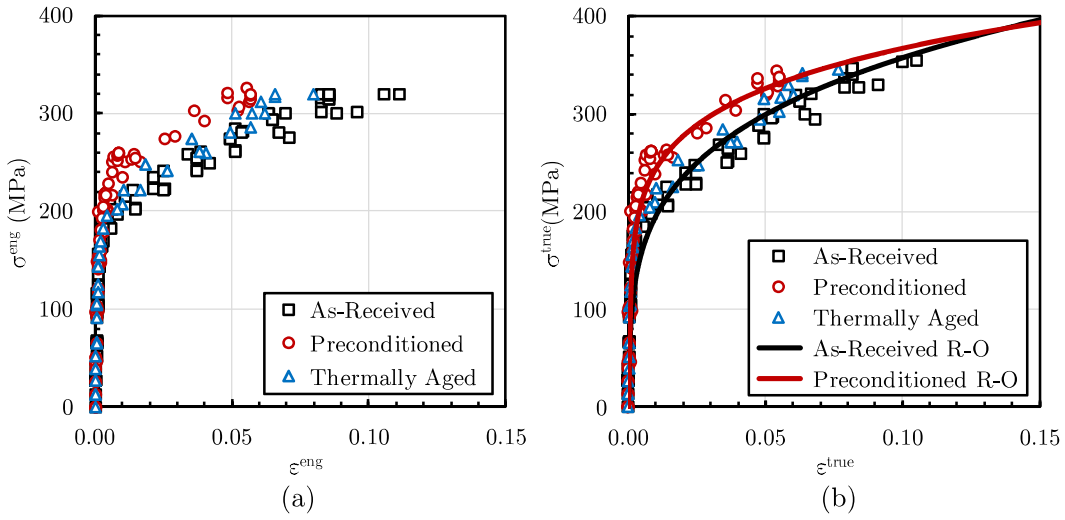


Figure 5.16: (a) Creep load-up data (b) compared with derived Ramberg-Osgood material models from Section 5.2.3.

The majority of samples exhibited significant plasticity upon loading, especially at the higher applied stresses of 300 MPa and above. At the same stress, preconditioned specimens generally displayed lower overall plastic loading strains when compared with their as-received counterparts i.e. 9.3% for as-received and 5.5% for preconditioned at 300 MPa. This was unsurprising given the enhanced yield stress of preconditioned

material. At the lower test stresses, samples remained largely elastic as they remained closer to yield with $\sigma^p_{0.2} = 223$MPa for preconditioned. The effect of additional thermal ageing on as-received material did not appear to be pronounced with only a slight increase in yield stress observed. Figure 5.16 (b) shows the derived material properties to be in excellent agreement with the load-up data, validating the assigned Ramberg-Osgood constants for this level of strain.

5.4.3. Creep Rupture Testing

Rupture testing was undertaken on as-received, preconditioned and thermally aged materials to examine the interaction between carburisation and creep damage. From this, a number of creep properties were derived for each specimen. An overview of these can be seen in Table 5.5 and the several paragraphs that follow describe how these were calculated.

Creep failure strain (or creep ductility) has been calculated according to both the change in axial displacement and the reduction of gauge length area (ROA) close to the fracture surface. Whilst the change in axial displacement averages the strain over the entire specimen gauge length, an ROA approach considers the strain local to the failure region thereby giving a more accurate representation of creep ductility. Both methods have been been used in Table 5.5 and are displayed in Equations 5.2 and 5.3.

$$\text{Axial} \quad \varepsilon^{eng}_{c,f} = \frac{\Delta_c}{l_o} \tag{5.2}$$

$$\text{ROA} \quad \varepsilon^{eng}_{c,f} = \left(\frac{A_o - A_f}{A_o}\right) - \varepsilon^{eng}_{p,load} \tag{5.3}$$

Δ_c is the axial displacement accumulated during creep and is equal to the total displacement less loading displacement. This is measured across specimen shoulders using a capacitive extensometer setup. l_o is the original gauge length prior to testing and A_0 and A_f denote the original and failed gauge length areas respectively, calculated from the measured fracture surface diameter using either vernier callipers or a shadowgraph. When calculating ROA creep failure strain, the plastic loading contribution has to be taken away from the overall strain value to negate the effect of necking upon loading. However, as it was not physically possible to measure the change in diameter after hot loading, Equation 5.3 instead utilises the measured axial plastic loading strain.

Stress and strain values have been provided in engineering and true form. True stresses have been calculated according to Equation 5.4 which simply employs the axial measured strain upon loading. The calculation of true axial strain is shown in Equation 5.5.

$$\sigma_{true} = \sigma_{nom}\left(1 + \varepsilon_{load}^{eng}\right) \tag{5.4}$$

$$\varepsilon_c^{true} = ln\left(1 + \varepsilon_c^{eng}\right) \tag{5.5}$$

Calculating true strain based on ROA requires a slightly different approach and is seen in Equation 5.6 where d_0 and d are the original and instantaneous diameter of the specimen, respectively. This can then be extended to evaluate the true creep strain at failure by removing the effect of plasticity upon loading, as shown in Equation 5.7.

$$\varepsilon^{true} = ln\left(\frac{A_0}{A}\right) = 2ln\left(\frac{d_0}{d}\right) \tag{5.6}$$

$$\varepsilon_{c,f}^{true} = 2ln\left(\frac{d_0}{d}\right) - \varepsilon_{p,load}^{true} \tag{5.7}$$

An overview of these measurements is provided in Table 5.5 for all rupture specimens. Carburisation was seen to significantly modify the creep behaviour of as-received material. Despite possessing a hardened outer layer, a higher yield stress and a lower plastic strain upon loading, specimens C1 & C2 failed in almost half the time of their as-received counterparts at much higher creep ductilities. ROA ductility values were markedly higher than those based on axial strain.

A comparison of the creep behaviour between as-received and preconditioned material is shown in Figures 5.17 and 5.18. Minimum creep rates are displayed alongside the normalised creep curves for each specimen. These were normalised against both creep failure strain (ε_f^c) and rupture time (t_f) to provide a clear comparison between the fraction of life spent in each creep region: primary, secondary or tertiary. Within these figures, the displayed strain corresponds to that calculated from the change in axial displacement. Plotting in terms of ROA was not possible as the change in gauge length diameter was not continuously measured during the test.

Table 5.5: Creep rupture and failure strain data.

ID	$\sigma_{\mathbf{true}}$ (MPa)	$\mathbf{t_r}$ (h)	$\varepsilon^{\mathbf{eng}}_{\mathbf{c,f}}$ Axial (%)	$\varepsilon^{\mathbf{true}}_{\mathbf{c,f}}$ Axial (%)	$\varepsilon^{\mathbf{eng}}_{\mathbf{c,f}}$ ROA (%)	$\varepsilon^{\mathbf{true}}_{\mathbf{c,f}}$ ROA (%)
ASR1	319	3183	2.70	2.67	3.73	5.23
ASR2	352	1481	2.99	2.95	3.49	4.19
C1	315	1199	4.46	4.36	8.07	9.30
C2	338	649	5.03	4.91	6.86	7.77
T1	317	9026	4.95	4.83	5.07	5.84

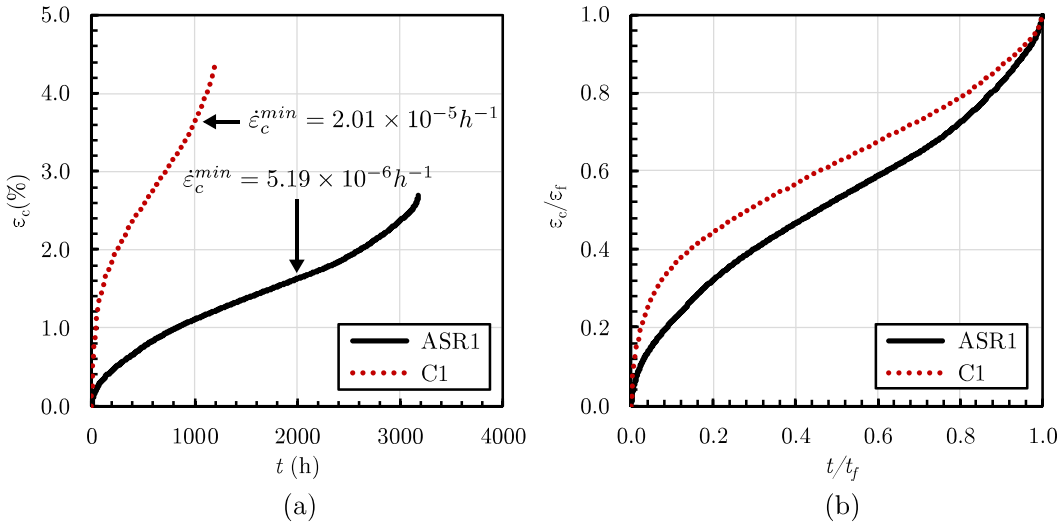


Figure 5.17: Creep rupture curves of as-received and preconditioned specimens tested at 300 MPa displayed in (a) absolute and (b) normalised form.

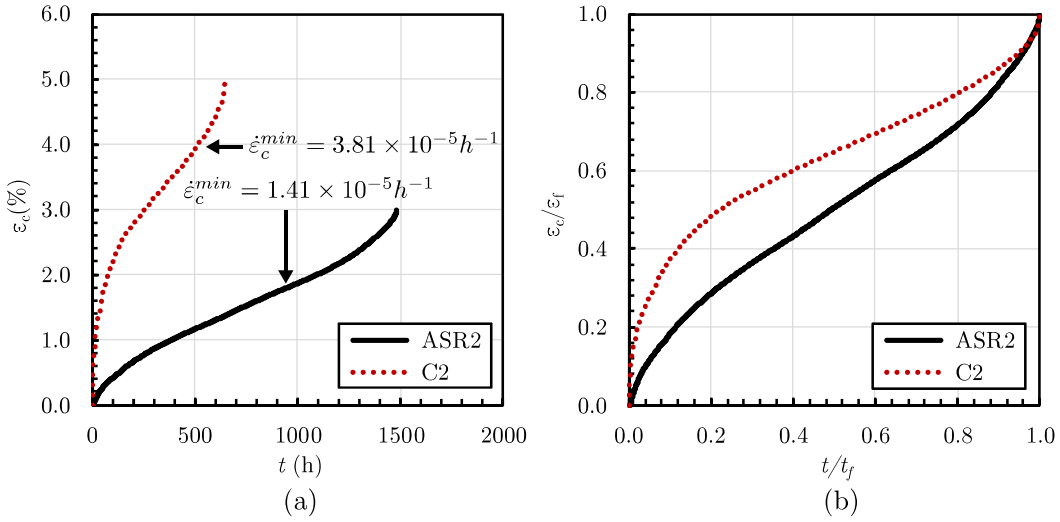


Figure 5.18: Creep rupture curves of as-received and preconditioned specimens tested at 320 MPa displayed in (a) absolute and (b) normalised form.

Despite being loaded to lower true stresses, the preconditioned material crept much faster compared to as-received. These specimens also displayed an enhanced primary region indicating a higher hardening response. The normalised creep curves for all tests are compared in Figure 5.19 which shows little impact of stress on deformation behaviour.

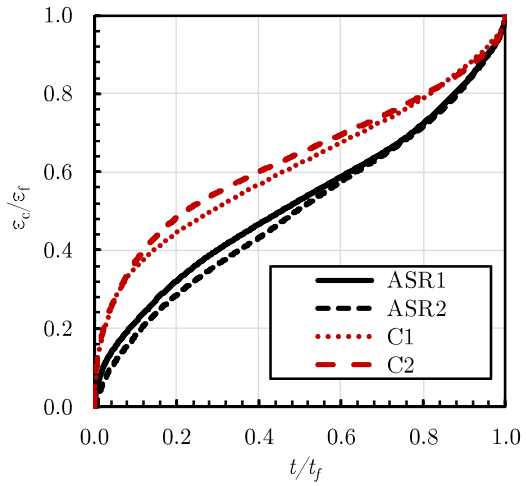


Figure 5.19: Comparison of normalised creep behaviour at 300 and 320 MPa.

Metallographic examination was undertaken on failed samples to understand how carburisation interacted with creep damage. This was conducted using a combination of optical and scanning electron microscopy.

Figure 5.20 compares the outer surfaces of ASR1 and C1 revealing a marked difference in exterior condition. In a similar manner to what was observed after tensile fracture (Section 5.2), the preconditioned material contained widespread surface cracking and significant spallation of the magnetite oxide. Cracks were orientated perpendicular to the direction of load and appeared to be partially circumferential. Evidence of such surface damage was not observed within the as-received sample.

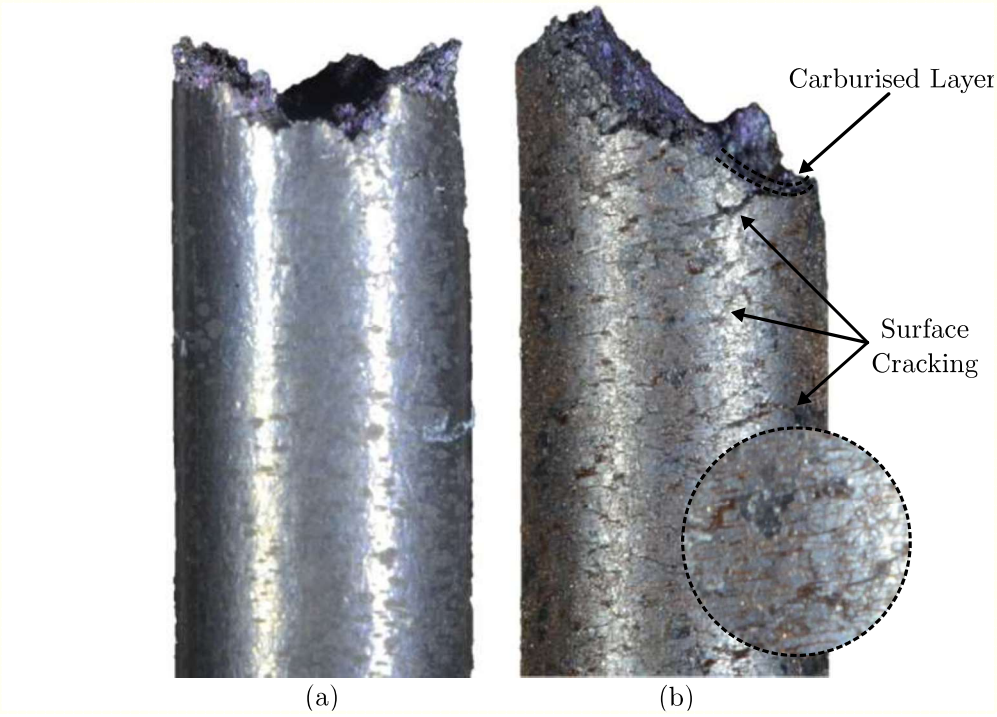


Figure 5.20: Comparison of failed creep sample surfaces from as-received ASR1 (a) and preconditioned C1 (b).

To investigate the nature of this surface cracking, samples were split through their axial mid-planes and imaged under optical microscopy. Sections were created through electrical discharge machining (EDM) to preserve any features of the outer surface such as the brittle oxide and carburised layers. These were then mounted in Bakelite resin to enable faces to be ground and polished to a 1 µm finish.

Figure 5.21 shows the half gauge length of preconditioned specimen C1 which exhibited widespread intergranular surface cracking with the average crack depth increasing towards the fracture surface. The majority of cracks had broken entirely through the carburised layer and had significantly propagated into the bulk material. A closer view of these cracks can be seen in Figure 5.22 which compares sections taken from ASR1 and C1. The outer spinel layer remained present in most regions.

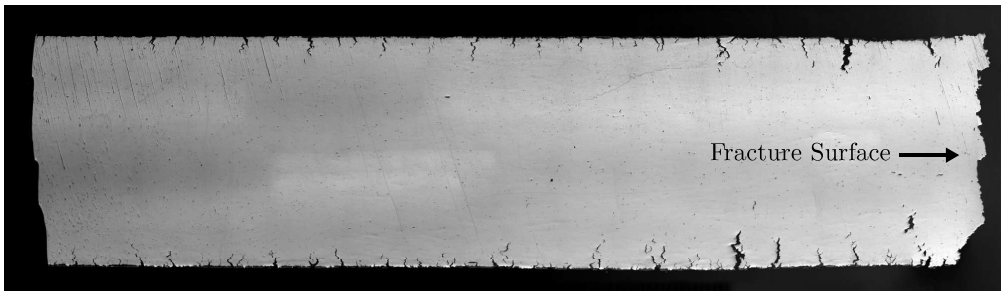


Figure 5.21: Half gauge length section view taken from preconditioned creep rupture specimen C1.

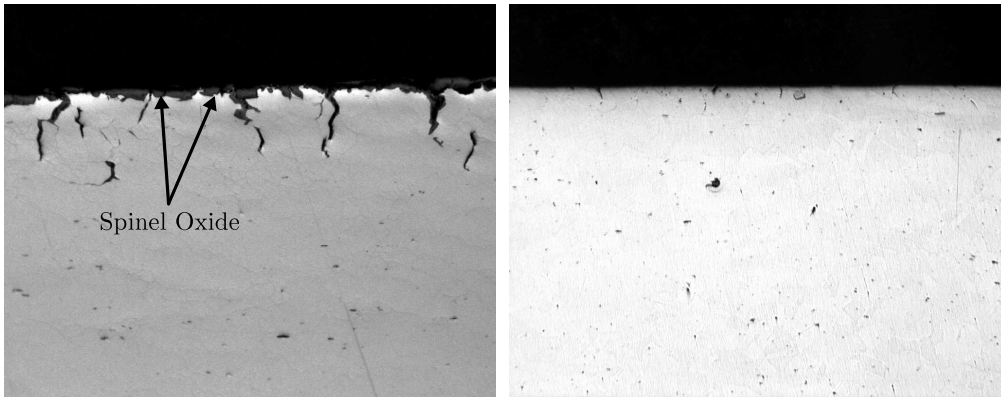


Figure 5.22: Surface metallography taken from creep samples (a) C1 (preconditioned) and (b) ASR1 (as-received).

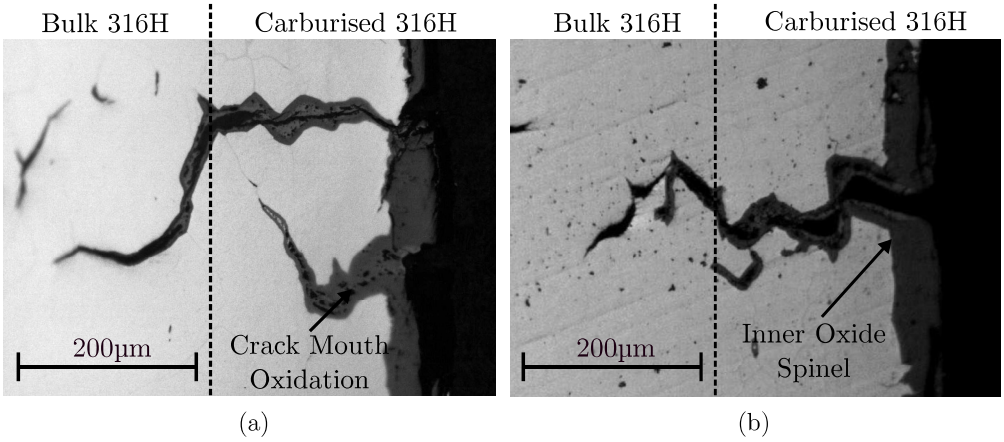


Figure 5.23: Oxidation of surface crack mouths from specimen C1 (a) near to and (b) far from the fracture surface.

Examination of individual cracks both near to and far from the fracture surface of sample C1 showed significant crack mouth oxidation across the carburised layer, Figure

5.23. Crack faces within the bulk material contained little to no oxidation indicating that cracking of the outer surface was occurring during the early stages of test followed by propagation into the bulk material during creep.

The fracture surfaces of ASR1 and C1 were imaged under scanning electron microscopy, seen in Figure 5.24. This showed a clear difference in creep failure mechanism between both materials. ASR1 failed via regular intergranular creep fracture across its entire gauge diameter. In contrast, preconditioned C1 exhibited intergranular fracture only within near surface gauge regions followed by ductile overload failure in the central portion. The circumferential intergranular cracking appeared to have initiated on the outer surface (marked by radial striations) and propagated to a depth of approximately 1.5 mm.

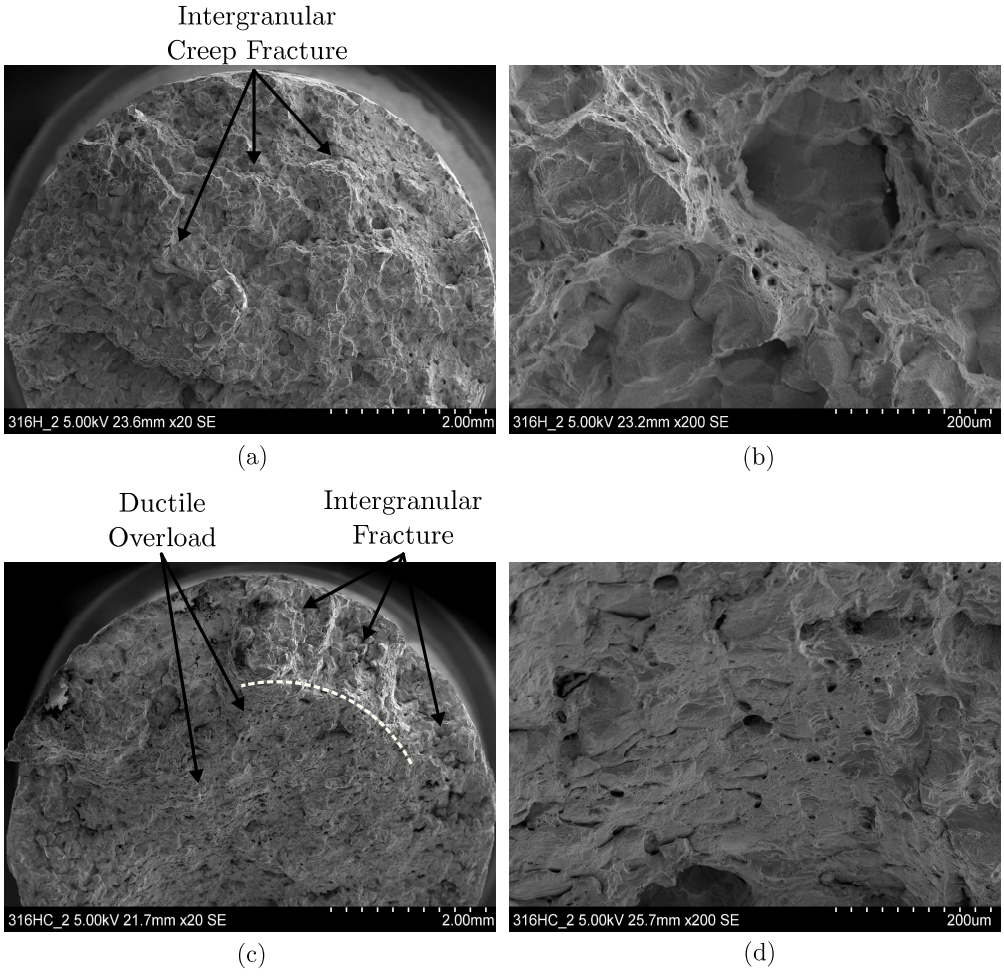


Figure 5.24: Fracture surfaces of (a)(b) ASR1 and (c)(d) C1 showing the difference in creep failure mode between as-received and preconditioned material.

5.4.4. Interrupted Creep Testing

Rupture testing confirmed that carburisation led to severely reduced creep lives and increased creep rates in comparison to as-received material. This was accompanied by widespread surface cracking that was likely to have initiated within the early stages of creep or upon loading. A number of interrupted tests were therefore conducted to attempt to better understand the initiation and propagation behaviour of these cracks. As it was thought that initiation could occur instantaneously upon loading, the interrupted tests were run at much lower nominal stresses, resulting in significantly reduced plastic loading strains.

The interrupted creep matrix is shown Table 5.6 with subscript 'int' denoting a value at test interruption. Four samples were interrupted at various stages of test (during primary and secondary creep) at two different stresses of 220 and 260 MPa. Interruption was not conducted during tertiary creep as it was thought that the majority of surface damage would have already initiated by this stage. The test procedure consisted of simply removing 80% of load from the specimen, switching off the furnace controller and allowing it cool to ambient temperature.

Table 5.6: Interrupted creep test matrix.

ID	$\sigma_{\mathbf{true}}$ **(MPa)**	$\mathbf{t_{int}}$ **(h)**	$\varepsilon^{\mathbf{eng}}_{\mathbf{c,int}}$ **Axial (%)**	**Stage**
C3	264	3982	3.02	Secondary
C4	262	404	1.31	Primary
C5	221	1871	0.35	Secondary
C6	221	333	0.13	Primary

Figure 5.25 presents the creep curves from all interrupted tests. Samples crept at the same stress followed very similar creep strain - time paths as expected. Specimen C5 exhibited two sharp increases in axial displacement over two 45 hour periods. These coincided with an 11 µm increase in total elongation and may be due to surface crack initiation and growth.

The hot inspection of all sample surfaces immediately after unloading revealed that the magnetite layer had spallaed off at every level of stress and creep strain. Brittle magnetite was scattered across the lower floor of each furnace. Section metallography was undertaken and can be seen in Figures 5.26 to 5.28.

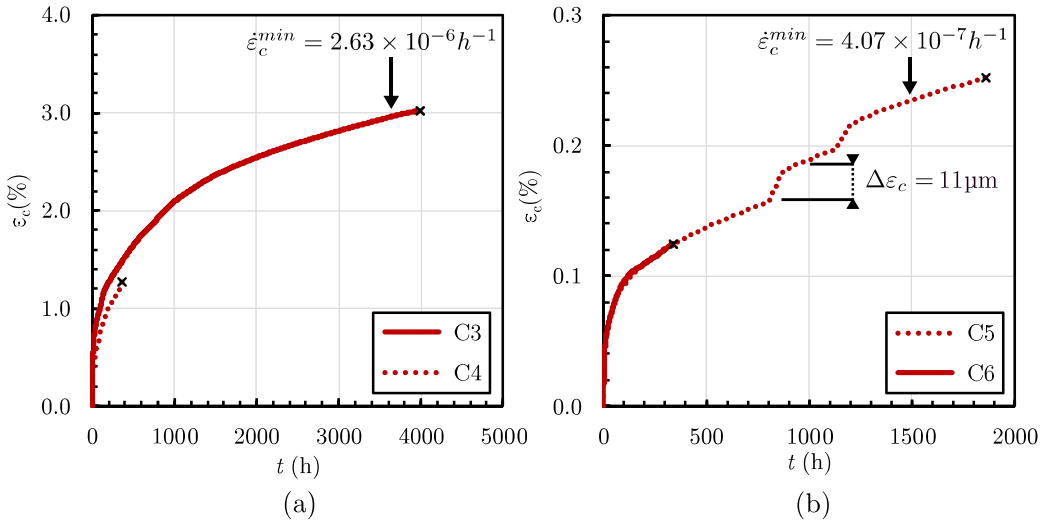


Figure 5.25: Interrupted creep test specimen curves at (a) 260 and (b) 220 MPa.

Comparing interruptions at 260 MPa, sample C3 interrupted at a higher creep strain than C4, contained a greater density of larger surface cracks (Figure 5.26). The majority of these appeared to have propagated to a depth much further than the carburised layer, well into the bulk material. Most cracking found in specimen C4 was still contained within the carburised layer. Maximum crack sizes were found to be similar however there appeared to be a marked difference in total thickness of crack mouth oxide scale (Figure 5.27). This indicated that cracking had initiated either upon loading or within the primary stages of creep and subsequently propagated.

Specimens C5 and C6, interrupted at much lower creep strains (and run at the lowest creep stress of 220MPa) showed very limited signs of surface damage (Figure 5.28). Whilst a single crack measuring 100 µm was found within C5, no evidence of cracking could be found C6. Apart from spallation of the outer magnetite layer, the inner oxide spinel appeared to be completely intact.

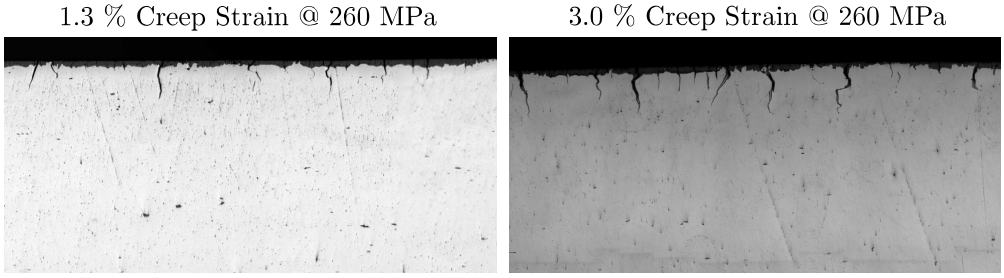


Figure 5.26: Micrographs of interrupted creep specimens (a) C4 and (b) C3 showing the contrast in surface crack density at different creep strains.

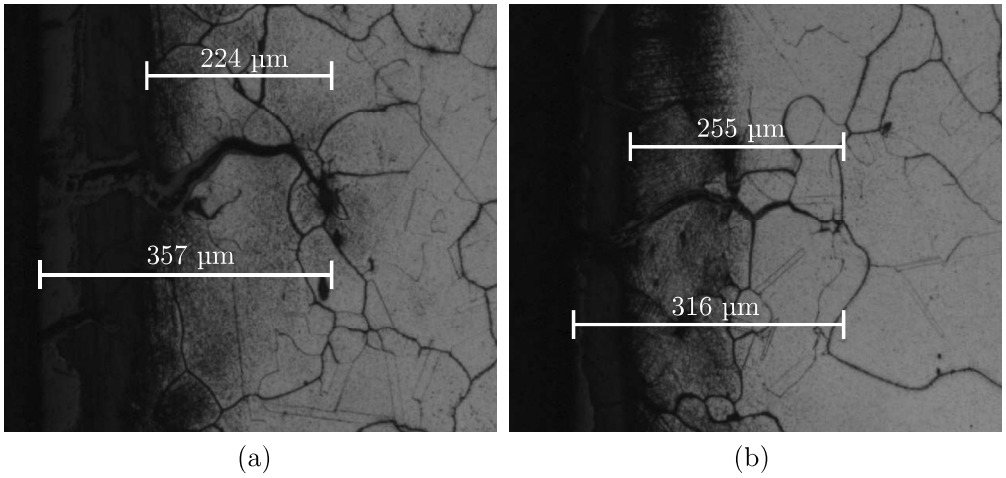


Figure 5.27: Maximum measured crack depth within interrupted creep specimens (a) C3 and (b) C4 showing the contrast in crack face oxide thickness.

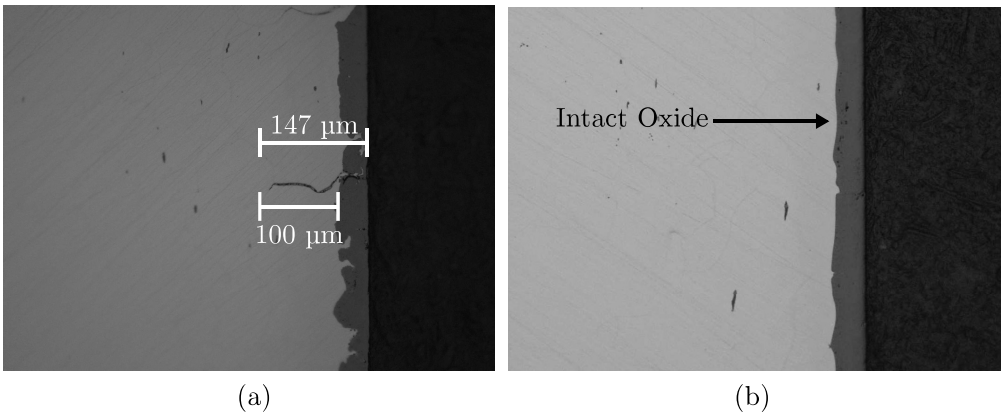


Figure 5.28: Maximum measured crack depth within interrupted creep specimens (a) C5 and (b) C6 showing limited surface damage.

5.4.5. Creep Strain - Crack Length Relationship

A series of additional interrupted tests were conducted by AMEC Foster-Wheeler and The University of Manchester. These were run over a range of nominal stresses (220 - 260 MPa) and interrupted at various stages up to a total creep strain of 4%. A measure of maximum crack size at each strain was recorded by sectioning samples and imaging under optical microscopy. By combining this data with that obtained from this study, a relationship between maximum surface crack length and strain can be constructed. This is presented in terms of both creep and total strain (creep plus strain on loading) in Figure 5.29. A single specimen was loaded to 260 MPa then immediately interrupted (0% creep strain) and this is identified as 'Tensile' in Figure 5.29 (b).

No cracking was observed at the very low creep strain of 0.13% or within the single tensile specimen taken to 0.78% total strain. Above this, maximum crack length progressively increased with strain up to an approximate depth of 250 µm. The lower bound creep ductility of the carburised layer was therefore estimated to be 0.13% with the overall lower bound estimate for tensile ductility anywhere between 0.50 - 0.78%.

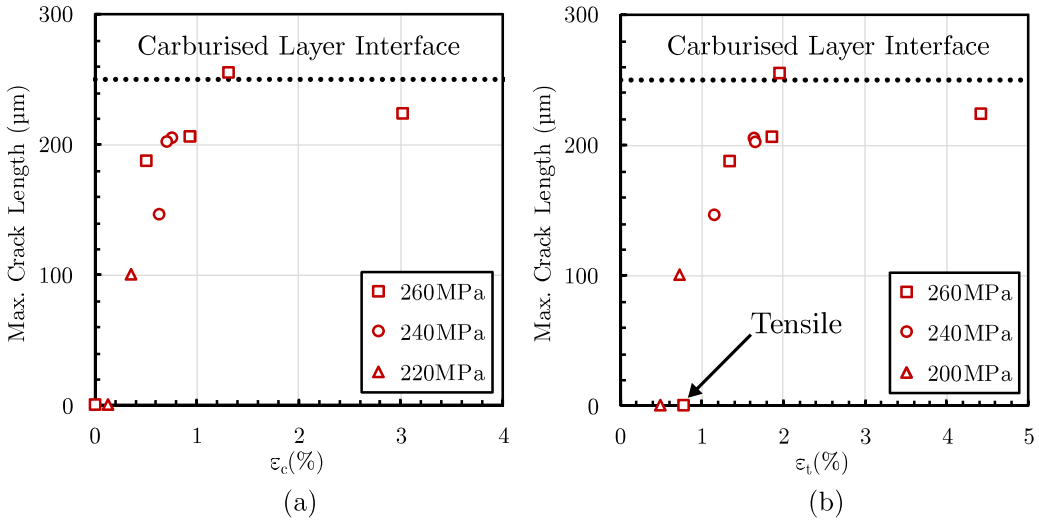


Figure 5.29: Maximum observed crack length plotted against (a) creep and (b) total strain in interrupted preconditioned creep specimens; the dotted line denotes the interface between the carburised layer and bulk material.

5.4.6. Review of Creep Data

A review of creep data generated from the ENVISINC project is presented in this section including the results from this study. When attempting to examine the effects of carburisation on 316H over a range of applied stresses, a large number of tests helped mitigate the statistical scatter associated with creep, enabling a more robust analysis to be undertaken. The impact on both rupture life and minimum creep rate have been investigated. All of the data shown is based on axial measurements of strain with true stress calculated according to Equation 5.4.

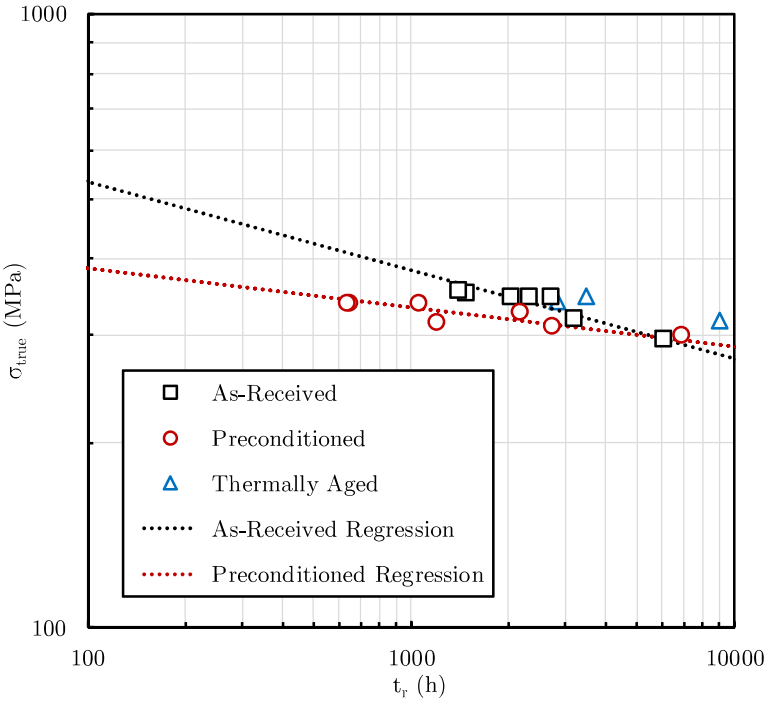
Figure 5.30 displays true stress plotted against rupture time and minimum steady-state creep rate. Power-law fits have been made to both as-received and preconditioned material data using a regression analysis and are denoted by the dotted lines. These have been plotted to determine the rupture and minimum creep rate constants which are summarised in Table 5.7. The fitted values of creep constants n and v_r within preconditioned material are much higher than as-received indicating a larger dependency of both rupture time and creep rate on stress. Figure 5.30 (a) shows that in general, for the same applied true stress, preconditioned samples failed much quicker than their as-received counterparts. This becomes more prevalent as the stress is increased. Towards the lower stress range, the rupture times of preconditioned material closely match or in one instance exceeded that of as-received. The effect of carburisation appeared to be stress dependent. A similar trend can be observed for minimum creep rates in Figure 5.30 (b) whereby the regression fits converge at the lower stress with preconditioned samples creeping much faster at the higher stresses.

Table 5.7: Uniaxial creep properties of as-received and preconditioned material.

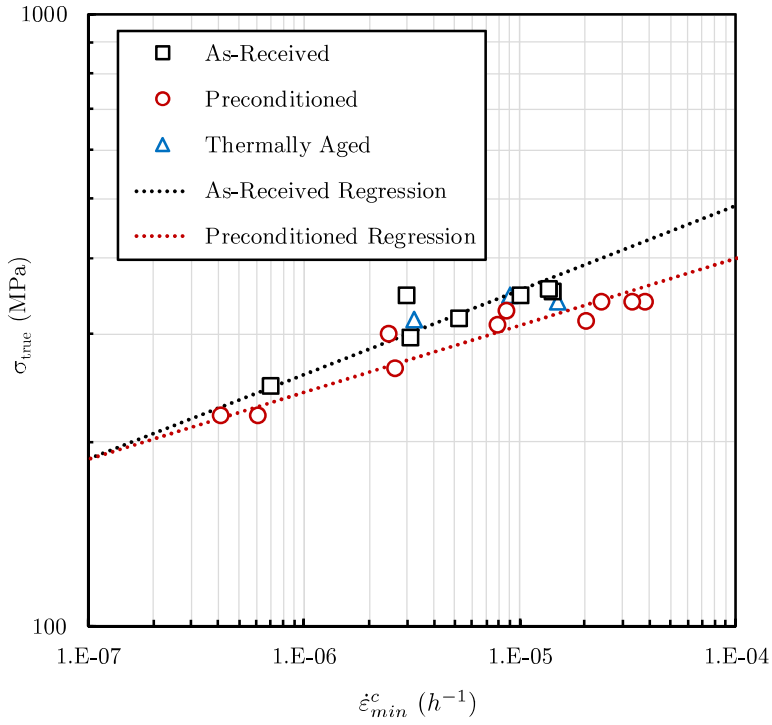
Material	$\boldsymbol{A}$ $(\mathbf{MPa}^{-n}\mathbf{h}^{-1})$	**n**	$\boldsymbol{B}_r$ $(\mathbf{MPa}^{-v_r}\mathbf{h})$	$\boldsymbol{v}_r$
As-Received	3.38×10^{-24}	7.24	8.76×10^{20}	6.94
Preconditioned	1.70×10^{-28}	9.14	3.34×10^{42}	15.67

5.4.7. Effect of Thermal Ageing

A number creep tests were conducted on thermally aged specimens to ensure that the additional thermal ageing induced during the preconditioning process was not significantly impacting on material properties. The recorded load up data, shown in Figure 5.16 displays a slightly elevated yield stress. The creep rupture and strain rate behaviour was generally consistent with that of as-received and fell within expected scatter for creep.



(a)



(b)

Figure 5.30: True stress plotted against (a) rupture time and (b) minimum creep rate for all specimen test data.

5.5. Discussion

This chapter has investigated the effect of carburisation on the tensile and creep properties of 316H stainless steel. The following section presents a discussion of results within the context of the literature and describes any possible limitations to these findings.

5.5.1. Tensile Response

Carburisation was found to significantly alter the tensile response of 316H with preconditioned material possessing an enhanced yield stress and reduced ductility in comparison to as-received. The increase in yield stress resulted from the addition of an outer hardened layer which, is consistent with previous findings on AGR carburised 9Cr1Mo steel in the literature [59]. A comparison of failed sample surfaces revealed widespread damage in the form of cracking across the carburised layer, indicating a substantial loss of surface ductility. The cracking was demonstrated to be intergranular and corroborates with previous metallurgical examination of preconditioned material undertaken by Younes et al. [43]. This revealed the presence of $M_{23}C_6$ carbides on grain boundaries. Intergranular carbide precipitation has been shown to result in a loss of material ductility [56, 90] within steels and was the leading cause of embrittlement of the outer surface. Despite being inherently harder, the outer carburised layer was much less ductile than the bulk material, leading to premature cracking and an overall loss of ductility across the entire specimen.

A comparison of fracture surfaces revealed a marked difference in failure mode between both materials with a noticeable region of intergranular cracking across the carburised layer that was not present in the as-received sample (Figure 5.4). Preconditioned material did not show any signs of necking in close proximity to the fracture surface. The formation of a neck is usually associated with the tensile failure of a ductile material such as 316H and the lack of thereof, indicates an alternative mode of failure resulting from carburisation. This is described as follows.

Within the initial stages of tensile loading, embrittlement of the carburised layer led to the initiation of widespread surface cracking at a strain much lower than the inherent ductility of 316H. These cracks propagated through the carburised layer as the test progressed, gradually reducing the specimen's net cross sectional area, increasing the level of stress within the remaining material. The majority of cracks were arrested at the carburised - bulk 316H interface due to a steady increase in grain boundary strength through depth (less carbon activity thus carbide precipitation) and the mechanism of

crack shielding from multiple interacting micro-crack stress fields. The effect of these interactions was shown in finite element modelling where the value of stress intensity K at each crack tip was significantly reduced in comparison with a single propagating crack.

Cracking of the entire carburised layer would have translated to a 12 % increase in net stress, assuming a depth of 250 µm. At the higher strains, gauge length necking was resisted by the hardened outer layer which, despite being cracked, was able to provide a significant level of constraint to the deformation of underlying bulk material, in the form of compressive hoop stresses generated to resist a reduction of area. Such behaviour was observed within elastic-plastic finite element modelling where the cracked carburised layer contained compressive hoop (S33) stresses. The effective stress in the remaining material eventually exceeded the UTS of 316H causing sudden ductile overload failure. This explains why both as-received and preconditioned materials displayed similar UTS values. Evidence of such behaviour was found in SEM fractography with similar findings having been reported by Jeffcoat [59] on carburised 9Cr1Mo steel. The lack of a neck and alternative failure mode also provides an explanation as to why no reduction in load was observed towards final fracture (Figure 5.1).

5.5.2. Creep Behaviour

The results of creep testing show that the impact of carburisation on the creep strength of 316H is dependent on the initial state of stress. This behaviour can be seen in Figures 5.30 (a) and (b) which present the entire creep data set. The difference in both rupture time and minimum creep rate between as-received and preconditioned samples at the same stress level is amplified at higher stresses; demonstrated by the diverging regression fits for each material. This stress dependence is driven by the initiation of premature cracking within the carburised layer at a given total strain that results from carbide embrittlement of the outer surface.

The lower bound creep ductility of the carburised layer was estimated to be around 0.13% creep strain with the overall lower bound tensile ductility between 0.50 - 0.78%. These values were taken from interrupted test data that plotted a relationship between maximum crack length and creep/total strain (Figure 5.29) and are only approximate values due to the inherent error in measuring maximum crack length in a single two dimensional plane.

Above 2% total strain, the maximum crack length was found to be larger than the depth of the carburised layer meaning that it had entirely cracked. A comparison of preconditioned loading data shows that above a nominal creep stress of 300 MPa, this strain is

significantly exceeded, strongly suggesting that the for these tests, the carburised layer was cracking upon loading. Further evidence of this was found upon examination of crack faces (Figure 5.23). Crack mouths within carburised regions contained a much higher level of oxidation compared to those in the bulk indicating that they had been exposed to air for a longer period of time. Instantaneous failure of the carburised layer in these tests would have immediately resulted in an increase in net section stress along with surface crack propagation via creep crack growth. The combination of these mechanisms would have continually increased the stress within the bulk until the UTS was surpassed, causing overload fracture in the centre. Indeed, such behaviour was observed in sample fractography (Figure 5.24) and as a result carburisation resulted in severely reduced creep lives.

A higher effective creep stress in the bulk would normally be associated with a smaller amount of primary creep as strain hardening effects become less significant. However, the opposite was seen within the preconditioned rupture samples which, displayed much larger primary creep regions compared to their as-received counterparts. Such behaviour may be explained by the propagation of multiple surface cracks into the bulk material that increased the total axial stress thus displacement which, translated to a larger observed axial strain hence 'primary' creep. The propagation of surface cracks would have slowed once they reach carburised layer - bulk material interface due to a progressive increase of grain boundary strength with depth. This would have led to a region of stabilised crack growth and steady-state creep.

For the interrupted tests run at a nominal creep stress of 260 MPa and below, the resultant loading strains ($< 1.5\%$) did not surpass the estimated ductility of the carburised layer which, initially remained intact alongside the oxide spinel, Figure 5.28. Cracking was found to have occurred during the primary and secondary stages of creep with multiple maximum crack depths contained in the carburised layer. This suggests that below a certain creep strain, the carburised layer is capable of carrying load.

In reference to Figure 5.29, there appeared to be a difference between the behaviour of preconditioned material under monotonic tensile and creep conditions. Whilst cracking was observed in creep at a total strain of 0.74% (0.39% strain on loading and 0.35% creep strain), no cracking was seen under a higher pure tensile strain of 0.78% [83]. This inconsistency in crack behaviour can be explained by the difference in the nature of total strain accumulation (plastic plus creep versus only plastic) and could be related to a dependency of crack initiation on either time or deformation mechanism. Creep strain may be inherently more damaging to the carburised layer than plasticity because of the focus of damage on grain boundaries. Similarly, a longer exposure to high tempera-

tures allows for the evolution of time dependent grain boundary damage mechanisms, such as oxygen penetration which favours boundary regions due to enhanced diffusion rates.

The rupture tests in this study were run at much higher nominal stresses than that experienced by components in plant. This created significant plasticity upon loading and resulted in widespread premature surface cracking that reduced creep life. At the lower stress levels of 260 MPa and below, the ductility of the carburised layer was not exceeded upon loading and was able sustain load. Interrupted tests showed no initial signs of cracking until 0.35 % creep strain. At these lower stress levels, the minimum creep rate of preconditioned material tended towards that of as-received. A similar trend was found for rupture times. At very low creep stresses, more representative of component operation (< 140 MPa), it could be the case that the load bearing capacity of the carburised layer is maintained, resulting in a reduction of steady state creep rates and enhancement of rupture life. This is because carburisation increases the surface yield strength of the material and induces surface residual compressive stresses that constrain deformation [60, 91]. The low stress rupture behaviour of carburised material requires further investigation.

Additional thermal ageing induced by the preconditioning process was not seen to have a significant impact on the tensile or creep behaviour of this cast of 316H. A slight increase in yield stress was observed (Figure 5.16) with no discernible effect on creep resistance (Figure 5.30). This suggests that the additional thermal ageing (3000 hours at 600°C) was not fundamentally changing microstructural features important for creep deformation which, is unsurprising given the length of thermal service exposure that the as-received header received prior to use within this research (100,000 hours at 500°C).

5.6. Conclusions

This chapter has investigated the influence of AGR carburisation on the tensile and creep properties of 316H. From this, it can be concluded that:

- Carburisation increases the yield stress and reduces the ductility of as-received material. This is due to the addition of an outer hardened layer and the initiation of widespread surface cracking. The loss of ductility across the carburised layer results from the weakening of surface grain boundaries through carbide precipitation.

- Even after cracking, the carburised layer is able to provide some level of constraint to the deformation of the bulk material.
- The overall impact of carburisation on the creep behaviour of 316H is highly dependent on the state of stress. This dependence is driven by the initiation of surface cracking within the carburised layer which has a lower bound creep ductility of approximately 0.13%. The lower bound tensile ductility is anticipated to be between 0.5% - 0.78%.
- Under high nominal creep stresses of 300 MPa and above, the carburised layer will crack on loading, resulting in a reduction of creep life and increase in creep rate compared with as-received material. This is due to an increase in effective creep stress within the bulk and a reduction of cross sectional area via surface creep crack growth.
- Below this stress, the carburised layer initially remains intact and can sustain load until a certain creep strain. This is less detrimental to the overall creep resistance of the bulk and leads to preconditioned material creeping in a similar manner to as-received.
- If the carburised layer does not crack on loading and is crept at a very low stress, carburisation could lead to an enhancement of creep strength.
- The additional thermal ageing induced by the preconditioning process does not have a significant impact on the tensile or creep behaviour of this cast (55915) of 316H.

6. Effect of Carburisation on Fatigue

6.1. Introduction

The fluctuating demand for electricity combined with the need for regular maintenance and refuelling means that AGR components experience variable loading conditions in the form of cyclic stresses and strains. These are generated from changes in both operating temperature and load, making components susceptible to the onset of fatigue and creep-fatigue degradation. The microstructural mechanisms responsible for fatigue damage have been described in Section 2.7.3. Under certain conditions, the initiation and growth of fatigue cracking can result in the failure of components. Understanding how carburisation interacts with fatigue damage is therefore essential in evaluating the impact of carburisation on component lifetime and forms the primary theme of this chapter.

Section 3.4 provided a review of the literature concerning the effects of carburisation on the fatigue strength of steels. This was found to be highly dependent on both the nature of carbide precipitation and applied loading conditions. When carbide precipitation was limited, carburisation resulted in an outer hardened layer with no discernible loss of ductility. This enhanced fatigue strength by suppressing crack nucleation mechanisms through the generation of surface residual stresses. On the other hand, carbide precipitation led to surface embrittlement and a significant loss of ductility that reduced fatigue endurance through the initiation and subsequent propagation of multiple cracks across the hardened layer. This behaviour was observed when the applied fatigue strains exceeded the ductility of the surface.

The following chapter investigates the influence of AGR gas carburisation on the fatigue and creep-fatigue behaviour of 316H stainless steel. This has been conducted through a series of high temperature LCF tests on as-received and preconditioned materials. Samples have been tested under fully reversed strain-controlled conditions as this was seen to closely resemble typical plant operation. Complete details of the carburisation process and specimen geometry are found Chapter 3. An extensive overview of the LCF test setup has been provided as high temperature, strain-controlled conditions require careful preparation to ensure a valid fatigue data. In a similar manner to previous chapters, the

results of this study have sometimes been assessed alongside data from project partners AMEC Foster-Wheeler. This was to help minimise the considerable scatter associated with fatigue testing and is mentioned where applicable.

6.2. High Temperature Fatigue Test Setup

6.2.1. Introduction

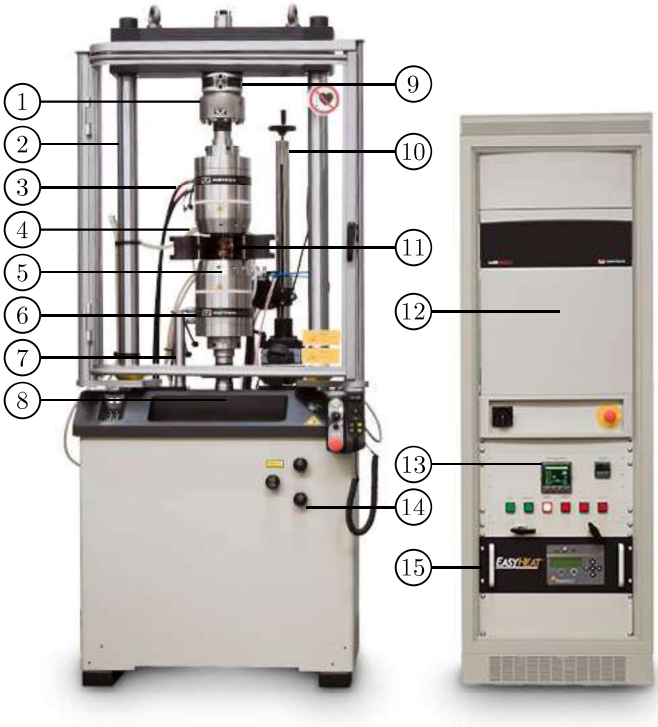
Under tensile and creep conditions, material properties such as ductility and creep life are usually reliant on microstructural changes averaged across the entire sample volume. This is not the case for LCF testing where, fatigue life is dependent on the initiation of a single flaw at one location across the sample surface. Fatigue crack initiation, by it's very nature, is a random process and is extremely sensitive to a number of factors including surface finish and experimental setup. This often results in a large range of scatter observed across multiple fatigue life data sets from the same material [92]. The considerable scatter is typically overcome by conducting a significant number of tests to which conservative design curves are then fitted [93]. However, due to time constraints and limited header material availability, this was not possible within this study. Therefore, an onus was placed on strictly controlling experimental setup in order to minimise any potential fatigue data scatter; essential when attempting to compare two similar materials such as as-received and preconditioned 316H. An overview of fatigue setup and test procedure is provided in the following sections.

6.2.2. Instron Thermo-Mechanical Fatigue (TMF) Machine

LCF testing was undertaken using an Instron Thermo-Mechanical Fatigue (TMF) setup consisting of a TMF Machine, 8800 controller, high pressure oil pump, low pressure water chiller and the Instron Fatigue software package. All testing followed ASTM Standard E606 [82] under high temperature strain-controlled, isothermal conditions. The TMF machine was servo-hydraulically driven and was capable of simulating both thermal and mechanical strains using induction heating to achieve heating rates in excess of $50°C\ s^{-1}$. An overview of the entire TMF system is shown in Figure 6.1.

Load Train

Load was applied via a servo-hydraulically driven actuator, capable of achieving forces of up to 100 kN in both tension and compression. The actuator was supplied with high



1. Load Cell
2. Load Frame
3. High Pressure Oil Feed
4. Cooling Water Feed
5. Upper Grip
6. Servo-Hydraulic Actuator
7. Anti-Rotation Shaft
8. Hydraulic Bearing
9. Instron Align-Pro Fixture
10. Induction Coil Guide
11. Induction Coil Setup
12. Instron 8800 Controller
13. Eurotherm Controller
14. Crosshead Adjustment
15. Induction Coil Controller

Figure 6.1: Instron TMF system overview, image adapted from [94].

pressure hydraulic fluid at 200 bar via oil feed lines from an external Instron 3520 power unit; responsible for pressurizing, cooling and filtering the fluid.

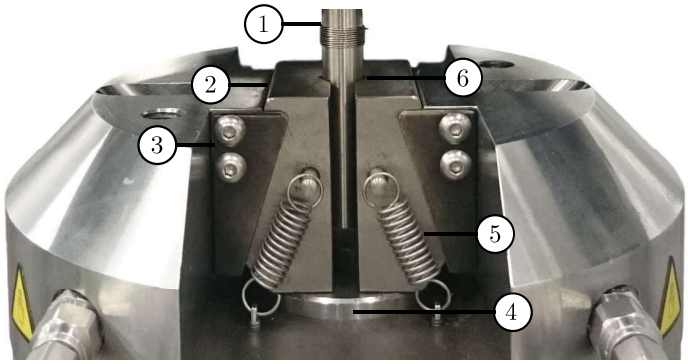
Control System

An Instron 8800 fatigue testing controller was used to control actuator position (in either displacement, stress or strain control) and specimen temperature. This relied on a series of digital feedback loops from measured values of load, strain and temperature which are discussed in detail in later sections. The controller was linked to a 64-bit operating system containing an installation of the the Instron Console software package. All user input was conducted via the software.

Hydraulic Sample Grips

Specimens were clamped and mounted via sets of hydraulic grips, seen in Figure 6.2. These provided a constant clamping force of up to 100 kN and were water cooled to prevent excessive heating. Low pressure cooling water was supplied via an external

chiller configured to a temperature set point of 16°C. Each half-grip featured a centralised wedge geometry to ensure continuous alignment as the clamping pressure was increased. A hydraulic piston provided the force necessary to clamp samples; this was adjustable via a variable pressure release valve. Upon gripping, the relative vertical position of the jaw faces remained constant to ensure no unnecessary load or strain was applied to the specimen.



1. Specimen
2. Grips
3. Grip Guides
4. Hydraulic Piston
5. Retaining Springs
6. Wedge Guide

Figure 6.2: Hydraulic TMF grips.

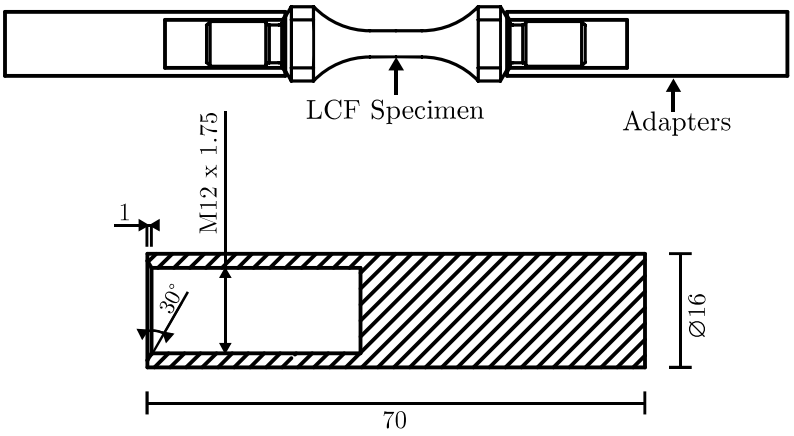


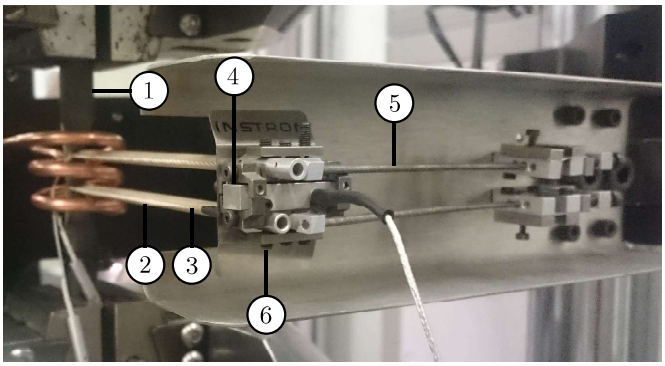
Figure 6.3: LCF sample adapters.

To maximize the use of available material and extract the highest number of samples from the header geometry, two types of specimen design were created. Details of these are provided in Section 4.3 and included both Instron fatigue and smaller, more traditional LCF samples. Because the smaller specimens contained threaded ends, multiple sets of adapters were manufactured to allow them to be gripped by the TMF machine. These were fabricated from Nimonic 90, and are seen in Figure 6.3. The adapters contained chambered inner edges to enable flush contact with specimen shoulders, ensuring that the threads could be torqued up to remain in tension during testing, preventing any backlash or loosening of the load train.

High Temperature Extensometer

A high temperature contact extensometer was used to both measure and control axial strain. This is shown in Figure 6.4 and meets ASTM E83 specification [95]. Sample displacement was transmitted via two quartz chisel end rods that were in low but continuous contact with the surface. When pushed apart, these flexed a metallic element that was housed in the main extensometer body which contained bonded strain gauges that translated physical axial displacement (accurate to 1 µm) into an electrical voltage signal. The extensometer had a relatively small mass thus high resonant frequency, making it particularly suitable for precise strain controlled LCF testing.

To ensure the continuous contact of the quartz knife edges with sample surfaces, the extensometer was mounted using a combination of heat-proof ceramic string and a leaf-spring loaded mechanism. This was fixed to the load frame and provided an adjustable contact force of up to 25 N. A gauge length of 12.5 mm was zeroed before each test using a pre-calibrated spacer tool. Extreme care was taken to minimize the possibility of any scratching or marring of the specimen surface during test setup as this could encourage the premature formation of a crack initiation site.



1. Specimen
2. Quartz End-Rods
3. Ceramic String
4. Strain Gauge Element
5. Leaf-Spring Mechanism
6. String Retaining Screws

Figure 6.4: High temperature LCF extensometer setup.

Induction Heating System

Samples were heated using a high-frequency induction heating system. This was driven by an Ambrell EASYHEAT power supply and controlled via a Eurotherm 2704 temperature controller. Both were linked to the Instron 8800 server to enable specimen temperature to be set from the Instron Console software. The heating setup consisted of a power supply (Ambrell EASYHEAT), temperature controller (Eurotherm 2704) and an induction coil. This was made from 4.76 mm copper piping and was water cooled

to prevent excessive heating when placed in close proximity to hot specimens for prolonged periods of time. Temperature was measured and controlled via 3 thermocouples attached onto sample gauge length surfaces.

Achieving uniform specimen heating is critical for fatigue testing as concentrated hot or cold spots can form early crack initiation sites. Induction heating works on the principle of electromagnetic induction whereby an alternating magnetic field generates internal eddy currents that heat the material. Sample temperature profile is determined by the shape of magnetic field which, is dependent on coil geometry. This must be optimised to heat specimens uniformly and maintain stable temperatures during test. According to ASTM standards, the variation in sample surface temperature must not be greater than $\pm 2°C$ or $\pm 1\%$ during isothermal fatigue testing. To ensure that this was the case, a number of coil geometries were trialled on both types of fatigue specimen using two different coil diameters. The efficiency of each coil and resulting specimen temperature profile was determined by the total number of turns, radius of turns, pitch in between turns and coil diameter. A minimum turn spacing was also required to allow for the insertion of extensometer end rods. The final coil design can be seen in Figure 6.5 which produced a maximum variation in temperature of 1°C across all samples. This was verified through the use of a laser thermometer and thermal camera.



Figure 6.5: Optimized induction coil design resulting in a maximum temperature variation of 1°C.

6.2.3. Load Frame Alignment

Fatigue testing is highly sensitive to any misalignment within the machine load train. The slightest degree of concentric or angular misalignment of axial force can result in the generation of bending stresses which can significantly impact on fatigue life [96]. This is especially true under fully reversed LCF conditions where materials exhibit both tensile and compressive plastic strains. Possible sources of misalignment are illustrated in Figure 6.6. Because misalignment can be so detrimental to fatigue life, adjustment and verification of the load frame was undertaken prior to any testing and was repeated between tests, as it was possible for the calibration to drift.

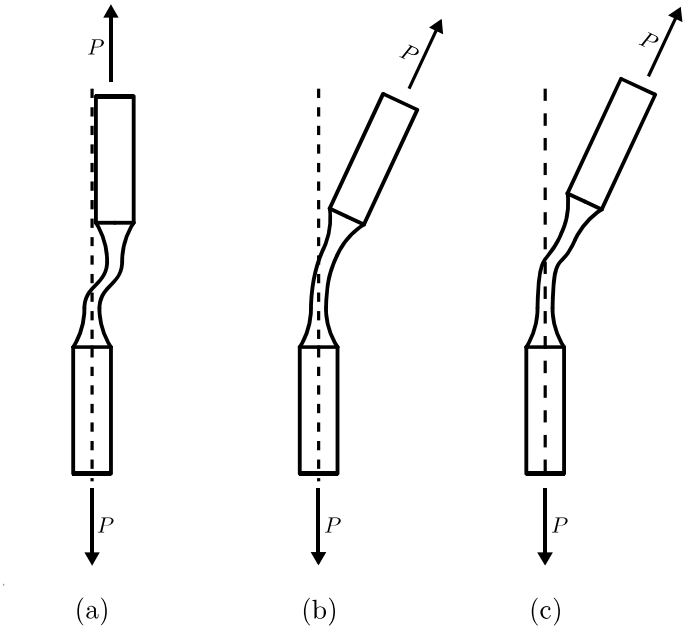


Figure 6.6: Possible sources of misalignment in fatigue testing (a) concentricity, (b) angularity and (c) a combination of both.

Alignment was conducted to ASTM 1012 [97] standard and used an Instron AlignPro package which included an alignment fixture (8800-082), strain gauged alignment cell, Instron software and calibration box. The fixture was installed between the load cell and upper crosshead of the machine and can be seen in-situ in Figure 6.1. An illustration of its working principle is shown in Figure 6.7. The adjustment of angularity and concentricity depended on the relative position of upper and lower collets which was modified by increasing the torque on the bolts in the ring housing.

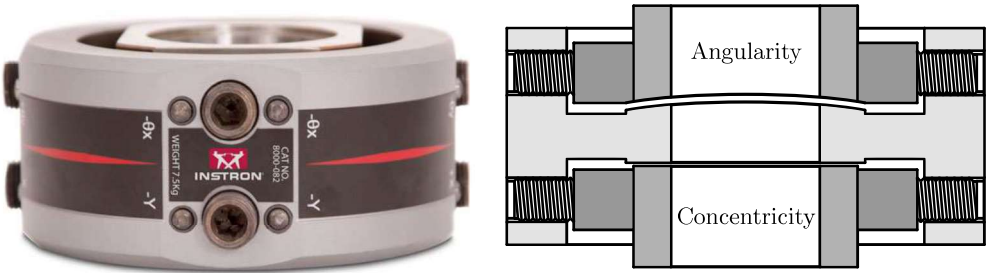


Figure 6.7: Instron AlignPro fixture, adapted from [94].

Alignment consisted of elastically loading the cell in tension and adjusting the bolts based on an observed value of bending strain. Each cell contained 8 strain gauges that provided a measurement of local axial strain at the upper and lower cardinal points of the gauge length. This data was fed back to the Instron software which calculated and displayed the total bending strain at the top and bottom according to Equations 6.1 - 6.4. Here, a and B are the bending constants, ε_i is the local strain at each cardinal point and ε_B is the overall bending strain. Based on this, the ring housing bolts were iteratively adjusted to minimise the total bending strain to a level acceptable within the ASTM standard. Verification of the alignment was then undertaken at a higher load of 10 kN to ensure continous alignment during test. A Class 5 ASTM load frame alignment was achieved prior to all tests which constituted to a total bending strain of less than 5% across the entire sample gauge length [97]. An example load frame alignment report can be seen in Appendix A showing the total bending strain at both alignment (3.0 kN) and verification (10 kN) loads to be within ASTM Class 5 bending.

$$a = (\varepsilon_1 + \varepsilon_2 + \varepsilon_3 + \varepsilon_4)/4 \tag{6.1}$$

$$b_i = \varepsilon_i - a \tag{6.2}$$

$$B = \sqrt{(b_1 - b_3)^2 + (b_2 - b_4)^2}/2 \tag{6.3}$$

$$\varepsilon_B = B/a \tag{6.4}$$

The use of specimen adapters to clamp the shorter LCF samples introduced an additional source of misalignment within the load frame. This originated from inherent thread machining tolerances and directly affected specimen concentricity. To correct for

this, an alignment procedure was undertaken using the adapters and a bespoke custom made alignment cell. This was based on the smaller LCF sample geometry and employed a similar design to the proprietary Instron cell; using the exact same strain gauges to ensure compatibility with the AlignPro system. The custom cell was fabricated from high strength EN-24T tool steel to prevent any plasticity at verification loads. Bonding and certification of strain gauges was undertaken externally by Vishay Intertechnoloy Inc and is shown in Figure 6.8. An alignment was carried out for every pair of adapters as each contained a unique error in machining tolerance.

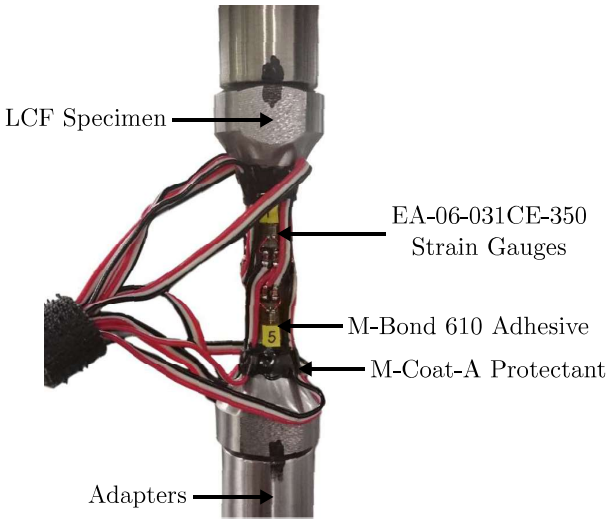


Figure 6.8: Bespoke alignment cell fabricated for use with LCF adapters.

The Instron AlignPro system was used to adjust the position and angle of the fixed upper grips relative to the bottom actuator. To ensure that this remained constant throughout test, any horizontal movement of the actuator had to be minimized as it displaced vertically to apply specimen load. This was achieved through the use of hydrostatic end bearings which tapped off the primary hydraulic feed and supplied pressurised oil onto the surface of the bottom piston. A thin film of lubricant in between the piston and bearing surfaces had a continuous centring effect on the actuator. In addition, the hydrostatic bearing design minimised any friction between contact surfaces, enabling precise control of actuator displacement. The presence of any out-of-plane movement was verified by mounting a magnetic dial gauge onto the load frame and measuring horizontal displacement whilst the actuator cycled in between it's upper and lower position limits (Figure 6.9).



Figure 6.9: Dial gauge used to check horizontal movement of the servo-hydraulic actuator.

6.2.4. Test Procedure

LCF setup required an extensive number of actions to be taken prior to testing to ensure accurate and valid results. These included both specimen and machine preparation and varied depending on the nature of material to be tested.

Sample Preparation

The surface finish of a material can greatly influence its fatigue life as any defect can encourage the premature nucleation of surface cracks at microscopic stress raisers. Therefore, to ensure consistent results, all as-received samples were prepared to an exact P2400 grit silicone carbide finish by polishing gauge lengths in the axial load direction. The preconditioned samples had to be finished to an OPS polish prior to carburisation to promote the rapid formation an outer duplex oxide. No surface preparation was undertaken prior to testing as this could have initiated microscopic cracks with the brittle oxide layer. Complete details of the preconditioning process can be found in Section 4.3.

Control of the induction heating system relied upon feedback given from 3 K-Type thermocouples spot welded on to sample surfaces. These were attached across the gauge

length of each specimen at different positions: top, middle and bottom. Whilst readings from the top and bottom thermocouples were used to control the heating system, the middle served only to verify and monitor any temperature variation. The position of each was carefully marked onto sample gauge lengths and attached using 3 spot welds of reducing intensity across each leg, illustrated in Figure 6.10. This ensured continuous adhesion and created a certain degree of redundancy in case a weld cracked during test. The legs were spaced 1 mm apart as recommended within the code of practice to avoid the conduction of heat through the thermocouple wire and subsequent generation of cold spots [98].

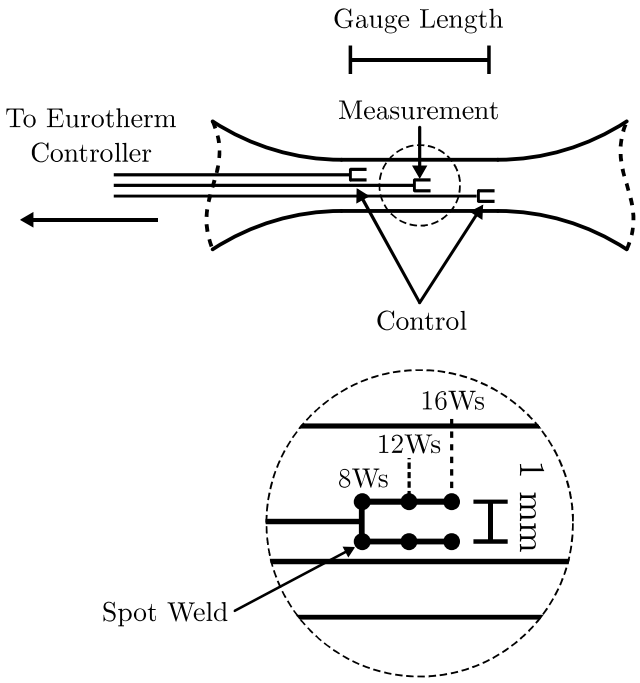


Figure 6.10: Illustration of thermocouple attachment to as-received LCF specimens.

Preconditioned samples contained a thick outer duplex oxide that had an extremely low electrical conductivity, making specimen gauges unsuitable for resistive spot welding. The two controlling thermocouples were instead welded onto the unoxidised specimen shoulders and a single measurement thermocouple tied to the centre of the gauge length using high temperature ceramic string. Although the shoulders were kept at a lower temperature (larger diameter of material), the coil design ensured an even temperature distribution across gauge lengths which was verified using a thermal imaging camera.

Temperature Calibration

The variation in temperature across sample gauge lengths was kept at a maximum of ± 2°C through careful calibration of the heating system. This included optimization of the coil design, coil position and tuning of the PID response. The final coil design can be seen in Figure 6.5. For each test, specimens were gradually heated in 25°C stages allowing for temperatures to stabilise before the coil position was iteratively modified. This minimised the risk of unintentionally heating samples above 550°C, potentially altering their microstructure.

PID Calibration & Loop Tuning

To modify actuator position and sample temperature, the TMF machine relied on a series of automatic feedback loops. These ran on a proportional-integral-derivative or PID controller which continuously calculated the error signal between the desired set temperature, load, strain or position and current measured value. This signal required amplification before being applied to either the servo valve or induction heating system, the magnitude of which depended on set PID variables. Whilst too little amplification led to peak set values being missed, too much led to unstable or 'run-away' machine behaviour. The process of tuning PID values to give both maximum control and stability is known as loop tuning and is essential when conducting strain controlled fatigue testing. The impact of tuning is illustrated in Figure 6.11 for both square and triangular requested wave forms.

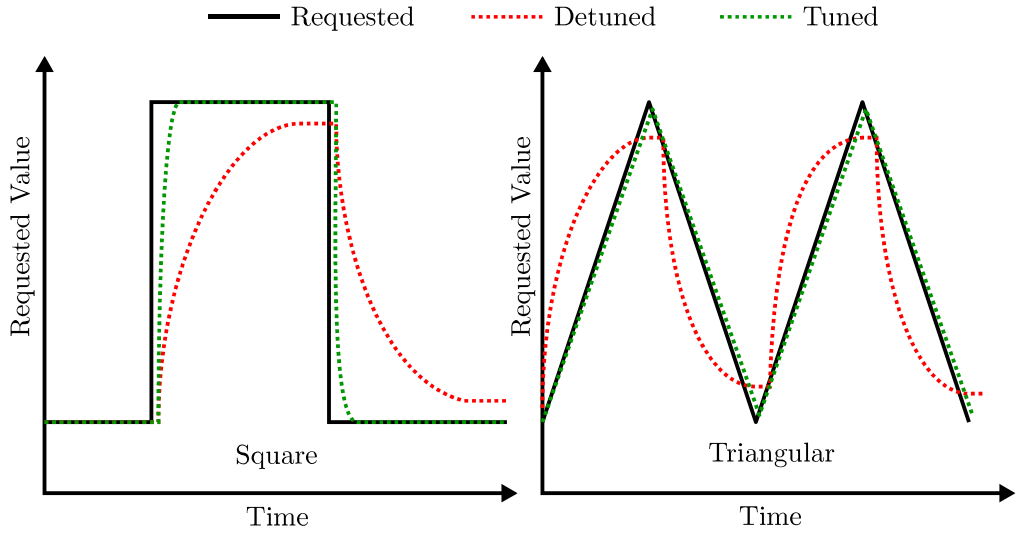


Figure 6.11: An illustration of the effect of PID tuning on requested waveform values.

Tuning was dependent on the optimization of three variables (proportional, integral and derivative) for each material, specimen design and temperature. This was because any change in stiffness of the load train could subsequently affect the machine response and lag time. For both as-received and preconditioned specimens, the variables were tuned by running square and triangular waveforms in position, load and strain control. The maximum error signal was monitored and manually tuned down to a minimum value. An overview of the PID constants for each material is seen in Table 6.1.

Table 6.1: TMF machine PID control variables for as-received and preconditioned fatigue specimens.

	As-Received			**Preconditioned**		
Variable	**Position**	**Load**	**Strain**	**Position**	**Load**	**Strain**
Proportional (dB)	38.5	9.8	16.2	38.5	9.6	15.8
Integral (I/sec)	1	0.48	1	1	0.48	1
Derivative (ms)	0.3	0	0.3	0.3	0	0.3
Lag (ms)	0.2	0	0.1	0.2	0	0.1

Extensometer Setup and Verification

The contact extensometer was routinely calibrated by applying a simulated strain gauge output to it's input terminals. This is known as indirect calibration and relies upon a factory shunt resistor contained within the extensometer housing [99]. The calibration was verified against a spacer tool of known exact thickness to ensure an accurate displacement was being measured. Direct verification was undertaken in the form of Young's modulus measurements on multiple as-received specimens. The obtained values from each test were comparable to those found within the literature for 316H at 550°C [100].

6.3. Fatigue and Creep Fatigue Testing

To investigate how carburisation affected the fatigue properties of 316H, a series of fully reversed (R = -1) fatigue and creep fatigue tests were undertaken. The entire test matrix can be seen in Table 6.2. All tests were run under strain controlled conditions

at a constant rate of 0.025% s^{-1} to enable a comparison to be made with EDF Energy R66 data [101]. To establish creep-fatigue conditions, hold times of 60 minutes were applied at peak tensile strains in every cycle. Unfortunately, due to repeated, continuous power-cuts of the three phase system at Imperial, a proportion of tests were interrupted before failure. Power failure caused the induction heating and actuator control systems to be offline for significant periods of time meaning that samples were held in tension as they cooled. This introduced additional plasticity, altering any material properties and invalidated any fatigue data collected after interruption (e.g. number of cycles to failure or associated maximum crack depths).

To maximise the number of fatigue samples that could be extracted from the header geometry, two types of specimen design were used, shown in Section 4.2. Each contained a different gauge length diameter but were all preconditioned in the same environment; resulting in comparable carburised layer depths (Table 6.2). This meant that the proportion of carburised material within each sample type varied, approximately 20% for the 5 mm samples versus 13% for the 7 mm, assuming a 250 µm carburised layer. Having a smaller diameter would therefore amplify the potential impact of carburisation on material properties. For this reason, it was anticipated that the fatigue response of the two sample types would greatly differ. This was especially true for values of N_f whereby a particular load drop would have constituted different maximum crack depths.

Table 6.2: Fatigue and Creep-Fatigue Test Matrix.

ID	**Material**	**Diameter (mm)**	**TSR (%)**	**Hold (min)**	**Interruption**
ASRF1	As-Received	5	1.2	0	After Stabilisation
ASRF2	As-Received	5	0.9	0	After Stabilisation
CF1	Preconditioned	5	1.2	0	N/A
CF2	Preconditioned	5	0.9	0	N/A
CF3	Preconditioned	7	0.6	0	N/A
CF4	Preconditioned	7	0.4	0	After Stabilisation
ASRCF1	As-Received	5	1.2	60	N/A
ASRCF2	As-Received	5	0.6	60	After Stabilisation
CCF1	Preconditioned	5	1.2	60	N/A
CCF2	Preconditioned	5	0.9	60	N/A

6.3.1. Fatigue

The results of fatigue testing undertaken on both preconditioned and as-received samples without any hold time are presented in this section. A comparison is made between the hardening behaviour and stabilised cyclic stress-strain response. Additional test data from project partners AMEC Foster-Wheeler is also included in order to evaluate strain versus fatigue life curves. Here, the criteria for specimen failure was based on a total reduction in stabilized load of 30% (N_{f30}) as this enabled comparison with EDF Energy R66 fatigue life data [101].

The cyclic hardening and/or softening behaviour of a material can be evaluated by plotting the evolution of maximum and minimum peak stresses within each cycle, the degree of which, is often dependent on the underlying material microstructure and test conditions (temperature, strain rate and applied strain range). A decrease in peak stresses towards the end of test is indicative of fatigue crack propagation and load drop during failure.

The response of as-received and preconditioned samples exposed to total strain ranges from 0.6 % to 1.2% are presented in Figures 6.12 - 6.14. Where appropriate, interruptions after stabilisation have been labelled. As-received specimens ASRF1 and ASRF2 cyclically hardened over the first 200 cycles with the increase in peak stresses being larger at the higher strain range. This behaviour is typical of 316 and results from the generation and pinning of dislocations within the crystal lattice, increasing the total resistance to deformation [102].

The preconditioned samples displayed a similar hardening response, albeit to a much lesser extent and generally stabilising within a lower number of cycles. The initial peak stresses, both tensile and compressive, were significantly higher than that observed for as-received material at the same strain range. Sample CF1 at $\Delta\varepsilon = 1.2\%$ saw little to no hardening at all which was accompanied by a reduction in load after the 10th cycle; usually associated with the initiation and propagation of fatigue damage. It is clear that the carburisation reduced the fatigue endurance of 316H between $\Delta\varepsilon = 0.9 - 1.2\%$ as failure of CF1 and CF2 occurred shortly after stabilisation of their as-received strain range counterparts.

A comparison of cyclic hysteresis loops is shown in Figures 6.15 to 6.17. The first cycle from each test shows that carburisation increased the yield stress of 316H with samples CF1 & CF2 exhibiting higher peak stresses compared with ASRF1 & ASRF2 respectively. As expected, the yield stress of the thicker 7 mm diameter samples was not as amplified and lay closer to that of as-received. The cyclic Young's modulus appeared to be unaffected by carburisation. The stabilised hysteresis loops show a reduction in

peak stresses at $\Delta\varepsilon = 1.2\%$ and increase at $\Delta\varepsilon = 0.9\%$. Samples CF3 and CF4, tested under much lower strain ranges, displayed less overall cyclic plasticity; represented by a reduction in loop area.

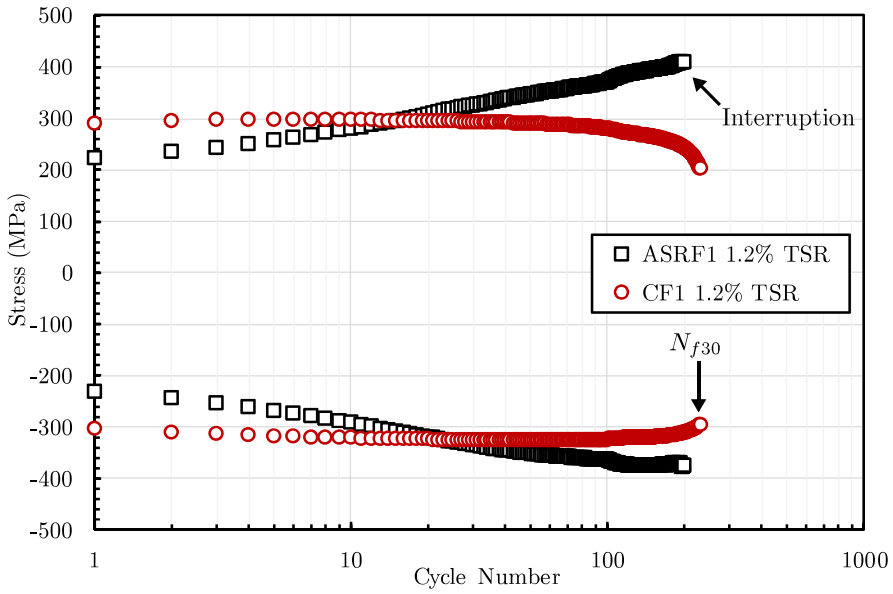


Figure 6.12: Cyclic stress response of as-received and preconditioned materials under $\Delta\varepsilon = \pm 1.2\%$ at 550°C.

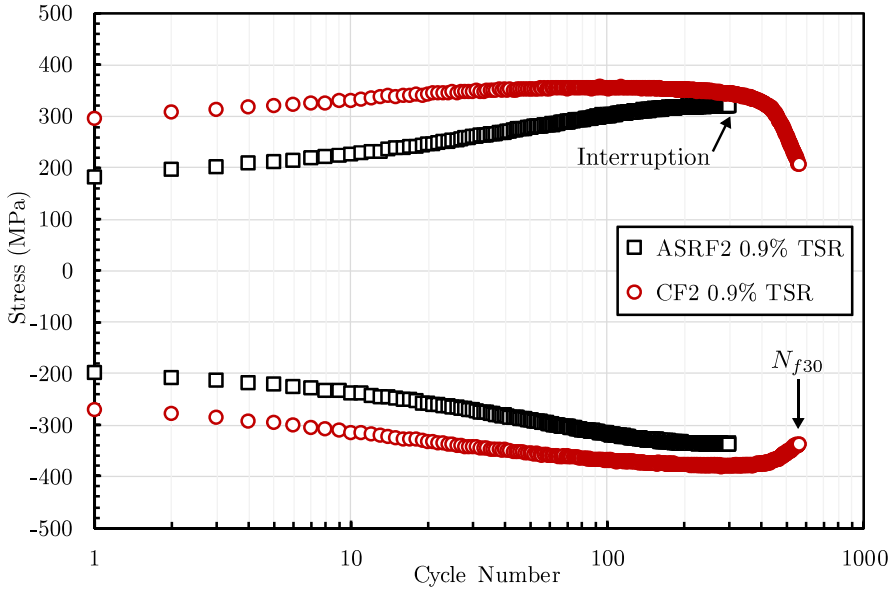


Figure 6.13: Cyclic stress response of as-received and preconditioned materials under $\Delta\varepsilon = \pm 0.9\%$ at 550°C.

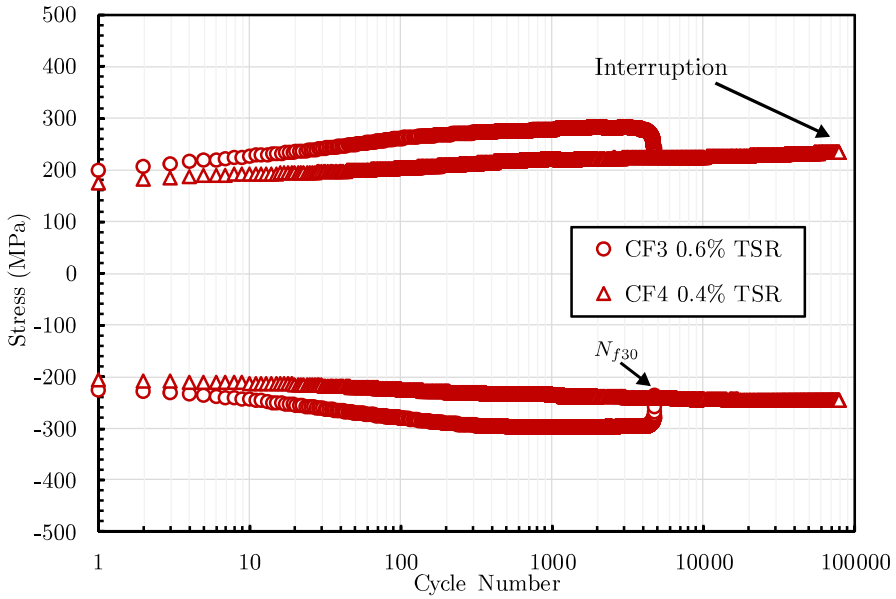


Figure 6.14: Cyclic stress response of preconditioned 316H under $\Delta\varepsilon = \pm 0.6\%$ and $\Delta\varepsilon = \pm 0.4\%$ at 550°C.

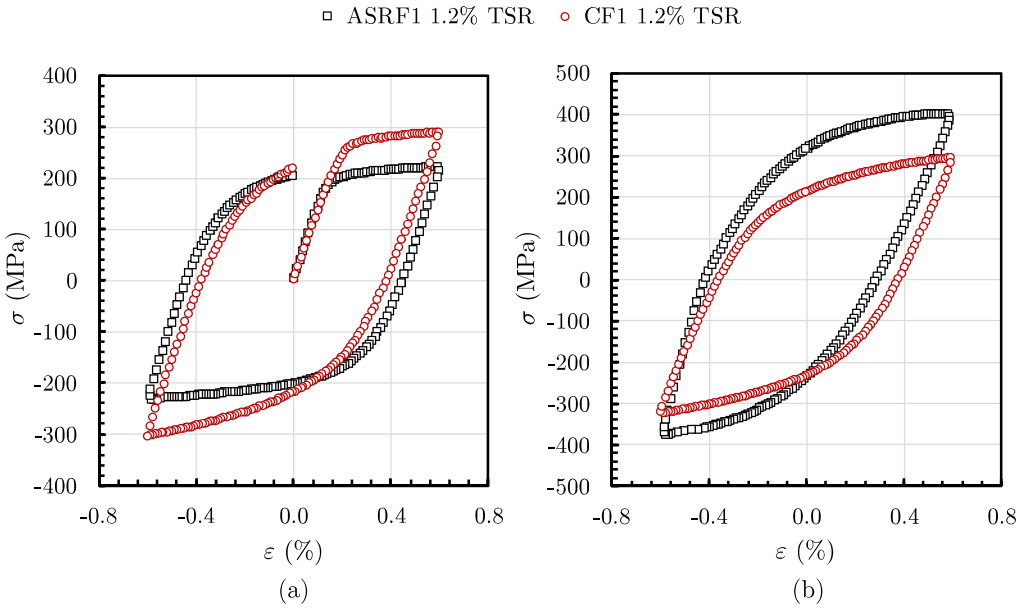


Figure 6.15: Stress strain response of as-received and preconditioned materials under $\Delta\varepsilon = \pm 1.2\%$ at (a) first and (b) stabilised cycles.

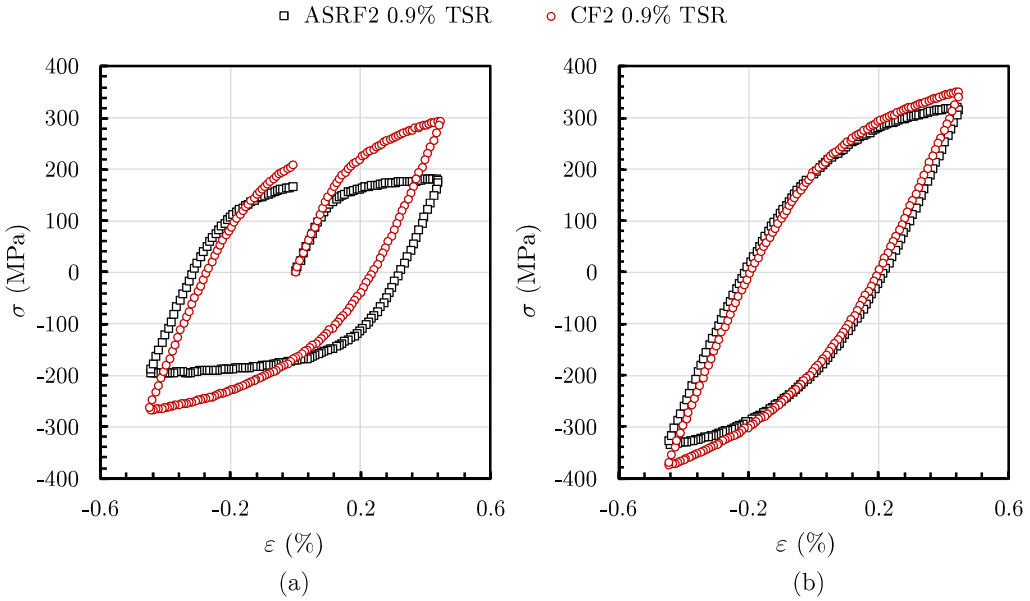


Figure 6.16: Stress strain response of as-received and preconditioned materials under $\Delta\varepsilon = \pm 0.9\%$ at (a) first and (b) stabilised cycles.

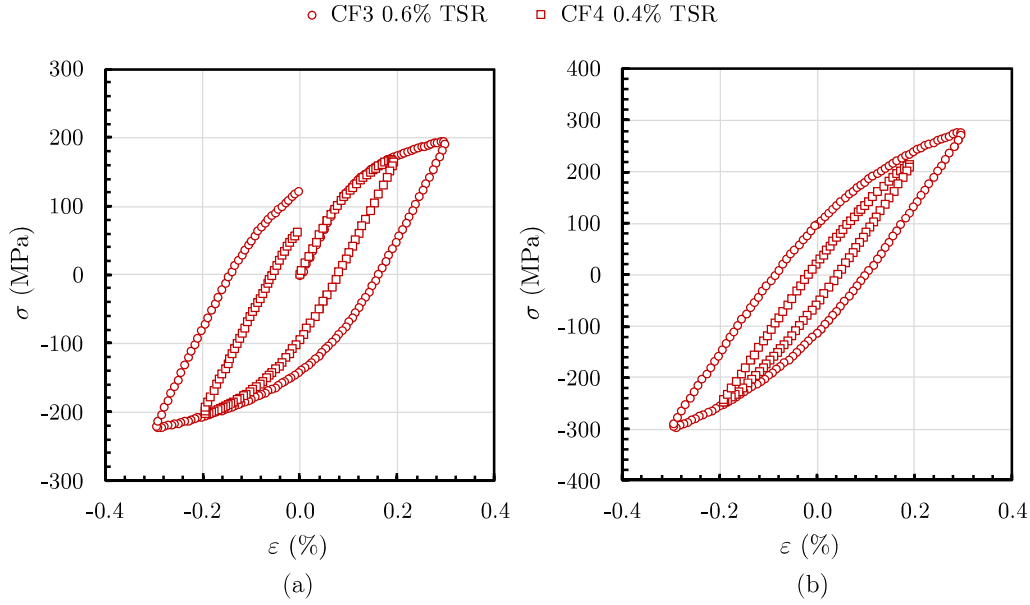


Figure 6.17: Stress strain response of 7 mm preconditioned samples under $\Delta\varepsilon = \pm 0.6\%$ and $\Delta\varepsilon = \pm 0.4\%$ at (a) first and (b) stabilised cycles.

Fatigue endurance data for as-received, preconditioned and thermally aged materials is presented in Figure 6.18 based on a 30% drop in peak load (N_{f30}). Additional test data from AMEC Foster-Wheeler has been included with all lives being based on a 7 mm gauge diameter unless otherwise specified. Best estimate and lower bound fits to R66 [101] predictions are also shown to serve as a baseline in comparison with as-received material. These were derived from data modified to account for the difference in gauge diameter in R66 and was done in accordance with R5 procedures [42].

The fatigue endurance of as-received material was found to be similar to the R66 best estimate fit. Preconditioned specimens generally failed much quicker than their as-received counterparts at the same applied strain range with the 5 mm diameter samples possessing the shortest lives, as expected. The effect of carburisation was more pronounced at the high strain ranges of 0.9% and above with preconditioned lives at 0.6% matching and even surpassing that of as-received. Specimen CF4 at $\Delta\varepsilon = 0.4\%$ was interrupted after stabilisation, showing no signs of load drop and surpassed the the lower bound and best estimate R66 lives. A single thermally aged sample showed similar endurance to that of as-received material.

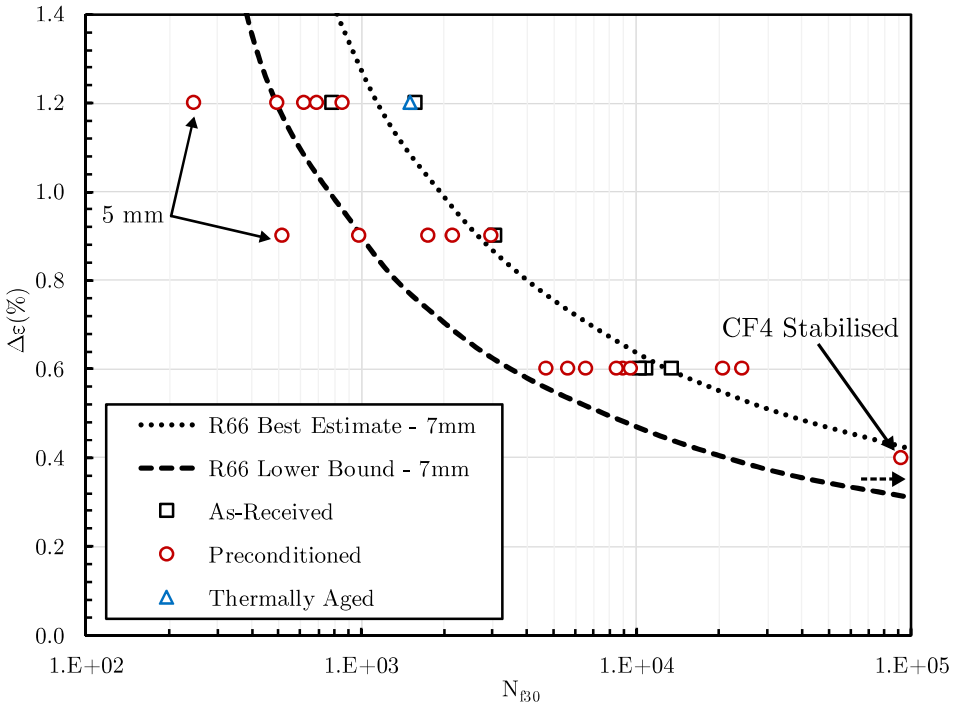


Figure 6.18: Strain-Life fatigue data for as-received, preconditioned and thermally aged materials.

6.3.2. Creep-Fatigue

Creep-fatigue tests were conducted to examine the influence of a hold time on the overall fatigue response of 316H. Samples were held in 60 minute strain controlled dwells at peak tensile strains to generate cyclic deformation enhanced by creep damage, the results are presented in this section. A comparison of cyclic hardening, hysteresis loop and total stress relaxation behaviour of as-received and preconditioned materials has been made. The influence of a hold time on fatigue endurance is presented through a series of strain-life data sets that have been supplemented with test data from AMEC Foster-Wheeler.

Figures 6.19 - 6.21 present the cyclic hardening behaviour of as-received and preconditioned specimens both with and without hold times. At $\Delta\varepsilon = 1.2\%$, carburisation resulted in a reduction in fatigue life and increased stress range when compared with as-received material. This was similar to that observed under pure fatigue conditions and was expected due to the increase in macroscopic yield stress resulting from the addition of an outer hardened layer. Figures 6.20 and 6.21 demonstrate the effect of a tensile dwell on both the hardening response and fatigue endurance of preconditioned material. A larger stress range and increased level of hardening was observed at $\Delta\varepsilon = 1.2\%$ which, appeared to be identical at $\Delta\varepsilon = 0.9\%$. Across both strain ranges, the addition of hold time slightly reduced fatigue life and was not seen to have a large impact.

The hysteresis loops taken from the first and stabilised cycles from each sample are plotted in Figures 6.22 - 6.24 . The stress - strain behaviour of samples ASRCF1 and CCF1 are shown in Figure 6.22 for $\Delta\varepsilon = 1.2\%$. It should be noted that data from the first cycle of ASRCF1 was only partially captured leading to the 'incomplete' loop observed. Carburisation increased the peak tensile and compressive loop stresses and resulted in a larger magnitude of stress relaxation and plastic strain range. Similar behaviour was seen for preconditioned material where the addition of a hold time was found to increase peak stresses and inelastic strain range.

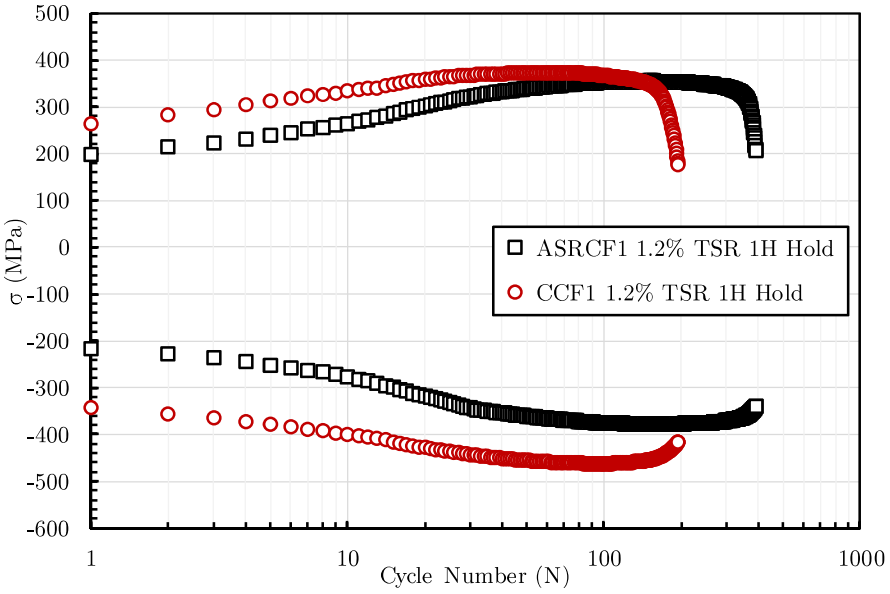


Figure 6.19: Cyclic stress response of as-received and preconditioned materials under creep-fatigue conditions at $\Delta\varepsilon = \pm 1.2\%$ with a 60 minute hold time.

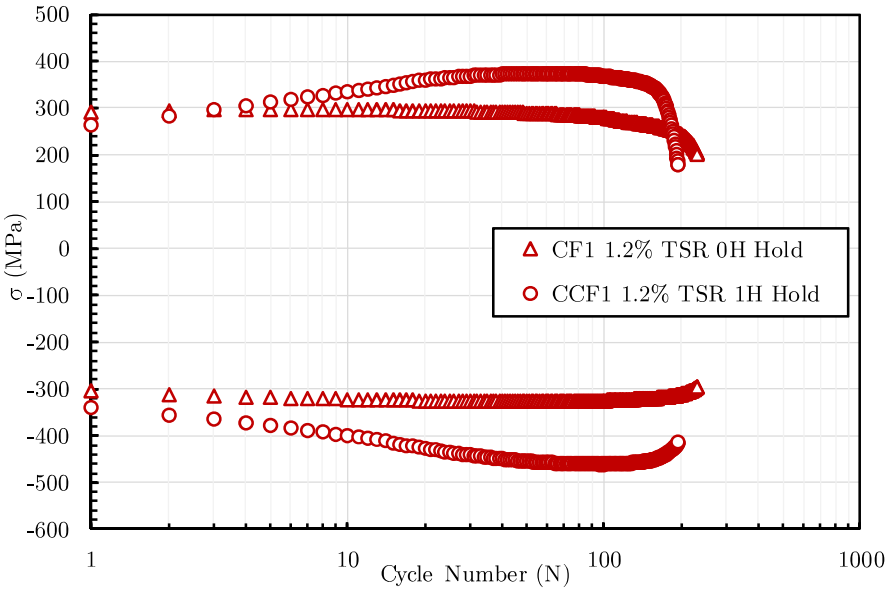


Figure 6.20: Cyclic stress response of preconditioned samples under fatigue conditions at $\Delta\varepsilon = \pm 1.2\%$ with and without a 60 minute hold time.

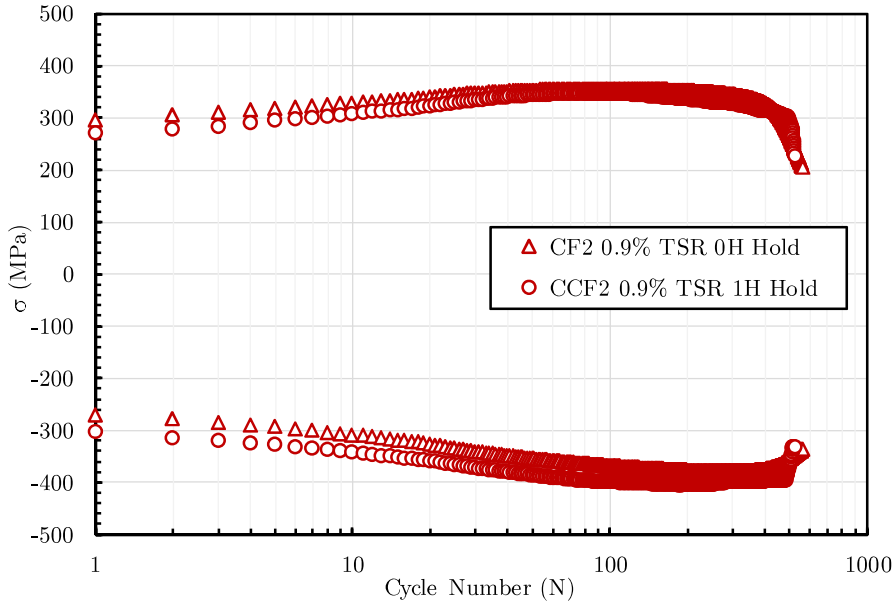


Figure 6.21: Cyclic stress response of preconditioned samples under fatigue conditions at $\Delta\varepsilon = \pm 0.9\%$ with and without a 60 minute hold time.

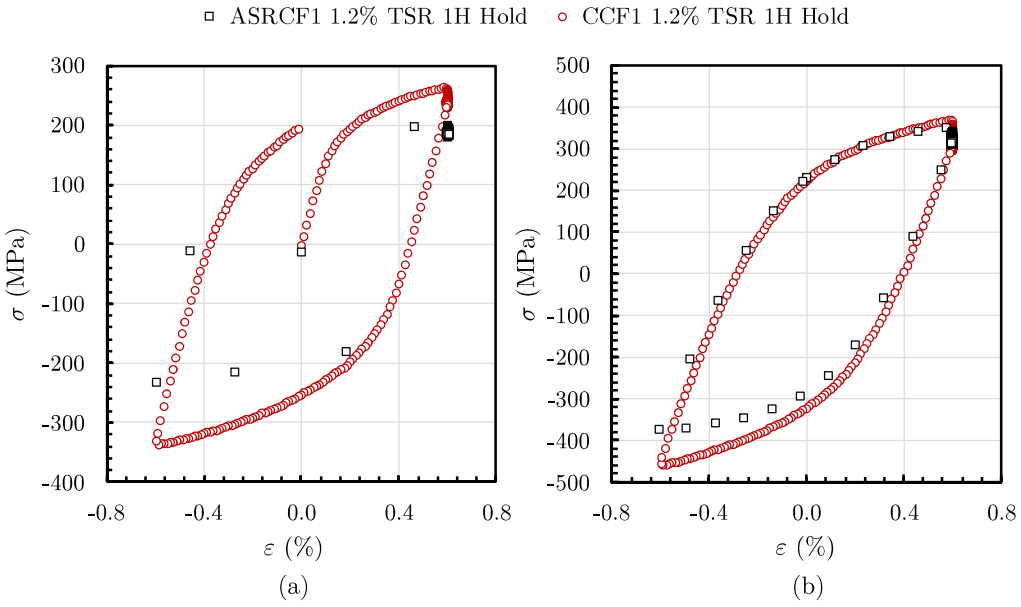


Figure 6.22: Stress strain response of as-received and preconditioned materials under $\Delta\varepsilon = \pm 1.2\%$ at (a) first and (b) stabilised cycles.

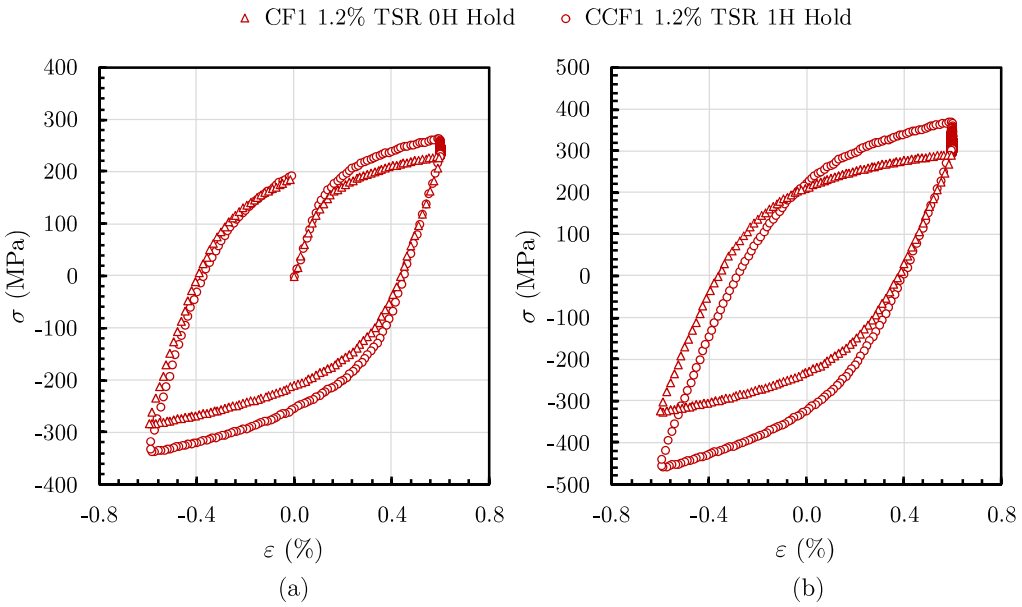


Figure 6.23: Stress strain response of preconditioned samples under $\Delta\varepsilon = \pm 1.2\%$ at (a) first and (b) stabilised cycles with and without a 60 minute hold time.

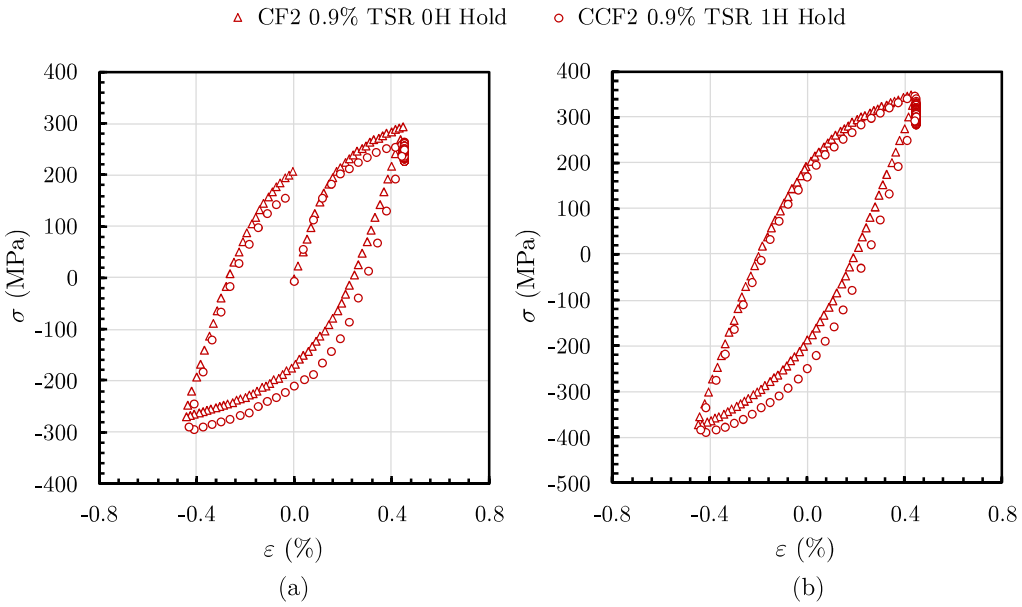


Figure 6.24: Stress strain response of preconditioned samples under $\Delta\varepsilon = \pm 0.9\%$ at (a) first and (b) stabilised cycles with and without a 60 minute hold time.

Under strain controlled conditions, stresses relax during tensile dwells as elastic strains convert to permanent plastic and/or creeps strain. The relaxation behaviour of all creep-fatigue specimens can be seen in Figure 6.25 for four consecutive stabilised cycles. The

average amount of relaxation is shown in Table 6.3 and has been calculated by summing the difference in stress at the start and end of each dwell and dividing by the total number of cycles. For both materials, a higher strain range resulted in an increase in peak tensile stress and hence a greater degree of relaxation. In addition, stresses did not appear to fully stabilise within the 60 minute dwell period. Comparing the behaviour of ASRCF1 and CCF1, higher peak stresses in the preconditioned material resulted in more relaxation to a stress value less than that of as-received.

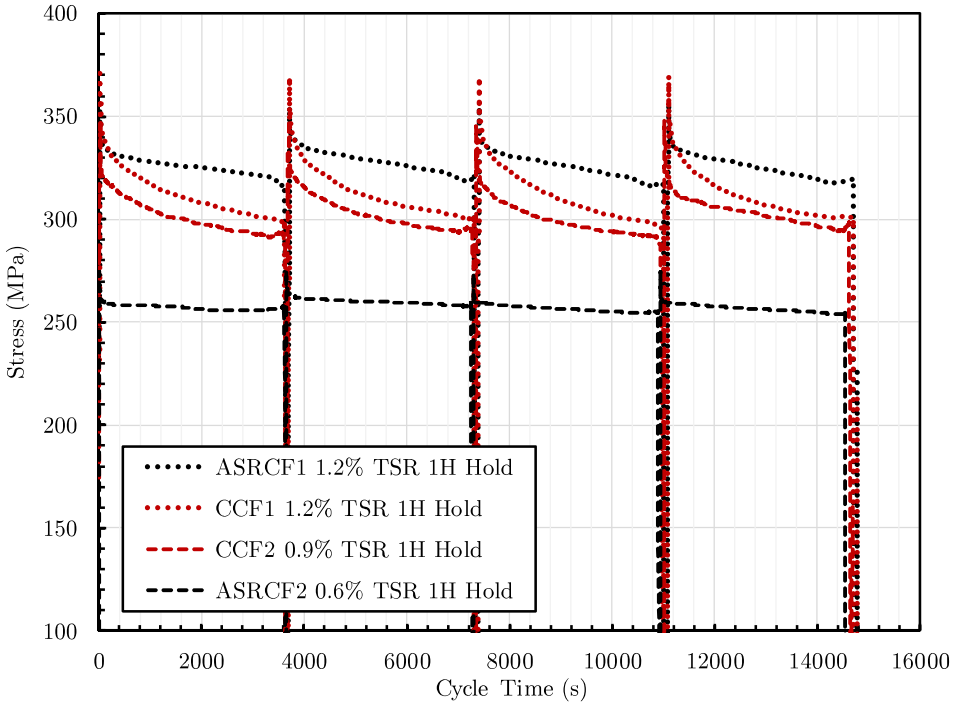


Figure 6.25: Stress relaxation during four stabilised cycles for as-received and preconditioned creep-fatigue samples.

Table 6.3: Average stress relaxation during creep-fatigue testing.

ID	TSR (%)	Relaxation (MPa)	Peak Stress (MPa)
ASRCF1	1.2	37.3	354.8
ASRCF2	0.6	19.0	274.2
CCF1	1.2	72.4	369.5
CCF2	0.9	56.4	347.4

The fatigue endurance data for as-received, preconditioned and thermally aged 316H is presented in Figure 6.26 for samples under continuous cyclic and creep-fatigue conditions. Additional test data from AMEC Foster-Wheeler has been included and where applicable, specimens with the smaller gauge diameter of 5 mm have been labelled.

The limited creep-fatigue failure data showed that in general, the addition of a dwell in tension led to a reduction in fatigue endurance. For $\Delta\varepsilon = \pm 1.2\%$, both thermally aged and preconditioned samples with a hold time failed quicker than those without. At this strain range, comparable data for as-received creep-fatigue specimens of the same diameter was not available. A similar trend was observed at $\Delta\varepsilon = \pm 0.6\%$ with a single creep-fatigue preconditioned sample displaying the lowest endurance. This limited data set did not appear to show a clear relationship between strain range, carburisation and the addition of a hold time.

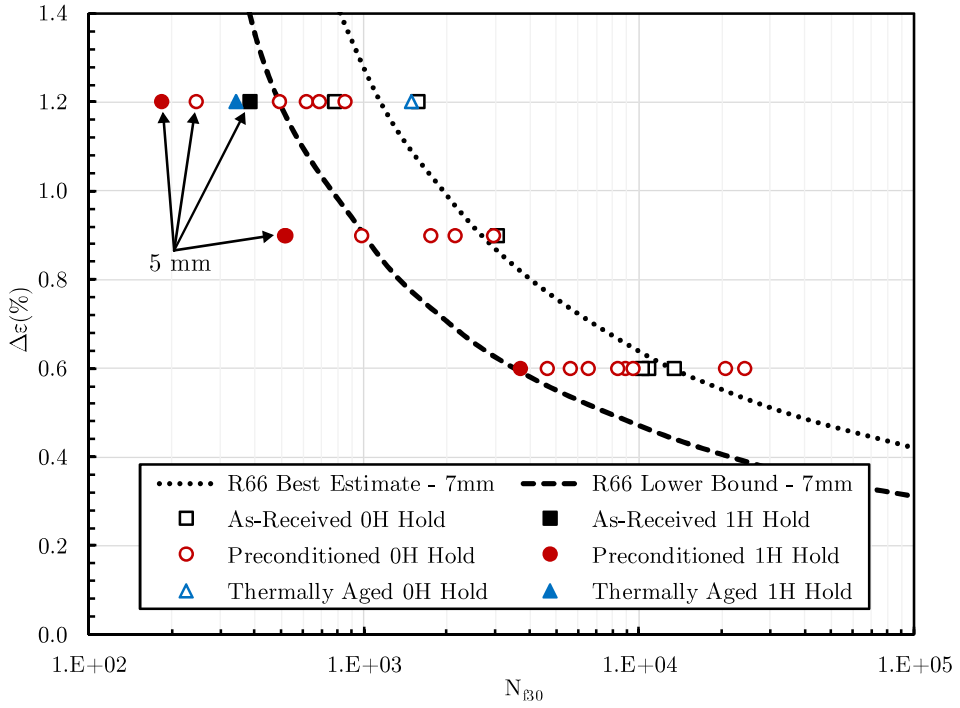


Figure 6.26: Strain-Life fatigue data for as-received, preconditioned and thermally aged materials both with and without hold times.

6.3.3. Comparison of Inelastic Strain Energy Density

The area under a uniaxial stress - strain curve equates to the overall work done on a specimen and represents the total mechanical energy that a material can absorb prior to fracture; known as material toughness. A similar concept can be applied to the area contained within a fatigue hysteresis loop. This is equal to the total strain energy absorbed per cycle. If the loop is presented in terms of stress versus inelastic strain, the area then corresponds to the inelastic strain energy density (ΔW). This includes both plastic and creep strain and is illustrated in Figure 6.27. ΔW is mathematically defined in Equation 6.5 where ε_{ie1} and ε_{ie2} are the inelastic strain tensors at the beginning and end of each cycle, σ_{ij} is the stress tensor and ε_{ij} is the inelastic strain tensor.

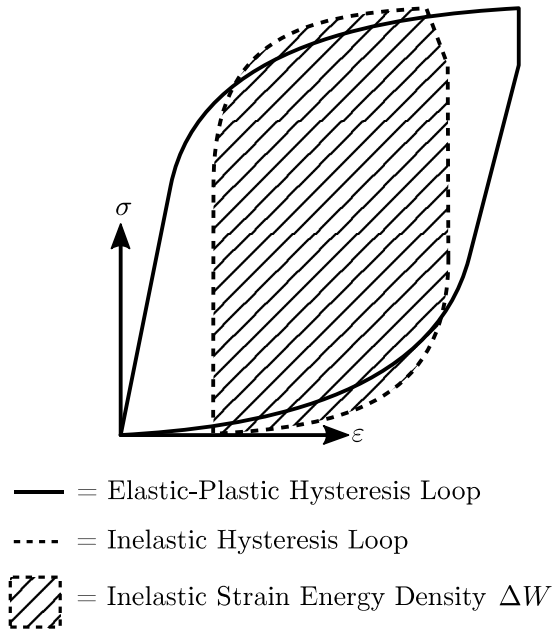


Figure 6.27: Illustration of inelastic strain energy density taken from a uniaxial cyclic hysteresis loop.

$$\Delta W = \int_{\varepsilon_{ie1}}^{\varepsilon_{ie2}} \sigma_{ij} d\varepsilon_{ij} \tag{6.5}$$

The stabilised inelastic strain energy density has often been used as a damage parameter to characterise fatigue life under LCF conditions [103, 104, 105]. It is particularity useful when comparing fatigue and creep-fatigue data as it enables quantification of the additional plasticity induced by creep. Figure 6.28 shows the evolution of strain energy for all uninterrupted tests within this study. The value of ΔW has been calcu-

lated by approximating the area within each inelastic loop using trapezoidal numerical integration. Hysteresis data has been converted to be in terms of inelastic strain by subtracting the instantaneous elastic strain from recorded total mechanical strain as shown in Equation 6.6. Here, $\varepsilon_{ie}(t)$ is the inelastic strain, $\varepsilon_t(t)$ the total strain and E_0 the Young's Modulus measured from the first cycle.

$$\varepsilon_{ie}(t) = \varepsilon_t(t) - \frac{\sigma(t)}{E_0} \tag{6.6}$$

For all samples, ΔW followed a similar trend to the peak stress history and displayed the three common stages of material behaviour under LCF conditions: hardening, stabilisation and the initiation of damage until failure. The higher strain ranges induced larger levels of plasticity which, translated to an increase in ΔW. The addition of a hold time increased the stabilised energy values and coincided with a reduction in fatigue endurance. Figure 6.29 plots the stabilised strain energy against the number of cycles to failure for each sample and has been supplemented with data from AMEC Foster-Wheeler. For the same ΔW, preconditioned material displayed a lower fatigue endurance compared to as-received. This was more pronounced at the higher strain energies, denoted by the diverging power law fits. Thermally aged samples displayed similar behaviour to that of as-received.

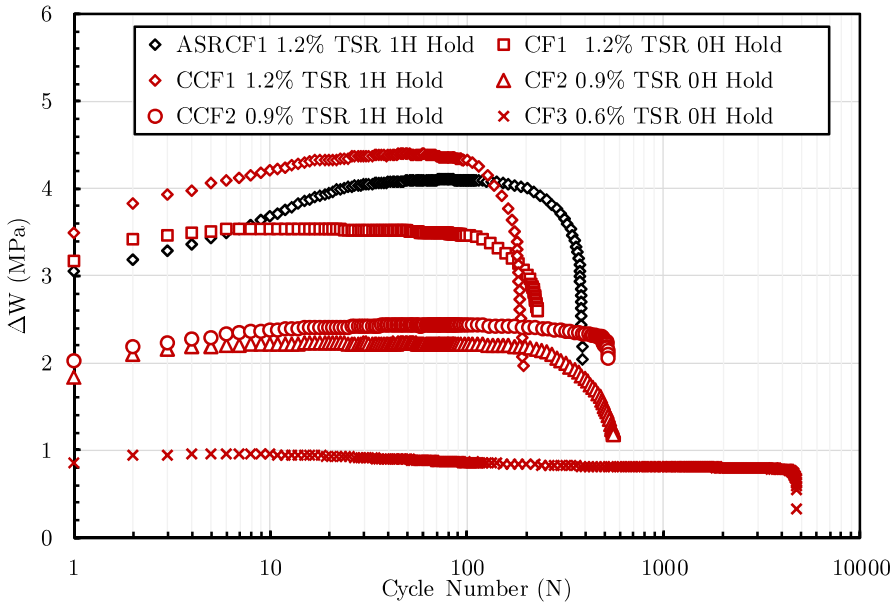


Figure 6.28: A comparison of the inelastic strain energy density against the number of cycles to failure for as-received and preconditioned specimens with and without hold times.

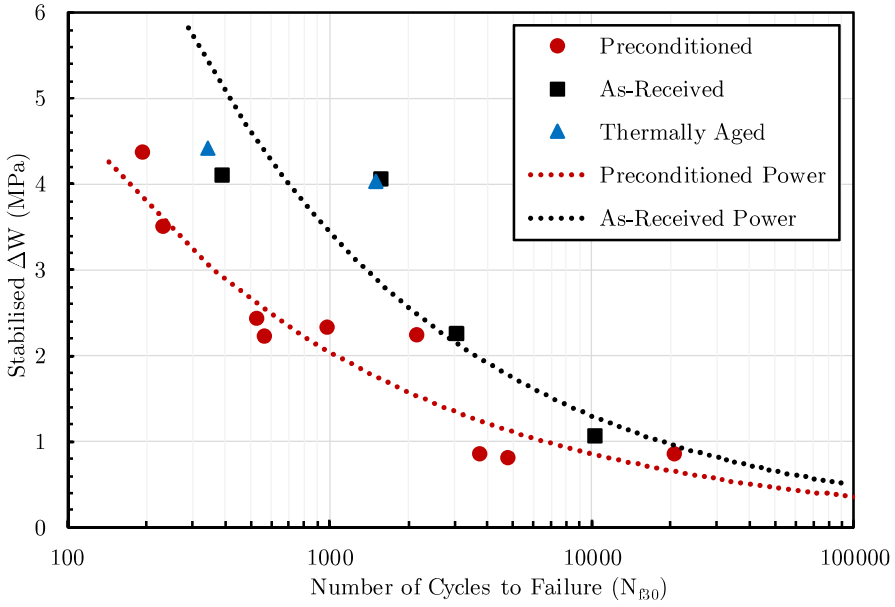


Figure 6.29: A comparison of stabilised inelastic strain energy density against the number of cycles to failure for as-received, preconditioned and carburised 316H.

6.3.4. Metallography

Metallographic examination was undertaken on select specimens to understand how carburisation interacted with and generally accelerated fatigue damage within as-received 316H. This was conducted using a combination of optical, scanning electron and X-Ray tomographic imaging to characterise crack behaviour. The results are presented within this section for both fatigue and creep-fatigue samples.

Fatigue

Carburisation generally decreased the fatigue strength of 316H with preconditioned samples failing earlier than their as-received counterparts. Figure 6.30 shows an initial comparison of failed surfaces from specimens ASRF2 and CF2. A clear difference in surface morphology can be seen with CF2 containing widespread surface cracking across it's entire gauge length alongside significant oxide spallation. Similar observations were made in both previous tensile and creep testing with cracking being circumferential and orientated perpendicular to the direction of load. No such surface damage was immediately seen within ASRF2.

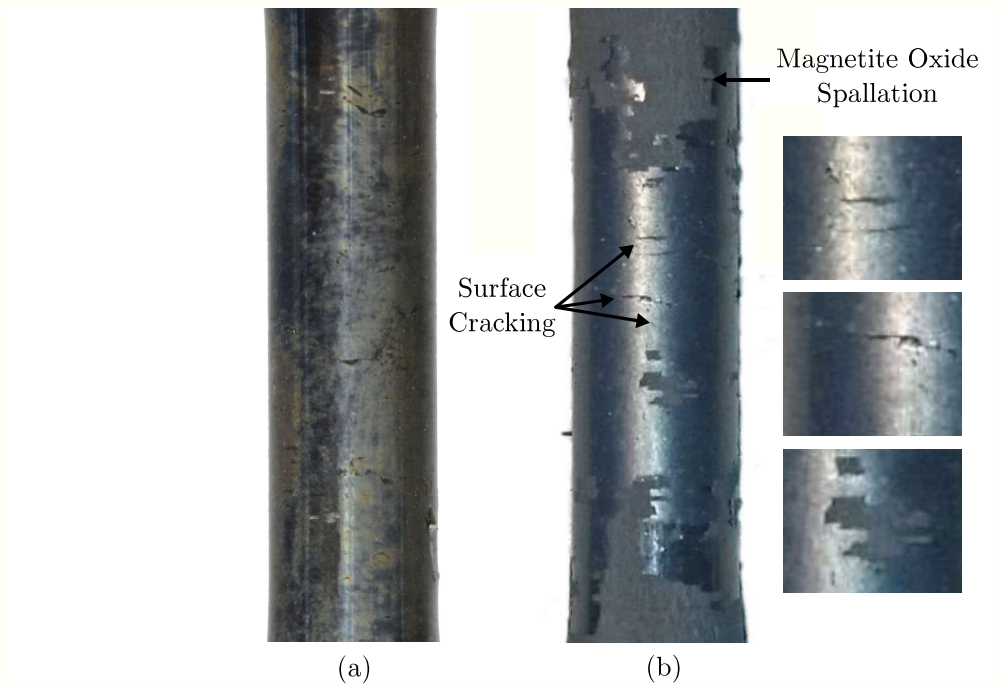


Figure 6.30: Comparison of fatigue sample surfaces (a) ASRF2, as-received and (b) CF2, preconditioned carburised.

To investigate the nature of surface cracking within CF2, X-Ray tomography was undertaken and is shown in Figures 6.31 and 6.32. This non-destructive imaging technique was conducted by the University of Manchester [106] and enabled the three dimensional visualisation of multiple major crack depths without the need for physical sectioning. The scanning resolution was a function of material density and sample size; for this diameter of 316H a 5 µm pixel size was achieved. The purple highlights within the tomograms represent voids within the same volume or crack faces. Numerous surface cracks were seen along the entire gauge length of CF2 with a large proportion of these having propagated into the bulk material. An axial view of all cracks shows striations orientated towards the central portion of the gauge length indicating multiple initiation sites and crack growth in the radial direction.

Using the results obtained from tomography to determine the axial plane of maximum crack depth, sample CF2 was section and imaged under optical microscopy. The sample was mounted in conductive Bakelite resin, polished to a 1 µm finish and etched using a 10% ferric chloride solution to reveal the underlying grain structure. Figure 6.33 shows the entire crack depth with transgranular fatigue crack propagation appearing as the dominant mode of failure.

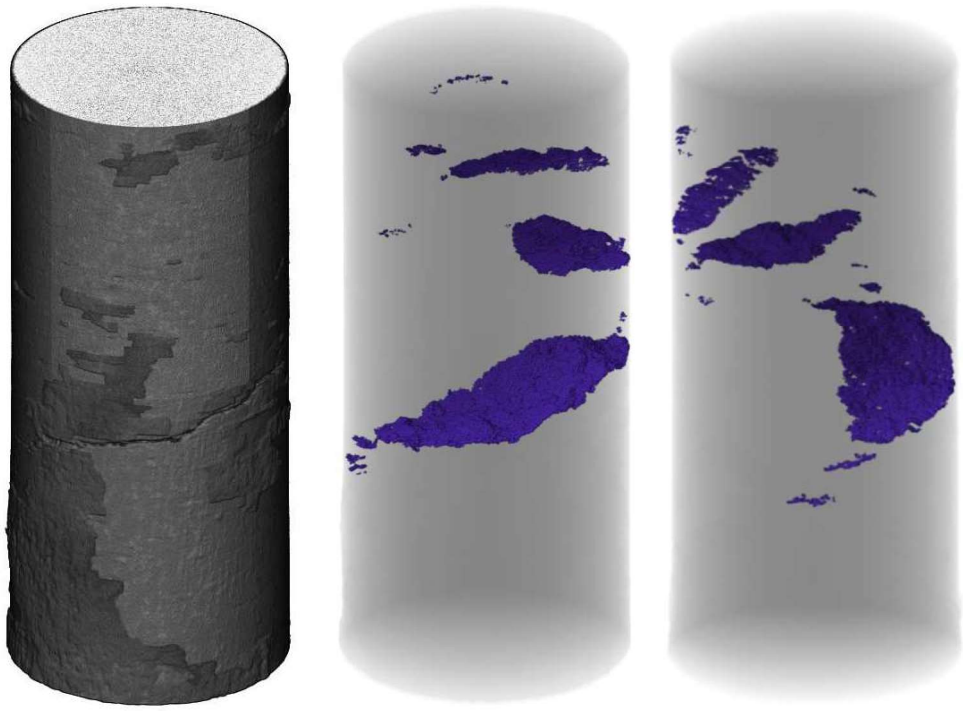


Figure 6.31: X-Ray tomogram of specimen CF2 showing multiple major surface cracks that had initiated within the carburised layer.

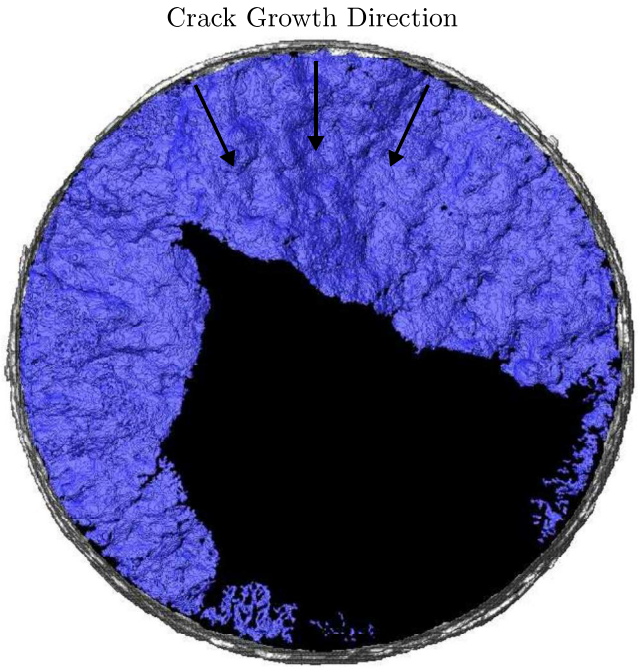


Figure 6.32: Axial tomogram showing multiple crack initiation sites and radial propagation in sample CF2.

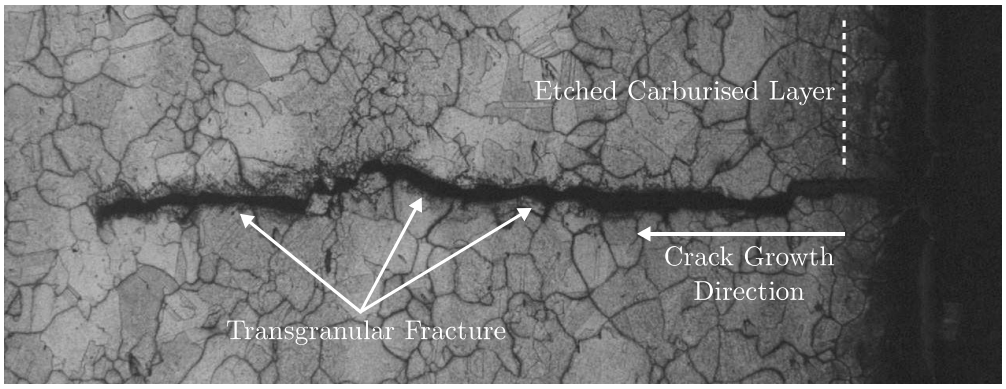


Figure 6.33: Section metallography of preconditioned fatigue sample CF2 displaying transgranular fatigue fracture.

To compare the fatigue crack behaviour of carburised 316H at two different strain ranges ($\Delta\varepsilon = 1.2\%$ and 0.6%), samples CF1 and CF3 were cryogenically broken open at the location of maximum crack depth and examined under SEM. This involved cooling specimens using liquid nitrogen and fracturing the remaining ligament in a brittle manner, ensuring that the fracture surfaces were preserved. The fractographs of each sample can be seen in Figures 6.34 and 6.35 alongside detailed views of key features.

An overview of both surfaces displayed a clear distinction between areas that had failed during fatigue and those that had fractured when broken open. Evidence for multiple initiation sites were found across the surface of both specimens alongside multiple fatigue ratchet marks orientated in a radial direction, towards the center of the gauge length. Surface cracking appeared to initiate circumferentially with Figure 6.34 showing cracking on the surface opposite the primary crack front. Detailed examination revealed typical fatigue crack striations that were orientated in multiple directions indicating numerous crack growth fronts.

The specimens were sectioned through their axial mid plane and imaged under optical microscope. Figures 6.36 and 6.37 show a section view of the fracture surface of each sample and reveal transgranular fatigue cracking across the primary crack fronts. No immediate difference in fracture mode was observed across the carburised layer (denoted by the inner darker shaded regions). Sample CF4, run at the lowest applied strain range, was interrupted after stabilisation at approximately 100,000 cycles and showed no signs of load drop. A section view taken of its gauge length is presented in Figure 6.38 which displays no evidence of surface cracking with even the inner spinel oxide remaining intact.

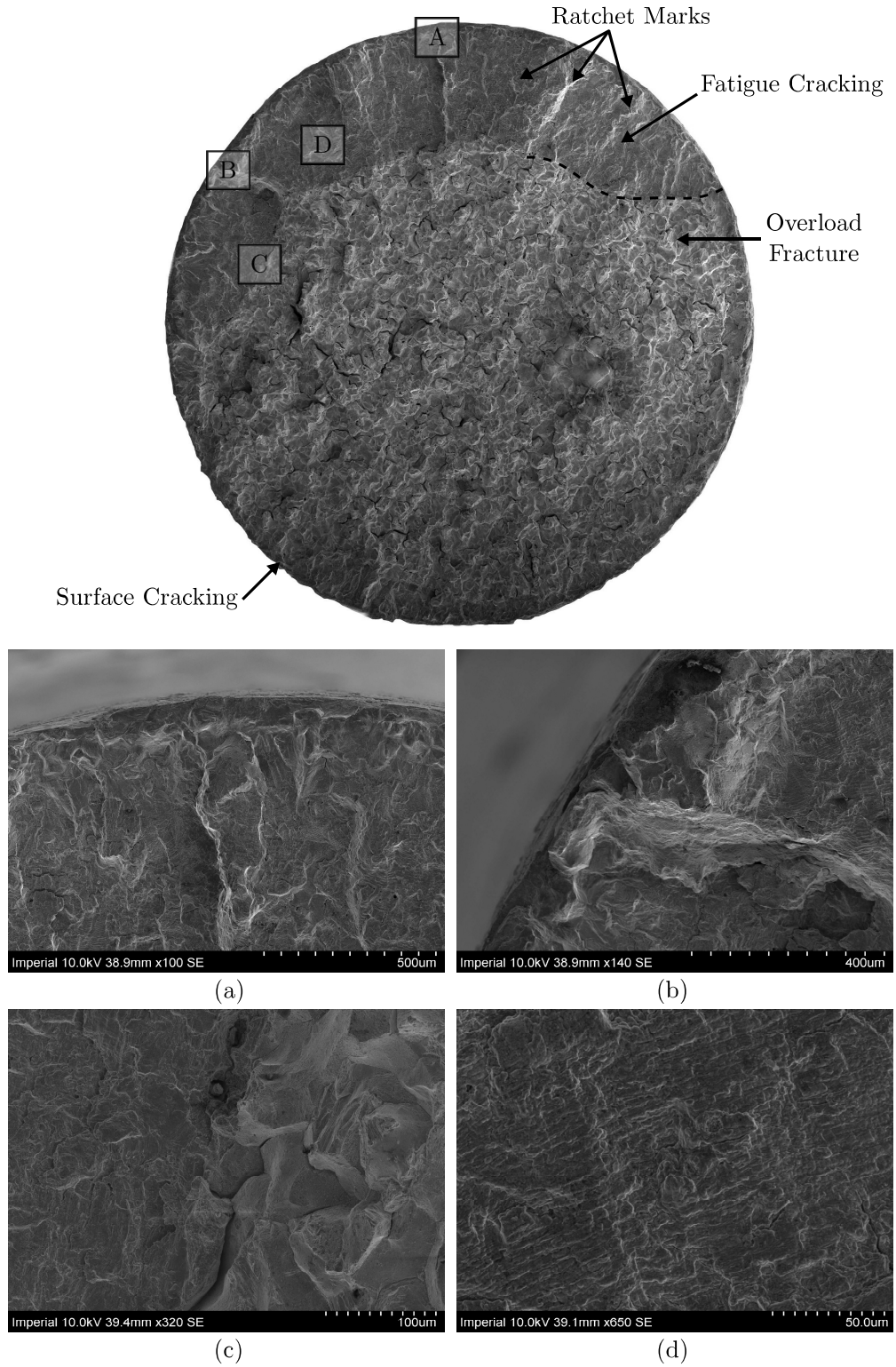


Figure 6.34: Fractograph of carburised fatigue specimen CF1 ($\Delta\varepsilon = 1.2\%$) showing the presence of (a)(b) multiple fatigue ratchet marks originating at the surface, (c) difference in failure modes and (d) striation-like features.

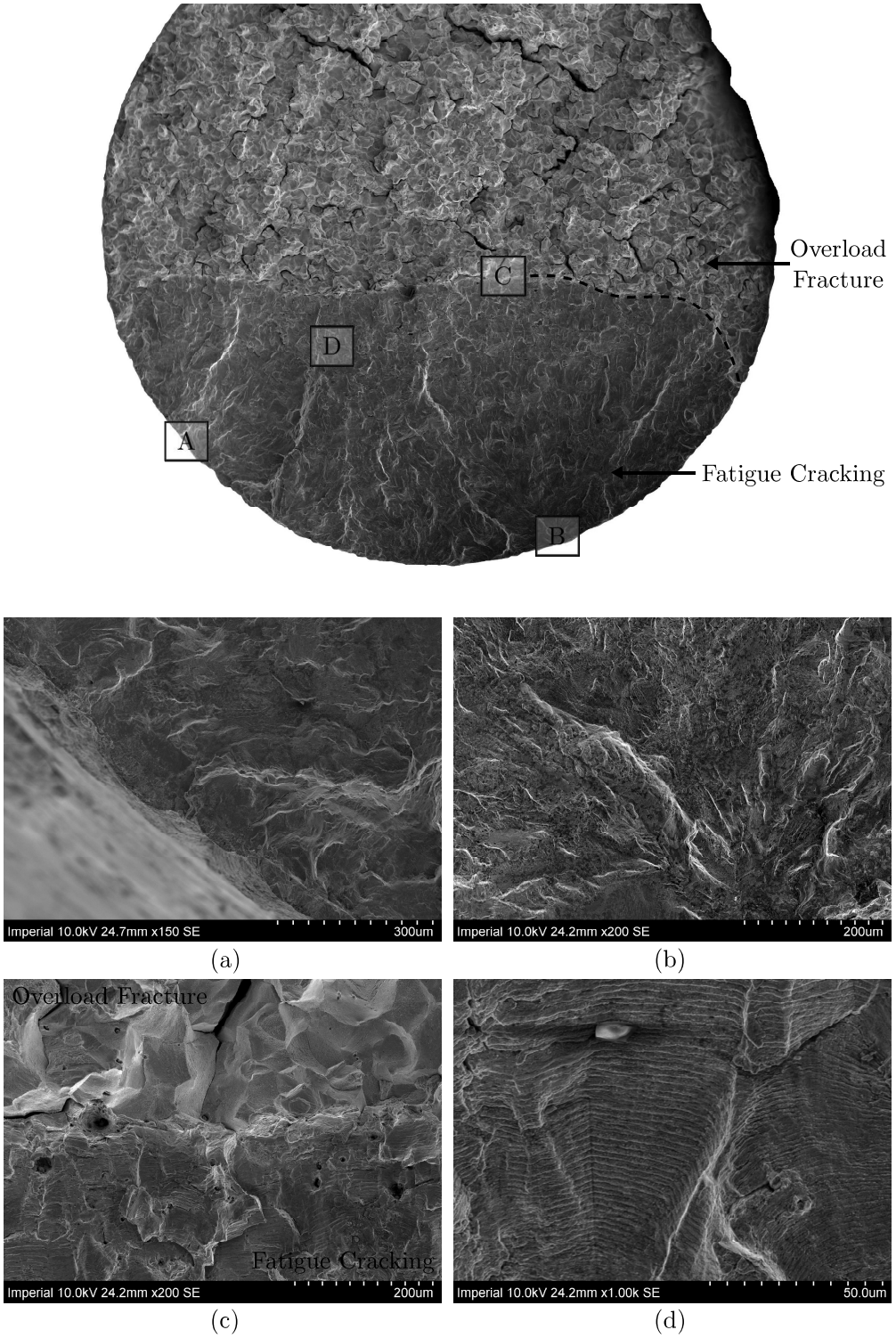


Figure 6.35: Fractograph of carburised fatigue specimen CF3 ($\Delta\varepsilon = 0.6\%$) showing the presence of (a) multiple ratchet marks (b) river markings at the surface, (c) difference in failure modes and (d) striation like features.

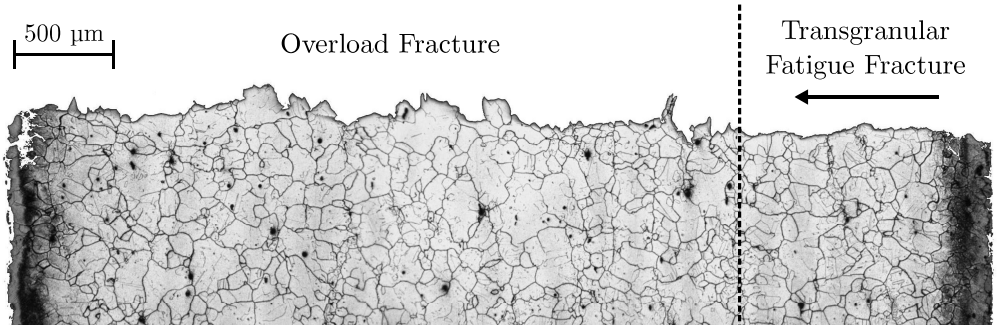


Figure 6.36: Section of the fracture surface of CF1 ($\Delta\varepsilon = 1.2\%$) showing transgranular fatigue failure across the primary crack front.

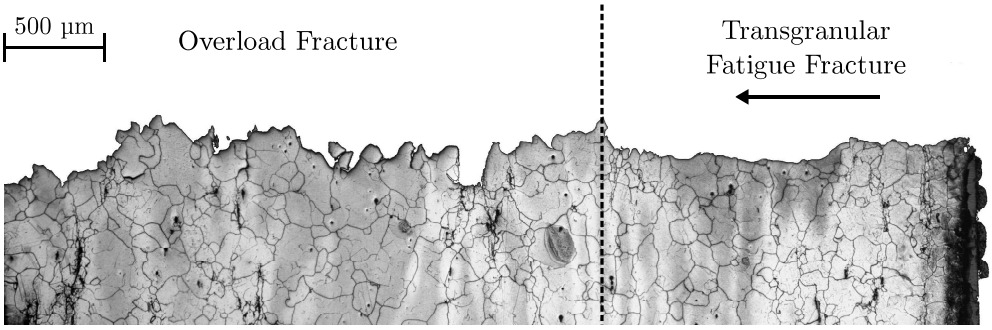


Figure 6.37: Section of the fracture surface of CF3 ($\Delta\varepsilon = 0.6\%$) showing transgranular fatigue failure across the primary crack front.

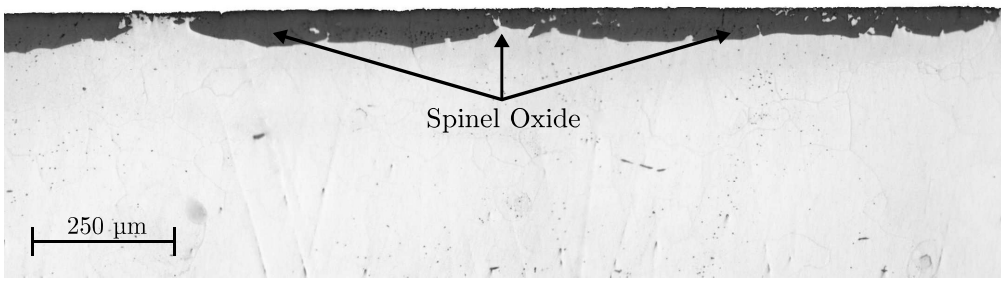


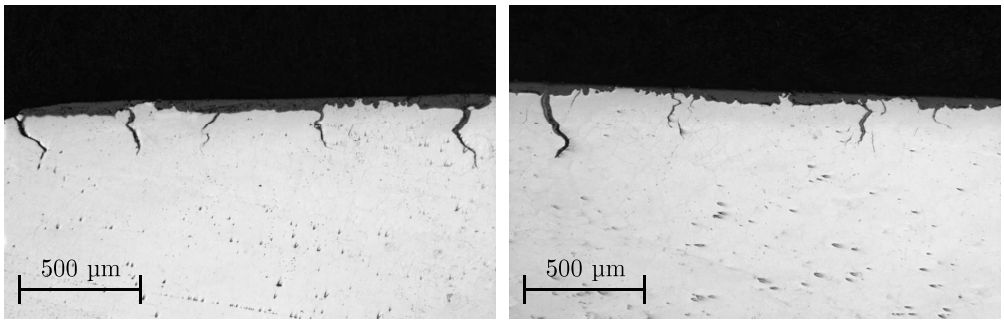
Figure 6.38: Section taken of the outer edge from sample CF4 $\Delta\varepsilon = 0.4\%$ showing no widespread surface cracking and an intact inner spinel oxide layer.

Creep Fatigue

When compared to continuous fatigue cycling, the addition of a hold time resulted in an increased averaged strain energy density thus inelastic strain range per cycle. This induced more damage within preconditioned samples and resulted in slightly lower fatigue endurances. Metallographic examination was undertaken on all uninterrupted creep fatigue samples in this study to investigate how the addition of a tensile dwell affected fracture behaviour across both as-received and carburised 316H.

The fracture surfaces of each sample can be seen in Figures 6.40 to 6.42. Distinguishing between areas that had failed during fatigue and those that had fractured when broken open was not as clear in comparison with samples tested under pure fatigue conditions. Failure appeared to be more intergranular in nature and presence of fatigue striations, less obvious. The preconditioned specimens displayed multiple fatigue ratchet marks that originated at the surface and were distributed circumferentially around the entire specimen edges; suggesting multiple initiation sites. Initiation within the as-received material appeared to originate from a single location. A difference in fracture morphology was observed between the carburised layer and bulk with the former displaying more brittle fracture behaviour, Figures 6.41 (c) & (d) and Figure 6.42 (a).

Section metallography taken through the mid-plane of each sample can be seen in Figures 6.43 – 6.45. Typical mixed mode trans- and intergranular fracture was observed across all primary crack fronts with the preconditioned sample CCF1 exhibiting initiation and crack growth from both sides. The gauge lengths of CCF1 and CCF2 are pictured in Figure 6.39 showing widespread surface cracking across both, with the majority of cracks propagating to a depth further than the carburised layer-bulk interface.



(a) (b)

Figure 6.39: Gauge length of samples (a) CCF1 & (b) CCF2 showing widespread surface cracking that had propagated into the bulk material.

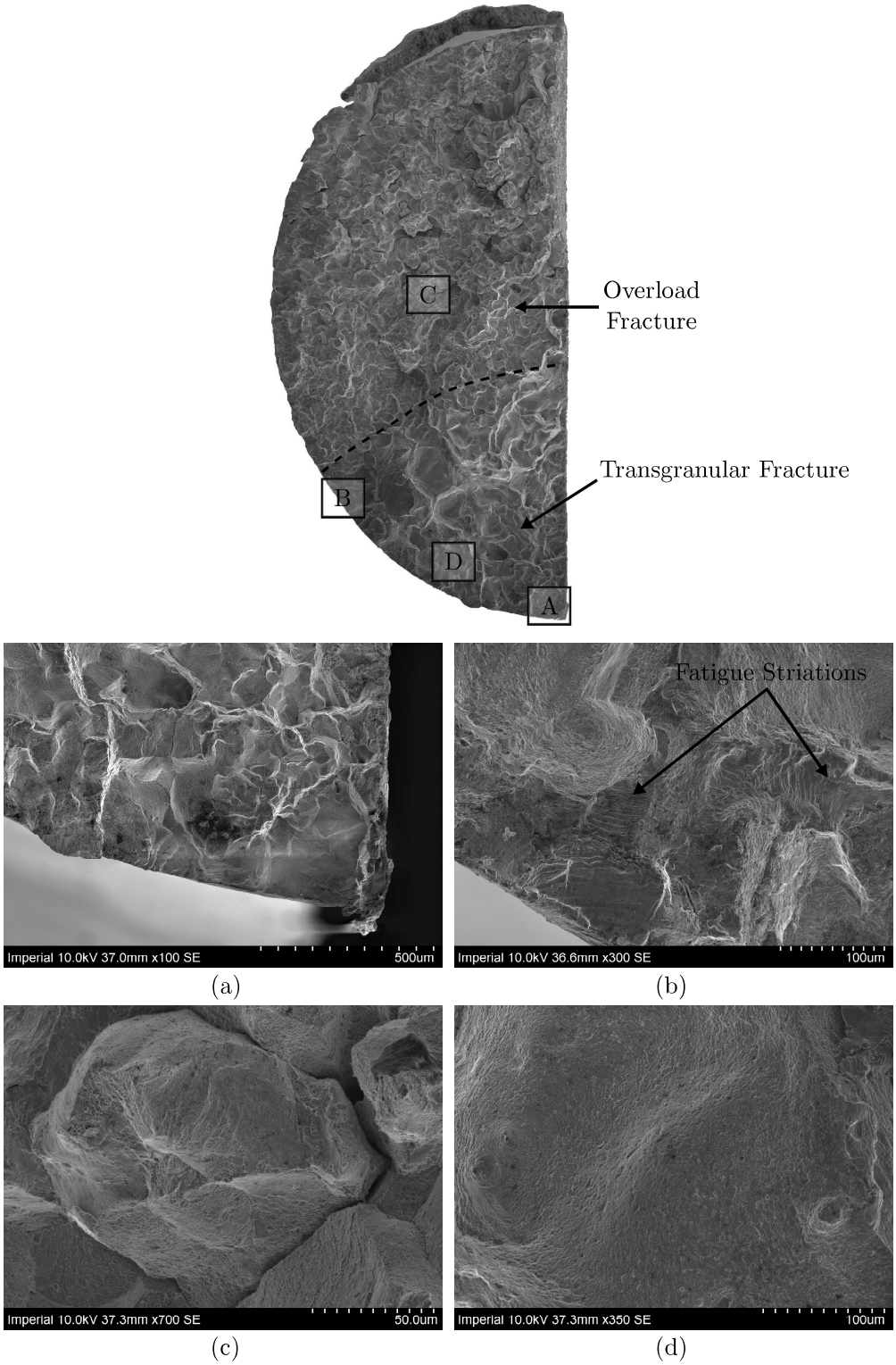


Figure 6.40: Fractograph of as-received creep-fatigue specimen ASRCF1 ($\Delta\varepsilon = 1.2\%$) with a 60 minute hold time, showing the presence of (a) multiple ratchet marks (b) fatigue striations at the surface and the difference in crack morphology in areas of (c) overload and (d) fatigue fracture.

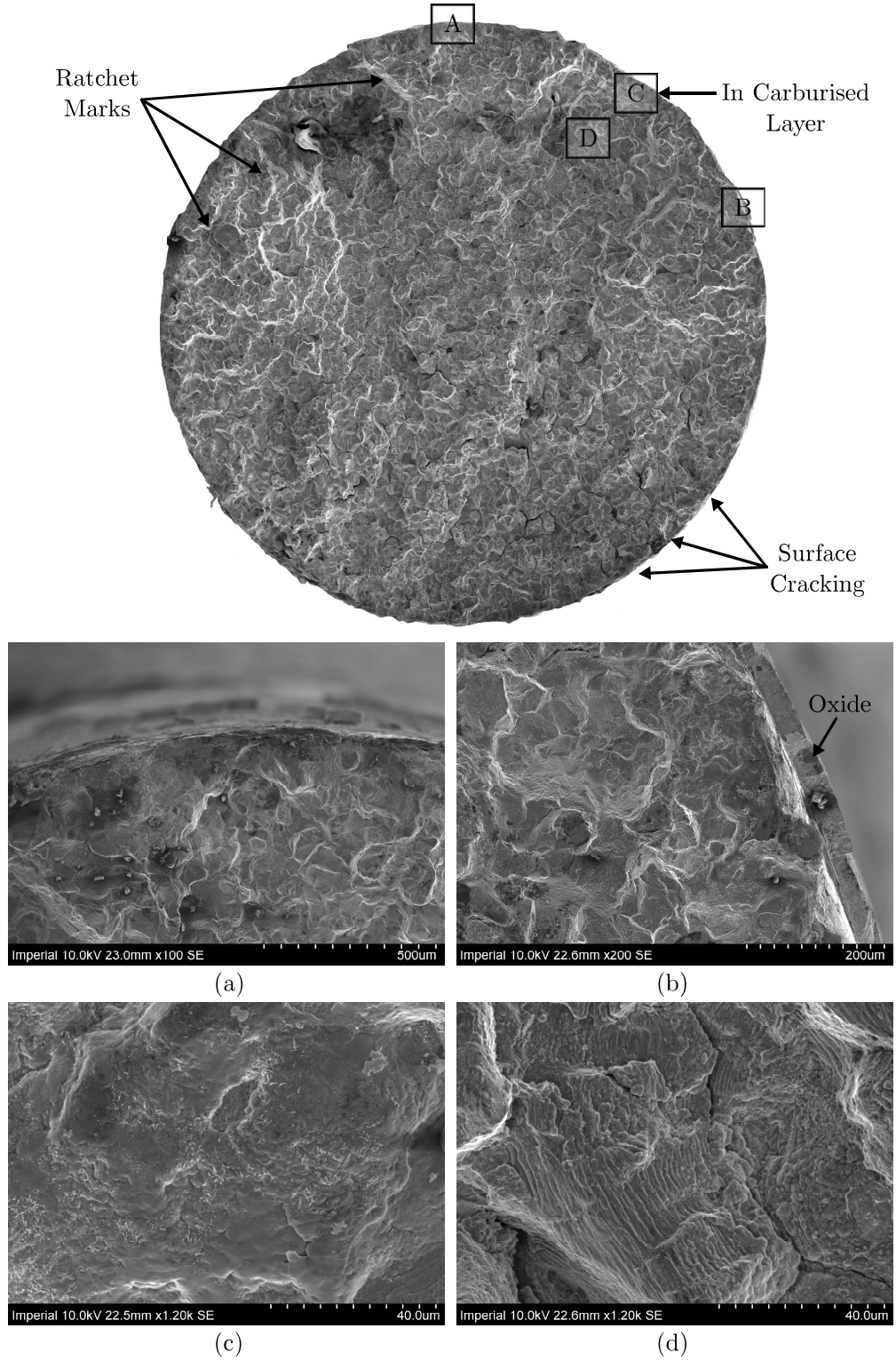


Figure 6.41: Fractograph of carburised creep-fatigue specimen CCF1 ($\Delta\varepsilon = 1.2\%$) with a 1 hour hold time showing the presence of (a) (b) multiple ratchet marks at the surface, difference in fatigue failure modes within the (c) carburised layer (brittle) and in the (d) bulk material (striations).

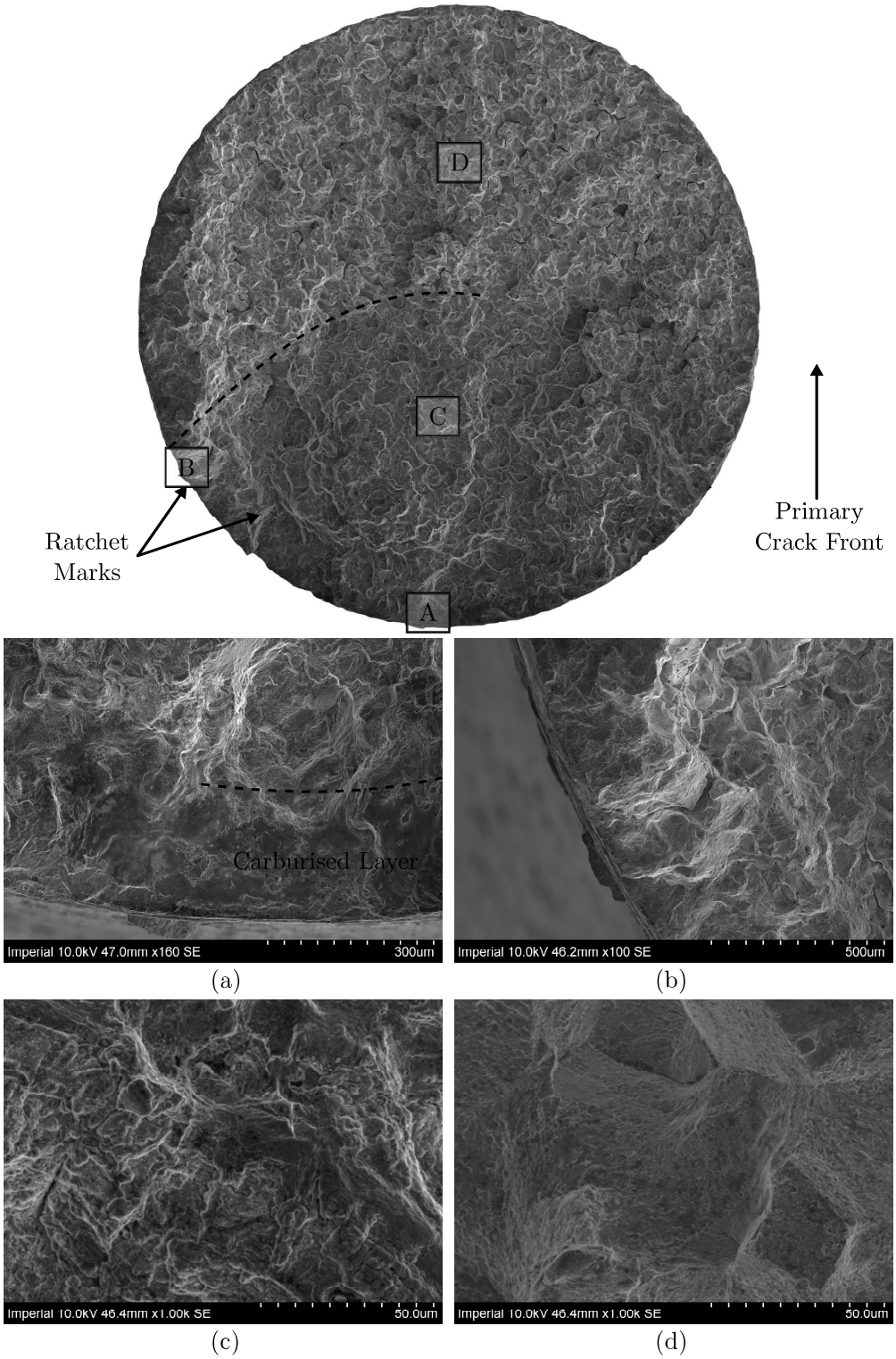


Figure 6.42: Fractograph of carburised fatigue specimen CCF2 ($\Delta\varepsilon = 0.9\%$) with a 1 hour time, showing the presence of multiple ratchet marks and cracks at the surface and the difference in failure mode within the (a) carburised, (c) bulk fatigue and (d) overload fracture surfaces.

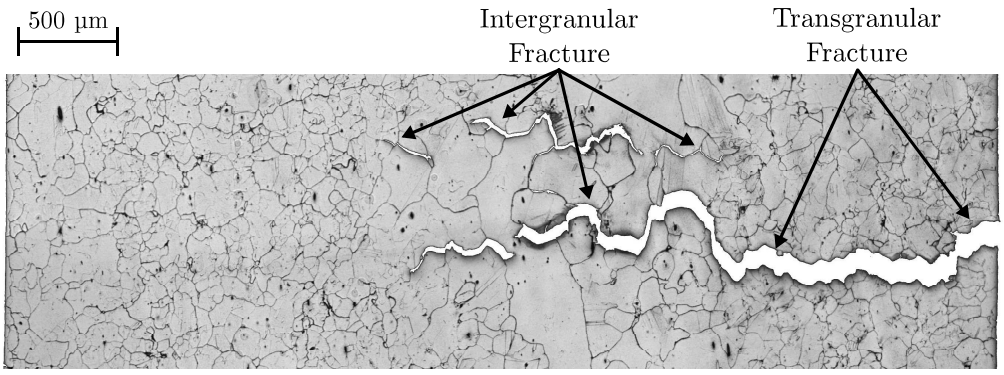


Figure 6.43: Major fatigue crack section within ASRCF1 $\Delta\varepsilon = 1.2\%$ showing mixed trans- and intergranular fracture.

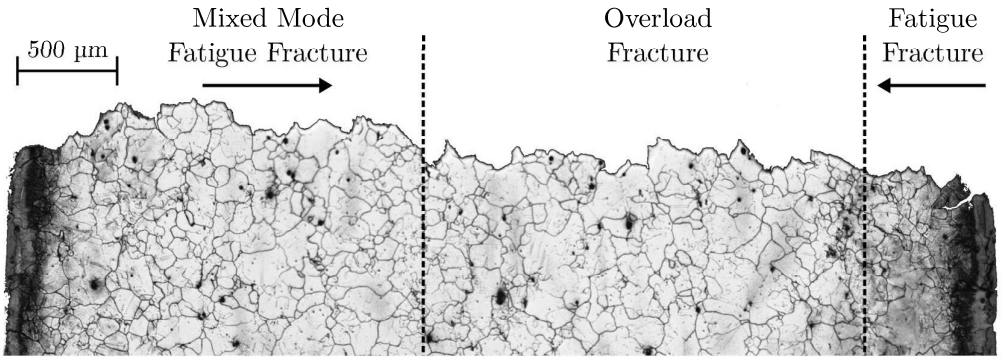


Figure 6.44: Section taken of the fracture surface of sample CCF1 $\Delta\varepsilon = 1.2\%$ showing mixed trans- and intergranular fracture across the crack front with crack initiation and growth from both sides.

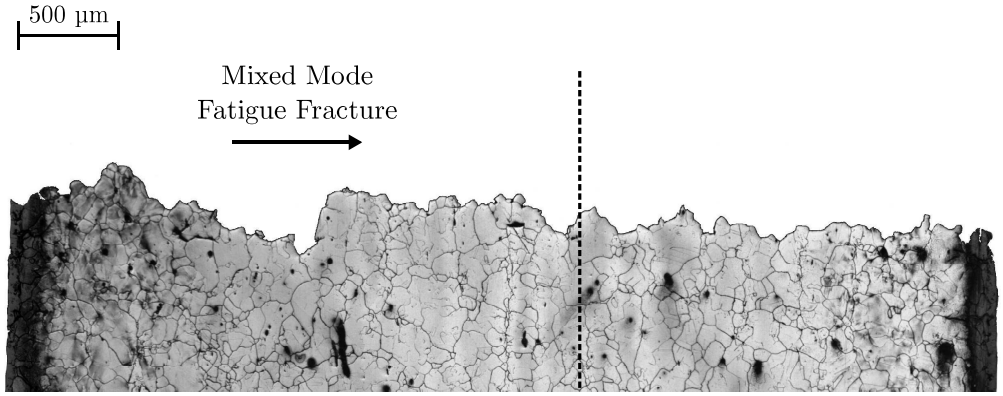


Figure 6.45: Section taken of the fracture surface of sample CCF2 $\Delta\varepsilon = 0.9\%$ showing mixed trans- and intergranular fracture.

6.4. Discussion

This study has investigated the effect of AGR carburisation on the fatigue and creep fatigue behaviour of 316H via a series of high temperature LCF tests. The remainder of this chapter discusses the results within the context of the literature and describes any possible limitations of these findings.

6.4.1. Fatigue

LCF testing was used to generate strain – life data of as-received and preconditioned materials which is seen in Figure 6.18. The impact of carburisation on fatigue endurance was found to be dependent on the applied strain. Under strain ranges of $\Delta\varepsilon = 0.9\%$ and above, preconditioned samples generally failed much quicker than their as-received counterparts. Below this, at $\Delta\varepsilon = 0.6\%$, carburised fatigue lives closely matched and in two cases even exceeded those of as-received by almost a factor of 2. In a similar manner to previous creep testing, this dependence of carburisation effect on applied strain is governed by the ductility of, and cracking within, the outer surface layer.

A comparison of as-received and preconditioned material behaviour at one of the more detrimental strain ranges ($\Delta\varepsilon = 0.9\%$) showed a clear difference in outer surface morphology. The carburised layer was found to contain widespread circumferential surface cracking that served to initiate fatigue damage at multiple locations across the sample. This was confirmed via X-Ray tomography and surface fractography which showed that a number of these cracks had propagated via fatigue crack growth with the varying striation orientation also providing evidence for multiple crack fronts. Such prevalent cracking suggests that the ductility of the carburised layer had been surpassed at the early stages of the test. This is also indicated by the reduced hardening response of preconditioned material. Premature cracking would have competed against cyclic hardening, affecting the overall increase in peak stress. The lower bound ductility of the outer surface has been estimated to fall between 0.50 - 0.78% which is reasonably close to peak strains exhibited here ($\pm$ 0.45%). The reduced ductility of the carburised layer is anticipated to result from the severe precipitation of carbides along grain boundaries which, matches observations of circumferential intergranular surface cracking across all preconditioned samples. Similar behaviour can be expected at the higher strain range of $\Delta\varepsilon = 1.2\%$.

Despite being interrupted, sample CF4, run under the lowest strain range of $\Delta\varepsilon = 0.4\%$, showed no signs of load drop or surface cracking with even the inner oxide spinel remain-

ing completely in tact. This suggests that the carburised layer retained strength during the majority of fatigue life and has a ductility of at least 0.2% total strain. The difference in fracture behaviour between samples CF1 and CF3 ($\Delta\varepsilon = 1.2\%$ and $\Delta\varepsilon = 0.6\%$ respectively) also supports this. Although both samples contained multiple initiation sites, CF1 contained a crack front that was indicative of having a circumferential high stress concentration (such as cracking of the carburised layer) from the start of test [107] whilst CF3 contained an elliptical crack shape suggesting that surface crack initiation was progressive.

The strain dependent fatigue behaviour of carburised 316H can therefore be summarised as follows. At the higher strain ranges ($\Delta\varepsilon \geq 0.6\%$), the carburised layer cracked in the early stages of testing, increasing the number of fatigue damage initiation sites. This was due to the very low ductility of the outer surface caused by the significant embrittlement of grain boundaries as a result of carbide precipitation which, is consistent with metallurgical examiantion by Younes et al. [43] and AMEC Foster-Wheeler [83]. Having multiple initiation sites encouraged crack nucleation and ultimately reduced endurance via the growth of premature fatigue cracking and damage. Similar findings have been reported on LCF testing of carburised 316H by Priddle [73]. At the lower applied strain ranges of 0.6% and below, the carburised layer was highly likely to have remained in tact for the majority of fatigue life. In some cases, this enhanced the observed fatigue strength of the bulk material by inhibiting surface crack nucleation through the generation of residual stresses [74, 108, 78, 27, 36] and a reduction in cyclic plasticity; resulting from an overall increase in yield stress.

6.4.2. Creep-Fatigue

A number of LCF tests included peak tensile dwells of 60 minutes to investigate the interaction between carburisation and creep-fatigue. Due to the limited test data, it was not possible to ascertain the overall impact of creep across a range of applied strains. However, the addition of a hold time was found to reduce the fatigue endurance of all carburised samples in comparison with continuous cycling conditions. This behaviour is demonstrated in Figure 6.26 and is expected due to the additional plasticity and damage introduced during stress relaxation [109, 110, 111]. Under a strain controlled tensile dwell, elastic strain is converted to inelastic (plastic or creep) which effectively increases the cyclic plastic strain range, inducing a higher level of damage per cycle [112]. The increase in plastic strain range can be represented by the inelastic strain energy density (ΔW) which is shown in Figure 6.28. For the same applied strain range, preconditioned creep-fatigue samples displayed higher values of ΔW compared with pure fatigue, resulting in a reduction of total endurance. The introduction of a hold time in tension was

likely to be creating additional damage within samples.

Evidence suggesting this was seen within fracture surface examination which showed creep-fatigue failure to be more intergranular in nature compared to that found under pure fatigue conditions. This coincided with section metallography that also demonstrated mixed mode trans- and intergranular crack propagation. The difference in crack morphology is likely to have resulted from the additional damage induced during relaxation in the form of cavities and eventual creep damage on grain boundaries [113]. This agrees with observations of intergranular micro cracks contained in the gauge length of as-received sample ASRCF1 which were positioned across the entire diameter and orientated perpendicular to the direction of load, suggesting internal creep damage [114]. Intergranular micro cracks were not found within preconditioned samples CCF1 or CCF2 and this can be explained by the less overall time spent under dwell conditions, limiting the extent of creep damage.

In a similar manner to pure fatigue, the high strain range ($\Delta\varepsilon \geq 0.9\%$) preconditioned samples displayed widespread surface cracking across their entire gauge length (Figure 6.39). Because all cracks were seen to penetrate through the carburised layer, it was highly likely that the cracking was initiating within the early stages of test and propagating via creep-fatigue fracture.

To compare the behaviour of as-received and preconditioned materials under both continuous cycling and creep-fatigue conditions, the stabilised inelastic strain energy density was plotted against the total number of cycles to failure for all specimens [115] to which power law fits were calculated. The reduction in endurance due to carburisation was found to be dependent on the value of stabilised strain energy, increasing at higher values of ΔW. This is represented by the diverging power law fits to as-received and preconditioned materials and stands to reason as higher strain energies are associated with larger cyclic strains that crack the carburised layer, reducing fatigue life. The opposite is true at the other end of the scale whereby carburised samples have shown endurances equal to or sometimes exceeding that of as-received.

Fatigue test data on thermally aged material is limited, making it difficult to reliably examine the effect of the additional thermal ageing induced during the preconditioning process. However, of the two tests conducted, both showed a similar endurance to as-received samples at the same strain range. Considering this alongside the similarities in observed tensile and creep properties, it highly likely that the effect of thermal ageing on fatigue life is minimal. This stands to reason as the header was already aged for a considerable amount of time prior to use within this research (100,000 hours at 500°C).

6.5. Conclusions

This chapter has investigated the effect of carburisation on the fatigue and creep-fatigue behaviour of 316H. It can be concluded that:

- The influence of carburisation on fatigue endurance is likely to be dependent on the applied total strain range and whether the carburised layer cracks in the early stages of life. The substantial reduction of surface ductility results from embrittlement of grain boundaries within the hardened layer.
- At strain ranges of 0.9% and above, widespread surface cracking initiates within the early stages of life, reducing fatigue strength through the development of premature nucleation and damage.
- At strain ranges of 0.6% and below, the carburised layer is likely to retain strength throughout life which can result in enhanced fatigue endurances due to the suppression of crack nucleation by residual compressive stresses and a reduction in cyclic plasticity due to an enhanced yield stress.
- The lower bound ductility of the carburised layer is postulated to lie between 0.2 - 0.45 % total strain which is in agreement with previous tensile testing and creep data.
- The introduction of a tensile dwell slightly increases the inelastic strain range and thus inelastic strain energy density dissipated per cycle. This causes a reduction in fatigue life and change in fracture morphology within preconditioned material.
- Additional thermal ageing introduced via preconditioning (3000 H at 600°C) has no significant impact on the fatigue behaviour of 316H.

7. Detecting Carburisation via Magnetic NDE Measurement

7.1. Introduction

Type 316H components operating in AGR gas environments are susceptible to carburisation, the degree to which is highly dependent on surface finish, metal composition, exposure temperature and gas mixture. Currently, the exact conditions that promote carburisation (within these components) are not well understood nor is there an established means to measure it's presence non-destructively. Predictions can be made based on component location, cast composition and averaged operating history, but it is difficult to reliably ascertain whether a component has carburised or not without physical removal and/or destructive testing. Due to severely limited component access and inherent radioactivity this is often problematic and time consuming. Since carburisation has been shown to affect mechanical properties, the ability to accurately identify and characterize it in plant will be of great advantage when conducting component lifetime assessment.

This chapter provides a preliminary study of the detection of carburisation using a magnetic non-destructive evaluation (NDE) method. Initial tests are conducted on both ex-service carburised and preconditioned 316H. These are then followed by a series of parametric finite element studies that explore extended magnetic NDE techniques. Finally, consideration is given to some of the potential challenges associated with applying these methods to examine carburisation in plant.

7.2. Carburisation and Induced Magnetism

AGR gas carburisation results in the diffusion of carbon into 316H and is accompanied by the formation of an exterior duplex oxide consisting of an outer magnetite layer (Fe_3O_4) followed by an underlying nickel and chromium rich spinel [43]. The diffused carbon either remains in solid solution or forms precipitates that are focused along

grain boundaries [86], leading to lattice expansion and the formation of an expanded austenite phase [25]. This alteration to the microstructure can lead to profound changes in electrical and magnetic material properties [116].

Austenitic stainless steels (such as 316H) are non-magnetic by nature as a result of their face centered cubic (FCC) crystal structure and corresponding atomic density/spacing. The size and shape of a single unit cell within a crystal lattice is known as the lattice parameter and this governs the magnetic moment that can be formed within a polycrystalline metal. Carburisation can alter this lattice parameter through interstitial carbon diffusion [117, 118] which, alongside carbide precipitation [119, 120] and an outer magnetite layer, can result in an increased level of surface magnetism (and magnetic permeability) in an otherwise non-magnetic material. Because these features (%WT C, carbide density and oxide thickness) become more pronounced as carburisation intensifies it was postulated that the severity of carburisation was related to the magnetic properties of 316H. It was thought that by measuring changes in magnetic response, the depth and severity of carburisation could be deduced non-destructively.

The non-destructive measurement of carburisation within steels has been widely investigated within the literature. NDE techniques such as eddy current testing and magnetic Barkhausen noise have been deployed to measure the change in both surface carbon content and phase [121, 122, 123, 124, 125]. These work on the principal of detecting a change in magnetic response induced by modification to the base material microstructure through the addition and/or subtraction of carbon. Of these two techniques, eddy current measurement has shown the greatest potential in characterizing carburisation within austenitic steels [117, 126, 119, 127, 128]. This chapter investigates the application of an alternative, simpler measurement method to evaluate AGR carburisation on 316H using a commercially availible magnetic measurement probe (Feritscope [129]).

7.3. Magnetic Measurement

To assess the potential of magnetic NDE in detecting AGR carburisation in plant, surface and through depth magnetic measurement was undertaken on carburised material. This was conducted using a commercially available low-frequency magnetic NDE probe, 'Feritscope'. This section provides an overview on the principal of measurement and reports the results of testing of as-received, preconditioned and ex-service carburised 316H.

7.3.1. Feritscope

The change in magnetic permeability as a result of carburisation has been measured using the Feritscope NDE inspection system. This is traditionally used to verify the ferrite content within (in terms of %WT or ferrite number (FN)) austenitic and duplex steel weldments, the presence of which can compromise weld quality by increasing the susceptibility to corrosion and reheat cracking. The system operates as a low frequency (160Hz) permeability measurement device and consists of a hand held probe connected to a calibrated data acquisition instrument. An illustration of the probe internals and Feritscope operating principle is shown in Figure 7.1.

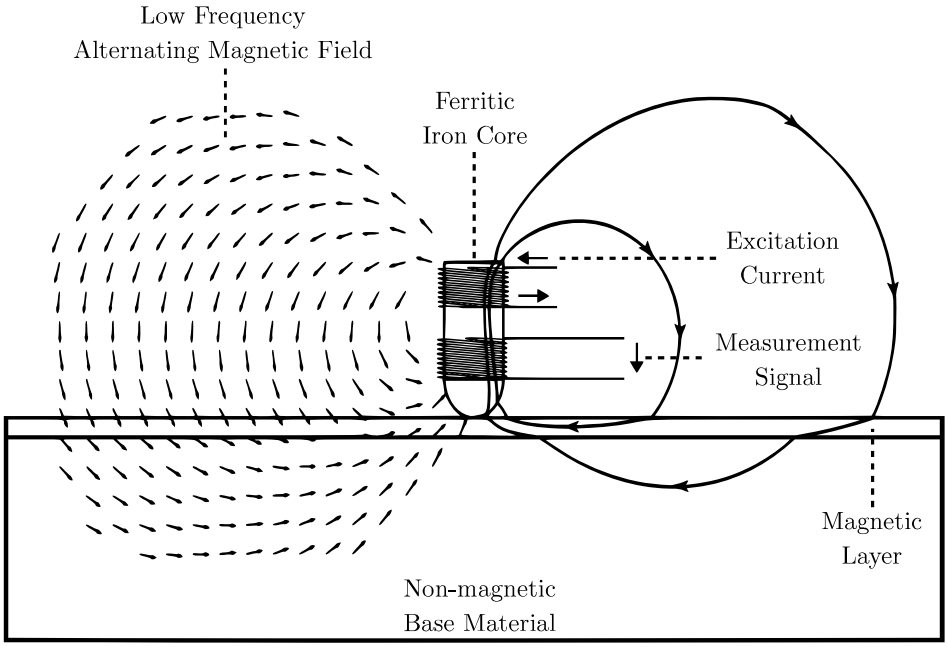


Figure 7.1: Illustration of Feritscope magnetic measurement principle.

A low frequency alternating current is injected into the upper primary coil which in turn, generates an alternating magnetic field (160 Hz). When placed onto an inspection surface, this field permeates into the sample thickness and interacts with any magnetic components. The depth of field penetration is governed by skin effects which determine the total skin depth and are a function of current excitation frequency, sample conductivity and material permeability. The influence of skin effects become negligible when testing stainless steels at a low frequency of 160Hz due to their low relative permeability. This is because the resulting skin depths are greater than sample thicknesses. Magnetic phases contained within the measured depth cause a change in the flux density of the primary magnetic field. The resulting change in inductance is measured by the secondary coil as a change in voltage which is then translated to a value of

%WT ferrite (or FN) by the calibrated instrument. The frequency of injected current is kept relatively low (160 Hz) to minimize the magnitude of any Eddy currents generated within the inspection volume. This ensures that they are too weak to perceivably influence the secondary coil voltage. As a result, the Feritscope is insensitive to any variation in electrical conductivity and only provides a measure of relative magnetic permeability.

7.3.2. Surface Measurement

A series of magnetic measurements were undertaken on various geometries of as-received, preconditioned and ex-service carburised 316H. The complete test matrix can be seen in Table 7.1 which contains the approximate in-service times and exposure temperatures of all samples.

The measurement procedure consisted of placing the probe onto a sample surface and recording the value shown on the FMP-30 instrument. The Feritscope system did not provide explicit voltage values therefore all measurements within this study have been presented as %WT ferrite or explicit ferrite number (FN). These values do not hold their physical meaning. Instead, they correspond only to the change in flux density induced by magnetic components within the material. This is directly proportional to the change in voltage.

The probe measurement volume (approximately 4 mm in diameter and 3 mm deep) was relatively small compared to the size of both the tube and plate samples. Therefore, a number of measurements were taken across the surface of each specimen which were then averaged. This was to offset any change in measured magnetism due to a variation in material microstructure. Figure 7.2 illustrates a typical inspection grid for each specimen geometry. Where applicable, the probe was placed either at the four cardinal points (0°, 90°, 180°, 270°) of each tube or across plate width, equidistant over the length. The ex-service tube specimens were extracted from various locations inside the AGR boilers and contained irregular geometric features such as flanges and mid-section weldments. Measurements taken on or in close proximity to these were deemed invalid and omitted from the data as they had potential to alter the Feritscope response from the true material value. Welds introduce additional ferrite into the austenitic matrix whilst irregular geometries can modify the true measured material volume.

Table 7.1: Magnetic surface measurement test matrix.

ID	Type	Material State	Service Time (H)	Service Temp. (°C)
A1	Tube	As-Received Sensitized	-	-
A2	Tube	As-Received Plain	≈ 100,000	550
A3	Tube	As-Received Plain	≈ 100,000	550
EXC1	Tube	Ex-Service Carb.	37,000	600
EXC2	Tube	Ex-Service Carb.	49,000	560
EXC3	Plate	Ex-Service Carb.	50,000	460
EXC4	Plate	Ex-Service Carb.	35,500	460
EXC5	Plate	Ex-Service Carb.	34,000	560
PC1	Plate	Preconditioned Carb.	≈ 100,000 + 3000	600
PC2	Plate	Preconditioned Carb.	≈ 100,000 + 3000	600

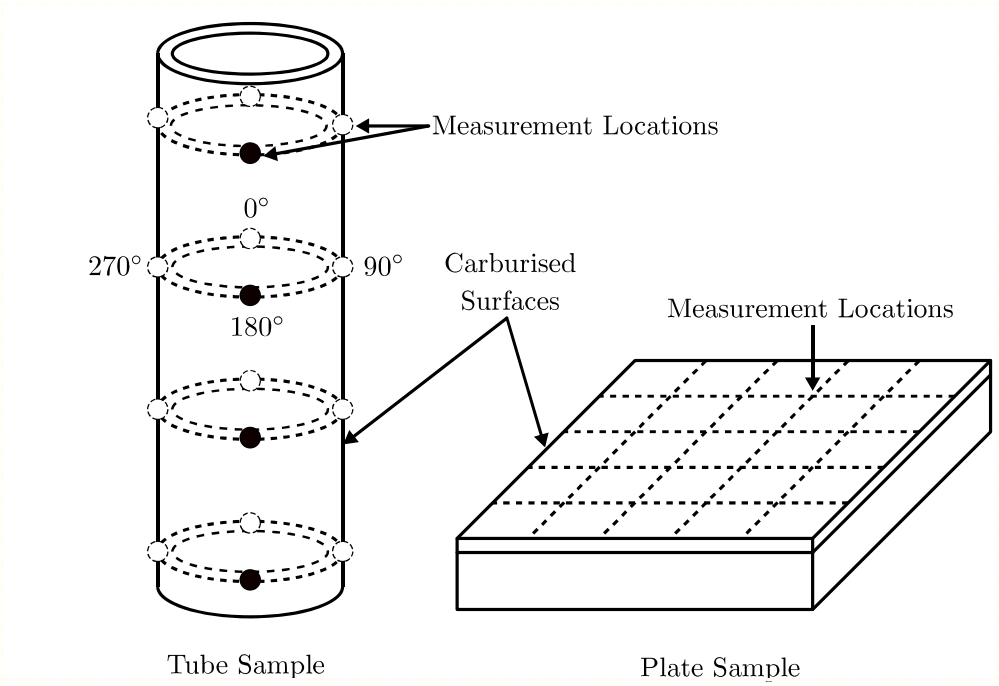


Figure 7.2: Magnetic inspection grid.

The results of magnetic surface measurement are presented in Figure 7.3 where individual location values have been overlain on top of specimen averages. All measurements were normalized according to Feritscope calibration curves. This took into account the difference between sample thickness and curvature and adjusted for location edge proximity. Carburisation was seen to have a significant impact on magnetic response of 316H with ex-service and preconditioned samples displaying significantly elevated Feritscope readings compared to those from as-received. All carburised specimens displayed a high degree of scatter across readings with the highest levels being within ex-service material.

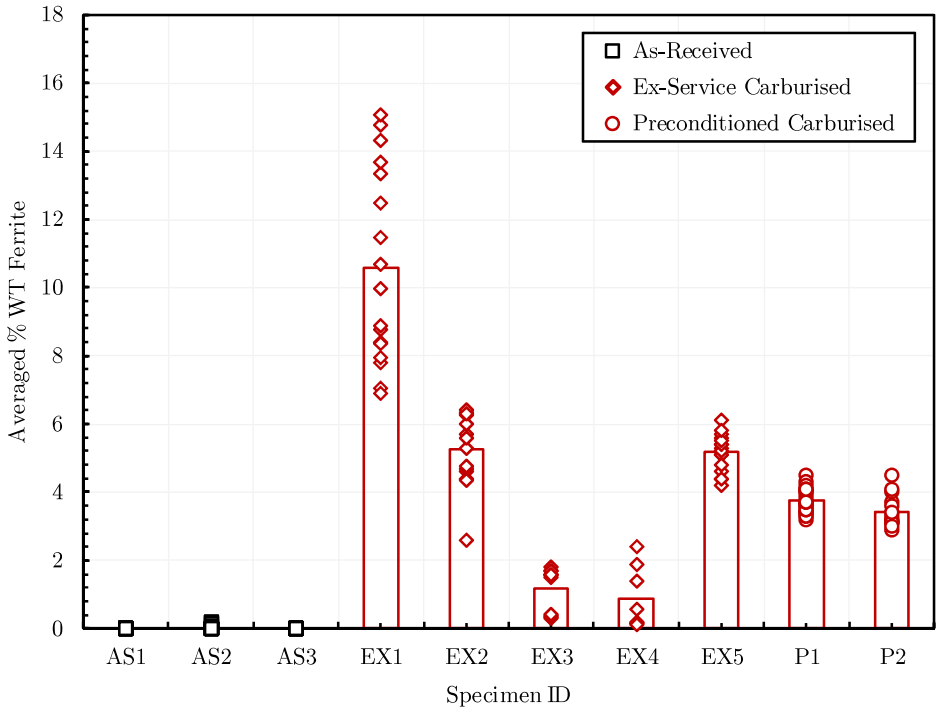


Figure 7.3: Magnetic surface measurements across as-received, ex-service carburised and preconditioned carburised 316H.

Metallographic examination was undertaken to provide an insight into the magnetic behavior of the different materials. Samples AS2, EX1, EX2 and P1 were sectioned through their depth (across the carburised layer), mounted in a conductive Bakelite resin and polished to a 1 µm finish. These were then imaged under optical microscope. The sections taken from each sample can be seen in Figure 7.4 where clear differences between oxide morphology and thicknesses were observed. The ex-service carburised samples contained the thickest outer oxide with the highest variation in depth. The as-received material not exposed to a CO_2 environment contained no oxide. Oxide thicknesses were calculated for each sample by measuring the total magnetite and spinel

depth at several locations and averaging. Figure 7.5 plots the average oxide thickness against average Feritscope value from each sample and shows a positive correlation between oxide thickness and magnetic response.

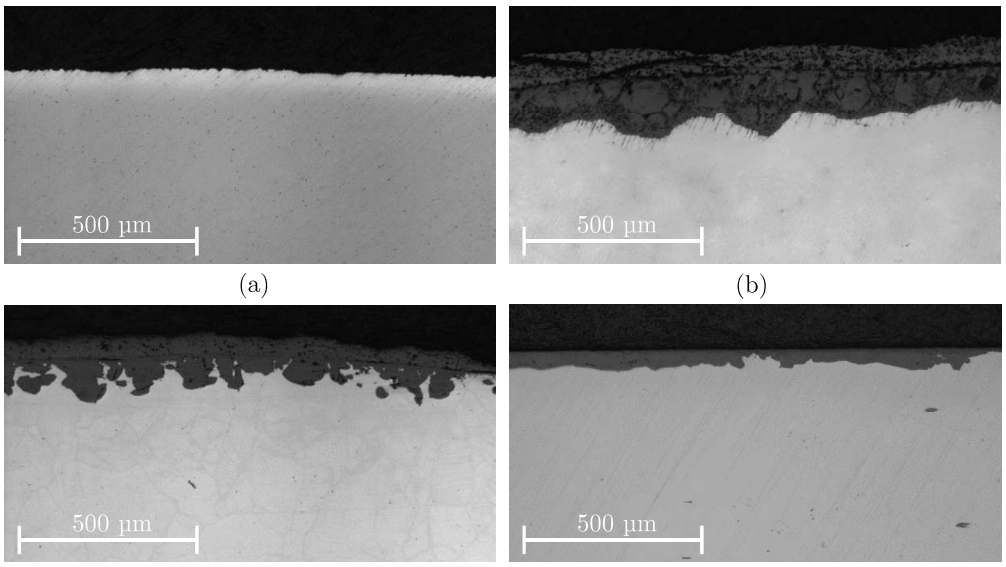


Figure 7.4: Sections taken from samples (a) AS1 (b) EX1 (c) EX2 (d) P1.

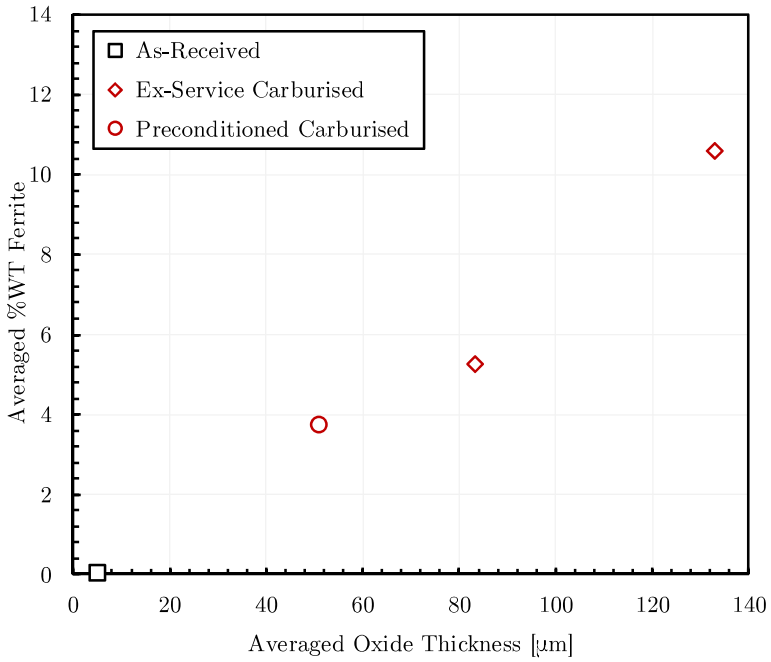


Figure 7.5: Average measured oxide thickness plotted against the averaged magnetic response from samples AS1, EX1, EX2 and P1.

7.3.3. Through Depth Measurement

Surface measurement confirmed that carburisation had a marked effect on the magnetic response of 316H. Samples containing a thicker outer oxide showed an increased level of magnetism at their surface. To investigate whether this was primarily due to the presence of a magnetite layer or underlying carburised material, a series of through depth magnetic measurements were undertaken. These aimed to evaluate the individual contribution from the oxide and carburised layers to the overall magnetic response of 316H.

For this investigation, a preconditioned plate was chosen over ex-service. Compared to ex-service carburisation, preconditioning resulted in significantly better defined and more coherent magnetite, spinel and carburised layers. This made it easier to accurately correlate magnetic response to material profile. Through thickness analysis was conducted by progressively removing a thin layer of material from the top surface of the specimen, taking Feritscope measurements at each stage. The sample was gradually ground using grade P2000 grit silicone carbide abrasive paper. This ensured that the amount of plasticity introduced was negligible and that the oxide layer was not excessively damaged. Abrasion also allowed for the controlled removal of material in micron stages. Figure 7.6 displays the resulting sample top surface at three distinct stages of testing: prior to grinding, at oxide removal and after removal of the carburised layer.

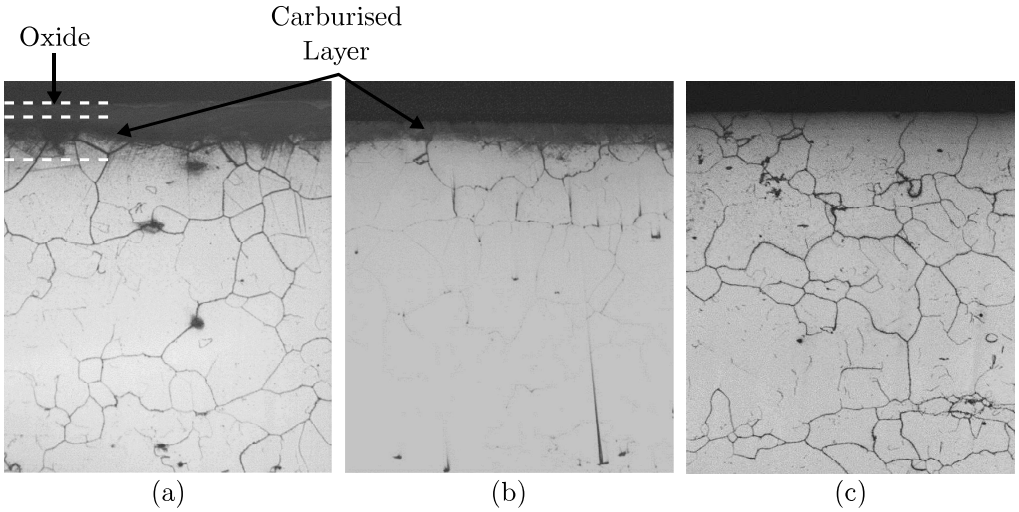


Figure 7.6: Preconditioned plate (a) prior to measurement (b) after 50 µm of oxide removal (c) after carburised layer removal.

A total of 10 measurements were taken across the sample surface at each stage of removal. These were then averaged to give a Feritscope value. The resulting through

depth magnetic profile can be seen in Figure 7.7. The outer oxide was seen to dominate the overall magnetic response of preconditioned material. Its removal resulted in a significant reduction of material magnetism; reflected by an 80% drop from peak values across the oxide layer. The remaining (smaller) decrease in magnetism to baseline values coincided with the removal of the carburised material.

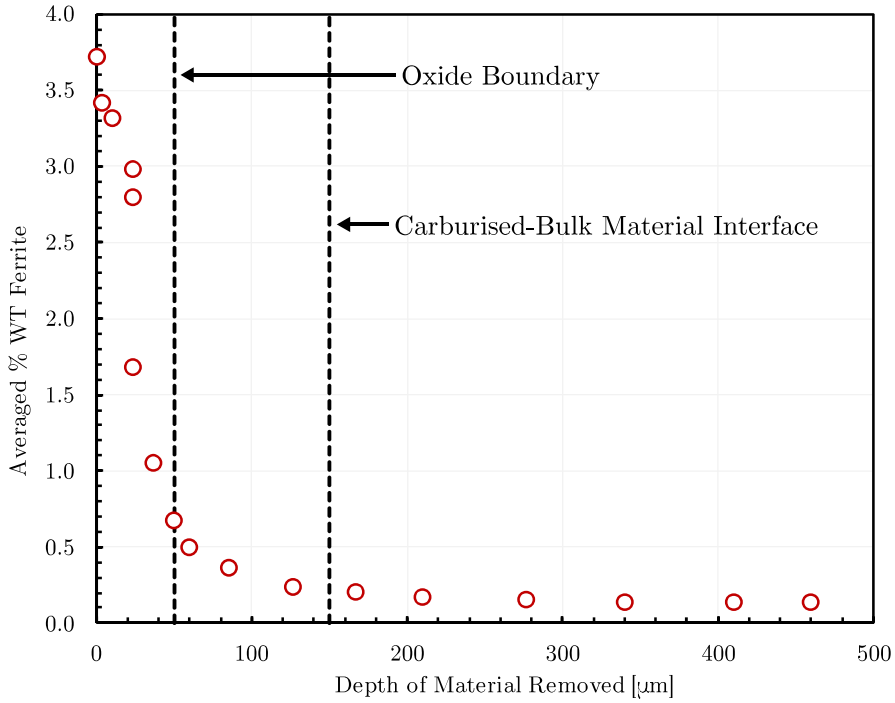


Figure 7.7: Through depth magnetic profile of preconditioned carburised material.

7.4. Multi-Frequency Finite Element Modeling

7.4.1. Introduction

Magnetic measurement confirmed that carburisation increased the level of surface magnetism within otherwise non-magnetic 316H and that the depth of outer oxide played an important role in the overall magnetic response. Despite showing a correlation between oxide thickness and averaged Feritscope measurement, the Feritscope provided little insight into evaluating the depth and severity of the underlying carburised material. It was thought that this could be achieved by modifying the frequency of excitation current. Due to skin effects this would effectively alter the measurement volume and allow for the Feritscope to scan through the depth of the specimen. Because the Fer-

itscope was locked at an operational frequency of 160Hz, this was investigated via a series of parametric finite element studies. These varied the excitation current between 160 Hz and 8 MHz. The remainder of this chapter describes the finite element model configuration, validation and outcomes of multi-frequency magnetic measurement.

7.4.2. Modeling the Feritscope

Modelling was undertaken using COMSOL Multiphysics [130] because of its capability in simulating combined magnetic and electrical alternating fields. It addition, it is also able to automatically remesh geometries, making it ideal for performing parametric studies involving a variety of frequencies and oxide/carburised layer depths. The Feritscope was modeled in a two-dimensional axisymmetric air domain and consisted of the following three components: a ferritic central core, a primary excitation coil and a secondary measurement coil. These can be seen in Figure 7.8. The primary and secondary coils were defined to be made of 0.1 mm diameter copper wire and consisted of 600 and 30 turns, respectively.

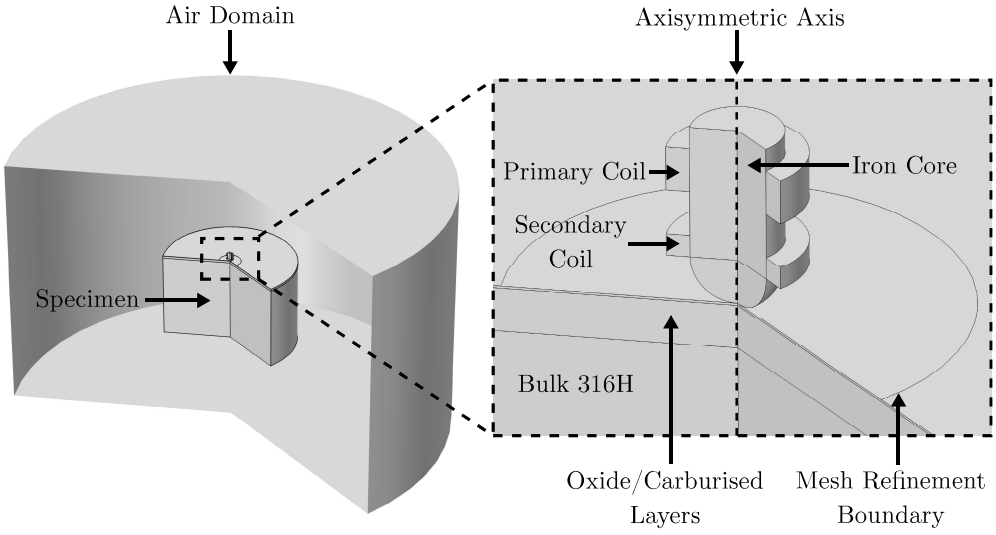


Figure 7.8: Feritscope finite element model configuration.

Samples were modeled as a cylindrical bodies containing three separate layers with each representing the outer oxide, carburised 316H and bulk material. Layer thicknesses were defined in accordance with metallographic examination of preconditioned material which contained a 50 µm outer oxide and a 250 µm carburised layer. Because carburisation is a diffusion based process, the material properties within the carburised layer were defined as a function of depth; following the hardness profile. This is seen in

Figure 7.9 where it was assumed that an increase in hardness directly correlated with an increase in magnetic permeability. Material properties within the oxide layer were isotropic.

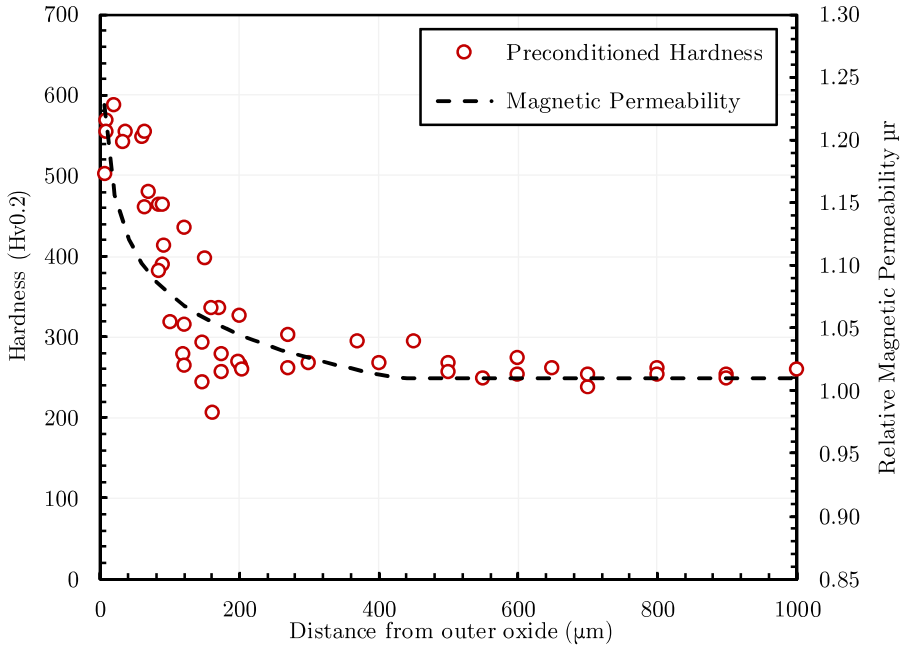


Figure 7.9: Material model of the magnetic permeability of carburised 316H based on trends observed from hardness testing.

Table 7.2: Feritscope model material properties.

Part	**Material**	μ_r **(-)**	σ **(S/m)**
Air Domain	Air	1	3.00×10^{-15}
Specimen	316H	1.0021	1.35×10^{6}
Specimen	316H Carburised	1.0021	1.25×10^{6}
Specimen	Oxide	7.16	1.00×10^{1}
Probe Core	Electrical Steel	4000	2.17×10^{6}
Probe Coils	Copper	0.9999	5.98×10^{7}

The magnetic permeability of each layer was derived from previous through depth measurement on preconditioned material. Values of %WT ferrite were converted to ferrite number (FN) which were then used alongside Equation 7.1 to calculate permeability [125]. The calculated material propertes are summarised in Table 7.2. Properties for

bulk 316H were taken from [131].

$$\mu_r = 0.001796(FN^2) + 0.2124(FN) + 1 \tag{7.1}$$

7.4.3. Mesh Configuration and Sensitivity Analysis

When attempting a multi-frequency electromagnetic analysis, it is important to ensure that the model can accurately capture skin depths over a range of given frequencies. This relies upon the set mesh geometry where it is recommended that the skin depth spans over at least three elements. This was achieved by creating an automatic bias mesh algorithm that varied element size in close proximity to specimen near surface regions as a function of input frequency and calculated skin depth. An example of this refinement near the probe tip can be seen in Figure 7.10. The entire mesh was composed of axisymmetric triangular elements.

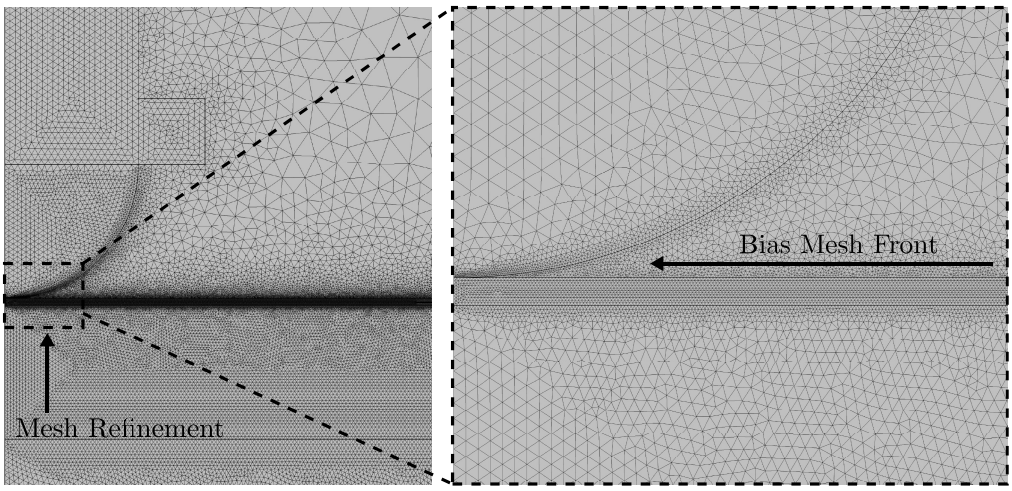


Figure 7.10: Feritscope model mesh configuration.

A parametric sensitivity study was conducted to verify the accuracy of the mesh over the range of frequencies to be tested. This involved gradually reducing element sizes over a fixed model until the resolved secondary coil voltage stabilized. Element size was controlled via a global scaling factor that allowed for the scaling of a bias mesh over each individual part. Mesh accuracy was determined by plotting the normalized magnitude of the secondary coil voltage against the total number of degrees of freedom. The results are presented in Figure 7.11. The magnitude of secondary coil voltage was normalized against a baseline value for that obtained from an extremely coarse mesh. This removed the natural effect of increasing frequency on voltage and allowed for a direct comparison of mesh performance. Across all frequencies, mesh conversion occurred at approximately

400,000 degrees of freedom (which constituted to 160,000 elements) with any successive decrease in element size having a minimal impact on the resolved voltage value. This mesh provided a good balance between accuracy and computational time and has been used in all models presented from this point forward.

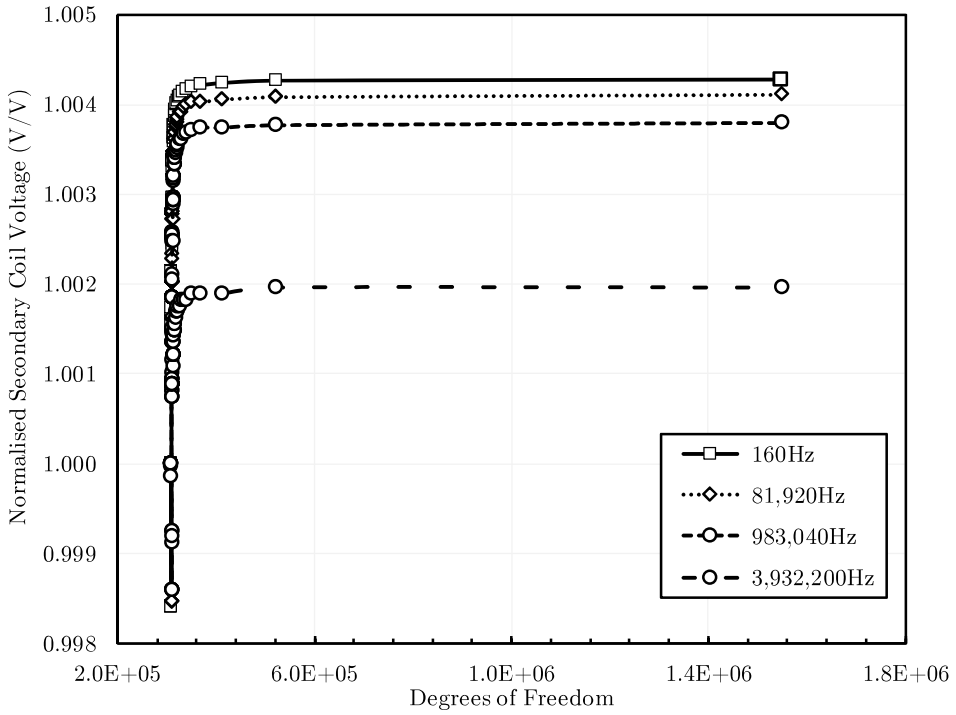


Figure 7.11: Feritscope model mesh sensitivity study.

7.4.4. Model Validation

A validation exercise was performed to assess the accuracy of calculated material properties. This involved simulating the through depth magnetic measurement undertaken in Section 7.3.3. To replicate the progressive removal of outer surface layers, a parametric study was setup to delete surface partitions at 10 µm intervals. After each layer was cut out, the entire model was remeshed ensuring that the probe tip was kept in continuous contact with the sample surface. The excitation current was set to the nominal Feritscope frequency of 160 Hz. Since COMSOL could only output secondary coil voltage, normalised Feritscope calibration curves were used to convert a change in voltage to % WT Ferrite [132]. This enabled a direct comparison to be made between finite element and experimental data which is shown in Figure 7.12. The model was found to be in very good agreement with the experimental data. The significant decrease in magnetism due to oxide removal and subsequent reduction through the carburised layer were both

captured. This provided confidence in the derived material properties and simplified material models. Peak and baseline Feritscope values were slightly under predicted by the model. The likely sources of this discrepancy lie within the calibration curves and material assumptions and are discussed in Section 7.5.

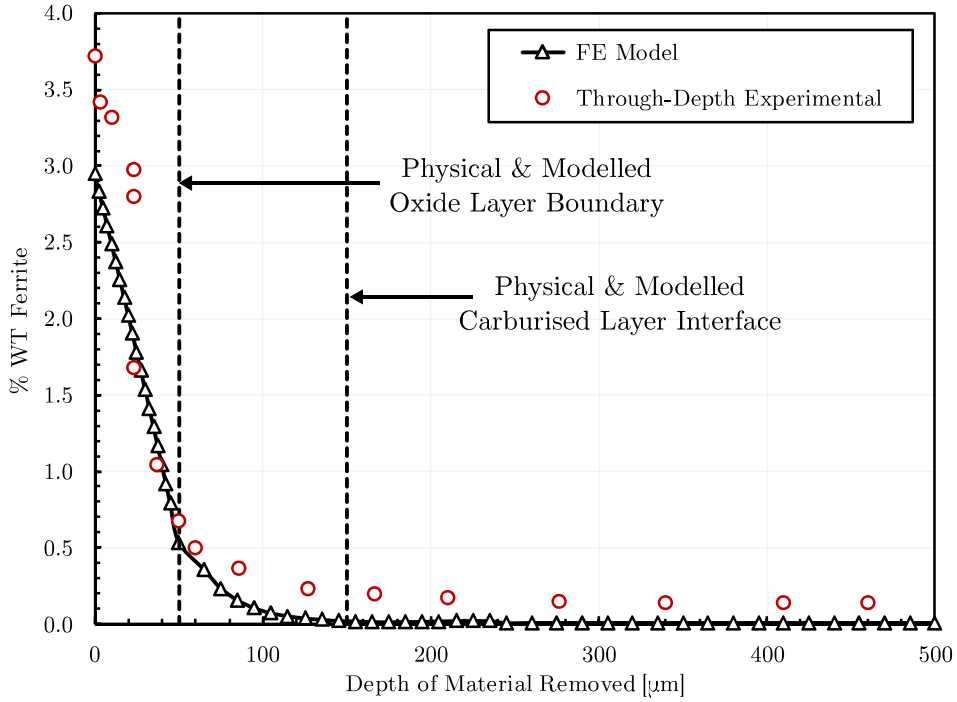


Figure 7.12: A comparison of experimentally measured and modelled through depth magnetic profiles for preconditioned carburised 316H.

7.4.5. Multi-Frequency Feritscope

A series of parametric finite element studies were undertaken to investigate the potential of multi-frequency magnetic measurement in evaluating the depth of carburisation. By progressively increasing the frequency of excitation current, a through depth magnetic profile could be created for each sample from which, the depth of carburisation could then be predicted. This relied upon modification of the Feritscope measurement volume which was governed by the formation of skin effects within near surface regions.

At a baseline frequency of 160 Hz, the Feritscope measurement depth is much greater than that of the carburised layer. As the frequency is increased, the measured volume reduces which leads to a gain in normalized secondary coil voltage. This is because the magnetic carburised layer is taking up an increasingly higher proportion of the measured

volume compared with the non-magnetic bulk material. At a certain frequency, the measurement depth would be exceeded by the depth of carburisation resulting in a saturation of measurement signal. Any further increase in frequency would not cause an increase in normalized secondary coil voltage as the entire measurement volume would be contained within the carburised layer. The minimum frequency at which signal saturation occured could then be used to calculate the depth of the carburised layer using Equation 7.2. Here, δ_s is the skin depth, f the excitation frequency, μ_0 the permeability of free space, μ_r the relative permeability and σ the conductivity of the material.

$$\delta_s = \sqrt{\frac{1}{\pi f \mu_0 \mu_r \sigma}} \tag{7.2}$$

Two parametric studies were created to assess the prediction of oxide and carburised layer depth using multi-frequency magnetic measurement. Each model progressively increased the thickness of it's respective layer (oxide or carburised) in 5 µm stages. After each iteration, the geometry was remeshed and the secondary coil voltage was evaluated over a range of frequencies (160 Hz - 8 MHz). The effect of increasing carburised or oxide layer depth on Feritscope voltages over a range of operational frequencies can be seen in Figures 7.13 and 7.14. The data has been presented in terms of normalized secondary coil voltage to enable a direct comparison to be made between different frequencies.

For frequencies of 81,900 Hz and above, an increase in the depth of carburisation eventually led to saturation of the secondary coil voltage with higher frequencies requiring smaller saturation depths. Such behavior was not observed in the case of a growing oxide layer. The normalized voltages continually increased with higher frequencies displaying a greater sensitivity to oxide thickness.

By isolating these results for set carburised layer depths, the effect of increasing frequency on the magnitude of secondary coil voltage can be seen more clearly. This effectively represents a multi-frequency magnetic scan being conducted on a carburised specimen and is shown in Figure 7.15. Voltage values at each frequency have been normalized against that corresponding to no carburised layer. Signal saturation is represented by a drop in peak voltage. By taking the frequency corresponding to the first voltage drop after peak, the depth of carburisation could be calculated. This frequency was used in conjunction with previously derived material properties (Table 7.2) and Equation 7.2 to predict the thickness of the set carburised layer depth. A comparison between actual and predicted depths can be seen in Figure 7.16 with a good agreement seen above 150 µm.

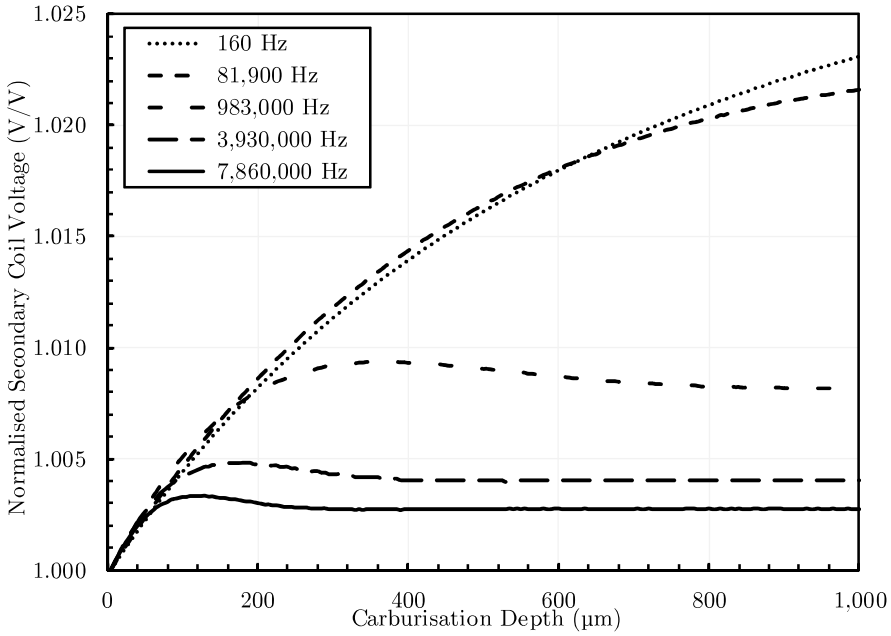


Figure 7.13: Comparison of the effect of increasing carburisation depth on different Feritscope measurement frequencies.

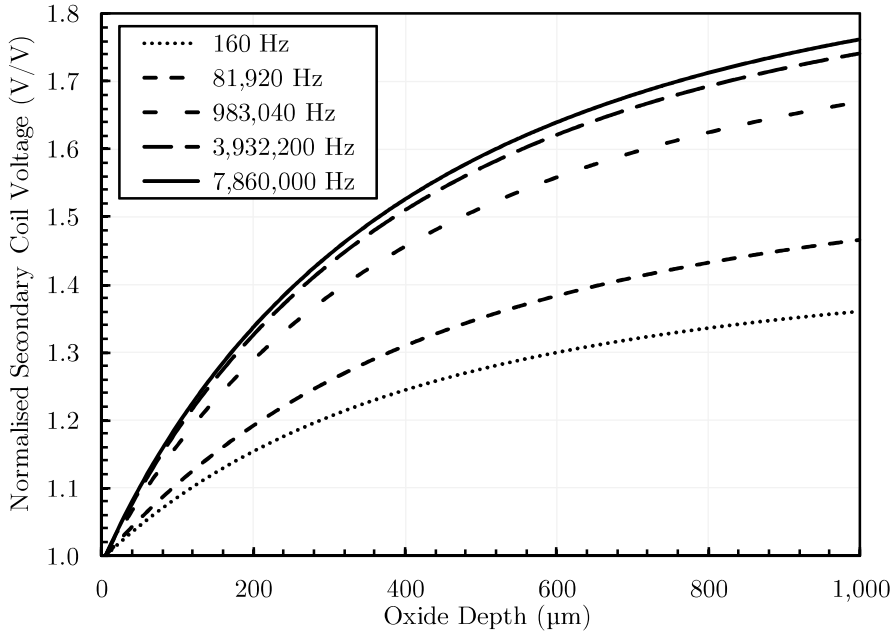


Figure 7.14: Comparison of the effect of increasing oxide depth on different Feritscope measurement frequencies.

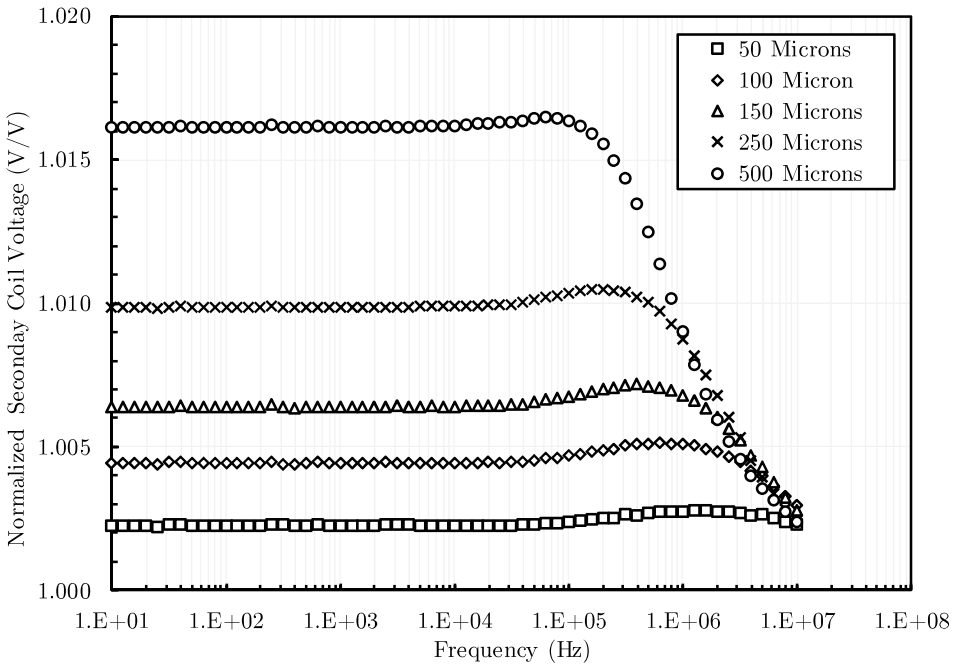


Figure 7.15: Effect of increasing excitation frequency on the Feritscope response to samples with different depths of carburisation.

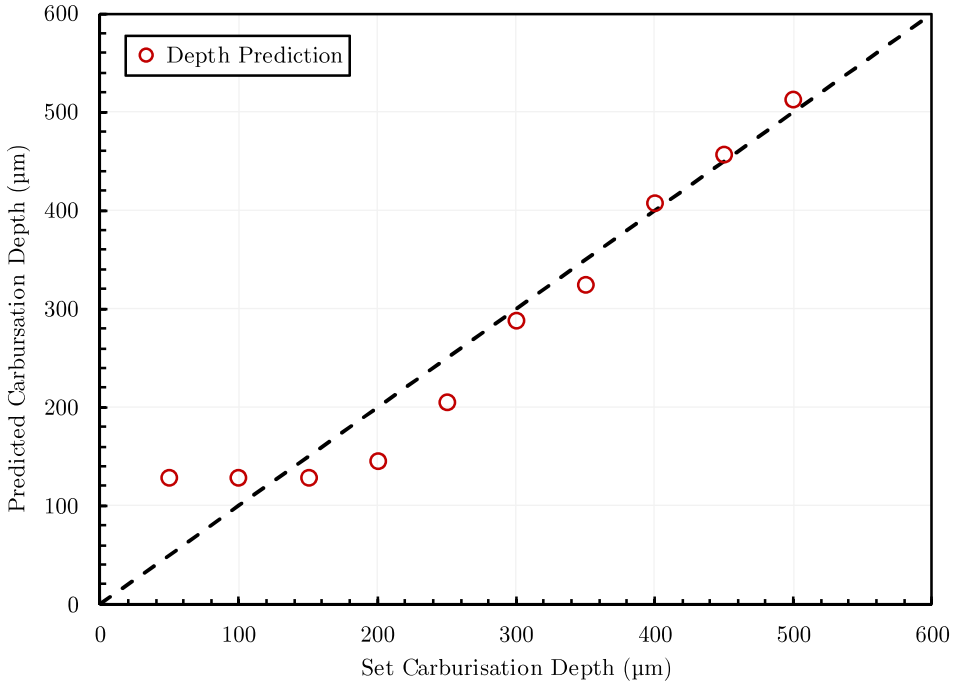


Figure 7.16: Set versus predicted carburised layer depths from multi-frequency magnetic measurement.

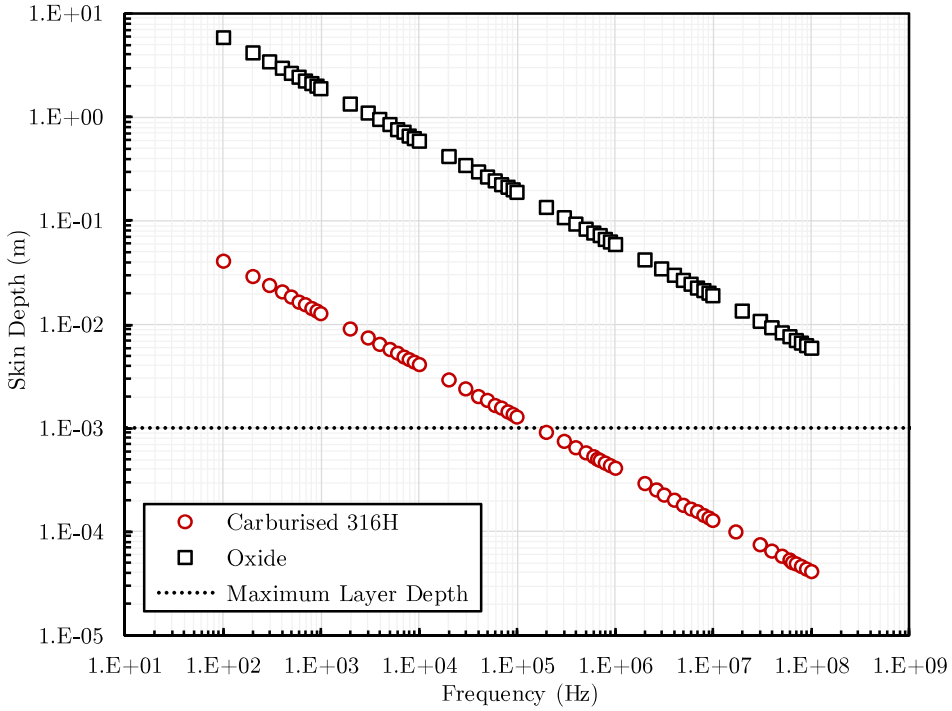


Figure 7.17: The effect of frequency on skin depth for modelled carburised and oxide layers.

7.5. Discussion

This chapter has investigated the potential of a magnetic NDE technique in detecting AGR gas carburisation. The following section presents a discussion of results and considers the implications of these findings to in-situ plant component assessment.

7.5.1. Magnetic Measurement

Magnetic measurement has shown that carburisation generally leads to an increase in the level of surface magnetism within 316H. This increase results from microstructural changes that have been observed during the carburisation process, namely, phase transformation (lattice expansion), carbide precipitation within grain boundaries and the deposition of a thick outer duplex oxide that includes magnetite. Such features have all been found to cause a certain degree of ferromagnetism within austenitic stainless steels in the literature [117, 118, 119, 120]. Subsequent metallography established that

the magnetic response of carburised samples was strongly related to the depth of outer oxide, Figure 7.14. This stands to reason as a thicker outer oxide is synonymous with a larger magnetite layer and higher level of carburisation [43]. This also leads to a larger volume fraction of carbides at the surface which, has been found to correlate with a higher increase in surface magnetic permeability [126].

The significant scatter observed in magnetic measurement across all carburised samples can be attributed to the irregular nature of carburisation and resulting variation in oxide layer depth. This is explained by through depth measurement which revealed that the outer oxide had a significantly higher contribution to the overall magnetic response compared to the underlying carburised layer. Ex-service carburised material displayed a higher variability in oxide thickness compared to preconditioned and subsequently, a larger scatter in magnetic readings. This is to be expected as unlike the strictly controlled preconditioning process, carburisation in plant is likely to promote irregular oxidation due to varying temperatures, pressures, surface finishes and stress gradients across components all affecting the formation and adhesion of the magnetite and underlying spinel.

7.5.2. Multi-Frequency Feritscope

A finite element model has been created to investigate the potential of a multi-frequency magnetic measurement approach. Validation of this model was conducted against through depth measurement and despite differences between peak and baseline values, it appeared to be in very good agreement with experimental data. This provided confidence in the representation of the Feritscope within the model and the derived material properties.

The differences between finite element and experimental Feritscope values are due to assumptions made within the material model and limitations within the voltage calibration curve data. The permeability of each material layer (oxide, carburised and bulk 316H) was calculated from previous through depth measurement on preconditioned material. When interpreting this data, it was not possible to delineate Feritscope values for the oxide layer in isolation. Therefore, a certain degree of approximation was required when identifying the overall contribution of the oxide to a particular Feritscope value which, relied upon metallographic examination and an assumed depth of oxide. In addition, to enable a direct comparison to be made between finite element and experimental data, it was necessary to convert the change in normalized secondary coil voltage (from the model) into an explicit value of %WT ferrite. This was conducted using standard Feritscope calibration curves that required interpolation betweens lines of best fit to

previous experimental data [132] and was likely to introduce additional error within the validation study.

Parametric studies were undertaken to examine the potential of using a multi-frequency magnetic approach in predicting the depth of the carburised and/or oxide layers. It was found that the depth of carburisation above 150 µm could be evaluated by taking magnetic measurements over a range of frequencies (160 Hz - 8 MHz) and examining the resulting through depth magnetic profile. At the higher frequencies of approximately 1 MHz and above, signal saturation occurred leading to a drop in the normalized secondary coil voltage. This was due to the measured skin depth (therefore measurement volume) becoming less than the depth of carburisation. The frequency at which this occurred was then used to calculate the total depth of carburisation. Prediction was not possible below 150 µm. This was because the frequency required to produce a skin depth smaller than this was not modeled and is primarily due to the relatively low magnetic permeability of the carburised layer. The relationship between skin depth and frequency for each layer can be seen in Figure 7.17.

It was not possible to predict the depth of the oxide layer as signal saturation did not occur at any given frequency, Figure 7.14. This was due to its low conductivity and resultant large skin depths which can be seen in Figure 7.17 where the value of skin depth is always greater than the maximum thickness of oxide modeled. Despite having a higher magnetic permeability, the skin depths produced were orders of magnitude larger than that of the carburised layer as permeability and conductivity play an equal role in determining skin depth (Equation 7.2). Any increase in oxide thickness across all frequencies therefore caused a proportional increase in measurement signal. This was because the magnetic oxide was taking up an increasingly larger proportion of the measured volume compared to the non-magnetic bulk material.

7.5.3. Application to Plant Components

These findings suggest that the Feritscope presents a viable solution in non-destructively detecting the presence of carburisation within 316H. However, application of this technique to plant components in-situ is likely to invite significant challenges due to uncertainty within the nature of carburised material.

It has been shown that the outer duplex oxide plays a significant role in determining the overall magnetic response of carburised 316H. This is due to the presence of a magnetite layer which can overshadow any changes in magnetism due to carburisation alone. In plant, it could well be the case that a component registers a large increase in magnetic response without containing severe underlying carburisation. This would not be unusual

for austenitic components operating in AGR environments whereby initial duplex oxide formation can be followed by the growth of a inner healing layer; limiting carbon diffusion [55, 44]. Simply opting to assume that the depth of oxide and therefore magnetic response is directly proportional to the depth of carburisation may lead to extremely over conservative estimates of carburisation depth.

Furthermore, to reliably evaluate the depth of carburisation using a multi-frequency approach, accurate knowledge of both oxide and carburised layer material properties is required. These are not only difficult to ascertain in plant but are also highly likely to vary with the depth and severity of carburisation and are therefore not consistent from component to component. A multi-frequency approach in practise is likely to produce significantly different results compared with the modelled idealised case in this investigation. The Feritscope therefore presents a simple, effective NDE method to detect changes in magnetic properties within plant components that alongside historical component data, can be used to determine the presence of carburisation.

7.6. Conclusions

- AGR gas carburisation alters the magnetic properties of 316H stainless steel which can be detected using a low-frequency magnetic NDE probe: Feritscope. This is due to a combination of microstructural changes and deposition of a duplex surface oxide containing magnetite.
- The change in magnetic response, measured as %WT Ferrite, is proportional to the depth and severity of both oxidation and carburisation with the thickness of outer magnetite dominating overall material behavior.
- Finite element modeling has shown that by simply measuring the magnitude of secondary coil voltage only, multi-frequency magnetic measurement using the Feritscope has the potential to evaluate the thickness of the carburised layer but may struggle in evaluating the depth of oxide. This is primarily due to low oxide conductivity promoting large skin depths and thus measurement volumes larger than the total depth of oxide.
- By examining the reduction from peak measurement signal values, the depth of carburisation can be accurately predicted above 150 µm using this magnetic NDE method.
- Application of this magnetic NDE technique to characterize carburisation in plant is likely to present many challenges due to the high variability and uncertainty of oxidation and carburisation across components.

8. Thesis Review and Future Work

In this thesis, considerable progress has been made in understanding the impact of AGR gas carburisation on the mechanical properties of type 316H stainless steel. A particular focus has been placed on it's behaviour under both creep and fatigue degradation conditions. Within each chapter, a detailed discussion of results has been provided alongside the main conclusions drawn. In this final chapter, a review of the entire thesis is presented together with a discussion focused on the potential impact of this work on component lifetime assessment followed by recommendations for future research.

8.1. Thesis Review

Chapters 2 & 3 introduce key theoretical concepts relevant to this research and provide a background into the nature of AGR gas carburisation. Historic analysis of plant data led to the hypothesis that some 316H components experience premature damage and shortened lifetimes when exposed to CO_2 gas coolant. Further examination confirmed that this was due to carburisation which had not previously been considered as a potential degradation mechanism. For EDF Energy, gaining an understanding of how carburisation affects mechanical properties (under creep and fatigue conditions in particular) is essential, as it underpins the ability for them to conduct accurate component lifetime assessment. This is vital when attempting to substantiate a nuclear safety case and therefore, plays a crucial role in ensuring continued plant operation; setting out the primary motivation for the work conducted within this EngD.

A detailed review of the literature has been undertaken that describes the mechanism of carburisation and subsequent effects on the mechanical properties of stainless steels. This was provided in the context of both industrial gas preconditioning and environmental plant corrosion. Although both types of carburisation result in the formation of an outer hardened case, their individual impact on material properties differs greatly. This is largely due to a variation in carbide precipitate morphology, the density of which, is a function of the gas mixture and exposure temperature. The presence of carbides

compromises on the ductility and corrosion resistance of steels through chromium depletion and embrittlement of grain boundaries at the surface and is therefore intentionally suppressed during industrial gas preconditioning. Coarse carbide precipitation has been found to adversely affect the tensile, creep and fatigue performance of steels as a result of premature damage initiation due to widespread surface cracking of the low ductility surface.

The preliminary examination of ex-service plant material revealed that AGR carburisation resulted in significant grain boundary carbide decoration which, coincided with observations of surface cracking on some components. For these reasons, it was initially postulated that AGR carburisation would lead to a degradation of mechanical properties in 316H.

This was investigated through a series of high temperature tensile, creep and fatigue laboratory tests. Since it was not possible to use ex-service material, all samples were first extracted from an as-received header and subsequently preconditioned within an accelerated AGR gas environment. Complete details of this process are presented in Chapter 4. Here, the carburisation mechanism was accelerated through optimization of surface finish and AGR gas composition, to obtain samples within a practical time-scale for this research. To ensure meaningful results, it was important that the preconditioned specimens accurately represented ex-service carburised 316H found in plant. A comparison of the two materials showed similarities between oxide thickness's, carbide morphologies, outer surface hardness values and through depth carbon profiles. The preconditioning process was therefore an effective method in rapidly inducing a level of carburisation comparable to that of ex-service material within a much shorter time-scale. To rule out the potential effect of any additional thermal ageing induced during the preconditioning process, a number of samples were heated under the same temperature and for the same duration as preconditioning (3kh @ 600°C).

Chapter 5 presents the results of tensile and creep testing undertaken on as-received, preconditioned and thermally aged materials. Under monotonic loading, it was found that carburisation increased the yield strength of 316H whilst decreasing total ductility. This resulted from the addition of an outer hardened case layer that exhibited widespread surface cracking at relatively low strains which was due to grain boundary embrittlement; a consequence of severe intergranular carbide precipitation during the preconditioning process.

Interrupted and rupture testing showed that the effect of carburisation on creep behaviour is dependent on the initial state of stress. This is driven by the initiation of surface cracking within the carburised layer and is therefore governed by it's ductility. Under stresses that induce total loading strains greater than approximately 0.5%

($\sigma_c \geq 260$ MPa), the ductility of the carburised layer is surpassed and cracks upon loading. This results in a higher effective creep stress in the remaining material and surface creep crack propagation, decreasing rupture life. It was found that loading strains at the lower stresses ($\sigma_c = 220$ MPa) do not cause the carburised layer to immediately crack and the resulting creep life is equivalent to or sometimes exceeds that of as-received material. This potential enhancement of creep properties was postulated to result from an increase in yield stress and the subsequent reduction of secondary strain rates.

Chapter 6 investigates the interaction between carburisation and fatigue. In a similar manner to creep, the influence of carburisation was found to be dependent on the applied strain range and was reliant upon the initiation of surface cracking. At the higher strains ($\Delta\varepsilon \geq 0.9\%$), the ductility of the carburised layer was exceeded at peak values, resulting in premature crack nucleation that severely reduced endurance via widespread surface fatigue crack growth. Such damage was not observed at lower strains ($\Delta\varepsilon \leq 0.6\%$) whereby the total endurance of carburised samples often exceeded that of as-received. This enhancement of fatigue strength likely resulted from the generation of high compressive residual stresses within the outer surface and a significant reduction in cyclic plasticity, suppressing the onset of fatigue crack initiation. The introduction of a hold time was shown to result in a reduction of fatigue strength for all materials due to the additional plasticity induced during stress relaxation.

It can be concluded that surface cracking dominates the overall effect of carburisation on the mechanical properties of 316H. This stems from severe carbide precipitation which leads to embrittlement of the outer carburised layer and a subsequent degradation in surface ductility. From creep and fatigue testing, the initiation of cracking hence lower bound ductility of the carburised layer is estimated to lie between 0.2% - 0.45% total strain.

Additional thermal ageing (3kh @ 600°C) introduced during the preconditioning process was not seen to have any profound effect on the tensile, creep or fatigue properties of as-received 316H. This was unsurprising given the length of thermal exposure that the header material had received in service (100kh at approximately 500°C) prior to use within this research.

The significant advantage of being able to detect component carburisation to lifetime assessment was highlighted in Chapter 7. Here, the potential of a magnetic NDE technique in characterizing carburisation in-situ was explored through both laboratory and finite element analysis. It was found that carburisation resulted in an increased level of surface magnetism which, could be detected using a low frequency magnetic measurement probe. This was due to a combination of micro-structural changes that occur

during the carburisation process. Namely, interstitial carbon diffusion, carbide precipitation and the deposition of an outer duplex oxide. A swept frequency measurement approach was then investigated through finite element modelling which showed that the depth of carburisation could be successfully predicted above 150 µm. Application of this technique to plant components was however concluded to invite significant challenges. This is due to the large uncertainty in the material properties of carburised 316H and the inherent high variability of oxide depth across both carburised and uncarburised materials.

Overall, the work of this thesis has significantly contributed to increasing the understanding of how AGR gas carburisation can affect the mechanical properties of type 316H stainless steel under high temperature creep and fatigue conditions. This had not been previously explored and is crucial in ensuring that EDF Energy can predict the lifetime of carburised AGR components with confidence.

The data generated from both experimental testing and metallurgical examination in this work have been used alongside output from the entire ENVISINC project in EDF Energy design reports [21]. These are preliminary reports aimed at offering guidance to design engineers on how to treat the presence of carburisation in plant from a component lifetime perspective. Here, the substantial reduction in both tensile and creep ductility of the carburised layer are of up-most importance in determining the potential for creep-fatigue damage and crack initiation. Values for these properties have been derived from the combined partner test data and metallurgical examination contained in Chapters 5 & 6 and are markedly lower than that for as-received material. The overall findings from the ENVISINC project have resulted in initial proposed changes to current R5 Volume 2/3 assessment procedures that are justified based on the observed change in mechanical properties and damage propagation within the carburised layer and the potential impact on the overall structural response of components under both/combined creep and fatigue conditions.

8.2. Recommendations for Future Work

The work of this thesis aimed to form an understanding of how AGR gas carburisation affects the mechanical properties of type 316H stainless steel under creep and fatigue conditions. Whilst it has been demonstrated that carburisation generally results in a degradation of mechanical properties, many opportunities for extending the scope of this research remain, especially in reinforcing conclusions applicable to component lifetime assessment.

The influence of carburisation on both the creep and fatigue behaviour of 316H has been shown to be dependent on the applied loading conditions. This results from the low ductility of the carburised layer which when cracked, adversely affects material performance. Due to time constraints within this project, the majority of creep and fatigue tests were undertaken at exaggerated stresses and strains that exceeded this ductility, resulting in almost instantaneous surface cracking and a degradation of sample life. A limited number of tests conducted at lower stresses and strains indicated that carburised material could possess enhanced creep and fatigue properties. These conditions are more representative of typical plant operation where significant material plasticity does not occur (maximum stresses around 50 MPa). Hence, a series of long term creep ($\leq$ 100 MPa) and fatigue ($\Delta\varepsilon \leq 0.6\%$) tests should be undertaken to increase confidence in understanding the low stress behaviour of carburised 316H.

The preconditioning process was necessary as it was not possible nor practical to test ex-service plant material due to it's limited availability and radioactive state. Although a comparison of both materials showed similar hardness and carbon profiles, there appeared to be slight differences in the overall carbide morphology. Ex-service material, aged for a longer period of time, had larger, more developed precipitates at grain boundaries. An increase in precipitate density can further reduce grain boundary strengths, potentially resulting in a lower ductility than that observed within the preconditioned material. Mechanical testing of ex-service samples should therefore be undertaken to investigate this and validate the preconditioning process.

The ductility assigned to the carburised layer plays a pivotal role when assessing the potential remaining lifetime of a component using R5 procedures [42, 87]. Testing has shown that the lower bound tensile and creep ductility of preconditioned carburised 316H lies anywhere between 0.2%-0.45% and 0.13% - 0.35% respectively. A more accurate determination of this ductility would be highly advantageous to component assessment and allow for less conservative design. This could be determined through a series of tensile and creep tests that utilize crack detection techniques such as digital image correlation (DIC) and high frequency alternating current potential drop (ACPD) monitoring. The results from a series of preliminary DIC four-point bend tests are shown in Appendix B. Cracking was first observed at 0.65% bending strain and this demonstrates the potential of the DIC technique in detecting crack initiation. It is thought that through improvement of the specimen preparation process, the sensitivity to cracking could be increased.

The testing of samples conducted in this thesis took place within a high temperature, atmospheric pressure, air environment. Many AGR components however, operate under high pressure coolant gas for their entire lifetime, making them susceptible to continu-

ous environmental attack. This is likely to affect the fracture behaviour of carburised material, especially under creep and fatigue conditions. The influence of the environment on crack nucleation and propagation behaviour is well documented and usually results in an acceleration of crack growth rates. Therefore, environmental creep and fatigue tests should be undertaken to examine the behaviour of carburised 316H under these conditions.

Bibliography

[1] "Innovate UK funded projects since 2004: ENVISINC - Project Number 101435," tech. rep., Innovate UK, 2017.

[2] N. E. Dowling, *Mechanical Behaviour Of Materials - Engineering Methods For Deformation, Fracture, And Fatigue.* Pearson Education, 1999.

[3] W. Ramberg and W. R. Osgood, "Description of Stress Strain Curves by Three Parameters," tech. rep., National Advisory Committee for Aeronautics, 1943.

[4] A. A. Griffith, "The Phenomena of Rupture and Flow in Solids," *Philosophical Transactions of the Royal Society A: Mathematical, Physical and Engineering Sciences*, vol. 221, no. 582-593, pp. 163–198, 1921.

[5] G. R. Irwin, "Analysis of stresses and strains near the end of a crack traversing a plate," *Journal of Applied Mechanics*, vol. 24, pp. 361–364, 1957.

[6] Y. Murakami, *Stress Intensity Factors Handbook.* Elsevier Science & Technology, 1986.

[7] G. R. Irwin, *Handbook of Physics Vol 6.* 1958.

[8] J. R. Rice, "A Path Independent Integral and the Approximate Analysis of Stress Concentration by Notches and Cracks," *Journal of Applied Mechanics*, vol. 35, pp. 379–386, 1968.

[9] H. J. Frost and M. F. Ashby, *Deformation-Mechanism Maps: The Plasticity and Creep of Metals and Ceramics.* Pergamon Press, 1982.

[10] C. Herring, "Diffusional Viscosity of a Polycrystalline Solid," *Journal of Applied Physics*, vol. 21, pp. 437–445, may 1950.

[11] G. Bernasconi and G. Piatti, *Creep of Engineering Materials and Structures.* Applied Science Publishers, 1979.

[12] G. A. Webster and R. A. Ainsworth, *High Temperature Component Life Assessment.* Springer Netherlands, 1994.

[13] H. E. Evans, *Mechanisms of Creep Fracture*. Elsevier Applied Science, 1984.

[14] A. Abel and H. Muir, "The Bauschinger Effect and Discontinuous Yielding," *Philosophical Magazine*, vol. 26, no. 2, pp. 489–504, 1972.

[15] G. R. Halford, "Brief Summary of the Evolution of High-Temperature Creep-Fatigue Life Prediction Models for Crack Initiation," tech. rep., National Aeronautics and Space Administration, 1993.

[16] G. Dieter, *Mechanical Mettallurgy*. McGraw-Hill Education, 1989.

[17] C. V. Cooper and M. E. Fine, "Coffin-Manson Relation for Fatigue Crack Initiation," *Scripta Metallurgica*, vol. 18, no. 6, pp. 593–596, 1984.

[18] G. Y. Lai, *High-Temperature Corrosion and Materials Applications*. ASM International, 2007.

[19] E. Oberg, "Machinery's Handbook: A Reference Book for the Mechanical Engineer, Designer, Manufacturing Engineer, Draftsman, Toolmaker, and Machinist," in *Machinery's handbook*, pp. 1004–1327, Industrial Press, 2012.

[20] C. Alello, "Carburisation and Creep Phenomena in High-Alloy Materials for Ethylene Pyrolysis Furnaces," *Welding International*, vol. 9, no. 8, pp. 634–636, 1995.

[21] M. Chevalier, "Development of R5 Volume 2/3 Methodology for the Treatment of Carburised Stainless Steels," tech. rep., EDF Energy, 2016.

[22] K. Aoki and K. Kitano, "Surface Hardening for Austenitic Stainless Steels Based on Carbon Solid Solution," *Surface Engineering*, vol. 18, no. 6, 2002.

[23] T. Christiansen and M. Somers, "Low Temperature Gaseous Nitriding and Carburising of Stainless Steel," *Surface Engineering*, vol. 21, no. 5-6, pp. 445–455, 2005.

[24] H. Tawancy and N. Abbas, "Mechanism of Carburization of High-Temperature Alloys," *Journal of Materials Science*, vol. 27, no. 4, pp. 1061–1069, 1992.

[25] S. R. Collins, P. C. Williams, S. V. Marx, A. Heuer, F. Ernst, and H. Kahn, *Low-Temperature Carburization of Austenitic Stainless Steels, ASM Handbook: Heat Treating of Irons and Steels*, vol. 4D. ASM International, 2014.

[26] P. Williams and S. Collins, "Mechanical Design Using Low-Temperature Carburization," *The Journal of The Minerals, Metals & Materials Society*, vol. 60, no. 12, pp. 27–30, 2008.

[27] N. Agarwal, H. Kahn, A. Avishai, and G. Michal, "Enhanced Fatigue Resistance in 316L Austenitic Stainless Steel Due to Low-Temperature Paraequilibrium Carburization," *Acta Materialia*, vol. 55, no. 16, pp. 5572–5580, 2007.

[28] J. Qu, P. J. Blau, and B. C. Jolly, "Tribological Properties of Stainless Steels Treated by Colossal Carbon Supersaturation," *16th International Conference on Wear of Materials*, vol. 263, no. 1-6, pp. 719–726, 2007.

[29] H. Kahn, a. H. Heuer, G. M. Michal, F. Ernst, R. Sharghi-Moshtaghin, Y. Ge, P. M. Natishan, R. J. Rayne, and F. J. Martin, "Interstitial Hardening of Duplex 2205 Stainless Steel by Low Temperature Carburisation: Enhanced Mechanical and Electrochemical Performance," *Surface Engineering*, vol. 28, no. 3, pp. 213–219, 2012.

[30] G. Michal, F. Ernst, H. Kahn, Y. Cao, F. Oba, N. Agarwal, and A. Heuer, "Carbon Supersaturation Due to Paraequilibrium Carburization: Stainless Steels with Greatly Improved Mechanical Properties," *Acta Materialia*, vol. 54, no. 6, pp. 1597–1606, 2006.

[31] D. E. Jiang and E. Carter, "Carbon Dissolution and Diffusion in Ferrite and Austenite from First Principles," *Physical Review B*, vol. 67, no. 21, pp. 214103–1 – 214103–11, 2003.

[32] L. Poirier, Y. Corre, and J. Lebrun, "Solutions to Improve Surface Hardness of Stainless Steels Without Loss of Corrosion Resistance," *Surface Engineering*, vol. 18, no. 6, pp. 439–441, 2002.

[33] Y. Sun, X. Li, and T. Bell, "Low Temperature Plasma Carburising of Austenitic Stainless Steels for Improved Wear and Corrosion Resistance," *Surface Engineering*, vol. 15, no. 1, pp. 49–54, 1999.

[34] T. Bell, "Surface Engineering of Austenitic Stainless Steel," *Surface Engineering*, vol. 18, no. 6, pp. 415–422, 2002.

[35] J. Jones, M. Koul, and J. Schubbe, "An Evaluation of the Corrosion and Mechanical Performance of Interstitially Surface-Hardened Stainless Steel," *Journal of Materials Engineering and Performance*, vol. 23, no. 6, pp. 2055–2066, 2014.

[36] G. Michal, F. Ernst, and A. Heuer, "Carbon Paraequilibrium in Austenitic Stainless Steel," *Metallurgical and Materials Transactions*, vol. 37, no. June, pp. 1819–1824, 2006.

[37] F. Ernst, Y. Cao, G. M. Michal, and A. H. Heuer, "Carbide Precipitation in Austenitic Stainless Steel Carburized at Low Temperature," *Acta Materialia*, vol. 55, no. 6, pp. 1895–1906, 2007.

[38] R. Skelton, "Strain-Induced Oxidation- Environment Interactions Relative to AGR Lifetime Assessment Procedures: A Review," tech. rep., Imperial Consultants, 2012.

[39] A. Wisbey, "Consolidated Metallographic Data from Ex-Service Bifurcations and Tailpipes," tech. rep., AMEC Foster-Wheeler, 2012.

[40] M. Chevalier, "AGR Carburisation of Type 316 Stainless Steel in an AGR Environment : Status of Current Understanding - E/REP/BBGB/0120/AGR/13," tech. rep., EDF Energy, 2013.

[41] R. Bradford, "Current Status of Understanding of the Cracking in the Superheater Bifurcations and Tailpipe- Pintle Welds : A Summary of Structural Analysis Work Undertaken in the Period 2007 to 2009," tech. rep., British Energy Generation Limited, 2010.

[42] "R5: Assessment Procedure for the High Temperature Response of Structures, Issue 3 Rev 001," tech. rep., EDF Energy Nuclear Generation Ltd, 2012.

[43] C. Younes and University of Bristol Interface Analysis Centre, "Oxidation and Carburisation of Type 316 Stainless Steel in AGR Environments - CMY/IAC/15//C04," tech. rep., 2015.

[44] M. Angell, "Surface Hardening and Oxide Fingers on Type 316 Boiler Tubing Oxidised Under AGR Conditions - 17777-TR-002," tech. rep., AMEC Foster-Wheeler, 2013.

[45] C. Younes and T. Scott, "An Investigation into Surface Hardenining Occuring in 316H Boiler Components During In-Service Lifetime," tech. rep., Interface Analysis Centre, University of Bristol, 2013.

[46] EDF Energy, "CO2 Oxidation Handbook, R67, Section 7, Issue 1," tech. rep., British Energy, 1976.

[47] I. M. Reaney, "Analytical Electron Microscopy of Some Oxide/Metal Interfaces," *Materials Science and Technology*, vol. 4, no. 5, 1989.

[48] A. Rao, "Review of Environmental Impact on the Structural Integrity of Type 316 Steels," tech. rep., ATKINS, 2013.

[49] D. Huenert and A. Kranzmann, "Impact of Oxyfuel Atmospheres H2O/CO2/O2 and H2O/CO2 on the Oxidation of Ferritic–Martensitic and Austenitic Steels," *Corrosion Science*, vol. 53, no. 6, pp. 2306–2317, 2011.

[50] D. Young, "Simultaneous Oxidation and Carburisation of Chromia Forming Alloys," *International Journal of Hydrogen Energy*, vol. 32, no. 16, pp. 3763–3769, 2007.

[51] S. Lister and A. Whittaker, "The Oxidation of 18/8 Steels in AGR Gas EPD/GEN/REP0076/96," tech. rep., Nuclear Electric, 1997.

[52] R. Beltran, J. G. Maldonado, L. E. Murrt, and W. W. Fisher, "Effects of Strain and Grain Size on Carbide Precipitation and Corrosion Sensitization Behaviour in 304 Stainless Steel," *Acta mater*, vol. 45, no. 10, pp. 4351–360, 1997.

[53] E. A. Trillo, R. Beltran, J. G. Maldonado, R. J. Romero, L. E. Murr, W. W. Fisher, and A. H. Advani, "Combined Effects of Deformation (Strain and Strain State), Grain Size, and Carbon Content on Carbide Precipitation and Corrosion Sensitization in 304 Stainless Steel," *Materials Characterization*, vol. 35, no. 2, pp. 99–112, 1995.

[54] A. H. Advani, L. E. Murr, D. G. Atteridge, and R. Chelakara, "Mechanisms of Deformation-Induced Grain Boundary Chromium Depletion (Sensitization) Development in Type 316 Stainless Steels," *Metallurgical Transactions A*, vol. 22, no. 12, pp. 2917–2934, 1991.

[55] M. Angell, "The Oxidation Behaviour of Production Boiler Tubing at 873 and 973K in CAGR Atmospheres RPC/CM/P(76) 3," tech. rep., National Nuclear, 1976.

[56] S. Lister, "CO2 Oxidation of 9Cr Steels: Treatment of the Carburised Layer for Integrity Assessments.," tech. rep., British Energy, 2003.

[57] M. Lynch, "Summary of AMEC Activities in Support of ENVISINC Project 2013," tech. rep., AMEC Foster-Wheeler, 2013.

[58] M. O'Donnell, R. Bradford, D. Dean, C. Hamm, and M. Chevalier, "High Temperature Issues in Advanced Gas Cooled Reactors (AGR)," *TAGSI/FESI Symposium 2013*, 2013.

[59] P. Jeffcoat and A. Thorley, "The Influence of Carburization on the Structure and Mechanical Properties of a 9Cr-1Mo Ferritic Steel," in *Liquid Metal Engineering and Technology*, 1984.

[60] C. Bolton, "The Structure and Mechanical Properties of Two AISI 316 Stainless Steel Superheater Tubes," tech. rep., Central Electricity Generating Board (CEGB), 1978.

[61] C. Bolton and I. McLauchlin, "Creep of 9Cr 1Mo Steel in a Carburising Environment," *Corrosion and Mechanical Stress at High Temperatures*, 1980.

[62] B. Fournier, M. Sauzay, C. Caes, M. Noblecourt, M. Mottot, A. Bougault, V. Rabeau, and A. Pi, "Creep Fatigue Oxidation Interactions in a 9Cr1Mo Martensitic steel. Part I: Effect of Tensile Holding Period on Fatigue Lifetime," *International Journal of Fatigue*, vol. 30, no. 4, pp. 649–662, 2008.

[63] B. Fournier, "Effect of Compressive Holding Period on Fatigue Lifetime," *International Journal of Fatigue*, vol. 30, no. 4, pp. 663–676, 2008.

[64] B. Fournier, M. Sauzay, C. Caës, M. Noblecourt, M. Mottot, A. Bougault, V. Rabeau, J. Man, O. Gillia, P. Lemoine, and A. Pineau, "Creep-Fatigue-Oxidation Interactions in a 9Cr-1Mo Martensitic Steel. Part III: Lifetime prediction," *International Journal of Fatigue*, vol. 30, no. 10-11, pp. 1797–1812, 2008.

[65] W. R. Martin and H. E. McCoy, "Effect of CO2 on the Strength and Ductility of Type 304 Stainless Steel and Elevated Temperatures ORNL-TM-339," tech. rep., ORNL, 1962.

[66] M. L. Calvar, P. M. Scott, T. Magnin, and P. Rieux, "Strain Oxidation Cracking of Austenitic Stainless Steels at 610C," *CORROSION*, vol. 54, no. 2, pp. 101–105, 1998.

[67] J. Francis and K. Hodgson, "Interaction of High Temperature Oxidation and Creep Processes in an Austenitic Steel," *Materials Science and Engineering*, vol. 6, no. 5, pp. 313–319, 1970.

[68] G. M. Quaglia, "Slow Strain Rate Tests on AISI 304 at 540 Degrees," in *Proceedings of EPRI VGB Conference 1992*, 1992.

[69] T. A. Ramanarayanan and R. Petkovic-Luton, "A Study of High Temperature Carburization and Its Correlation with the Creep-Rupture Properties of a 30 Cr/30 Ni Austenitic Steel," *Corrosion*, vol. 37, no. 12, pp. 712–721, 1981.

[70] V. Guttman and R. Burgel, "The Creep Behaviour of HK40 and Alloy 800H in a Carburising Environment," in *Corrosion and Mechanical Stress at High Temperatures: Proceedings of the European Symposium*, 1981.

[71] V. Guttman and R. Burgel, *The Effect of a Carburising Environment on the Creep Behaviour of Austenitic Stainless Steels*. 1983.

[72] S. Khodamorad, D. Haghshenas Fatmehsari, H. Rezaie, and A. Sadeghipour, "Analysis of Ethylene Cracking Furnace Tubes," *Engineering Failure Analysis*, vol. 21, pp. 1–8, 2012.

[73] E. Priddle, "The Fatigue and Fatigue Crack Growth Performance of a Service Aged Type 316 Stainless Steel," tech. rep., CEGB, 1985.

[74] H. Kahn, a. H. Heuer, G. M. Michal, F. Ernst, R. Sharghi-Moshtaghin, Y. Ge, P. M. Natishan, R. J. Rayne, and F. J. Martin, "Interstitial Hardening of Duplex 2205 Stainless Steel by Low Temperature Carburisation: Enhanced Mechanical and Electrochemical Performance," *Surface Engineering*, vol. 28, no. 3, pp. 213–219, 2012.

[75] G. Michal, F. Ernst, and A. Heuer, "Carbon Paraequilibrium in Austenitic Stainless Steel," *Metallurgical and Materials Transactions*, vol. 37, pp. 1819–1824, 2006.

[76] L.-H. Cheng and K.-S. Hwang, "Strengthening of Sintered Austenitic Stainless Steels through Low-Temperature Carburization," *Materials Transactions*, vol. 53, no. 1, pp. 179–184, 2012.

[77] K. Tokaji, K. Kohyama, and M. Akita, "Fatigue Behaviour and Fracture Mechanism of a 316 Stainless Steel Hardened by Carburizing," *International Journal of Fatigue*, vol. 26, no. 5, pp. 543–551, 2004.

[78] M. Akita and K. Tokaji, "Effect of Carburizing on Notch Fatigue Behaviour in AISI 316 Austenitic Stainless Steel," *Surface and Coatings Technology*, vol. 200, no. 20-21, pp. 6073–6078, 2006.

[79] L. Podesta, *Environmentally Assisted Creep Crack Growth in 316H Stainless Steel*. PhD thesis, Universite Montpellier, 2014.

[80] ASTM International, "Standard Test Methods for Tension Testing of Metallic Materials E8/E8M - 15a," tech. rep., 2009.

[81] ASTM International, "E139 Standard Test Methods for Conducting Creep , Creep-Rupture , and Stress-Rupture Tests of Metallic Materials," *Annual Book of ASTM Standards 4*, vol. i, pp. 1–14, 2014.

[82] ASTM International, "E606: Standard Test Method for Strain-Controlled Fatigue Testing," 2012.

[83] S. Flanagan, "Summary of Amec Foster-Wheeler Testing Activities in Support of ENVISINC Project - AMEC/203963-01/001," tech. rep., AMEC Foster-Wheeler, 2015.

[84] B. Chen, J. Lindsay, R. A. Ainsworth, and F. Scenini, "Oxidation Behavior of an Austenitic Stainless Steel used in the UK Advanced Gas-Cooled Reactors," in *CORROSION 2015 Conference and Expo*, 2015.

[85] C. Austin, S. May, and L. Hugham, "Tensile Properties and Metallography of Thin Section Type 316H Stainless Steel Tube Materials and Associated Welds," tech. rep., AMEC Foster-Wheeler, 2015.

[86] C. Younes, "Environmental Impact on the Structural Integrity of Nuclear Components: Work Progress - Task 1.2a," tech. rep., University of Bristol, 2014.

[87] M. Chevalier and J. Aveson, "Carburised Material Properties for R5 Volume 2/3 Assessments," tech. rep., EDF Energy Nuclear Generation Limited, 2017.

[88] Dassault Systems, "ABAQUS Version 6.14," 2017.

[89] H. Tada, P. C. Paris, and G. R. Irwin, *The Stress Analysis of Cracks Handbook, Third Edition*. Three Park Avenue New York, NY 10016-5990: ASME, 2000.

[90] H. Grabke and I. Wolf, "Carburization and Oxidation," *Materials Science and Engineering*, vol. 87, pp. 23–33, 1987.

[91] I. McLauchlin, "A Model for the Secondary Creep behaviour of Steel Deforming in a Carburising Environment, and its Application to the Creep of 9Cr Steel in CO2-CO," tech. rep., Central Electricity Generating Board, 1976.

[92] L. P. Pook, *Metal Fatigue*, vol. 145 of *Solid Mechanics and Its Applications*. Dordrecht: Springer Netherlands, 2007.

[93] O. Chopra and J. Shack, "Review of the Margins for ASME Code Fatigue Design Curve - Effects of Surface Roughness and Material Variability," tech. rep., Argonne National Laboratory, 2003.

[94] Instron, "Instron TMF Test Manual," tech. rep., 2009.

[95] ASTM International, "ASTM E83-16: Standard Practice for Verification and Classification of Extensometer Systems," tech. rep., 2017.

[96] S. R. Swanson, *Handbook Of Fatigue Testing*. ASTM International, 1974.

[97] ASTM International, "ASTM 1012: Standard Practice for Verification of Testing Frame and Specimen Alignment Under Tensile and Compressive Axial Force Application," tech. rep., ASTM International, 2017.

[98] P. Hahner, "Validated Code-of-Practice for Strain-Controlled Thermo Mechanical Fatigue Testing," tech. rep., Joint Research Centre, Institute for Energy, Petten NL, 2006.

[99] Vishay Precision Group, "Shunt Calibration of Strain Gage Instrumentation TN-514," tech. rep., 2013.

[100] A. Mehmanparast, *The Influence of Inelastic Damage on Creep, Fatigue and Fracture Toughness*. PhD thesis, Imperial College London, 2012.

[101] EDF Energy, "AGR Material Data Handbook R66 Rev. 007," tech. rep., EDF Energy.

[102] R. Hormozi, *Experimental and Numerical Simulations of Type 316 Stainless Steel Failure under LCF/TMF Loading Conditions*. PhD thesis, Imperial College London, 2014.

[103] D. Kujawski, "Fatigue Failure Criterion Based on Strain Energy Density," *Journal of Theoretical Applied Mechanics*, vol. 27, no. 1, pp. 15–22, 1989.

[104] K. M. Golos, "Total Strain Energy Density Parameter for Fatigue Analysis," *Journal of Applied Mathematics and Mechanics*, vol. 80, no. S2, pp. 469–470, 2000.

[105] K. Golos and F. Ellyin, "Total Strain Energy Density as a Fatigue Damage Parameter," in *Advances in Fatigue Science and Technology*, pp. 849–858, Dordrecht: Springer Netherlands, 1989.

[106] The University of Manchester, "Henry Moseley X-Ray Imaging Facility," 2015.

[107] ASM, *ASM Handbook Volume 11: Failure Analysis and Prevention*. ASM International, 2002.

[108] K. Tokaji, K. Kohyama, and M. Akita, "Fatigue Behaviour and Fracture Mechanism of a 316 Stainless Steel Hardened by Carburizing," *International Journal of Fatigue*, vol. 26, no. 5, pp. 543–551, 2004.

[109] J. Wareing, "Creep-Fatigue Interaction in Austenitic Stainless Steels," *Metallurgical Transactions A*, vol. 8, no. 5, pp. 711–721, 1977.

[110] C. Levaillant, A. Pineau, and B. Rezgui, "Effects of Environments and Hold Times on High Temperature Low Cycle Fatigue Behaviour of 316L Stainless Steel," in *Mechanical Behaviour of Materials*, pp. 163–172, Elsevier, 1980.

[111] C. Levaillant, J. Grattier, M. Mottot, and A. Pineau, "Creep and Creep-Fatigue Intergranular Damage in Austenitic Stainless Steels: Discussion of the Creep-Dominated Regime," in *Low Cycle Fatigue*, pp. 414–414–24, ASTM International.

[112] R. Meltzer, Y. Fiorini, R. Horstman, I. Moore, A. Batik, and W. Ostergren, "A Damage Function and Associated Failure Equations for Predicting Hold Time and Frequency Effects in Elevated Temperature, Low Cycle Fatigue," *Journal of Testing and Evaluation*, vol. 4, no. 5, p. 327, 1976.

[113] O. E. Andreikiv, R. M. Lesiv, and N. M. Levyts'ka, "Crack Growth in Structural Materials Under the Combined Action of Fatigue and Creep," *Materials Science*, vol. 45, no. 1, pp. 1–17, 2009.

[114] Ogata and Arai, "Continuous SEM Observations of Creep-Fatigue Damage Processes," *Fatigue & Fracture of Engineering Materials & Structures*, vol. 21, no. 7, pp. 873–884, 2002.

[115] Y. Takahashi, B. Dogan, and D. Gandy, "Systematic Evaluation of Creep-Fatigue Life Prediction Methods for Various Alloys," *Journal of Pressure Vessel Technology*, vol. 135, no. 6, p. 061204, 2013.

[116] D. Wu, H. Kahn, G. M. Michal, F. Ernst, and A. H. Heuer, "Ferromagnetism in Interstitially Hardened Austenitic Stainless Steel Induced by Low-Temperature Gas-Phase Nitriding," *Scripta Materialia*, vol. 65, no. 12, pp. 1089–1092, 2011.

[117] I. C. Silva, J. M. A. Rebello, A. C. Bruno, P. J. Jacques, B. Nysten, and J. Dille, "Structural and Magnetic Characterization of a Carburized Cast Austenitic Steel," *Scripta Materialia*, vol. 59, no. 9, pp. 1010–1013, 2008.

[118] E. Menéndez, C. Templier, P. Garcia-Ramirez, J. Santiso, A. Vantomme, K. Temst, and J. Nogués, "Magnetic Properties of Single Crystalline Expanded Austenite Obtained by Plasma Nitriding of Austenitic Stainless Steel Single Crystals," *ACS Applied Materials & Interfaces*, vol. 5, pp. 10118–26, oct 2013.

[119] K. J. Stevens and W. J. Trompetter, "Calibration of Eddy Current Carburization Measurements in Ethylene Production Tubes using Ion Beam Analysis," *Journal of Physics D: Applied Physics*, vol. 37, no. 3, pp. 501–509, 2004.

[120] G. Palasantzas, H. Kooij, and J. DeHosson, "Carbon Induced Metal Dusting of Iron–Nickel–Chromium Alloy Surfaces: A Scanning Auger Microscopy Study," *Applied Surface Science*, vol. 229, no. 1, pp. 190–196, 2004.

[121] S. Vaidyanathan, V. Moorthy, T. Jayakumar, and B. Raj, "Evaluation of Induction Hardened Case Depth Through Microstructural Characterisation using Magnetic Barkhausen Emission Technique," *Materials Science and Technology*, vol. 16, no. 2, pp. 202–208, 2000.

[122] M. Blaow, J. T. Evans, and B. A. Shaw, "Surface Decarburisation of Steel Detected by Magnetic Barkhausen Emission," *Journal of Materials Science*, vol. 40, no. 20, pp. 5517–5520, 2005.

[123] D. Mercier, J. Lesage, X. Decoopman, and D. Chicot, "Eddy Currents and Hardness Testing for Evaluation of Steel Decarburizing," *NDT and E International*, vol. 39, no. 8, pp. 652–660, 2006.

[124] X. J. Hao, W. Yin, M. Strangwood, A. J. Peyton, P. F. Morris, and C. L. Davis, "Off-line Measurement of Decarburization of steels using a Multifrequency Electromagnetic Sensor," *Studies in Applied Electromagnetics and Mechanics*, vol. 31, pp. 86–89, 2008.

[125] W. Yin, X. J. Hao, A. J. Peyton, M. Strangwood, and C. L. Davis, "Measurement of Permeability and Ferrite/Austenite Phase Fraction using a Multi-frequency Electromagnetic Sensor," *NDT and E International*, vol. 42, no. 1, pp. 64–68, 2009.

[126] I. C. Silva, L. L. Silva, R. S. Silva, J. M. A. Rebello, and A. C. Bruno, "Carburization of Ethylene Pyrolysis Tubes Determined by Magnetic Measurements and Genetic Algorithm," *Scripta Materialia*, vol. 56, no. 4, pp. 317–320, 2007.

[127] K. Stevens, A. Tack, C. Thomas, and D. Stewart, "Through-Wall Carburization Detection in Ethylene Pyrolysis Tubes," *Journal of Physics*, vol. 34, pp. 814–822, 2001.

[128] A. C. Mcleod, C. M. Bishop, K. J. Stevens, and M. V. Kral, "Microstructural Characterization and Image Analysis in Ex-Service Ethylene Pyrolysis Tubes," *Metallography, Microstructure, and Analysis*, vol. 21, no. 0227, pp. 453–454, 2015.

[129] Fischer, "FERITSCOPE ® FMP30 Measurement of the Ferrite Content in Austenitic and Duplex Steel," tech. rep., Helmut Fischer, 2014.

[130] COMSOL, "COMSOL Multiphysics v5.1," 2016.

[131] N. Wilson and P. Bunch, "Magnetic Permeability of Stainless Steel for use in Acclerator Beam Transport Systems," *Conference Record of 1991 IEEE Particle Accelerator Conference*, pp. 2322–2324, 1991.

[132] W. Staib and H. Künzel, "In-situ Ferrite Content Measurement of Duplex Steel Structures in the Chemical Industry. Practical Applications of the Alternating Field, Magnetoinductive Method," in *Nondestructive Characterization of Materials: Proceedings of the 3rd International Symposium*, pp. 614–621, Springer Berlin Heidelberg, 1989.

[133] N. McCormick and J. Lord, "Digital Image Correlation," *Materials Today*, vol. 13, no. 12, pp. 52–54, 2010.

[134] GOM MBH, *ARAMIS Software - User Manual*. 2009.

[135] B. P. Hohmann, P. Bruck, T. C. Esselman, and T. Schmidt, "Digital Image Correlation (DIC): An Advanced Nondestructive Testing Method for Life Extension of Nuclear Power Plants," in *International Conference on Nuclear Power Plant Life Management (PLiM) for Long Term Operations (LTO)*, pp. 1–8, 2012.

Appendix A. LCF Alignment Reports

Alignment Verification Report

Verified using AlignPRO™ V2.1.3

General Parameters

Operator:	MR-MN
Reference Nº:	8801
Temperature:	0 °C
Frame ID:	8801_TMF
Date:	12:27 pm - 21/Jun/16
Company:	Imperial College
Address:	London
Specification:	ASTM E1012 : 2005
Unit System:	S.I.
Hardware ID:	AP-USB-350-01 [A]
Description:	cylindrical:8

Specimen Parameters

Alignment Cell:	Custom
Cell Description:	cylindrical:8
Material:	N80A
Total Length (lt):	200.0 mm
Length (l):	15.0 mm
Diameter (Ø):	7.0 mm
Area:	38.5 mm²
Count:	8
Type:	350 ohms
Factor:	2.16
Separation (lg):	11.3 mm
Attachment:	Bonding
Alignment Force:	3.0 kN

Results

	Top	Bottom
e1	360.36	367.80
e2	358.65	372.73
e3	357.03	370.30
e4	354.33	371.99
Ave (a)	357.59	370.70
b1	2.77	-2.90
b2	1.05	2.03
b3	-0.57	-0.41
b4	-3.26	1.28
Max Bending	2.72	1.30
% Bending	0.76	0.35

ASTM Calculations

General

$a = (e1 + e2 + e3 + e4) / 4$

$b1 = e1 - a$

$b2 = e2 - a$

$b3 = e3 - a$

$b4 = e4 - a$

$\%B = (B/a) \times 100$

Thick Flat

$B = (|b1 - b3|) / 2 + (|b2 - b4|) / 2$

Cylindrical

$B = \sqrt{((b1 - b3)^2 + (b2 - b4)^2)} / 2$

Thin Flat

$e1 = a - [a - (e5 + e8) / 2][w / (w - 2d)]$

$e3 = a - [a - (e6 + e7) / 2][w / (w - 2d)]$

$c2 = (c5 + c6) / 2$

$e4 = (e7 + e8) / 2$

Test Comments

Aligned with Uni LCF specimen + adapters

Signed: ..... Date: 21/06/2016

Alignment Verification Report

Verified using AlignPRO™ V2.1.3

General Parameters

Operator:	MR-MN
Reference Nº:	8801
Temperature:	0 °C
Frame ID:	8801_TMF
Date:	12:27 pm - 21/Jun/16
Company:	Imperial College
Address:	London
Specification:	ASTM E1012 : 2005
Unit System:	S.I.
Hardware ID:	AP-USB-350-01 [A]
Description:	cylindrical:8

Specimen Parameters

Alignment Cell:	Custom
Cell Description:	cylindrical:8
Material:	N80A
Total Length (lt):	200.0 mm
Length (l):	15.0 mm
Diameter (Ø):	7.0 mm
Area:	38.5 mm²
Count:	8
Type:	350 ohms
Factor:	2.16
Separation (lg):	11.3 mm
Attachment:	Bond
Alignment Force:	10.0 kN

Results

	Top	Bottom
e1	1,256.94	1,266.48
e2	1,192.43	1,247.02
e3	1,261.78	1,264.00
e4	1,318.22	1,303.21
Ave (a)	1,257.34	1,270.18
b1	-0.40	-3.70
b2	-64.91	-23.15
b3	4.43	-6.18
b4	60.88	33.04
Max Bending	62.94	28.12
% Bending	5.01	2.21

ASTM Calculations

General

$a = (e1 + e2 + e3 + e4) / 4$

$b1 = e1 - a$

$b2 = e2 - a$

$b3 = e3 - a$

$b4 = e4 - a$

$\%B = (B/a) \times 100$

Thick Flat

$B = (|b1 - b3|) / 2 + (|b2 - b4|) / 2$

Cylindrical

$B = \sqrt{((b1 - b3)^2 + (b2 - b4)^2)} / 2$

Thin Flat

$e1 = a - [a - (e5 + e8) / 2][w / (w - 2d)]$

$e3 = a - [a - (e6 + e7) / 2][w / (w - 2d)]$

$e2 = (e5 + e6) / 2$

$e4 = (e7 + e8) / 2$

Test Comments

See 3.0kN sheet (Alignment)

Signed: ..... Date: 21/06/2016

Appendix B. Four-Point Bend Digital Image Correlation

Introduction

The reduced ductility of the carburised layer has been shown to greatly affect the performance of preconditioned 316H under both creep and fatigue conditions. When exceeded, widespread surface cracking occurs which leads to a degradation in mechanical properties. The values assigned to both the tensile and creep ductility of a material play a crucial role in determining the remaining lifetime of a component in structural integrity assessment. Therefore, the accurate determination of these for carburised 316H is essential when assessing and designing against the potential impact of AGR carburisation.

Previous laboratory testing found that the tensile and creep ductility of preconditioned 316H lay between 0.2%-0.45% and 0.13% - 0.35%, respectively. These were based on the destructive examination of failed specimens at pre-set levels of stress and strain, resulting in a wide range of possible values. A more accurate determination of ductility would be highly advantageous to component assessment and allow for more robust and less conservative component analysis. This has been explored through preliminary bend testing using an optical strain measurement technique: digital image correlation or DIC. This section presents the initial results of a single bend test conducted on carburised 316H and explores the potential of DIC in determining the ductility of the carburised layer.

Four Point Bending

Typically, the ductility (tensile or creep) of a material is determined by uniaxial tensile testing through measurement of gauge length displacement or a reduction in gauge area. However, when considering a surface effect such as carburisation, it can be useful to conduct bend testing. Naturally, the maximum stresses (tensile and compressive) are concentrated towards the surface regions and this can exaggerate any changes in material properties due to the surface layer which may provide additional information that could not otherwise be obtained from a single uniaxial test. For example, the tensile and creep ductility of the outer surface. Four-point bend testing was therefore used over uniaxial for this DIC investigation.

Compared to three point bending, four point allows for the maximum bending stress to be distributed across the entire sample section, between the two loading pins. This makes it easier to identify cracking and determine the true ductility of the surface as the stress is not concentrated at a single location. This is illustrated in Figure B.1.

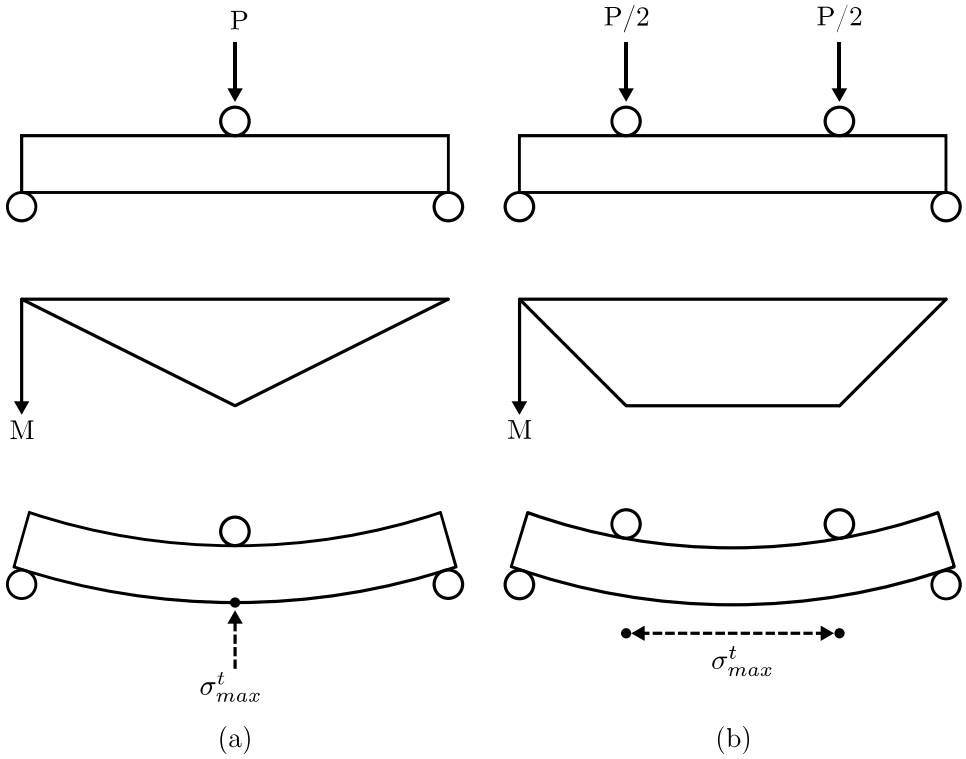


Figure B.1: Difference in distributed moment and maximum tensile stress between (a) three and (b) four point bend testing.

Digital Image Correlation

Digital image correlation in two dimensions was used to detect the presence of any cracking within the carburised layer at a given strain. This is a non-contact optical measurement technique that is able to evaluate the strains on the surface of a body during deformation and is described as follows.

A sequence of images are taken before and after deformation which are then compared to evaluate total relative displacement thus strain [133] (Figure B.2). This relies upon the correlation of a stochastic intensity pattern that is usually created by speckling a surface with contrasting paint coatings which deform with the material. Analysis of the images is undertaken using a software package, such as ARAMIS by GOM [134]. This divides

the measurement surface pattern into individual facets, each with a unique identifier for light intensity. The relative movement of each facet is computed by comparing the position of each before and after deformation which is then used to build up a full strain field across the entire surface in multiple directions.

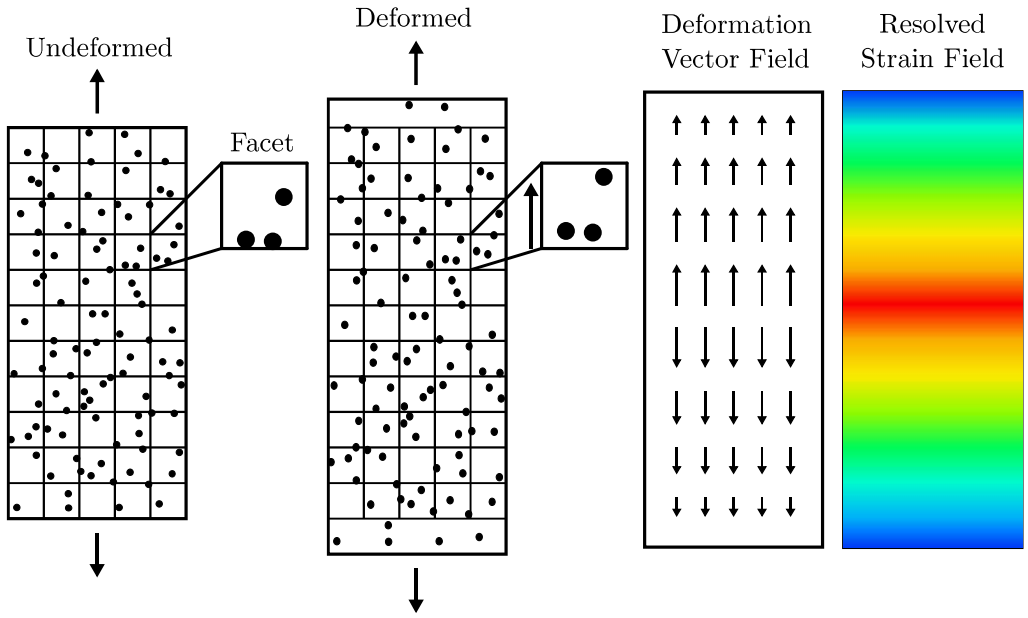


Figure B.2: Illustration of the DIC measurement technique.

The DIC technique offers multiple advantages over traditional strain measurement methods, especially when attempting to detect crack initiation. Whilst these conventional methods (e.g. strain gauges and extensometers) typically evaluate strain over a prescribed distance at a certain location, DIC can provide a strain field across the entire surface of a material. This allows for the evaluation of strains at multiple locations within a single test and is therefore more suited to irregular geometries and the detection of stress concentration factors such as cracks [135].

When attempting to detect the initiation of cracks, it is desirable to maximize the resolution and accuracy of the DIC technique. This depends on a number of variables. Namely, the specimen geometry, optical resolution of images taken and the density and quality the speckle pattern. A finer speckle pattern will enable a smaller facet size to be created, increasing the resolution of the generated strain field.

Sample and Rig Design

A bespoke four point bend rig was designed to test miniature carburised bar samples under high temperature conditions, an illustration of which can be seen in Figure B.3. The rig was fabricated from high strength Nimonic 90 steel and mounted in a servo-hydraulic testing frame. This was capable of applying loads of up to 100kN in both tension and compression. The entire rig was housed within a windowed furnace capable of achieving temperatures of up 1100°C. DIC images were captured through an SLR digital camera using a fixed zoom macro lens. This was set to take photographs at 10 second intervals during testing. The commercial software ARAMIS [134] was used to post-process all image data, computing the total displacement and strain fields. Testing was run under displacement controlled at a constant rate of 0.01 mm/s whilst images were set to be taken at 10 second intervals.

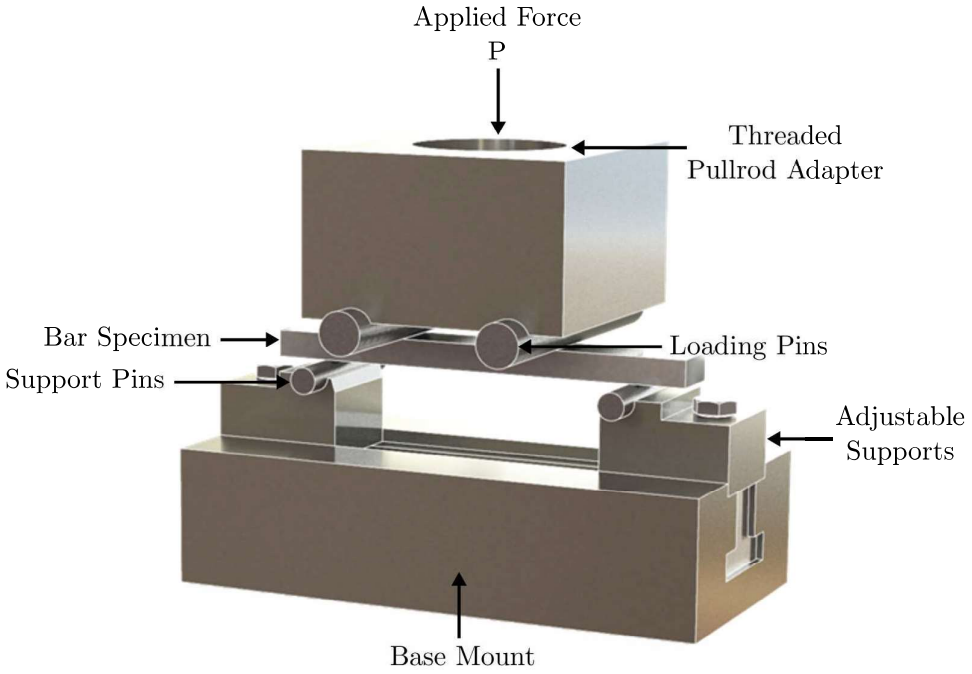


Figure B.3: Illustration of the DIC measurement technique.

Rectangular bend samples were extracted from an as-received header and subsequently preconditioned within the same carburising environment described in Chapter 4. Polishing was undertaken on a single face resulting in carburisation of the bottom surface only (Figure B.4). A high contrast, black on white speckle pattern was sprayed onto the side of samples using a compressed air gun which ensured an even distribution of small speckles across the entire gauge length. This was required to create

facets that could resolve the small-scale strain fields associated with crack initiation ($< 1\%$).

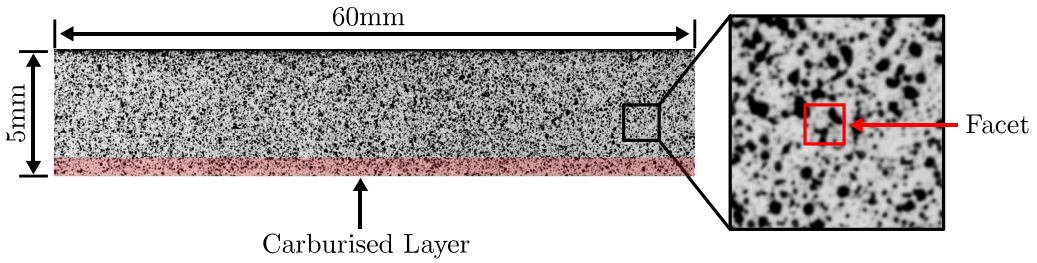


Figure B.4: Speckle pattern on a carburised four point bend specimen showing the typical facet size computed using DIC.

Preliminary Results

Figure B.5 displays the computed strain field at the stage where crack initiation was detected. Surface cracking across the carburised layer can be identified by the strain concentrations on the bottom surface which first appeared at approximately 0.65% total bending strain. These were verified to be initiation sites by tracking subsequent crack growth throughout the remainder of the test. This is shown in Figure B.6. It can be seen that were multiple initiating surface cracks within the carburised layer, the majority of which propagated into the bulk material. Spalling of the paint was also observed in the later stages of test and this was due to the high compressive stresses generated at the surface.

Concluding Remarks

A preliminary study has been undertaken to explore the potential of the DIC technique in detecting crack initiation and thus determining the ductility of the surface of carburised 316H. From this it can be concluded that:

- The DIC technique is capable of resolving small strains ($< 1\%$) under high temperatures within a bend sample geometry.
- The tensile ductility of the carburised layer was found to be approximately 0.65% which is comparable, albeit slightly higher, than that evaluated from creep and fatigue testing.

- Refinement of the speckle pattern is likely to produce more accurate values of ductility as the resolution of the strain field will increase. This will enable the detection of smaller strain concentrations and can be made possible by reducing the area to be examined and processed.
- Four-point bend DIC presents a potential method in determining the creep ductility of carburised 316H, which is likely to differ from the tensile ductility (indicated by the creep crack measurement in Chapter 5).
- Further work should be undertaken, aiming to improve the resolution of the DIC system and trailing the four-point bend test setup under high temperature creep conditions.

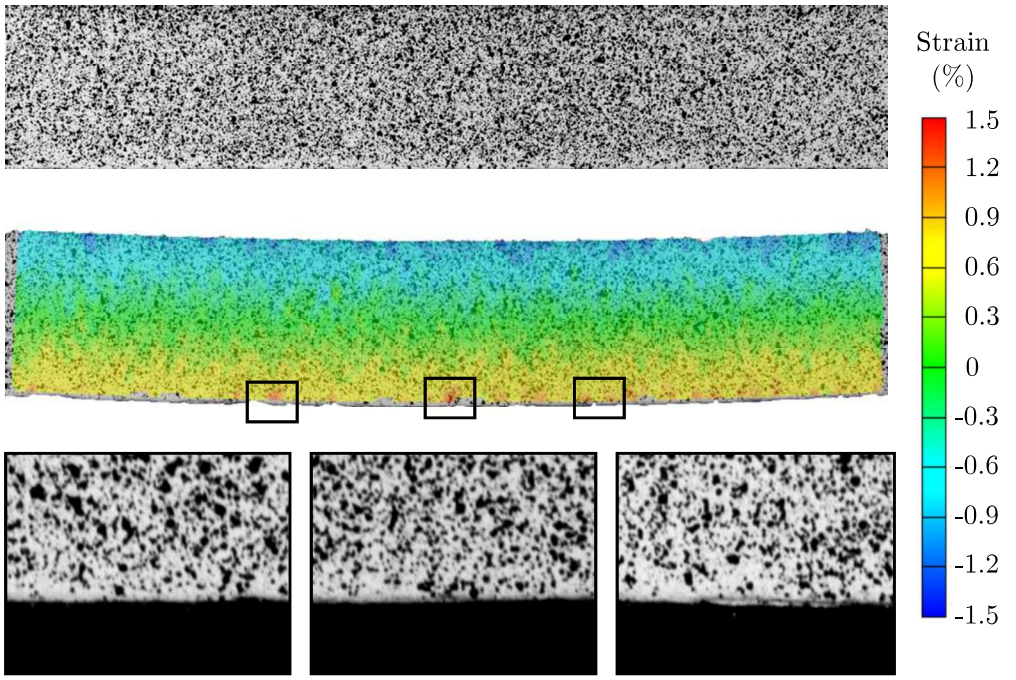


Figure B.5: The strain field of a carburised bend specimen captured using digital image correlation, showing the onset of widespread cracking at approximately 0.65% bending strain.

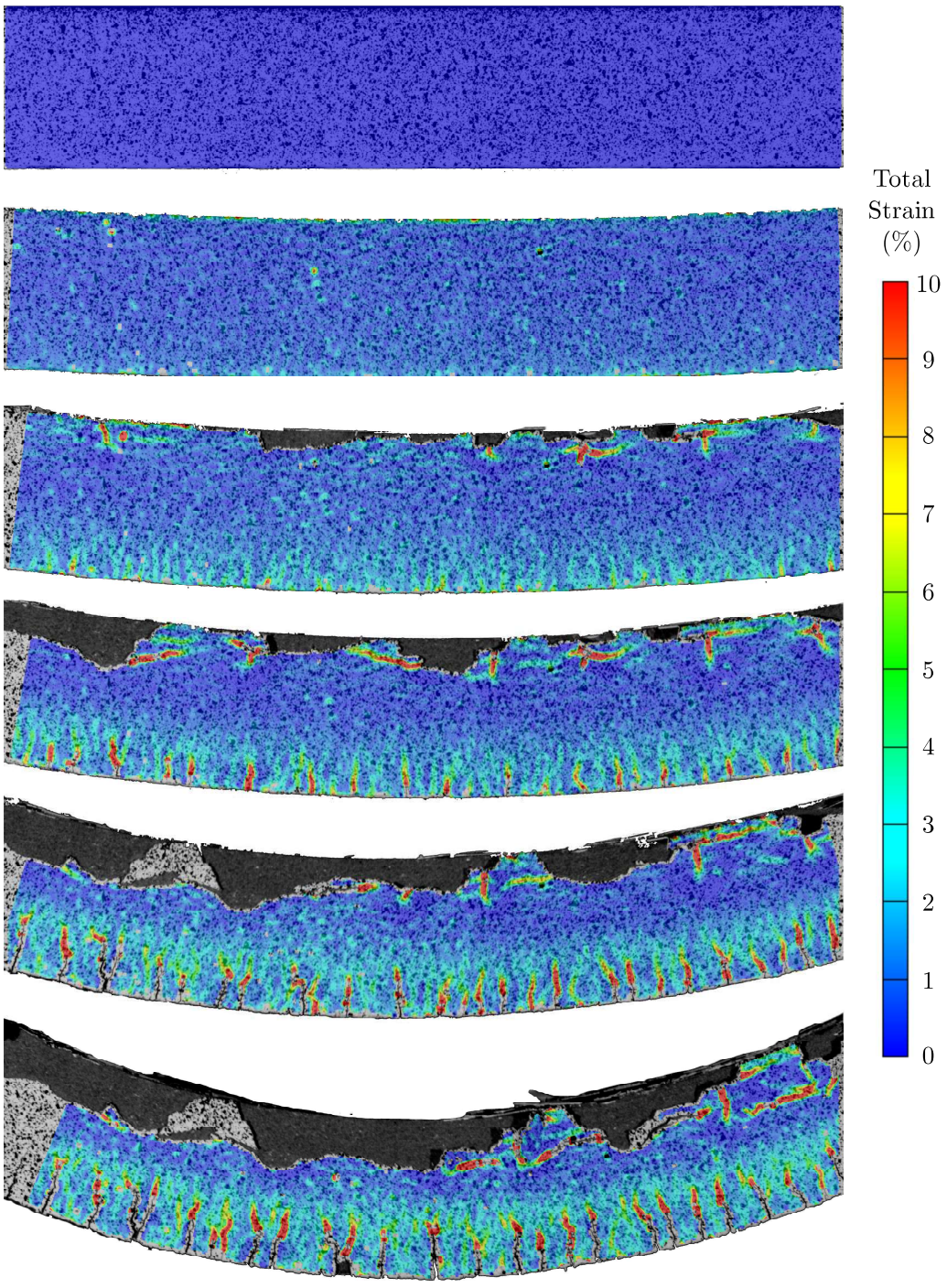


Figure B.6: The evolution and growth of surface cracks during four-point bend testing of carburised 316H and resulting localized crack tip strain fields.